DISSERTATION

ELECTROCHEMICALLY PREPARED METAL ANTIMONIDE NANOSTRUCTURES FOR LITHIUM ION AND SODIUM ION BATTERY ANODES

Submitted by

Everett D. Jackson

Department of Chemistry

In partial fulfillment of the requirements

For the Degree of Doctor of Philosophy

Colorado State University

Fort Collins, Colorado

Fall 2016

Doctoral Committee:

Advisor: Amy Prieto

Anthony Rappe
David Dandy
Travis Bailey
Charles Henry

Copyright by Everett D. Jackson 2016

All Rights Reserved

ABSTRACT

ELECTROCHEMICALLY PREPARED METAL ANTIMONIDE NANOSTRUCTURES FOR LITHIUM ION AND SODIUM ION BATTERY ANODES

The use of energy fundamentally enables and globally supports post-industrial economies and is critical to all aspects of modern society. In recent years, it has become apparent that we will require superior energy technologies to support our society, including improved methods of generating, storing, and utilizing energy resources. Battery technology occupies a critical part of this new energy economy, and the development of electrochemical energy storage devices will be a critical factor for the successful implementation of renewable energy generation and efficiency strategies at the grid, transportation, and consumer levels. Current batteries suffer from limitations in energy density, power density, longevity, and overall cost. In addition, the inherent tradeoffs required in battery design make it impossible to create a single battery that is perfect for all applications. To overcome these issues, the development of low-cost and high-throughput methods, new strategies for materials design, and a comprehensive understanding of electrochemical mechanisms for battery performance is necessary.

Herein, an in-depth study on the electrochemistry of a model anode system for rechargeable batteries based on metal antimony alloys produced through an electroplating approach is detailed. The first chapter of this dissertation provides a brief introduction of lithium ion and sodium ion battery technology. In the second chapter, a detailed review of the literature on antimony and metal antimonide alloys for battery anodes is provided. The third chapter details a study on copper antimonide thin films with varying stoichiometry produced through a facile electrodeposition

process. In the fourth chapter, stoichiometric Cu_2Sb thin films are studied as potential anodes for sodium ion batteries. The fifth chapter details the development of a process for electroplating zinc-antimony alloy thin films onto zinc and their electrochemical properties in sodium ion cells.

The sixth and seventh chapters report the synthesis and characterization of copper-antimony alloy nanowire arrays produced through an alumina-templated process. These nanowire arrays are first used in an electrolyte-additive study to show the importance of surface stabilization for high surface area electrodes in chapter five. In chapter six, the rate performance is characterized under different thermal conditions for different compositions of copper-antimony alloy nanowire arrays as an assessment of the kinetic limitations of this electrode. The final chapter briefly describes some preliminary experiments that have been performed on characterizing the electrochemistry of metal salts in a deep eutectic solvent as a potential method for co-deposition of new metal antimonides.

TABLE OF CONTENTS

ABSTRACT……..……..ii

CHAPTER 1: AN INTRODUCTION TO LITHIUM ION AND SODIUM ION BATTERIES ……..……1

CHAPTER 2: ANTIMONY AND METAL ANTIMONIDES FOR LITHIUM ION AND SODIUM ION BATTERY ANODES…….……...15

CHAPTER 3: LITHIUM ION ANODE PERFORMANCE OF ELECTRODEPOSITED THIN FILM COPPER ANTIMONIDES……...……..….81

CHAPTER 4: REVERSIBLE CONVERSION OF COPPER ANTIMONIDE WITH SODIUM IONS ENABLED BY FLUOROETHYLENE CARBONATE……119

CHAPTER 5: ELECTRODEPOSITED ZN4SB3 THIN FILMS FOR SODIUM-ION BATTERY ANODES……..…132

CHAPTER 6: COPPER ANTIMONIDE NANOWIRE ARRAY LITHIUM ION ANODES STABILIZED BY ELECTROLYTE ADDITIVES ……..……...……..….161

CHAPTER 7: EFFECTS OF COMPOSITION AND MORPHOLOGY ON THE ELECTROCHEMICAL PERFORMANCE OF COPPER ANTIMONY ALLOY NANOWIRE ARRAYS…….185

CHAPTER 8: DEEP EUTECTIC SOLVENTS AS A MEDIUM FOR THE ELECTROCHEMICAL SYNTHESIS OF INTERMETALLIC COMPOUNDS…..……..……206

CHAPTER 1: AN INTRODUCTION TO LITHIUM ION AND SODIUM ION BATTERIES

This chapter was written by Everett D. Jackson with assistance with editing and direction provided by Amy L. Prieto.

1.1 The Secondary Alkali Metal Ion Battery

The rechargeable battery has become a key piece of modern technology, enabling a wide range of technologies spanning from consumer electronics and hybrid electric vehicles, and is now a critical part of upcoming technologies such as grid energy storage and all-electric vehicles.[1-3] The lithium-ion battery in particular has become the most important battery technology in the early 21st century and can be found in all new laptops, cell phones, and electric vehicles as a result of its high efficiency and energy density relative to other electrochemical power sources. This chapter is split into three sections, with the first focusing on the chemistry of these devices. The second section briefly provides a background for experiments that are critical to battery characterization and their importance, and the final section details sodium-ion technology. The focus of this dissertation is on the specific material copper antimonide, but this chapter deals more generally with battery technology. A more in-depth review of the literature and background of metal antimonides can be found in chapter 2.

Undoubtedly, the lithium ion battery has been transformative to the modern world. The mobile revolution has relied on the large energy density provided by lithium ion batteries to produce compact cell phones, laptop and tablet computers, video cameras, etc.[1] The lithium ion battery is now being pushed to the limits of its technological capabilities in order to bring electromobility (all-electric vehicles) as an alternative to chemical fuel driven vehicles. This future advancement is dependent on the ability of scientists and engineers to deliver safe and cost

effective batteries with the highest possible energy and power densities. Unfortunately, these are often competing requirements, as putting more energy into a smaller space requires pushing the energetic materials that store the energy to their thermodynamic limit and reducing any kinetic limitations as far as possible. Advances in chemistry, materials science, and engineering are necessary to push the boundaries of stability and reactivity and find suitable lithium ion cells to satisfy these requirements.[4,5]

Before considering next-generation lithium ion battery technologies, it is necessary to understand the electrochemistry predating their commercial appearance. The development of the lithium ion cell has been long researched due to the obvious advantages of lithium: an extremely negative standard reduction potential, high charge to mass ratio, and small volume.[2] These properties suggest that it is possible to build a battery with a high operating voltage and both low volume and weight per unit charge, leading to a very high theoretical energy density. Initial research attempted to use batteries with the cell type of Li | Li^+ (~1 M) || Li^+ | MnO_2, but were limited to primary operation and could not be regenerated.[6] This was primarily the result of the irreversibility of conversion chemistry, as prototype cathode materials such as CuS and V_2O_5 underwent total structural reformation upon lithium incorporation as shown in eq. 1 and eq. 2. A critical development was the discovery of lithium intercalation into TiS_2 by Whittingham in 1976 as shown in eq. 3.[7]

(1) $CuS + 2Li^+ + 2e^- \rightarrow Cu + Li_2S$

(2) $V_2O_5 + 10Li^+ + 10e^- \rightarrow 2V + 5Li_2O$

(3) $TiS_2 + Li^+ + e^- \rightarrow LiTiS_2$

In contrast to the conversion reactions above, intercalation reactions proceed by introduction of lithium ions into void space within a material's crystal lattice.[7-9] The resulting lithiated compound does not undergo structural rearrangement, which leads to high reversibility and stability for both lithium insertion and desertion. Despite the enhanced stability of intercalation compounds, the use of a lithium anode caused early attempts to suffer from safety and reliability issues. Exxon attempted to commercialize a Li-TiS_2 lithium battery in 1977, but dendritic growth of lithium caused internal short circuiting, resulting in fires.[2] This was initially corrected by the use of Li-Al alloy anodes, which did not produce dendrites but only provided lifetimes of *ca. 10* cycles.[10] These were apparently sufficient, as the electrolytes used at the time also deteriorated quickly.

All early attempts at making secondary cells suffered from issues arising from instability of the state of the art non-aqueous organic solvents, lithium salts, the lithium metal surface, as well as the low energy density of the TiS_2 cathode due to a modest cell potential of ~2.2 V v. Li/Li^+ (although the energy density was still higher than other cell chemistries at the time). The discovery of the high-voltage (> 4 V v. Li/Li^+) intercalation cathode material $LiCoO_2$ by Goodenough *et al.* in 1980 realized the high theoretical energy density that modern lithium ion batteries are known for.[11] The higher voltage offered by transition metal oxide intercalation materials allowed for the subsequent use of anodes aside from lithium metal, while still maintaining an overall high cell voltage. This was particularly critical, as lithium metal anodes suffered from dendritic plating and significant side reactions with electrolytes, leading to instability and poor safety. The lithium-graphite compound LiC_6, originally studied as early as 1965, ultimately proved to be an excellent anode, especially when paired with organic carbonates for the electrolyte.[12] The cathodic instability of the R_2O_2CO functional group of the carbonate reacts with the surface of the graphite

particles to create *in-situ* a protective layer that provides full cell reversibility. This type of cell is shown schematically in Fig. 1, below.

The commercially useful implementation of the lithium ion cell utilizes a thin-cell configuration, where the anode and cathodes sandwich a porous polymer membrane film. The anode consists of graphite particles with a suitable binder, generally polyvinylidene difluoride (PVDF), and the cathode utilizes a lithium metal oxide, PVDF binder, and carbon black for electrical conductivity. This cell stack is flexible, and can be rolled or stacked to produce a battery with many layers of cathode and anode and fit into a flat package or cylindrical cell. The energy density and power density are then optimized by adjusting the relative thickness of the metal foil, separator, and active material films to achieve the desired power characteristics.

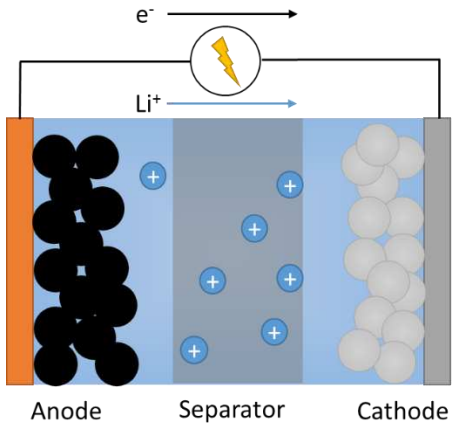

Figure 1.1.1. Schematic representation of a lithium-ion battery cell. Two electrodes are separated by a porous polymer film soaked with an electrolyte of lithium salt in organic carbonate solvent. The anode is a film of carbon particles and polymer binder pasted onto a thin copper foil, and the cathode is a film of metal oxide particles, small carbon particles, and a polymer binder pasted on thin aluminum foil. Typical dimensions of one full cell are 100-200 µm in diameter.

Commercialization of the lithium ion cell proceeded in 1991 by Sony as a graphitic carbon and lithium cobalt oxide cell.[2] Since this inception, the materials have evolved, but maintained the

principle structure of this original cell. As a result, there have been large but not revolutionary enhancements in the safety, cost, energy and power densities, and longevity of lithium ion battery cells. There remains a significant demand for substantial increases in battery performance, and subsequent decreases in cost, to enable all-electric vehicles with acceptable ranges (>200 miles) at reasonable prices (<$30,000). Other technologies, such as grid storage, require significant reductions in the price in terms of kWh $^{-1}$.[13] There remain significant technological limitations in terms of what can be achieved by current lithium ion cells as a result of fundamental materials and architecture limits. In order to achieve significant advancement, new technologies must be explored, while still taking advantage of the great wealth of knowledge learned from decades of experimentation with lithium ion cells.

1.2 Determining the Performance of Anode Materials in Lithium Ion Cells

Materials discovery and analysis remains a pivotal part of the development of new battery technologies. Understanding how the individual materials, as well as the transformations that occur during electrochemical reactions, is critical to their successful implementation.[3] It should come as no surprise that the number of publications dealing with lithium ion battery materials has become enormous. To date, at least 47,000 reports on the subject have been published, with over 500 such papers being published monthly since 2013. Even within the smaller subset of anode materials, over 12,000 reports have been published, with over 10,000 since 2010. In the face of such a rapid expansion of the literature, it is important to understand the experiments involved in electrochemical characterization and their implications towards battery materials.[14] The importance of this cannot be understated, as despite nearly forty years of intensive research, and thousands of reports of "superior" anode materials, graphite remains the only heavily commercialized anode material to date.[2]

Every battery operates on the principle of using an electrochemical cell with two electrodes that contain compounds at different electrochemical potentials. The voltage of a battery is given by the difference in the electrochemical potential of the two compounds, while the capacity is governed by the number of electrons required for the reaction and the number of ions produced during one full discharge. For an ideal cell, the energy of a battery is simply the product of these two quantitites. These values are typically normalized to the volume and/or mass of the material under evaluation as a way of interpolating the materials prospective performance in a useful battery. An electrochemical half-cell is generally employed to perform experiments that provide these quantities, where one electrode is lithium metal and has a voltage of the Li/Li^+ electrochemical couple and an effective infinite capacity as it is used in significant molar excess over the electrode being studied. These types of experiments allow for the determination of most critical anode figures of merit, when appropriately assessed.

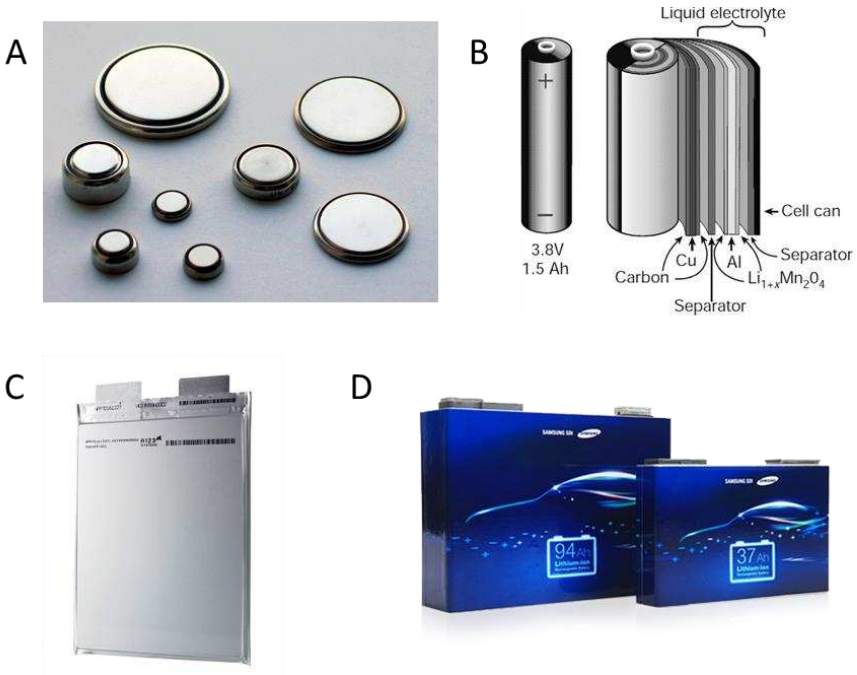

Figure 1.2.1. Some common electrochemical cells used in battery materials evaluation at different device levels. (A) Coin cells (wiki), (B) a cylindrical cell, (C) a pouch cell (A123), and (D) a prismatic cell.

Typical battery cells are shown in Fig. 1.2.1. The geometry of a lithium ion cell can vary significantly from small coin cells suitable for watches to large prismatic cells capable of powering electric vehicles. Nevertheless, the underlying geometry of the components remains similar for all of these cases, with the components being a stack of anode, then separator, then cathode, then separator again, wound repeatedly until the desired volume is achieved. To simulate the conditions of one of these cells, a material is generally assembled as the working electrode in either a laboratory coin or Swagelok™ half-cell assembled with a lithium metal counter electrode with an internal geometry like that shown in Fig. 1.2.2A. Many novel *in-situ* electrochemical cells (e.g. X-ray diffraction, Mossbauer spectroscopy, electron microscopy) have also been developed to extract detailed information about battery materials during electrochemical reaction.[15-19] These cells are used in conjunction with laboratory electrochemical test equipment to extract fundamental thermodynamic and kinetic information about the materials under study.

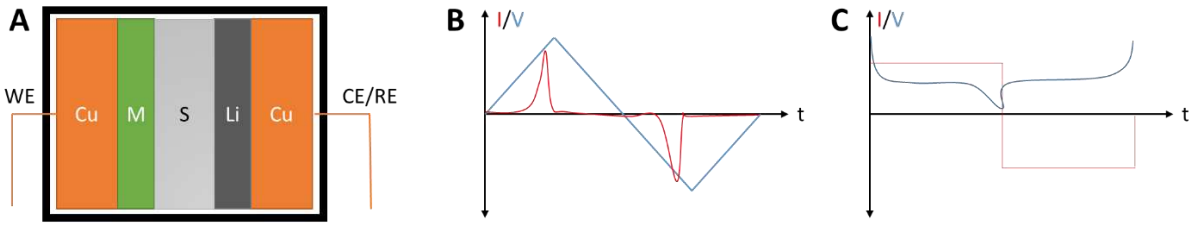

Figure 1.2.2. Electrochemical experiments used in battery materials evaluation. (A) An internal schematic of a typical half-cell (M = material, S = separator, Li = Lithium metal, Cu = copper metal), (B) a cyclic voltammogram, (C) a galvanostatic charge-discharge cycle test.

Cyclic voltammetry is often used as a first test, and can provide some useful kinetic and thermodynamic information. However, these measurements are limited in applicability for bulk electrode experiments due to the impacts of bulk diffusion and solid-state reaction kinetics. As a result, the more common and useful experiment is a galvanostatic (constant current) charge-discharge experiment with voltage limits. These are shown schematically in Fig. 1.2.2. These

experiments are used to determine the reversibility of a reaction, the electrochemical potential at which a material is useful, and as a rudimentary test for electrode performance. In a galvanostatic cycle experiment, it is possible to determine the amount of charge that a material can hold, usually given in mAh g^{-1} or mAh cm^{-3}, and the electrochemical potential at which redox chemistry occurs, in volts v. Li/Li^+. In addition, it is possible to determine the reversibility of the cell by taking the ratio of charge to discharge capacities as a percentage, which is referred to as coulombic efficiency. To provide a useful frame of reference with regard to the power capability of a material, the current is often expressed in terms of "C rate", which is defined as the fraction of charge passed per hour relative to the total charge of the electrode. For example, a C/5 rate provides the current required to fully (dis)charge an electrode in five hours, whereas a 5C rate would fully (dis)charge an electrode is 12 minutes (1/5 of an hour). The capacity and coulombic efficiency under a given set of voltage limits and C rates is often the primary figure of merit presented for new battery materials.

Table 1.2.1. Graphite versus silicon as anode materials.

	Graphite	Silicon
Capacity (mAh g^{-1} / Ah L^{-1})	350 / 719	3579 / 2194
Potential (V v. Li/Li^+)	0.125	0.40
Expansion (%)	10	280

The internal architecture of the lithium-ion battery allows for some clear predictions for what materials should theoretically make good anode materials. To maximize the volumetric and gravimetric energy density, the reversible capacity should be as large as possible and the material should be as dense as possible. In addition, energy will be maximized when the electrochemical potential of the redox couple is as close to lithium metal as possible (leading to a high full cell

voltage). The power capability will be maximized when electronic conductivity and ionic conductivity are as high as possible. To produce high energy and power density anode materials, researchers have primarily focused on four types of materials: carbons,[20] alloys,[21] oxides,[22] and sulfides.[23] Only carbons and alloys have the prerequisite properties to make useful anodes, however, as the oxides and sulfides operate under excessively high voltages and with unacceptably large voltage hysteresis for a practical battery.[21] Currently, graphite is the primary commercial anode material, but silicon alloy anodes are becoming increasingly common due to the substantial gains in capacity over graphite (Table 1.2.1), and commercial examples of mixed carbon-silicon electrodes now exist.[24]

1.3 Sodium Ion Batteries as an Alternative to Lithium Ion Batteries

In recent years, a clear need has been identified for lower-cost and sustainable technologies that can be deployed at medium and large scales to provide reliable energy storage for applications such as backup power supplies and grid energy storage for renewable energy production.[25] Although lithium ion chemistry provides exceptional energy and power densities, it uses relatively costly and toxic cobalt in the cathode.[26] Furthermore, there have recently been some worries about the availability of high quality global lithium supplies.[27,28] As an alternative, sodium ion battery cells have been suggested as sodium is exceptionally abundant and inexpensive, yet possess very similar chemistry to lithium.[29] As a result, a great deal of research in the last five years has been devoted to studying materials that can act as sodium ion storage materials to provide batteries that provide performance near that of lithium ion cells but with potentially lower cost.[30]

Anode materials for sodium ion batteries have been identified as one of the major limiting factors preventing a practical battery cell.[31] Unlike lithium, sodium does not intercalate into graphite at room temperature or alloy with silicon. Similar to lithium, however, sodium does alloy with tin and antimony. Sodium reacts with tin to form $Na_{15}Sn_4$ with a capacity of 847 mAh g^{-1}, and with antimony to form Na_3Sb with a capacity of 660 mAh g^{-1}. Early discussions on the subject of alloy anodes for sodium ion battery noted that it implementation would likely be challenging due to the significantly larger size of sodium ions.[32] Despite the larger size of sodium relative to lithium, anodes using antimony and tin have shown surprising reversibility, suggesting that alloy anodes may be suitable for sodium ion battery cells.[33,34]

Compared to the thousands of papers that have been published on lithium ion batteries, sodium ion battery research is still in its infancy. Some notable progress has been made in cathode chemistry, enabling prototype full cells to be studied.[35] Significant progress has also been made

on anode chemistry in recent years.[31] At this point in time, electrolyte issues are still a substantial issue, mirroring the difficulties that were found with early lithium ion cells.[36] At this time, it is difficult to predict how far sodium ion chemistry can advance since there are no defined "standard" materials that can be used as a benchmark to date.

1.4 Summary

This chapter has briefly discussed lithium ion and sodium ion batteries and their materials. The primary focus of this dissertation is on the use of electrodeposited metal antimonides as potential anode materials for lithium on and sodium ion batteries. Chapters 3 and 4 detail the performance of copper antimonide thin films in each type of cell. In chapter 5, a new procedure for preparing zinc antimonide thin films and the first investigation of sodium ion alloying with this material is presented. Chapters 6 and 7 present a modified method for producing copper antimonide nanowire arrays from alumina templates with a high degree of control over the composition and morphology compared to similar studies. Finally, preliminary results on using deep eutectic solvents as potential electrodeposition electrolytes that allow for the deposition of new metal antimonides is provided in chapter 8. These works provide insight into some of the advantages and disadvantages of electroplated antimony compounds as anode systems for lithium ion and sodium ion batteries.

REFERENCES

1. Armand, M.; Tarascon, J. M. *Nature* **2008**, *451*, 652.

2. Whittingham, M. S. *Proceedings of the IEEE* **2012**, *100*, 1518.

3. Crabtree, G.; Kócs, E.; Trahey, L. *MRS Bulletin* **2015**, *40*, 1067.

4. Whittingham, M. S. *Chemical Reviews* **2014**, *114*, 11414.

5. Arico, A. S.; Bruce, P.; Scrosati, B.; Tarascon, J.-M.; van Schalkwijk, W. *Nat Mater* **2005**, *4*, 366.

6. Whittingham, M. S. *Chemical Reviews* **2004**, *104*, 4271.

7. Whittingham, M. S. *Journal of The Electrochemical Society* **1976**, *123*, 315.

8. Whittingham, M. S.; Chianelli, R. R. *J. Chem. Educ* **1980**, *57*, 569.

9. Whittingham, M. S. *Progress in Solid State Chemistry* **1978**, *12*, 41.

10. Rao, B. M. L.; Francis, R. W.; Christopher, H. A. *Journal of The Electrochemical Society* **1977**, *124*, 1490.

11. Mizushima, K.; Jones, P. C.; Wiseman, P. J.; Goodenough, J. B. *Materials Research Bulletin* **1980**, *15*, 783.

12. Yazami, R.; Touzain, P. *Journal of Power Sources* **1983**, *9*, 365.

13. Amjad, S.; Neelakrishnan, S.; Rudramoorthy, R. *Renewable and Sustainable Energy Reviews* **2010**, *14*, 1104.

14. Winter, M.; Brodd, R. J. *Chemical Reviews* **2004**, *104*, 4245.

15. Reimers, J. N.; Dahn, J. R. *Journal of The Electrochemical Society* **1992**, *139*, 2091.

16. Nakai, I.; Nakagome, T. *Electrochemical and solid-state letters* **1998**, *1*, 259.

17. Dahn, J.; Py, M.; Haering, R. *Canadian Journal of Physics* **1982**, *60*, 307.

18. Fong, R.; Jones, C.; Dahn, J. *Journal of Power Sources* **1989**, *26*, 333.

19. Orsini, F.; Du Pasquier, A.; Beaudoin, B.; Tarascon, J.; Trentin, M.; Langenhuizen, N.; De Beer, E.; Notten, P. *Journal of power sources* **1998**, *76*, 19.

20. Wu, Y.-P.; Rahm, E.; Holze, R. *Journal of Power Sources* **2003**, *114*, 228.

21. Obrovac, M. N.; Chevrier, V. L. *Chemical Reviews* **2014**, *114*, 11444.

22. Poizot, P.; Laruelle, S.; Grugeon, S.; Dupont, L.; Tarascon, J. M. *Nature* **2000**, *407*, 496.

23. Malini, R.; Uma, U.; Sheela, T.; Ganesan, M.; Renganathan, N. *Ionics* **2009**, *15*, 301.

24. Service, R. F. *Science* **2016**, *352*, 1046.

25. Luo, X.; Wang, J.; Dooner, M.; Clarke, J. *Applied Energy* **2015**, *137*, 511.

26. Nelson, P. A.; Gallagher, K. G.; Bloom, I. D.; Dees, D. W. *Modeling the Performance and Cost of Lithium-Ion Batteries for Electric-Drive Vehicles*, Argonne National Laboratory (ANL), 2012.

27. Vikström, H.; Davidsson, S.; Höök, M. *Applied Energy* **2013**, *110*, 252.

28. Tarascon, J.-M. *Nat Chem* **2010**, *2*, 510.

29. Nithya, C.; Gopukumar, S. *Wiley Interdisciplinary Reviews: Energy and Environment* **2015**, *4*, 253.

30. Palomares, V.; Serras, P.; Villaluenga, I.; Hueso, K. B.; Carretero-González, J.; Rojo, T. *Energy & Environmental Science* **2012**, *5*, 5884.

31. Kim, Y.; Ha, K. H.; Oh, S. M.; Lee, K. T. *Chemistry–A European Journal* **2014**, *20*, 11980.

32. Chevrier, V. L.; Ceder, G. *Journal of The Electrochemical Society* **2011**, *158*, A1011.

33. Darwiche, A.; Marino, C.; Sougrati, M. T.; Fraisse, B.; Stievano, L.; Monconduit, L. *Journal of the American Chemical Society* **2012**, *134*, 20805.

34. Xiao, L.; Cao, Y.; Xiao, J.; Wang, W.; Kovarik, L.; Nie, Z.; Liu, J. *Chemical Communications* **2012**, *48*, 3321.

35. Han, M. H.; Gonzalo, E.; Singh, G.; Rojo, T. *Energy & Environmental Science* **2015**, *8*, 81.

36. Ponrouch, A.; Monti, D.; Boschin, A.; Steen, B.; Johansson, P.; Palacin, M. R. *Journal of Materials Chemistry A* **2015**, *3*, 22.

CHAPTER 2: ANTIMONY AND METAL ANTIMONIDES FOR LITHIUM ION AND SODIUM ION BATTERY ANODES

This thesis chapter was written by Everett D. Jackson with guidance and editing by Amy L. Prieto as a review article. This chapter was conceived as a review article for summarizing the work done to date on antimony based anode materials for lithium ion and sodium ion batteries, as this subject has not received a dedicated review to date despite nearly two decades of many publications.

2.1 Alloying Anodes and Antimony in Lithium Ion Batteries

Many elements undergo two-phase reactions with lithium in electrochemical cells. These reactions have been extensively studied for use in batteries as they operate at a constant electrochemical potential and provide much higher gravimetric and volumetric capacities than intercalation compounds. Many useful reviews have been published on this subject(*1-10*). In particular, a recent review has reported the history and prospects of these materials in great detail(*11*). The elements known to form lithium alloys in electrochemical cells of interest are Mg, Ag, Cd, Zn, Al, Si, Ga, Ge, In, As, Te, Sn, Sb, Au, Hg, Pb, and Bi(*12-17*). Some other elements, such as Ca, Sr, Rh, and Ir may also alloy but are unlikely to be of any significant use due to toxicity, safety, or low abundance. Among this long list, the alloys of primary interest have been Al, Si, Sn and Sb, owing to their relatively high theoretical capacities, high abundance, and low toxicity. Nevertheless, alloying electrodes have rarely been commercialized, with the only notable example being Sony's Sn-Co-O anode used in Nexelion batteries(*18*) released in 2005. A detailed review of antimony-based electrodes does not currently exist. As such, this chapter will focus on the potential of antimony and antimony alloys as an anode material.

The use of antimony as an electrochemically active material in a lithium-ion cell was first described by Besenhard and Fritz in 1974,(*19*) where they noted that a Li/Sb cell possesses high energy density and coulombic efficiency in cells using $LiClO_4$/PC electrolyte. Shortly thereafter, Weppner and Huggins studied the thermodynamics and kinetics of antimony electrodes while developing methods to reliably test ionic conduction in mixed-conductors in high temperature cells.(*16, 20, 21*) Huggins revisited the Li-M (M = Sn, Sb, Bi) system in 1986 to determine their suitability as negative electrodes to pair with lithium-ion cathodes that were being developed at the time, but concluded that "The potentials of these plateaus are too high (over 0.8V vs. pure lithium at room temperature) to be useful as a negative electrode materials in most lithium-based cells."(*12*) Despite this, antimony still possesses high enough volumetric and gravimetric capacities to provide higher energy density than graphite in full-cell models.(*11*) A fundamental redesign of the lithium ion battery cell using antimony as an active material has been proposed as a low cost, safer alternative to graphite for high-power applications and is now being commercialized, suggesting that this type of anode material warrants a detailed evaluation.(*22*)

Antimony anodes have been reported to suffer serious pitfalls, including pulverization from the large volume change during cycling of approximately 150%, fast capacity fade, low coulombic efficiency, and high average voltage of 0.95V. Progress was made by Besenhard and Winter by reducing the particle size less than a micron, leading to better reversibility.(*8*) The Li-M-Sb compounds were also targeted as potential materials to overcome this issue by providing a volume buffer, improved mechanical properties, and improved electronic properties provided by the secondary metal. Yang, Winter, and Besenhard then further improved this system by applying it to the multiphase metallic host materials Sn/$SnAg_x$ and Sn/$SnSb_x$.(*23*) Skutterudite $CoSb_3$ was the first transition metal antimonide to be studied, with markedly different results compared to pure

antimony.(*24*) Specifically, the material was found to become amorphous upon lithiation, form a thick passivating layer due to electrolyte decomposition, retain capacity better than equivalent pure antimony electrodes, and undergo conversion to a two-component system of amorphous cobalt and Li_xSb. Vaughey, O'Hara, and Thackeray then studied antimony as an electrode material in 2000 in the form of InSb while studying the electrochemistry of Li-M-M' electrodes (M = any metal, M' = Sn or Sb) in lithium ion cells and concluded that an improved cycle life was due to an intercalation mechanism. Follow-up of this study using *in situ* X-ray diffraction showed conclusively that this type of anode undergoes conversion to form a multiphase material consisting of Li-M + Li-M' or M + Li-M' if M is unreactive towards lithium.(*25*) Hewitt, Beaulieu, and Dahn also performed *in situ* X-ray diffraction on pure antimony electrodes, and confirmed the structural transformations and reversibility of the Li-Sb and Li-In-Sb alloying reactions.(*26*)

Up to this time, alloy anodes had only received modest interest. A review by Huggins in 1999 on alloy anodes cited only 37 publications.(*7*) The rise of lithium-ion batteries in cell phones, laptops, cameras, and the booming electronics industry has since led to an unprecedented rise in interest in high capacity batteries and there are now over 100 publications on antimony anodes for lithium ion batteries alone. To cover this topic thoroughly, a perspective on the use of Sb compounds as anode materials will be discussed. Following this, the Li-Sb system will first be discussed, followed by ternary Li-M-Sb materials. Following this, studies on alternative-ion batteries using antimony anodes will be briefly overviewed, and finally the consequences of battery architecture will be discussed.

2.2 Perspective and Outlook

Antimony has received significant attention as a potential lithium ion anode material since *ca.* 2000. The literature is less extensive than that for graphite, the current state of the art anode material, and Si, the material currently expected to replace graphite. Unlike either of these materials, antimony alloys readily with other materials, producing a chemically rich system of study. The use of secondary elements provides a method to tune and control reaction pathways, mechanical and electrical properties, and surface chemistry. This type of study is exemplified in the fundamental studies that have been performed on many of the metal antimonides. Nevertheless, there remain significant deficits in the performance of Sb-based electrodes, and some skepticism of practicality. This section provides a critical analysis of the potential benefits and pitfalls of an electrode using antimony as the active component in a lithium ion or sodium ion anode.

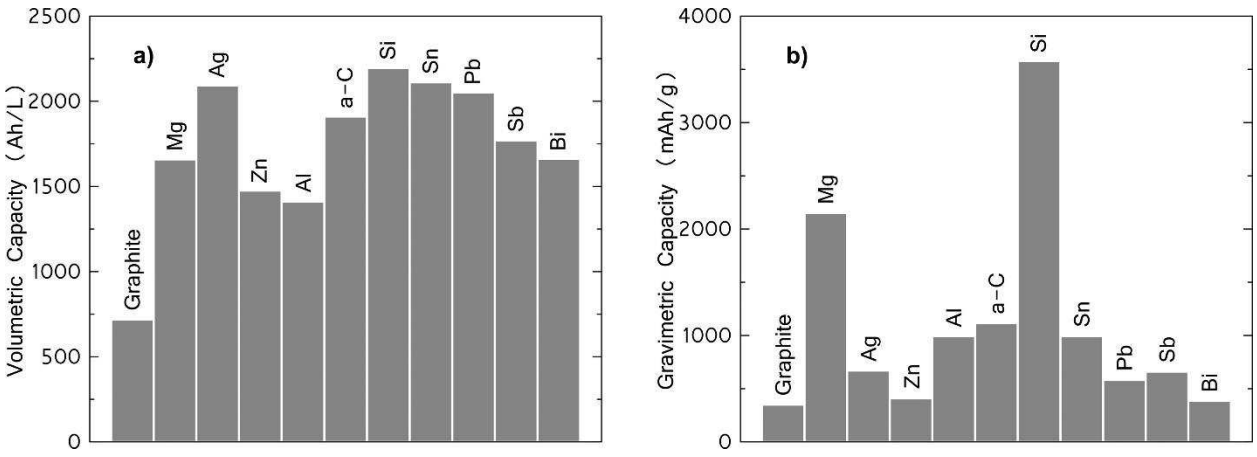

Figure 2.1. (a) Volumetric capacities calculated at the state of full lithiation and (b) gravimetric capacities of selected elements. Reprinted (adapted) with permission from ref. 11. Copyright © 2014 American Chemical Society.

It should be noted that antimony has long been considered a relatively low energy density compound owing to its higher electrochemical potential (~1 V v. Li/Li^+) compared to other anode materials that usually operate between 0.1 and 0.5 V v. Li/Li^+. Many researchers have therefore

been skeptical that it could ever be used in a practical battery.(*11, 12*) This is compounded with the relatively modest gravimetric capacity of antimony compared to other alloying materials (660 mAh g^{-1} v. 993 mAh g^{-1} for Sn and 3579 mAh g^{-1} for Si). Nevertheless, antimony does possess a high volumetric capacity comparable to other alloys and higher gravimetric capacity than graphite (Fig. 2.1). When used in conventional lithium ion cells, a simple theoretical cell level model proposed by Obrovac and Chevrier has shown that antimony has improved energy density over graphite.(*11*) The advantage is relatively small, however, and the metal antimonides discussed in this review often have reduced gravimetric and volumetric capacities due to the incorporation of inactive transition metals.

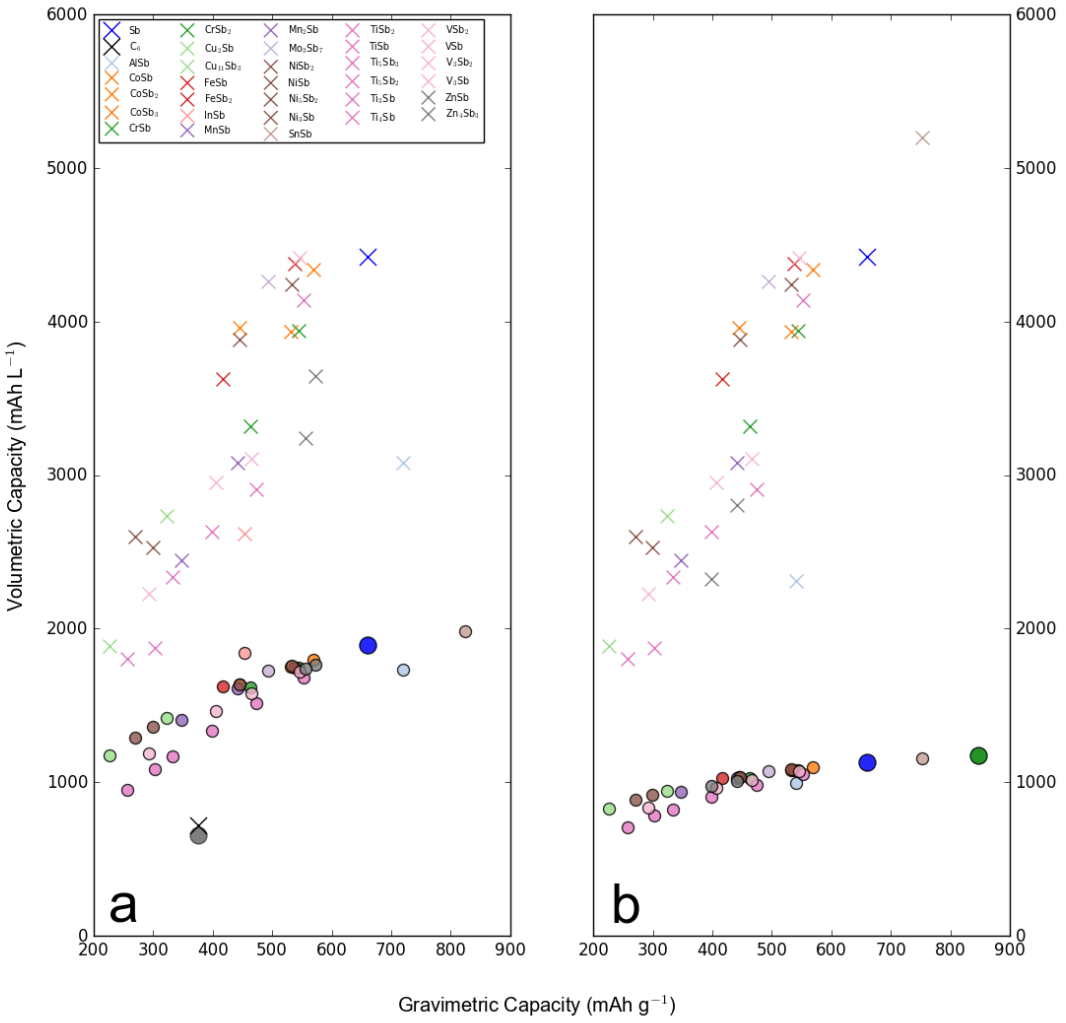

Figure 2.2. Gravimetric vs. volumetric capacity for the metal antimonides in the fully (a) delithiated / (b) desodiated state (x markers) and (a) fully lithiated / (b) sodiated (circle markers) states. Graphite (grey) is shown for reference. Each cross has a corresponding circle directly underneath it, with the colors corresponding to the metal present in the compound. The lowest gravimetric capacity compound for each metal type corresponds to the intermetallic with the highest metal content, and each set of markers with the next highest gravimetric capacity corresponds to the next phase with higher antimony content.

The volumetric capacities are plotted against gravimetric capacities for the metal antimonides in Fig. 2.2. Compared to graphite, all of the metal antimonides are capable of holding

more capacity in terms of volume due to the higher volumetric density of Li in Li_3Sb compared to LiC_6. The relatively modest decrease in volumetric capacity at increasing transition metal content is a result of the much higher densities of extruded metals of ~2-3x that of Li_3Sb. In contrast, the gravimetric capacity is linearly related to the transition metal content, and when the transition metal content reaches a stoichiometric ratio to antimony of approximately 2:1, the gravimetric capacity falls below that of graphite. Interestingly, many of these compounds provide exceptionally high volumetric capacities when the initial material is considered. This is the result of the high density of most of the metal antimonides. Nevertheless, most of these compounds do not experience full reversibility, and instead convert to a mixture of nanostructured metal particles and antimony. Thus, the use of these values is dubious because the theoretical capacity is never achieved, and due to the way that battery cells operate the volume in the fully lithiated state must still be accommodated in the total volume of the electrode. This issue is rarely acknowledged in the literature for these compounds.

Comparison of the volumetric capacities in lithium ion and sodium ion cells the disadvantage of the larger volume of sodium ions. For most antimonides, the reaction products are equivalent in stoichiometry for both lithium and sodium, where Na_3Sb is the final product instead of Li_3Sb. A few minor differences exist for the cases of AlSb, ZnSb, and Zn_4Sb_3, as sodium does not form aluminum alloys and the only sodium-zinc intermetallic is $NaZn_{13}$, compared to LiZn in the lithium-zinc system. While InSb and Ag_3Sb have been studied extensively for lithium ion batteries, they have been excluded from the sodium ion chart since they are unlikely to be useful due to the high cost of silver and indium. Critically, the volumetric capacity of antimony in a sodium ion cell when fully sodiated is lower than that of all the metal antimonides in a lithium ion cell except for the titanium-rich intermetallics Ti_4Sb and Ti_3Sb. Sodium ion cells still possess

higher capacities than current state of the art graphite, but are unable to be competitive in terms of volumetric and gravimetric energy density with high capacity anodes using lithium ion chemistry.

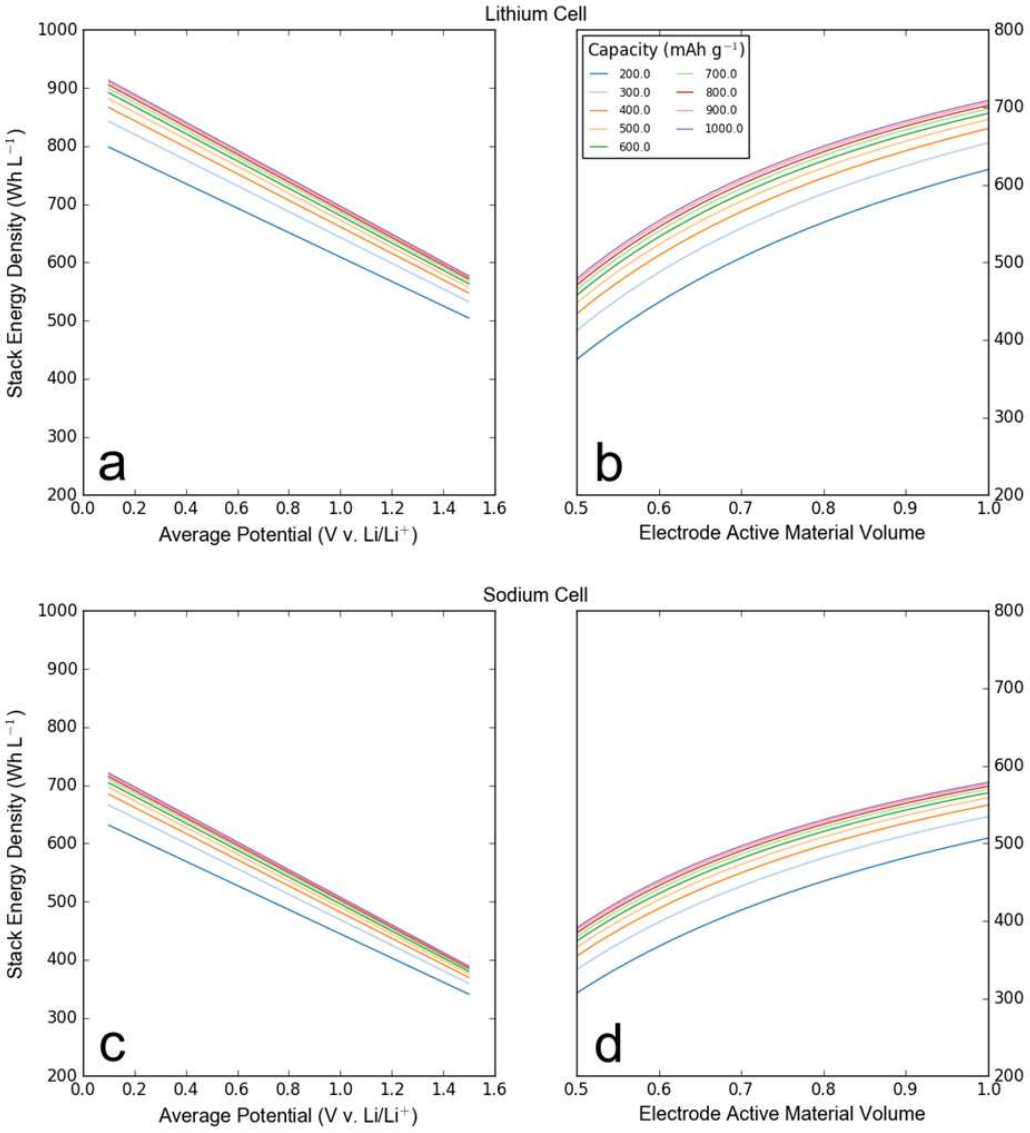

Figure 2.3. The influence of the electrochemical potential of the anode material on the cell energy of a prototypical lithium ion cell (a/b) or sodium ion cell (c/d) showing the effect of changes in electrode potential (a/c) and changes in the active material volume (b/d). The model is discussed in the text and is described in detail elsewhere.(*11*) For the sodium-ion cell, an identical cathode was used except that $LiCoO_2$ was replaced with $NaFe_{0.5}Co_{0.5}O_2$.(*27*)

The use of antimony in a full cell configuration comes at the cost of a significant amount of cell potential compared to other alloy compounds. We have adapted the model by Obrovac and Chevrier to use an anode consisting of antimony with figures of merit based on data from Darwiche *et al.(11, 28)* For the purpose of this investigation, we used a capacity of 660 mAh g^{-1}, a crystallographic density of 6.69 g cm^{-3}, an initial coulombic efficiency of 70%, average electrode potentials of 0.95 V v. Li/Li^+ or 0.70 V v. Na/Na^+, 100% active material volume, and expansion factors of 2.34 for lithium and 3.90 for sodium. To demonstrate the effect of anode potential on cell energy density, Fig. 2.3a and 2.3c show the effective cell energy density of an antimony full-cell with varying electrode potential. While this demonstration is mostly impractical since the electrode potential is fixed by the active material, there is some variation of the electrode potential among the metal antimonides to lower values for alloys containing Zn, Ag, In, or Al. The loss in capacity due to increasing voltage is also of importance when considering rate performance. For the example here, the loss in cell energy density is 235 Wh L^{-1} V^{-1} (~34% V^{-1}) for the lithium ion cell and 232 Wh L^{-1} V^{-1} (~46% mV^{-1}) for the sodium ion cell, assuming a reversible capacity of 600 mAh g^{-1}. This clearly illustrates the critical impact that a high electrode impedance can cause on effective energy density, even when the full capacity is still being delivered.

The effect of porosity and the ratio of inactive components to active material are also noteworthy, and the predicted impact is presented in Fig. 2.3b and 2.3d for a lithium ion and sodium ion cell, respectively. In traditional electrodes, the active material volume is generally ~70%, with the remainder composed of additives, binder, and void space. Since this value corresponds to the fully lithiated state, it may be as high as 95% in practice for a well-engineered antimony electrode. It remains uncertain at this point whether such an electrode is feasible, as most stable electrodes have used techniques that involve the use of significant porosity or large amounts

of inactive additives to stabilize the electrode. In practice, highly dense electrodes such as pure antimony or metal antimonide thin films do not display good long-term performance because of pulverization and poor passivity with organic electrolytes.

It is clear from Fig. 2.3 that making a high-energy density battery from antimony is a difficult task. Using figures of merit from the existing literature, an electrode using antimony is only expected to an energy density comparable to a standard graphite cell. This may be improved if better surface stabilization can be achieved, either through electrolyte formulation or surface modification, such that the initial coulombic efficiency is increased to ~90%. Other potential improvements could be realized in the case of unconventional manufacturing methods, if the price can be decreased to values lower than that of current graphite electrodes. The flexibility of processing antimony compared to graphite makes some proposed "beyond lithium-ion" battery cell systems possible, such as those using 3D and solid state architectures,(*29-31*) that are difficult to achieve using conventionally slurry techniques. Additionally, the energy density of antimony in a sodium ion cell is reasonably high, allowing for the potential for lower cost sodium ion alternatives with energy densities approaching those of current lithium ion cells. Thus, there remains potential for the use of antimony-based negative electrodes for some applications where traditional lithium ion chemistry is not ideal.

2.3 Antimony Electrodes for Lithium Ion Cells

This section is provided primarily to provide a semi-chronological account of the research done to date on antimony-based anodes for lithium ion and sodium ion battery cells. The purpose of this is to give a historical account of the literature and provide a perspective of the multiple decades of work on this somewhat niche class of materials within the very broad lithium ion battery

literature that now exists. To the best of the knowledge of the authors, the citations provided are comprehensive for this topic.

2.3.1. Conventional Antimony Electrodes

Antimony undergoes direct phase transitions following the thermodynamic phase diagram during electrochemical cycling, first yielding Li_2Sb, then Li_3Sb.(*19, 26, 32*) This reaction provides a stable electrode voltage as the chemical potential of lithium in these phases remains constant while the antimony in the electrode is converted (Fig. 2.4). The three equivalents of lithium per mole of antimony results in a high gravimetric capacity of 660 mAh g^{-1} and volumetric capacity of 1771 mAh cm^{-3} when fully lithiated. These reactions occur at 0.82 V and 0.78 V v. Li/Li^+ during lithiation, respectively. Delithiation occurs by a single phase transition from Li_3Sb to Sb at 1.02 V.(*12, 16, 32*) An average voltage of about 0.95 V puts antimony on the upper limit of usefulness for an electrode material when paired with conventional cathode materials and electrolytes, but provides the potential advantage of a safer electrode material by operating well outside the bounds of lithium metal plating.

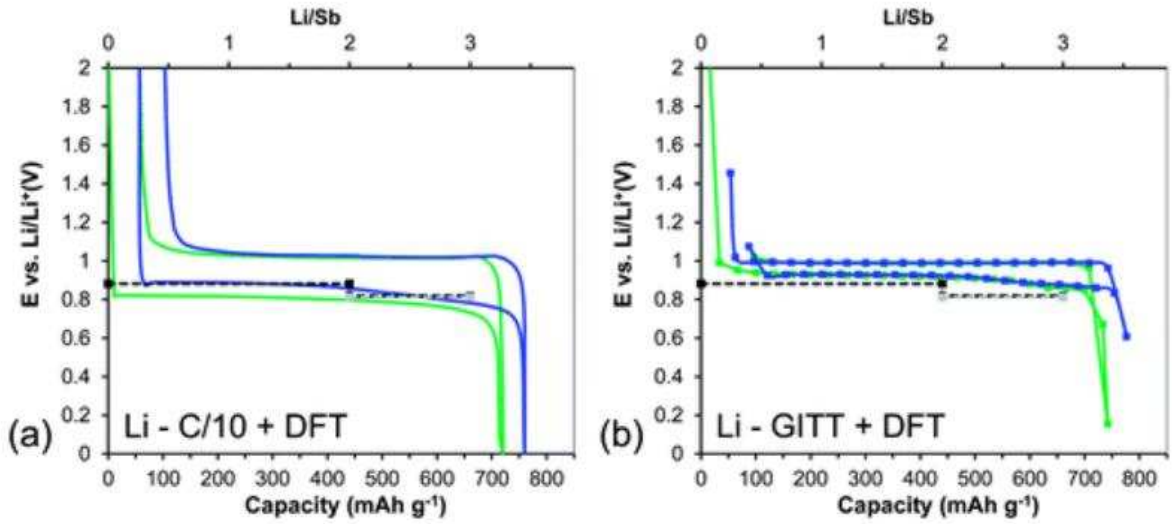

Figure 2.4. Comparison of the potential profiles for Sb electrodes during the reaction with Li predicted from DFT calculations (black dashed lines) with the (a) electrochemical constant current and (b) quasi-equilibrium (GITT) potential profiles. First and second cycles are represented by green and blue curves, respectively. For Li, the DFT predicted potentials for the formation of cubic $Fm\bar{3}m$ with combining macron]m Li_3Sb (black) and hexagonal P63/mmc Li_3Sb (gray) are both given, resulting in plateaus at 0.818 and 0.813 V, respectively. Reproduced from Ref. 32 with permission from The Royal Society of Chemistry.

Several studies have sought to overcome the issues with antimony-based electrodes. Despite significant early interest, attempts at creating useful electrode materials that are "drop-in ready" for application in lithium-ion battery cells were not described until recently. Aside from the strategy of creating M-Sb alloys, which will be described in detail later, the primary foci have been material size reduction,(*8, 23*) carbon containing composites,(*33*) and novel nanostructures.(*34*) The figures of merit are usually reported in terms of gravimetric capacity (mAh g^{-1}), volumetric capacity (mAh cm^{-3}), first cycle irreversible capacity, coulombic efficiency, and cycle life (usually to 80% initial reversible capacity).

The first report on cycle stability and electrode performance of pure Sb anodes was reported by Bryngelsson et. al. using electrodeposited coatings with varying amounts of Sb_2O_3 present.(*35,*

36) In agreement with previous results by Chen et. al., antimony provided nearly theoretical capacity, but failed quickly, retaining only ca. 250 mAh g^{-1} by cycle 30 at a C/10 rate. It should be noted that these films likely contained NiSb from the substrate, as a plateau at 0.40 V was observed. The formation of intermetallic phases is typical for samples prepared by electrodeposition, but convolute the analysis as they have substantial differences in chemical, mechanical, and electronic properties.

Kim and Cho attempted to overcome the short cycle life by creating a nanostructured Sb electrode consisting of hollow Sb nanoparticles from a SiO_2 template.(*34*) They were able to demonstrate 84% initial coulombic efficiency and a reversible capacity of 665 mAh g^{-1} (the excess likely due to minor impurities such as oxides). They found that, unlike solid nanoparticles, the hollow nanoparticles could retain 94% (615 mAh g^{-1}) reversible capacity for 100 cycles, in far excess of any previous reports.

The instability of electrolytes towards antimony was known since early studies, but this issue was revisited by Martin et. al. using the surface-stabilizing additive vinylene carbonate (VC) that had been used to increase the longevity of typical graphite-containing lithium ion batteries.(*37*) Using a cellulose-supported antimony electrode, a cycle life of ~40 was shown, as opposed to failure by 20 cycles. The topic of additives and surface stabilization is covered in more detail in chapter 6.

Following these works, interest in antimony gained significant attention due to Darwiche and co-worker's publication detailing its use in sodium-ion batteries (SIBs) using 325 mesh (~44 micron) antimony particles.(*28*) The details of sodium ion cells will be covered later, but it should be noted that the majority of the literature since 2012 regarding antimony reports new materials in both lithium ion and sodium ion cells. Unlike previous studies, antimony electrodes were tested

under varying rates with and without the electrolyte additive fluoroethylene carbonate (FEC). Like the previous study using VC, the electrodes without additives lost all capacity within 30 cycles, but retained 92% capacity at the 80th cycle with VC present. Higher rates led to faster decay with only 69% capacity retention by the 80th cycle. In both cases, reported coulombic efficiency is initially very low (<90%) for the first 10-15 cycles, but then stabilizes at 98-99% for subsequent cycling. While this still is too low for practical applications, these values are a substantial improvement over early experiments. Baggetto *et al*. followed this work to clarify diffusion rates for both Li^+ and Na^+ in antimony electrodes using PITT, GITT, and DFT calculations.(*32*) Hou *et al.* revisited the hollow nanoparticle concept using a modified synthesis, but primarily focused on SIB applications. The remaining publications on this subject have reported specialized cases of antimony-carbon composites, which are discussed in detail in the next section.

In contrast to earlier studies, later studies have conclusively shown that it is possible to create stable antimony-based electrodes, if certain criteria are satisfied. Specifically, the electrode must provide a way to relax strain and prevent mechanical failure (e.g., by using nanostructures and judicial selection of binders), and the surface electrolyte interface (SEI) must be stable during the large (~150%) volume changes during cycling (e.g. by using electrolyte additives or electrode coatings). Despite achieving reasonable cycle lives, there are two critical issues that must be addressed before antimony electrodes can be realized in a practical cell. Firstly, the first cycle irreversible capacity must be reduced to ~10% to match the irreversible capacity of current cathode materials. Second, the surface stability must be increased to achieve >99.99% coulombic efficiency during cycling to allow for long-lived full cells.(*11*) Antimony-based anodes are particularly well suited for high-power applications where safety is a concern, due to the relatively high operating voltage. It is likely that successful implementation will require any anode using

antimony chemistry to be either lower in cost than a typical graphite anode, capable of higher rates, or rely on a significant redesign of the anode architecture to create a cell with real potential towards creating a lithium ion battery that is superior to state of the art lithium ion batteries.

2.3.2 *Sb-C Composites*

Most Sb-based electrodes that do not incorporate a metal alloy component reported in the literature are composites with carbon. Since graphite is the current state of the art material for lithium-ion batteries, incorporation of Sb to provide increased energy density or power density has been long considered. Most publications using this type of compound have focused on using sp^2-type carbon materials, such as graphite, graphene, and carbon nanotubes. Generally, the carbon component provides a robust framework that can prevent electrode pulverization, loss of electronic conductivity, and facilitating better SEI stability. These electrode properties are achieved through synthetic methods that reduce antimony directly onto (or into) carbonaceous materials. The electrochemical characteristics of these electrodes are similar to pure Sb for all carbons with the exception of Dailly *et al.*,(*33*) due to the contribution of graphite. A clear disadvantage for these composite cells is the reduction of the electrode density, effectively circumventing the advantage of high volumetric capacity offered by pure Sb. Even modest amounts of inactive material may reduce the energy density of a lithium ion full cell below that of graphite.(*11*) Despite this, carbon modification may be a viable approach for stabilizing Sb when the amount of inactive carbon in the electrode is small.

Chen et. al. published the first attempt at making a usable Sb-based carbon composite electrode using nanoparticles of Sb reduced from solution onto carbon nanotubes (CNTs), far earlier than any reports attempting to stabilize Sb alone.(*38*) They compared the pure nanoparticles to the CNTs-Sb network, finding that while pure Sb worked at near theoretical reversible capacity

(648 mAh g^{-1}, 98% theoretical), the capacity faded extremely quickly and retained only 115 mAh g^{-1} by the 30th cycle. In contrast, the CNTs-Sb (36 wt% Sb) provided 462 mAh g^{-1} initial capacity and decayed to 287 mAh g-1 by the 30th cycle. The first cycle efficiencies for the Sb nanoparticles and CNTs-Sb composite were 36.5% and 63.3%, respectively. This work provided a basis for using carbon-modification to create Sb electrodes stable enough for lithium-ion electrode studies.

A similar approach was used by Dailly et. al., where an Sb-containing graphite was produced by reduction of $SbCl_5$-intercalated graphite with cesium gas.(*33*) The resulting antimony-containing graphite was shown to provide the nearly theoretical reversible capacity of 490 mAh g^{-1} for a 46 wt% Sb composite. Importantly, no significant capacity fade was observed for the first 40 cycles. No other figures of merit were provided in that work, but the reported results indicate that carbon supported antimony could be a viable material for lithium-ion battery anodes.

Hassoun *et al.* produced Sb-C composite electrodes consisting of Sb co-reduced with a resorcinol-formaldehyde gel.(*39*) This structure provided nanoparticles attached to a carbon substrate with control of the Sb nanoparticle size. They demonstrated a relatively long cycle life of 100 cycles for particles 10-50 nm in size, but fast capacity fade for larger nanoparticles on the order of 500 nm. The synthesis used required that the smaller nanoparticles had relatively more inactive carbon present, and this may be significant in the stabilization of the electrode as well. As a result, a stable capacity of only 220 mAh g^{-1} was reported. A similar approach to stabilization was attempted by Zhang *et al.* by reduction of $SbCl_3$ with $NaBH_4$ in solution with graphene oxide in ethylene glycol.(*40*) This procedure formed Sb nanoparticles of 50-100 nm directly attached to a graphene substrate. In the lithium-ion cell, the composite showed only modest cycle life, decaying during the initial 40 cycles, but faring significantly better than pure sby electrodes prepared without the graphene present. Based on their studies using cyclic voltammetry and

electrochemical impedance, the authors concluded that graphene helps reduce interfacial resistance, prevent aggregation, and retain electrical conductivity within the electrode.

A novel material consisting of small, carbon-coated Sb nanoparticles of 200 nm aggregated into micron-sized nanorods was synthesized by Fan *et al.* using acetylene gas for thermal reduction of Sb_2O_3 prepared by precipitation from solution. The material provided a high initial capacity of 687.1 mAh g^{-1} and retained nearly 70% capacity at the 100^{th} cycle. A rate study was performed and this composite could deliver 60% reversible capacity at a rate of approximately 1C.

These works on Sb-C composites have suggested a beneficial role of carbon in stabilizing antimony nanoparticles in lithium ion cells. In many cases, superior results are reported with respect to control experiments where no carbon in present. There has been no systematic study on the effect of carbon loading on electrode performance to date, making a direct comparison between carbon free and carbon coated materials different when evaluating at the electrode level. Nevertheless, carbon coating is one of the most widely used and successful method for increasing the cycle life of Sb electrodes.

2.4 Ternary Li-M-Sb Electrodes

In contrast to pure Sb, a significantly larger number of studies have been published on electrodes that are an alloy of Sb with another metal. At the time of this writing, there are over 110 publications on this subject, and so this section will be split into subsections based on the alloying metal in descending order of number of publications. This is followed by a critical analysis of the potential benefits of this class of electrode materials.

2.4.1. Li-Cu-Sb

Alloys of Cu-Sb have been extensively studied due to the unusually high reversibility of this system. The Cu-Sb phase diagram consists of two copper antimonide intermetallic phases, tetragonal Cu_2Sb and orthorhombic $Cu_{11}Sb_3$, with limited to no solid solution behavior.(*41*) The majority of research has concentrated on the antimony-rich Cu_2Sb phase, and little study has been paid to the Cu-rich $Cu_{11}Sb_3$ phase due to a low theoretical capacity of only 226.6 mAh g^{-1}. Unlike other transition metals, the thermodynamics and kinetics of copper allow for a unique reversible formation of ternary phases that influence the electrochemistry of the material even after prolonged cycling.

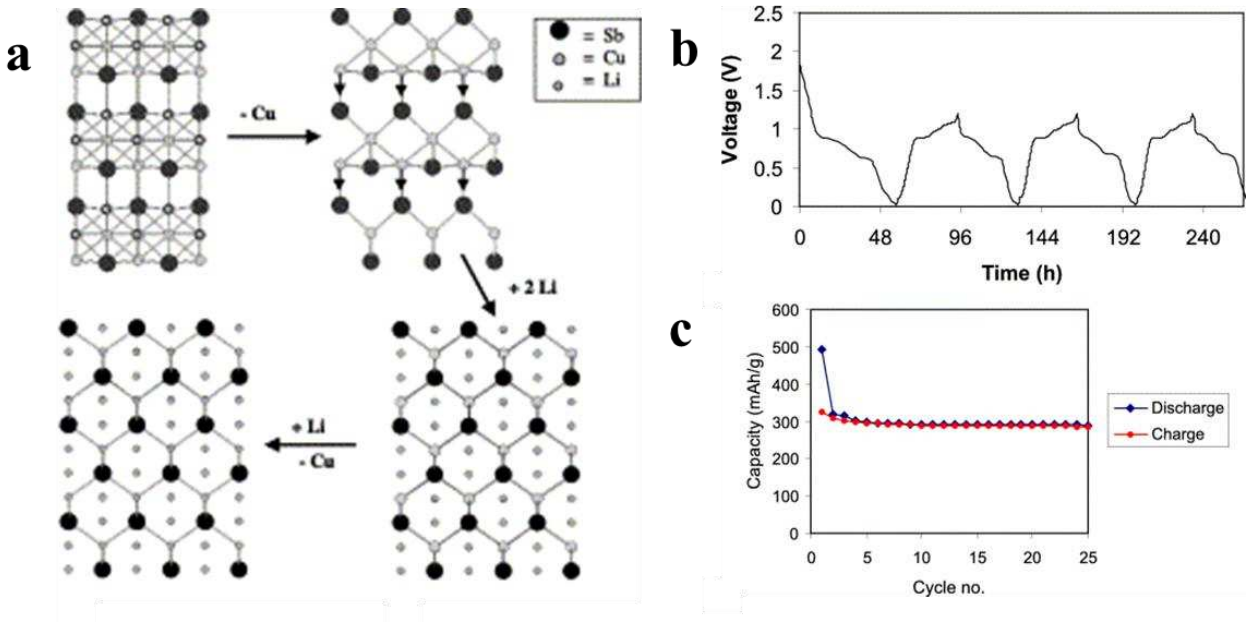

Figure 2.5. (a) Schematic illustrations of the structures formed during the electrochemical transformation of Cu_2Sb to Li_3Sb: Cu2Sb, [0 1 0] projection; "CuSb" component of Cu_2Sb, Li_2CuSb, [1 1 0] projection; and Li_3Sb, [1 1 0] projection. (b) Voltage profile for the first three cycles of a Li/Cu_2Sb cell and (c) a plot of capacity vs. cycle number for the first 25 cycles. Reproduced with permission from ref. 42.

Fransson *et al.* first studied th Cu_2Sb system in 2001, using X-ray diffraction to study the insertion and desertion of lithium from the intermetallic Cu_2Sb phase.(*42*) This investigation led to the discovery that ternary Li-Cu-Sb phases were formed as intermediates during cycling, and the re-formation of Cu_2Sb during full delithiation (Fig. 2.5). The presence of these phases corresponds to a decrease in the average electrode potential by ~100 mV, providing similar energy density to pure Sb in volumetric terms but a low gravimetric capacity of 317 mAh g^{-1}. This is unusual for the metal antimonides, as the reversible formation of crystalline intermetallics is not normally observed. Thus, the electrode undergoes a conversion reaction, and the reduced potential is lost after the first cycle. Even this first report found high reversibility, showing a stable capacity for 25 cycles. This gives Cu a clear advantage over other metals that have been studied, as will be discussed later.

This material was further studied by Song *et al.* in the form of sputtered thin-films of Cu_2Sb.*(43)* In particular, it was shown that under a limited cycling range reasonable stability can be achieved for many cycles. It was also determined that the surface electrolyte interface (SEI) layer is significantly different in composition and much thicker than the SEI typically found on graphite, leading to the large first cycle irreversible capacity loss and poor long term stability. Ren *et al.* used chemical reduction to produce Cu_2Sb nanoparticles and found reasonable stability for 50 cycles at a modest capacity of about 200 mAh g^{-1}. Between these two studies, it was thoroughly confirmed that Cu_2Sb has high reversibility, especially when nanostructured. The conventional EC/DEC electrolytes using $LiPF_6$ as the lithium salt are not stable however, and anodes using Cu_2Sb show high irreversible capacities on the first cycle and relatively low coulombic efficiencies on subsequent cycles.

Much of the work following these publications focused on new synthetic strategies to make Cu_2Sb to elucidate the influence of nanoscale and microscale structural motifs using solution synthesis(*44*), arc-melt method(*45, 46*), and electrodeposition(*47-49*). The studies by Matsuno *et al.(45, 46)* are particularly useful to those looking to understand the Li-Cu-Sb system and they provide a thorough evaluation of the mechanism of lithium alloying with Cu_2Sb anodes using a high purity electrode. Bryngelsson *et al.* provided the first study of a copper antimonide with different stoichiometry than Cu_2Sb, also providing data for "Cu_9Sb_2" produced by annealing thin-films of antimony electrodeposited on copper foil. They show that beyond the first cycle, the copper rich sample forms Cu_2Sb, suggesting that the thermodynamic pathway favors this phase regardless of the original material composition.

Following these works, He *et al.* attempted to produce carbon-coated Cu_2Sb nanoparticles, although their results do not indicate they were successful.(*50*) A study on the low-temperature performance of alloy anodes by Jansen *et al.* noted that Cu_2Sb has a similar decrease in performance to graphite under these conditions.(*51*) Perre *et al.* and Tan *et al.* produced nanowire electrodes of Cu_2Sb using porous alumina templates and electrodepositions to study as prototype 3D microbattery electrodes.(*52, 53*) They showed a successful half-cell design using a polymer electrolyte, albeit with relatively fast capacity fade.

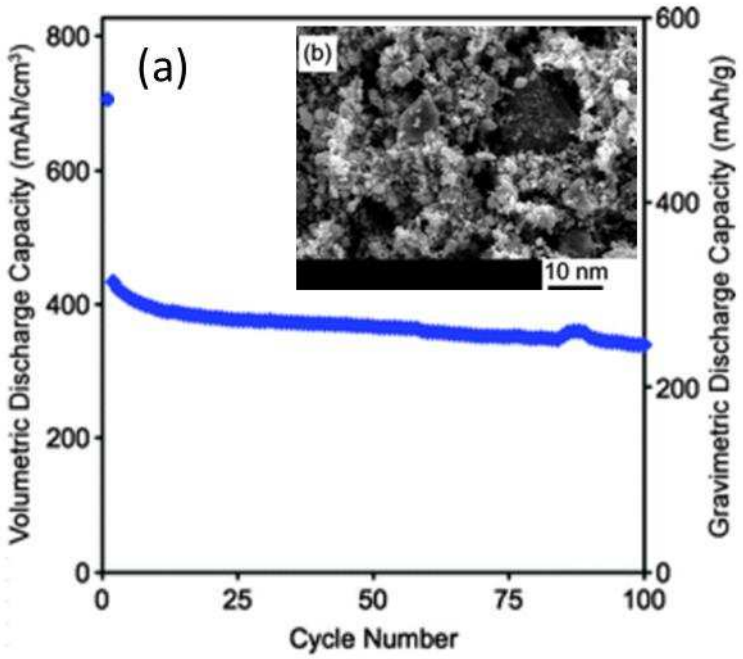

Figure 2.6. (a) Cycle lifetime of a full-cell lithium ion cell using a Cu_2Sb-Al_2O_3-C composite negative electrode and $LiMn_2O_4$ spinel pouch cell at 25 °C between 0–2 V vs.Li/Li^+ at a current of 100 mA g^{-1} of active electrode material, and (b) scanning electron microscope image of the composite electrode. Reproduced with permission from ref. 55.

Recent work by Allcorn *et al.* and Applestone *et al.* have focused on the use of composite electrodes containing an inert particle (TiC or Al_2O_3), Cu_2Sb, C, and binder homogenized through conventional methods to create a stable Cu_2Sb-based electrode. These studies have looked at the electrolyte stability using symmetric cells(*54*), the effect of the inactive particle on electrode cycle stability(*55*), and thermal stability(*56, 57*). Importantly, they have shown good capacity retention for a Cu_2Sb derived anode for a full lithium ion cell using a spinel $LiMn_2O_4$ cathode (Fig. 2.6). This is one of the few studies reporting a lithium ion full cell, and the retention over 100 cycles suggests good promise for electrodes of this type.

At the time of the preparation of this chapter, there have been a great deal of studies on Cu_2Sb, and the mechanism of reversible alloying is generally well understood. Nevertheless, the

role of copper in these electrodes is still not fully understood due to a lack of reports on electrodes using stoichiometries other than the Cu_2Sb phase. In addition, and despite the large number of publications, there are unresolved issues with the practical application of Cu_2Sb as an anode material. A large first-cycle irreversible capacity, poor stability with conventional electrolytes, and modest mechanical stability have prevented the realization of a long-lived full cell. The requirement of high coulombic efficiency and good surface passivation will need to be met before a useful electrode using this material can be realized.

2.4.2. Li-Sn-Sb

Alloys of Sn and Sb are well studied since both elements reversibly alloy with lithium, resulting in high volumetric and gravimetric capacities in contrast to transition-metal alloys where one component is not active. There exists only hexagonal SnSb as a stable room-temperature intermetallic phase in this system.(*58*) Unlike the case for Cu_2Sb, however, extensive solid solution regions exist for all three phases, with Sb being stable with up to 8% Sn, SnSb being stable for ±5% at% Sn, and Sn being stable for up to 3% Sb. The gravimetric capacity for these materials is high across the entire composition and have often been reported to provide more stable cycling compared to either element alone.

Yang *et al.* first studied this alloy as an extension of the mixed-conductor matrix concept, where a lithium host material is contained within another material that is not reacted for a given voltage range.(*59*) They demonstrated hundreds of cycles reversibility when the charge capacity was limited to ~360 mAh g^{-1}. The authors suggested that the reversible coulombic efficiency of ~98% for this material was too low for consideration in full-cells, but that there was no theoretical reason that limits such anodes from achieving 100% reversibility. Li *et al.* studied dendritic nanoparticle SnSb particles and found structural reversibility of the original β-SnSb phase and

determined that the reaction was more reversible than equivalent electrodes they had previously reported using pure Sb and Sn particles. Li *et al.* followed this work and focused on methods to mitigate the low coulombic efficiency by modification with coatings and deposition of nanoparticulate SnSb onto carbon particles.(*60*, *61*) Their results suggest that preventing particle aggregation by dispersing onto carbon and using coated nanoscale particles could help alleviate the aforementioned issues with stability.

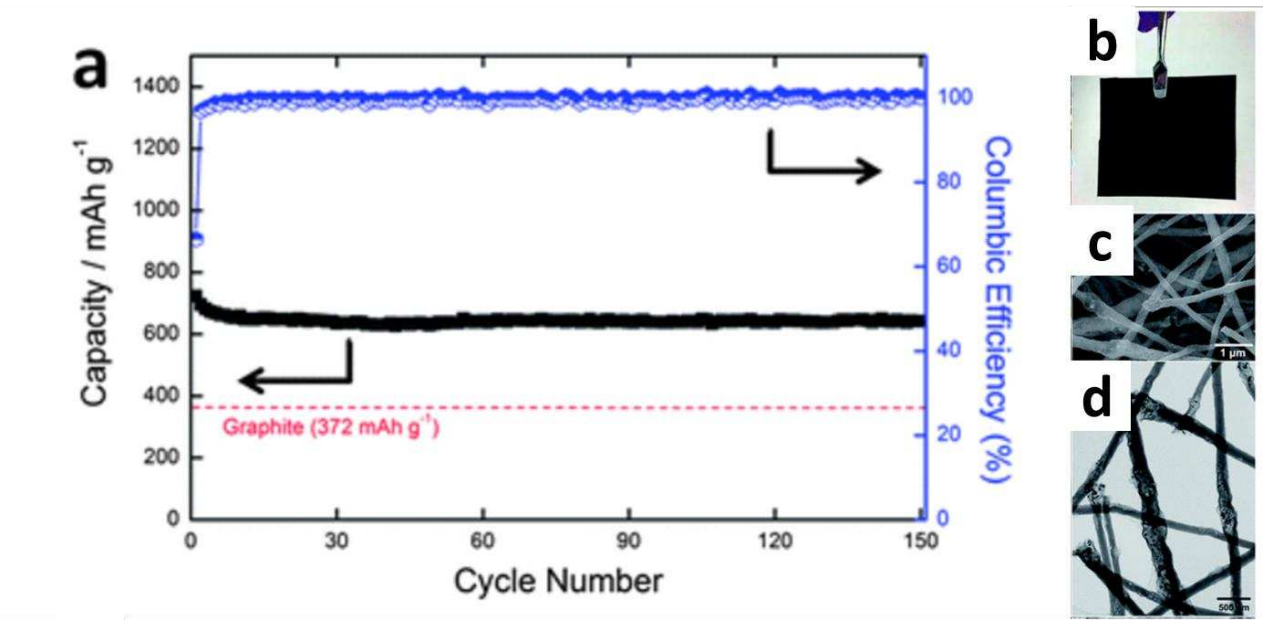

Figure 2.7. (a) Cycling performance of porous SnSb/C composite nanofibers at a current density of 50 mA g^{-1} and within a voltage window of 0.02–2.7 V vs. Li^+/Li. (b) Optical image of the SnSb/C composite nanofiber electrode, (c) scanning electron microscope image, and (d) transmission electron microscope image. Reprinted with permission from ref. 65.

The first demonstration of (nearly) full utilization of SnSb was reported by Mukaibo *et al.*, but immediate degradation of the material was observed in this experiment.(*62*) Needham *et al.* tested high weight loading of carbon black additive to stabilize SnSb powders, and found improvement of the usable capacity of the particles but the carbon did not eliminate capacity fade from repeated cycling.(*63*) Wang *et al.* produced Sn_2Sb-encapsulated carbon particles that displayed impressive capacities of nearly 650 mAh g^{-1} and good stability for 60 cycles.(*64*) A similar material consisting of Sn-Sb alloy embedded in carbon nanotubes was reported by Yong and Jim, and exhibited high capacities of >700 mA h g^{-1} for the 80 cycles presented. Zhao *et al.* studied micrometric SnSb at elevated temperatures, and found that the cycle performance was better at 40 °C but suffered from electrolyte instability at 55 °C. Recently, Xue *et al.* revisited carbon-encapsulated SnSb and found a porous carbon fiber composite allowed a stable reversible

capacity of 650 mAh g^{-1} after 150 cycles (88% retention), longer than reported for conventional preparations (Fig. 2.7).(*65*) Aside from these studies, a number of reports were published considering different ways of synthesizing SnSb and preparing electrodes, but no substantial progress in stabilizing this material or overcoming the aforementioned limitations were reported.(*66-76*)

While SnSb has high theoretical capacity and has been shown in some cases to display good reversibility, a lack of progress has been made in creating stable electrodes with this material. Currently, the longest cycle lifetime reported is 150 cycles, and little work is being done to overcome the outstanding issue of poor surface passivity that limits the initial and reversible coulombic efficiencies to unsuitably low values. Further work on this material is warranted given the potential for high energy density electrodes, although there is not substantial evidence that these alloys perform better than pure Sb or Sn electrodes, which have recently shown promising performance when appropriately formulated.

2.4.3. Li-Co-Sb

Three intermetallic cobalt antimonides exist, hexagonal CoSb, monoclinic $CoSb_2$, and cubic $CoSb_3$.(*77*) Only the CoSb phase exhibits solid solution phase, with a stability window of ca. ±2 at%. Although these have all been studied as anode materials, most attention has been paid to the antimony rich $CoSb_3$ phase which provides a theoretical capacity of 568.95 mAh g^{-1}. In view of practical potential, however, Co does not appear to have significant value as cobalt is toxic, expensive, and relatively uncommon. Nevertheless, cobalt-antimony alloys have received significant attention as potential anode materials. This likely stems from early studies that demonstrated enhanced performance in Sn-Co-C composites that could not be achieved using other first row transition metals. Nevertheless, the practical use of this alloy in a commercial

battery has a low chance of being realized. Most research on these compounds was conducted in the early years of transition metal antimonide anode research, and so is one of the most thoroughly studied systems presented in this review.

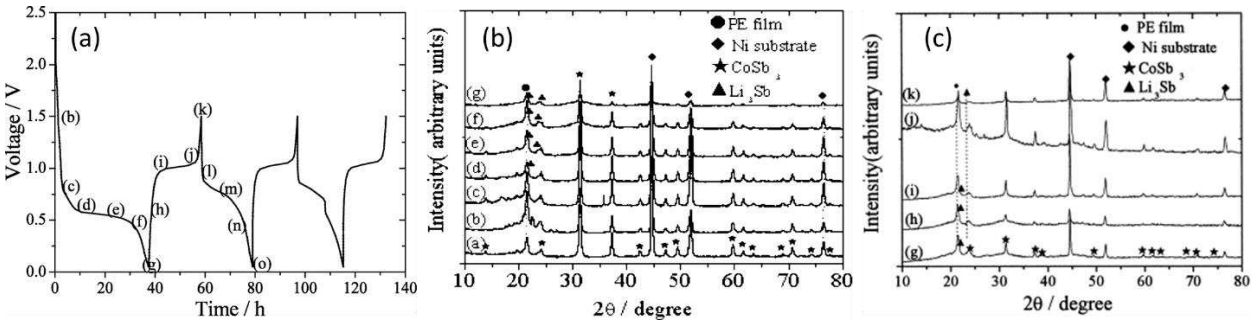

Figure 2.8. (a) Charge-discharge cycles of a $CoSb_3$ electrode, with letters marking points where *ex situ* X-ray diffraction data was collected. (b) First lithiation half-cycle X-ray diffraction patterns showing the conversion reaction of $CoSb_3$ to Co + $3Li_3Sb$. (c) First delithiation half-cycle X-ray diffraction patterns showing conversion of the electrode to a mostly amorphous material. Reproduced with permission from ref. 78.

The first publication of a cobalt-antimony alloy by Alcántara *et al.* reported the reversible alloying of $CoSb_3$ with lithium.(*24*) The material was found to become amorphous upon incorporation of lithium, and the original $CoSb_3$ phase was not reformed. Evaluation of the charge-discharge curves indicated that the active material was antimony, and the electrode material is likely a composite of metallic cobalt and antimony finely interspersed. Although the performance of the anode was modest, less capacity fade was observed when compared to an equivalent pure antimony anode. Xie *et al.* reported an ex-situ X-ray diffraction study that confirmed the results reported by Alcánatra.(*78*) Tarascon *et al.* followed this work with an in-depth study of the mechanism by in-situ X-ray diffraction and kinetic measurements, confirming the mechanism proposed by Alcántara.(*79*) Comparison with $CoSb_2$ showed a similar mechanism, and they concluded that the fully delithiated product was a form of amorphous cobalt antimony alloy and suggested that the reaction is reasonably reversible. Further evaluation of the mechanism was

provided by Devos *et al.* and Ionica *et. al.* using ^{121}Sb Mössbauer spectrometry and X-ray absorption spectroscopy, where the results indicated that there may be the formation of some ternary Li-Co-Sb species during the reaction with lithium during the first cycle (subsequent cycles were not studied).(*80, 81*)

Subsequent studies have focused on different ways of preparing Co-Sb alloys to improve performance. Pralong *et al.* studied thin films of Co, $CoSb_3$, Co_3O_4 and Sb produced by pulsed laser deposition.(*82*) Xie *et al.* prepared $CoSb_2$ and $CoSb_3$ by solvothermal methods as reported in a series of papers.(*78, 83-89*) Wang *et al.* studied micrometric CoSb and found similar performance and mechanism to the previously reported phases.(*90*) Co-Sb alloy nanowires were synthesized by Yang *et al.*, but displayed poor stability during the first few cycles.(*91*) Xie *et al.* found modest improvement in the performance for $CoSb_3$ nanoparticles anchored on graphene.(*92, 93*) The most recent publication by Park *et al.* has demonstrated that high energy ball milling of Co-Sb intermetallics with carbon can increase the stability significantly, leading to stable capacity retention for at least 100 cycles.(*94*)

The original studies on cobalt-antimony alloys were of significant interest because cobalt was observed to be relatively unreactive in this system, unlike the equivalent cases for cobalt oxides and cobalt nitrides. Some modest performance gains have been reported, but except for ref. 87, these materials do not show significant improvements over pure antimony. Furthermore, this class of compounds is unlikely to be useful in practical applications due to the high cost and toxicity of Co. Further studies of lithium electrochemistry with these materials is not warranted in the context of lithium-ion battery technology.

2.4.4. Li-Ni-Sb

Of the four intermetallic nickel antimonide phases in the Ni-Sb system, three ($NiSb_2$, NiSb, and Ni_5Sb_2) have been studied for use as lithium ion battery anode materials.(*95*) Xie *et al.* provided the first report of cycling $NiSb_2$ prepared by solvothermal as well as ball milled samples and reported modest cycling results but did not propose a mechanism.(*96*) Following this work, Villevieille *et al.* focused on the $NiSb_2$ intermetallic due to its' high active material content and positive results of stable cyclability and have provided significant depth of the mechanism using X-ray diffraction and Mössbauer spectroscopy.(*97-99*) Some other groups have also produced $NiSb_2$ and cycled it with limited success.(*100-102*) Recently, Allcorn and Manthiram reported that their method of producing metal antimonide composites is capable of creating NiSb based electrodes with stable lifetimes of >1000 cycles.(*103*) Hou *et al.* have shown that hollow nanoparticles of NiSb are stable for at least 50 cycles and at high rates.(*104*) These studies show that NiSb is capable of sustained reversibility, although there is remains a limited understanding of the role of nickel outside of the specific case of $NiSb_2$.

2.4.5. Li-Fe-Sb

Two intermetallic phases exist in the Fe-Sb system, hexagonal $Fe_{1.27}Sb$ and orthorhombic $FeSb_2$.(*105*) The iron antimonides have followed a similar pathway of study as nickel antimonides, with initial publications reporting on the $FeSb_2$ phase.(*106, 107*) Unlike the isostructural nickel antimonides $CrSb_2$ and $NiSb_2$, however, $FeSb_2$ undergoes a conversion reaction that first produces a ternary intermediate Li_4FeSb_2 before fully converting to Li_3Sb + Fe.(*99, 108, 109*) Following the first cycle, $FeSb_2$ does not reform and the reaction scheme follows the same pathway as nanocrystalline antimony. For the case of $Fe_{1.27}Sb$, no intermediate is formed and the reaction pathway proceeds by conversion to iron and antimony during the first half-cycle.(*110*) The iron

released by this reaction helps to prevent grain aggregation and promotes higher electrical conductivity, and in most cases provides somewhat better performance than antimony alone.

The first report on $FeSb_2$ showed modest performance, with an initial capacity of 500 mAh g^{-1} and only 55.6% retention after 15 cycles.(*107*) Similar experiments using micrometric particles and nanorods of $FeSb_2$ yielded similar performance.(*106*) More recently, nanocomposites made by high energy mechanical milling powders of $FeSb_2$ with carbon were shown to provide much better performance with 75% capacity retention after 100 cycles.(*109*) Solvothermal synthesis of graphene-$FeSb_2$ nanocomposites did not show as good performance, retaining only ca. 60% capacity after 30 cycles.(*101*) Recently, Allcorn *et al.* provided a series of publications on nanocomposite electrodes consisting of $FeSb_2$-Al_2O_3-C and FeSb-TiC-C synthesized by mechanochemical high energy mechanical milling.(*110, 111*) These electrodes display high stability, retaining 61% capacity after 500 cycles for optimized composites. Kinetic measurements on these same composites suggested that the composites with higher inactive material content tended to have significantly improved rate capability.(*112*) Based on these studies, there is a basis for the use of iron to stabilize the Sb and provide better long-term performance, but currently these electrodes are only stable with high amounts of inactive materials. As a result, a high energy density electrode with even short term stability has not been demonstrated to date.

2.4.6. Li-Zn-Sb

Two intermetallic phases, orthorhombic ZnSb and hexagonal Zn_4Sb_3, exist in the Zn-Sb phase diagram at room temperature.(*113*) Among the first row transition metals, Zn is unique as it is the only one that forms lithium alloys in lithium ion cells. As such, it is similar to Sn in the sense that high Zn contents do not cause an unacceptably large decrease in reversible gravimetric capacity. Importantly, Zn has a theoretical reversible capacities of 1476 Ah L^{-1} and 410 mAh g^{-1},

compared to 1771 Ah L^{-1} and 660 mAh g^{-1} for Sb at full lithiation.(*11*) Due to the low cost, low operating potential (0.25 V v. Li/Li^+), and high abundance of Zn, it could be argued that Zn is one of the most appealing alloying materials. Unlike the other transition metals used to alloy with Sb, however, Zn contributes to volume expansion having an expansion of 98% between metallic Zn and the fully lithiated LiZn phase. This issue is compounded with studies on pure Zn that have suggested that Zn is particularly unstable towards electrolytes and has poor kinetics when at low levels of lithiation.(*114, 115*) It is possible that alloys and intermetallics incorporating Sb could therefore provide better performance than zinc alone and provide a low-cost material with relatively high performance if the antimony can reduce electrolyte decomposition and enable better rate performance for the Zn.

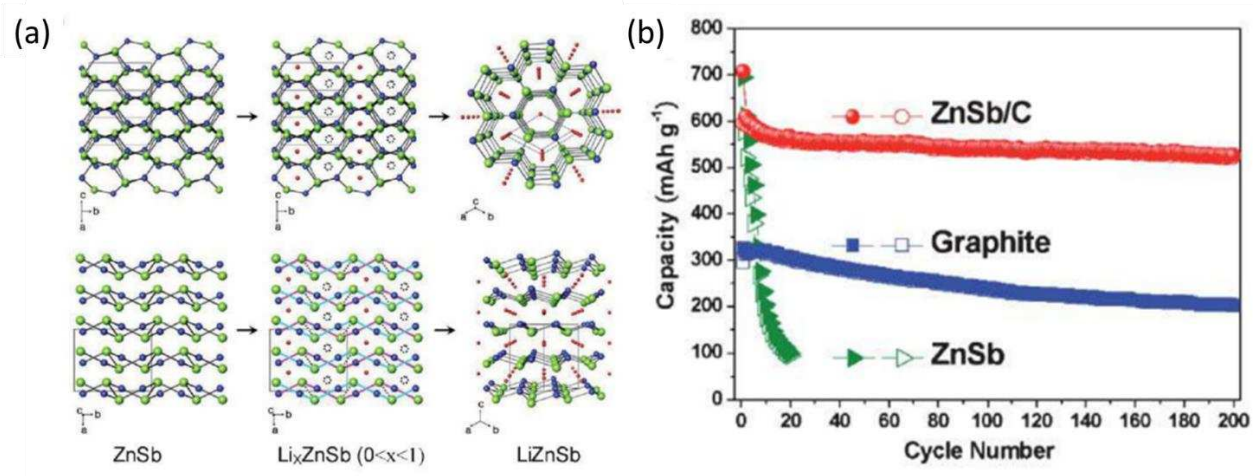

Figure 2.9. (a) mechanism of quasi-intercalaiton between ZnSb and LiZnSb (Zn atoms; blue, Sb atoms; green, Li atoms; red, dotted circles; available Li sites). (b) Comparison of the cycle performances of the ZnSb/C nanocomposite, ZnSb, and graphite (MCMB) electrodes between 0.0 and 2.0 V (vs. Li/Li^+) at a cycling rate of 100 mA g^{-1}. Reproduced with permission from ref. 116.

Zhao and Cao first reported the electrochemistry of Zn_4Sb_3 and a carbon composite. While the pure material was found to perform poorly, the carbon modified Zn_4Sb_3 displayed reasonably

good performance for initial experiments, retaining 68% capacity after 10 cycles. Like $FeSb_2$ and Cu_2Sb, Zn_4Sb_3 was found to proceed through a ternary intermediate LiZnSb phase. Park *et al.* later investigated layered ZnSb, and found that a carbon composite was able to retain a high capacity retention of 88% after 200 cycles.(*116*) Other reports have demonstrated promising initial results for nanomaterials such as electrodeposited ZnSb nanostructures,(*117*) Zn_4Sb_3 nanotubes,(*118*) and ZnSb nanocomposite electrodes.(*119*) It is interesting to note that the literature of zinc-antimony alloys is small compared to many other antimonides. Like many other metal antimonides, only the intermetallic phases have been investigated, and it is unclear if there are synergistic advantages to amorphous mixtures of Sb and Zn.

2.4.7. Li-Ti-Sb

Seven intermetallic phases exist in the Ti-Sb system.(*120*) Despite the large number of potential phases to choose from, only the most Sb rich phase $TiSb_2$ and ternary phase TiSnSb have been studied as potential anode materials. $TiSb_2$ was first studied as part of a comprehensive study of compounds with the Al_2Cu structure.(*121*) The initial electrochemical results provided showed good reversibility and near theoretical capacity. A later comparison study of $TiSb_2$ to a Sb/TiC/C composite electrode showed that the later had better overall performance, with the $TiSb_2$ electrode dropping to less than 50% capacity within 100 cycles.(*122*) Recently, the use of lithium polyacrylate binders with TiSb2 were shown to provide a capacity retention of 80% at 120 cycles.(*123*) Currently, no reports have shown long-term stability for this compound.

The ternary TiSnSb phase has been recently studied as an alternative to SnSb.(*124*) Extensive surface analysis of SEI films have been provided for this compound, although cycle experiments have been kept short.(*125-127*) At 50 cycles, the reversible capacity remained at 91% for conventional electrodes prepared with this material.(*125*) At this time, it is unclear if there are

particular advantages to the use of titanium over other transition metals, but early results suggest it is possible to obtain reasonably good performance for $TiSb_2$ and TiSnSb.

2.4.8. Li-In-Sb

Only one indium antimonide intermetallic, cubic InSb, exists in the In-Sb system.(*58*) Although indium contributes to the capacity by formation of LiIn, this system is only of interest academically due to the cost of indium. Study of InSb began following a report of lithium insertion into zinc blende Cu_6Sn_5, Vaughey *et al*. investigated InSb due to its structural similarity.(*25, 128*) Initial results were promising, showing a slow capacity fade over the first 25 cycles and the existence of several unique voltage plateaus corresponding to the formation of the ternary phase Li_2InSb. A pitfall of this system is the extrusion of indium in the form of whiskers which causes long term stability issues.(*129*) In contrast to these initial studies, Hewitt *et al.* suggested that the insertion only accounts for ~5% of the capacity, and that the mechanism is similar to that of a mixture of Sb and In.(*26*) A theoretical study has suggested that a $Li_{5/4}In_{3/4}Sb$ structure should exist, but that Li_2InSb is not energetically favorable.(*130*) These results seem to indicate that the reaction mechanism is similar to other metal antimonides that have at least one stable ternary intermediate, but the extrusion of In is not particularly reversible. Since these early investigations, no work has been performed, likely due to the impracticality of indium in a practical battery.

2.4.9. Li-Mn-Sb

Two manganese antimonide intermetallic compounds exist in the Mn-Sb system, tetragonal Mn_2Sb and hexagonal MnSb.(*131*) Fransson *et al.* first studied these two compounds as a comparison to Cu_2Sb, which is isostructural to Mn_2Sb.(*132*) They found that unlike Cu_2Sb, Mn_2Sb proceeds by conversion directly to manganese metal and Li_3Sb. In contrast, MnSb proceeds

through a layered ternary compound LiMnSb. They suggested that the kinetics were poor due to the slow diffusion of manganese and antimony in the system. In a follow-up study, X-ray diffraction and Mössbauer were used to determine that both MnSb and Mn_2Sb proceed through an amorphous LiMnSb material, but that the material eventually converts to manganese metal and antimony after only a few cycles.(*133, 134*) No long-term studies of the cycle performance of these intermetallics have been reported to date.

2.4.10. Li-Cr-Sb

The Cr-Sb system has two stable intermetallics, hexagonal CrSb and orthorhombic $CrSb_2$.(*135*) Of these, only $CrSb_2$ has been studied in lithium ion cells. An early report determined that this compound undergoes direct conversion to chromium metal and Li_3Sb.(*136*) Early cycle performance showed a low capacity of 350 mAh g^{-1} and a fast fade to ~180 mAh g^{-1} in the first ten cycles. A later study found good initial performance, but also reported fast decay for CrSb2 samples prepared by high energy mechanical milling.(*109*) The lack of extensive studies on these compounds likely stems from the high toxicity and cost of chromium, limiting practicality.

2.4.11 Li-V-Sb

While no phase diagrams have been reported for the V-Sb system, there are reports of V_3Sb and VSb_2 intermetallic compounds.(*137*) VSb_2 was investigated as a potential anode material by Larcher *et al.* as part of their study of Al_2Cu-type structures. This compound undergoes direct conversion to vanadium metal and Li_3Sb. No prolonged cycle experiments or in depth investigations have been performed on this system.

2.4.12 Other Li-M-Sb

The previous subsections have considered the first row transition metal antimonides and a few other metal antimonides that have received substantial attention. Some other antimonides that have been studied are Mg-Sb(*138, 139*), Ag_3Sb(*140*), $NbSb_2$(*141*), AlSb(*142*), and Mo_3Sb_7(*143*). Some additional materials containing antimony in ternary compounds have also been studied.(*68, 144, 145*) To the best of the knowledge of the authors, all the antimony containing compounds studied to date for lithium ion battery anodes have been listed in this section.

2.5 Na-Sb Electrodes

The prospect of using sodium ions instead of lithium ions has recently gained attention due to proposed deficiencies in worldwide lithium supply, the lower cost of sodium, and the strong similarities between lithium and sodium ion chemistries.(*146*) Compared to lithium, sodium ions are significantly heavier (23 g/mol v. 7 g/mol), have a larger ionic radius (116 pm v. 90 pm), and a more positive reduction potential (-2.71 V v. -3.04 V). As a result of these differences, a sodium ion battery would have lower energy and power densities, given everything else equal. This is further complicated by the more positive reduction potential preventing the use of graphitic carbon and silicon, and the sodium ion analogues of current state of the art lithium ion cathodes do not operate well in sodium ion cells. These issues require new materials to be developed to serve as sodium ion storage materials for the anode and cathode, and so significant room remains to study and understand the transformations of materials in nonaqueous sodium ion cells.

Initial perspectives on sodium ion alloying materials were skeptical of their use, owing to the significantly larger volume expansion that must occur as the result of the larger radius of sodium ions.(*147*) Nevertheless, early reports on Sn and Sb alloying have shown particularly

promising results, as will be discussed later. As a result, a significant amount of attention has been devoted to using these two metals as the sodium ion storage material at the anode side. Compared to the lithium/graphite anode system, Sb and Sn electrodes for sodium ions possess higher volumetric and gravimetric capacities, and could lead to comparable energy density full cells if equivalent cathode materials can be found. This section is separated into two parts, one focusing on pure Sb electrodes and the other on transition metal antimonides.

2.5.1 Na-Sb

Antimony undergoes a similar reaction with sodium as with lithium, leading to the formation of Na_3Sb and providing a capacity of 660 mAh g^{-1} but a lower volumetric capacity of only 1061 Ah L^{-1} due to the lower density of Na_3Sb compared to Li_3Sb. The first report on the subject by Qian *et al.* showed surprising reversibility for a ball-milled Sb/C composite when the electrolyte additive fluoroethylene carbonate was used, providing a stable capacity of 575 mAh g^{-1} after 100 cycles. Following this work, Darwiche *et al.* found similar stability and performance for micrometric antimony powders in contradiction to the previously mentioned work (Fig. 2.10), which they reported as unexpected since the performance of micron sized antimony in lithium ion cells is generally poor.(*28*) They attributed this to differences in the electrode formulation, and postulated that the stability of large antimony particles in the sodium ion cell was the result of a different insertion mechanism for sodium compared to lithium. While lithiation is known to occur by an alloying mechanism that produces firstly crystalline Li_2Sb, then Li_3Sb, sodiation proceeds through amorphous intermediates and culminates in the formation of a mixture of high pressure cubic Na_3Sb and the ambient hexagonal Na_3Sb phase. Baggetto *et al.* provided thermodynamic and kinetic measurements on antimony thin films in both lithium ion and sodium ion cells.(*32*)

These works provided a basis for a large number of more recent publications which have primarily dealt with different electrode formulations.

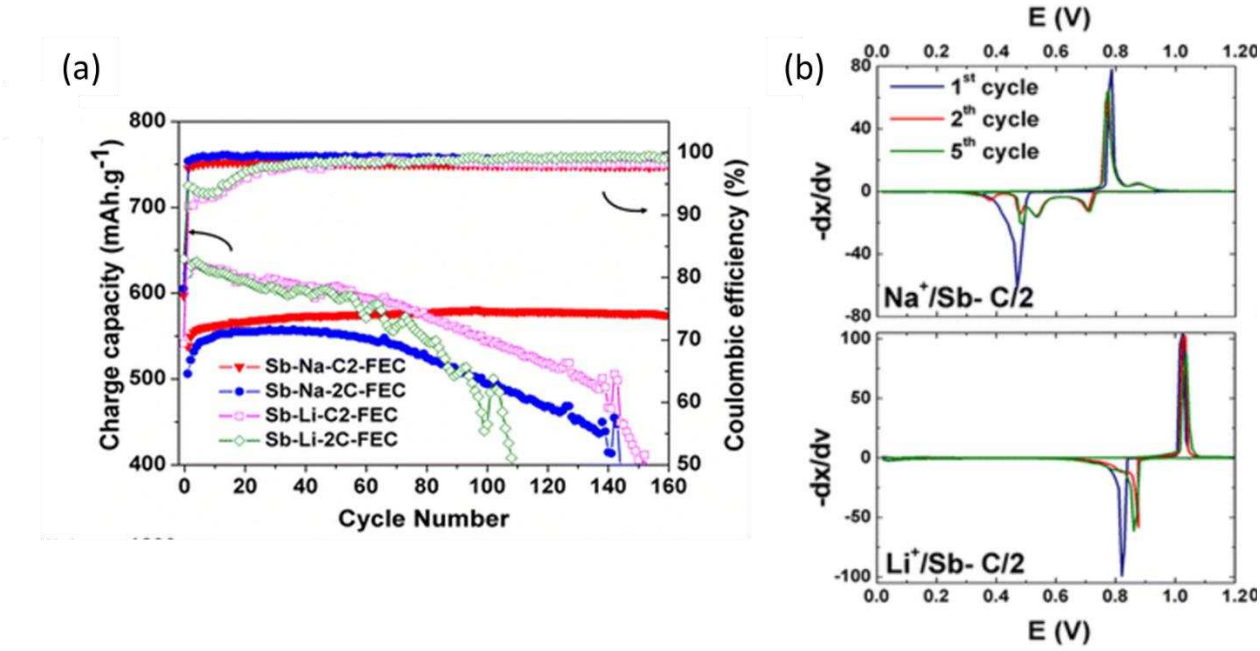

Figure 2.10. (a) Cycling performance of Sb electrode vs Na^+ and Li^+ at C/2 and 2C with 5% FEC. (b) Derivatives of the composition–voltage profiles for Sb/Na and Sb/Li cells cycled at C/2 and 2C rates between 1.5 and 0.02 V. Reprinted with permission from ref. 28.

Following early reports that were able to show that pure Sb can cycle with high stability for at least 100 cycles, many groups have worked on enhancing the performance by modifying the particle morphology and size(*148-151*), modifying the formulation of the electrolyte or electrode(*152-158*), or by using carbon modified antimony materials(*159-164*). Currently, it appears a practical Sb based sodium ion negative electrode could be realized. Despite the good preliminary reports on this system, it should be noted that sodium ion cells using antimony are still inferior to current lithium ion battery cells. To be practical, low-cost synthetic methods and high longevity of Sb electrodes will need to be realized to bring the cell cost lower than equivalent lithium ion cells.

2.6 Na-TM-Sb

Compared to the electrochemistry of lithium with metal antimonides, relatively little research has been published on the electrochemistry of sodium ions. This is in part due to the relatively newness of the field, but also because a recent focus on the discovery and use of earth abundant and non-toxic materials in academic science. As a result, the only metal antimonides that have been studied to date are alloys of Sn, Cu, Fe, Ni, Zn, Mo, and Al. Similar to the case of sodium ions with pure Sb, the mechanism is generally different for the reaction of sodium ions compared to lithium ions, generally favoring amorphization instead of well-defined ternary intermediates. Although still in the early stages, these compounds have shown promising performance and may be capable of sustained long-term operation in sodium ion batteries if compatible electrolytes and cathode materials can be discovered.

2.6.1. Na-Sn-Sb

Early reports on both Sb and Sn in sodium ion cells reported higher than expected reversibility. As a result of investigations on SnSb in lithium ion cells that suggested better performance than either individual element alone, this material has been a clear candidate for sodium ion anodes. Full lithiation of SnSb forms an equal mixture of Li_3Sb and $Li_{3.75}Sn$, providing a high theoretical capacity of 753 mAh g^{-1}.

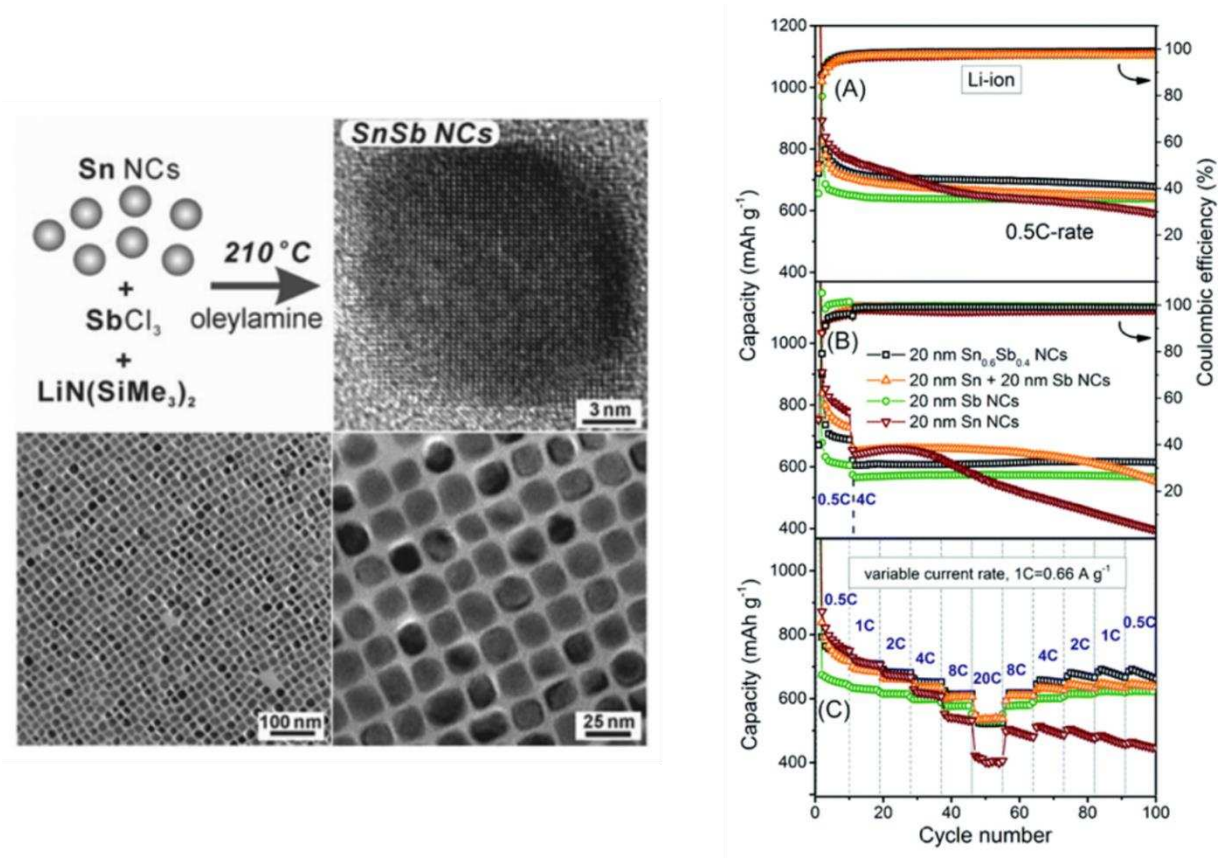

Figure 2.11. Left: Synthesis of monodisperse SnSb nanocrystals and electron microscope images of the particles. Right: (A, B) Galvanostatic cycling stability tests at current densities of 0.33 A g^{-1} and 2.64 A g^{-1}, and (C) rate capability tests (0.5–20C rates, 1C = 660 mA g^{-1} based on the theoretical capacity of pure Sb) for Li-ion anodes composed of SnSb, Sn and Sb NCs. The first two cycles for all electrodes shown in (B, C) were carried out at 0.1C rate. All batteries were cycled in the voltage window of 0.02–1.5 V. Reprinted with permission from ref. 148.

An initial report by Xiao *et al.* provided a promising reversible capacity of 544 mAh g^{-1} and 80% capacity retention for a SnSb/C nanocomposite.(*165*) Darwiche *et al.* studied ball-milled SnSb and has shown it is possible to achieve hundreds of cycles with minimal capacity fade for nearly 200 cycles.(*166*) In contrast to the previous work, they proposed that SnSb undergoes a different mechanism than the reaction of pure Sn and Sb with sodium on the basis of differing differential capacity plots and Mössbauer data.

A number of other reports have used various forms of SnSb in electrodes with reasonable success. Nanocomposites with carbon nanofiber were shown to provide stable capacity when fluoroethylene carbonate was used as an additive.(*167*) A SnSb-C-TiC composite similar to those reported for other alloying materials has been studied as well.(*168*) Another composite of nanoparticles of SnSb bonded to reduced graphene oxide have displayed good kinetic performance and reasonable short term cycle stability.(*169*) He *et al.* tested high quality monodisperse SnSb nanoparticles and found improved performance over elemental nanoparticles of Sn and Sb (Fig. 2.11).(*148*) A following study was performed by Walter *et al.* on SnSb nanocrystals that contrasted the performance of their electrodes in both lithium ion and sodium ion cells. Using a $Na_{1.5}VPO_{4.8}F_{0.7}$ cathodes, they demonstrated a working sodium ion full cell with an average voltage of 2.7 V and a capacity usage of 400 mAh g^{-1} for the SnSb anode stable for at least 60 cycles. This is currently one of the few demonstrations of a working sodium ion full cell with an alloy anode.

2.6.2. Na-Cu-Sb

The intermetallic Cu_2Sb has been the subject of a small number of focused studies. Baggetto *et al.* first studied this system in the form of sputtered films.(*170, 171*) Initial results indicated this reaction proceeds by amorphization of the Cu_2Sb electrode and formation of Na_3Sb at full sodiation, followed by the formation of a mostly amorphous electrode at full desodiation. This mechanism was further studied by Mössbauer and X-ray absorption spectroscopy in a follow-up paper. Fast capacity fade was determined as the result of instability of the electrolyte with the electrode, but later reports have shown >100 cycle stability when FEC is added to the electrolyte. In the follow-up study, more detailed *ex-situ* data was collected that showed evidence for the

reformation of Cu_2Sb if the electrode is completely desodiated by holding at ~1.5 V until the current being passed is negligible.

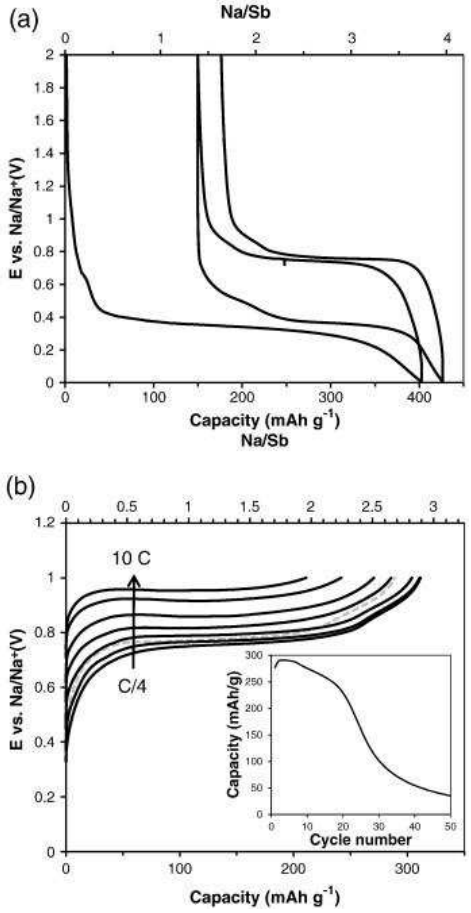

Figure 2.12. (a) Electrochemical characterization of Cu_2Sb thin films: (a) Electrochemical potential profiles during the first two cycles for micro-weighted 3 μm thick electrodes at 20 μA cm^{-2}. (b) Rate performance from 20 to 800 μA cm^{-2}, corresponding to C/4 and 10 C-rates, and cycle life of 200 nm thick Cu_2Sb electrodes at 100 μA cm^{-2} (insert). The gray curve was measured at C/4 after the rate experiment to highlight the decrease in capacity during the rate test. Reproduced with permission from ref. 170.

Other reports on the compound have detailed a Cu_2Sb-Al_2O_3-C nanocomposite(*172*) and a Sb/Cu_2Sb nanoporous foam electrode.(*173*) These have shown modest capacity retention for ~100 cycles. One major limitation is the generally low capacity of this material, offering practical

capacities of only ~250 mAh g^{-1} at slow rates. Unless copper can be shown to provide a significant kinetic improvement or increase in cycle life, it is unlikely to useful as an anode material.

2.6.3. Na-Fe-Sb

The iron antimonide $FeSb_2$ was first studied in the form of $FeSb_2$-Al_2O_3-C nanocomposites by Kim *et al.(172)* They reported an initial capacity of 350 mAh g^{-1} (compared to 250 mAh g^{-1} for Cu_2Sb), but with faster capacity fade than comparable NiSb and Cu_2Sb electrodes. A more detailed mechanistic study was performed by Baggetto *et al.* using *in situ* X-ray diffraction and Mössbauer spectroscopy.(*174*) They also found a similar reversible capacity of 360 mAh g^{-1}, but noted that this is very low compared to the theoretical value of 537 mAh g^{-1}. They attributed this to the irreversible formation of an irreversible amorphous material with a stoichiometry of Fe_4Sb, causing a significant amount of antimony to be unavailable for sodiation. This result suggests that Fe-Sb alloys may be an unsuitable electrode material for sodium ion cells.

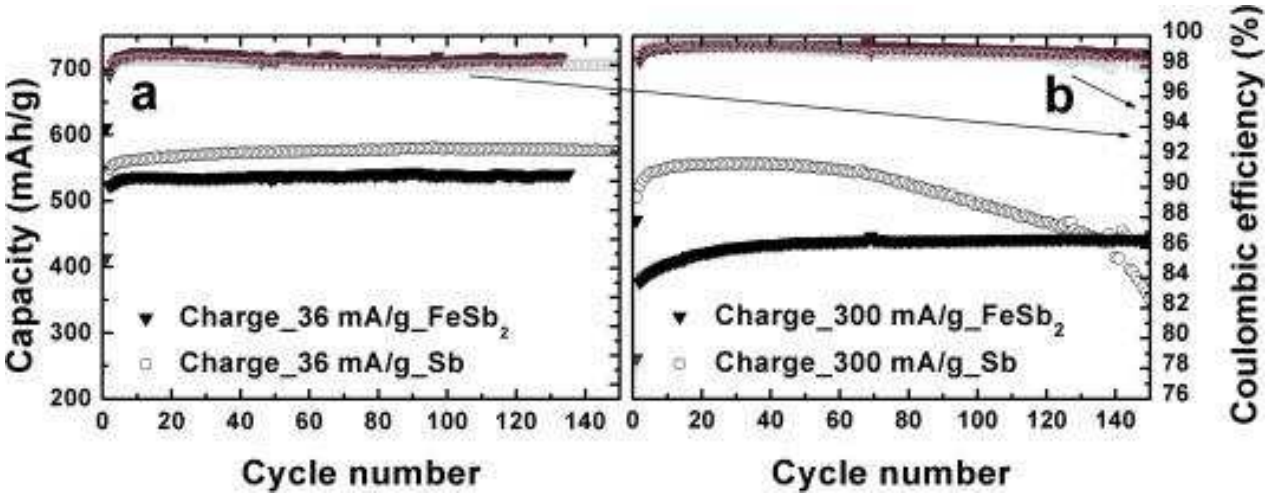

Figure 2.13. Cyclability and coulombic efficiency measured for $FeSb_2$/Na and Sb/Na (a) at 36 mA/g and (b) at 300 mA/g. Reproduced with permission from ref. 175.

Despite the early reports that suggested that $FeSb_2$ had poor reversibility, a study conducted by Darwiche *et al.* found that the low reversible capacity could be overcome by modifying the electrode formulation (Fig. 2.13).(*175*) Using carboxymethyl cellulose binder, carbon black, and vapor ground carbon fibers, they were able to reach a reversible capacity of 540 mAh g^{-1} and retain 440 mAh g^{-1} at 130 cycles. Mössbauer and *in situ* X-ray diffraction experiments showed that these electrodes were able to fully utilize the antimony and undergo complete conversion to metallic iron and antimony. Another study has detailed the performance of an iron rich alloy "$Fe_{1.18}Sb_{1.82}$", but using a similar formulation to Baggetto *et al.*, and achieving similar performance to the earlier studies.(*176*) Kim *et al.* also studied a FeSb-TiC-C nanocomposite and were able to get a high stable capacity of nearly 400 mAh g^{-1} for ~250 cycles when FEC is used as an additive.(*177*) These more recent studies have shown that proper formulation can allow for high reversibility of iron antimonide alloy materials.

2.6.4. Na-Ni-Sb

The nickel antimonide NiSb was first reported by Kim *et al.* in conjunction with $FeSb_2$ and Cu_2Sb in the form of a NiSb-Al_2O_3-C nanocomposite.(*172*) Compared to the other two intermetallics, nickel antimonide provided lower capacity but more stable performance. Similar electrochemistry was reported for this compound compared to the others studied. Lee *et al.* have studied nanowire arrays of Sb electrodeposited onto Ni nanowires, where significant NiSb is formed at the nanowire interface.(*178*) They report a good initial reversible capacity of 502 mAh g^{-1} (with respect to antimony only) and 391 mAh g^{-1} after 300 cycles, but relatively low coulombic efficiencies of <95%. Currently, there is still a need for fundamental studies on this system as none have been undertaken to date.

2.6.5. Na-Zn-Sb

The zinc antimonide system has been studied in the form of Zn_4Sb_3 electrodeposited thin films.(*179*) Highly crystalline films have been found to achieve near theoretical capacity, and when sufficiently thin can retain 90% of their capacity after 250 cycles. Unlike other similar systems, multiple features were observed after the first cycle for both charge and discharge, which appeared for crystalline films, but not amorphous ones (Fig. 2.14). On the basis of the near-theoretical capacity for complete conversion of only the antimony, and the absence of extra peaks in *ex situ* X-ray diffraction experiments, we concluded that zinc was not likely to act as an active material and crystallize into $NaZn_{13}$, the only reported sodium-zinc intermetallic.

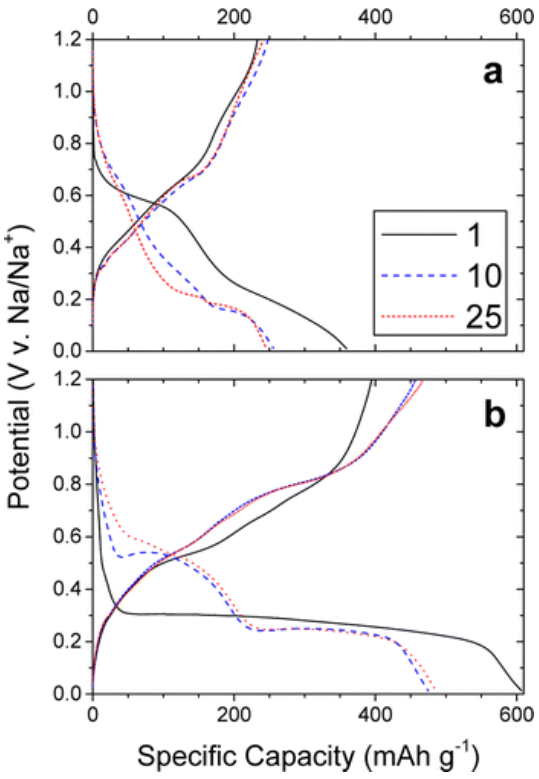

Figure 2.14. Charge–discharge voltage profiles for the 1st (black solid), 10th (blue dashed), and 25th (red dotted) cycles for (a) an amorphous 4:3 Zn:Sb thin film deposited for 240 s and (b) an annealed 2:3 Zn:Sb thin film annealed for 6 h at 300 °C under argon to produce Zn_4Sb_3. Films were cycled in a sodium-ion cell between 0.01 and 1.20 V. The electrolyte used is 1 M $NaClO_4$ in PC with 5% FEC additive. Reprinted with permission from ref. 179.

More recently Nie *et al.* studied Zn_4Sb_3 nanowires using *in situ* transmission electron microscopy.(*180*) They were able to identify the $NaZn_{13}$ phase by electron diffraction, as well as an intermediate ternary phase during cycling, NaZnSb. The interaction of both zinc and antimony with sodium, the existence of a ternary intermediate, and the ability to extract the full capacity of this material, and the high abundance and low cost of zinc, make zinc antimonide particularly interesting for further consideration as a sodium ion battery anode material.

2.6.6. Na-Mo-Sb

Only one Mo-Sb intermetallic is known to exist under ambient conditions, tetragonal Mo_3Sb_7. Baggetto *et al.* first studied this material in a sodium ion cell, noting that it has particularly high rate capability in both lithium ion and sodium ion cells (Fig. 15).(*181*) A reasonable initial reversible capacity of 330 mAh g^{-1} was reported with stable cycling for about 60 cycles. Unlike many of the other transition metal antimonides, a completely amorphous fully sodiated product was observed by *ex situ* X-ray diffraction. Li *et al*. reported improved performance from carbon coated Mo_3Sb_7, which provided 352 mAh g^{-1} initially but increased to 445 mAh g^{-1} after 100 cycles, with a retention of 338 mAh g^{-1} after 800 cycles. A full cell was also reported in this study, providing reasonable short term stability over 20 cycles and an average cell potential of 2.0 V using carbon coated $Na_3V_2(PO_4)_3$ as the cathode material. Compared to studies on other metal antimonides, this study has shown remarkable long term stability in half cells and is one of only two studies reported to date providing data for a metal antimonide in a sodium ion full cell configuration.

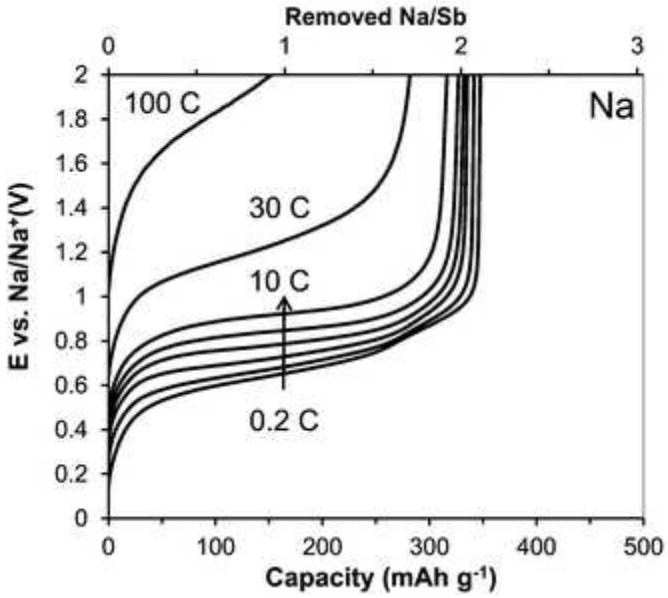

Figure 2.15. Rate performance of 0.8 μm thick Mo_3Sb_7 film electrodes during charge (sodium ion removal) measured from 0.2 C to 100 C-rate. All discharges were performed using constant current constant voltage steps with 1 C current until 0.005 V was reached, and held till the current dropped below 0.2 C. Reproduced with permission from ref. 181.

2.6.7. Na-Al-Sb

In contrast to the Li-Al system, no Na-Al intermetallics exist in the ambient condition phase diagram. Baggetto *et al.* first studied this system in sodium ion cells and found a reasonable reversible capacity of 450 mAh g^{-1} but relatively short cycle life.(*182*) The kinetic performance was shown to be unacceptably poor, however, unlike many of the other metal antimonides discussed here and unlike the case of AlSb in lithium ion cells. It is unclear at this time if this particular antimonide has any real potential due to this issue.

2.7 Conclusion

Two decades of research effort has been devoted to investigations of Sb alloy anode materials for lithium ion batteries, and significant work is currently being undertaken for developing analogous sodium ion battery analogues. Similar to other alloying materials, Sb

provides high volumetric and gravimetric capacities at a moderate voltage, making it an interesting material with figures of merit that can exceed graphite in some cases. In order to make efficient electrodes incorporating antimony, the major issues with low initial coulombic efficiency, fast electrolyte degradation, and high electrode volume change must all be overcome. Attempts at this using carbon coating and incorporation of transition metals have been covered in this review, but at the time of this writing, current materials have not achieved the performance necessary to best state of the art graphite electrodes in terms of energy density. Realization of an Sb-based electrode with high energy density will require new approaches to increasing cycle efficiency to match intercalation materials.

REFERENCES

1. M. T. McDowell, S. W. Lee, W. D. Nix, Y. Cui, 25th Anniversary Article: Understanding the Lithiation of Silicon and Other Alloying Anodes for Lithium-Ion Batteries. *Advanced Materials* **25**, 4966-4985 (2013).

2. W.-J. Zhang, A review of the electrochemical performance of alloy anodes for lithium-ion batteries. *Journal of Power Sources* **196**, 13-24 (2011).

3. W.-J. Zhang, Lithium insertion/extraction mechanism in alloy anodes for lithium-ion batteries. *Journal of Power Sources* **196**, 877-885 (2011).

4. C.-M. Park, J.-H. Kim, H. Kim, H.-J. Sohn, Li-alloy based anode materials for Li secondary batteries. *Chemical Society Reviews* **39**, 3115-3141 (2010).

5. D. Larcher *et al.*, Recent findings and prospects in the field of pure metals as negative electrodes for Li-ion batteries. *Journal of Materials Chemistry* **17**, 3759-3772 (2007).

6. U. Kasavajjula, C. Wang, A. J. Appleby, Nano- and bulk-silicon-based insertion anodes for lithium-ion secondary cells. *Journal of Power Sources* **163**, 1003-1039 (2007).

7. R. A. Huggins, Lithium alloy negative electrodes. *Journal of Power Sources* **81–82**, 13-19 (1999).

8. J. O. Besenhard, J. Yang, M. Winter, Will advanced lithium-alloy anodes have a chance in lithium-ion batteries? *Journal of Power Sources* **68**, 87-90 (1997).

9. M. Winter, J. O. Besenhard, Electrochemical lithiation of tin and tin-based intermetallics and composites. *Electrochimica Acta* **45**, 31-50 (1999).

10. B. Liang, Y. Liu, Y. Xu, Silicon-based materials as high capacity anodes for next generation lithium ion batteries. *Journal of Power Sources* **267**, 469-490 (2014).

11. M. N. Obrovac, V. L. Chevrier, Alloy Negative Electrodes for Li-Ion Batteries. *Chemical Reviews* **114**, 11444-11502 (2014).

12. J. Wang, I. D. Raistrick, R. A. Huggins, Behavior of Some Binary Lithium Alloys as Negative Electrodes in Organic Solvent-Based Electrolytes. *Journal of The Electrochemical Society* **133**, 457-460 (1986).

13. A. N. Dey, Electrochemical Alloying of Lithium in Organic Electrolytes. *Journal of The Electrochemical Society* **118**, 1547-1549 (1971).

14. Z. Lu, A. Schechter, M. Moshkovich, D. Aurbach, On the electrochemical behavior of magnesium electrodes in polar aprotic electrolyte solutions. *Journal of Electroanalytical Chemistry* **466**, 203-217 (1999).

15. B. M. L. Rao, R. W. Francis, H. A. Christopher, Lithium-Aluminum Electrode. *Journal of The Electrochemical Society* **124**, 1490-1492 (1977).

16. W. Weppner, R. A. Huggins, Thermodynamic Properties of the Intermetallic Systems Lithium-Antimony and Lithium-Bismuth. *Journal of The Electrochemical Society* **125**, 7-14 (1978).

17. M. R. St. John, A. J. Furgala, A. F. Sammells, Thermodynamic Studies of Li-Ge Alloys: Application to Negative Electrodes for Molten Salt Batteries. *Journal of The Electrochemical Society* **129**, 246-250 (1982).

18. J. Wolfenstine, J. L. Allen, J. Read, D. Foster, "Chemistry and Structure of Sony's Nexelion Li-ion Electrode Materials," (DTIC Document, 2006).

19. J. O. Besenhard, H. P. Fritz, Reversibles elektrochemisches legieren von metallen der V. hauptgruppe in organischen Li+—Lösungen. *Electrochimica Acta* **20**, 513-517 (1975).

20. W. Weppner, R. A. Huggins, Determination of the Kinetic Parameters of Mixed-Conducting Electrodes and Application to the System Li3Sb. *Journal of The Electrochemical Society* **124**, 1569-1578 (1977).

21. W. Weppner, R. A. Huggins, Electrochemical investigation of the chemical diffusion, partial ionic conductivities, and other kinetic parameters in Li3Sb and Li3Bi. *Journal of Solid State Chemistry* **22**, 297-308 (1977).

22. A. Prieto. (2015), vol. 2015, pp. Prieto Battery Website.

23. J. Yang, M. Winter, J. O. Besenhard, Small particle size multiphase Li-alloy anodes for lithium-ionbatteries. *Solid State Ionics* **90**, 281-287 (1996).

24. R. Alcántara *et al.*, Electrochemical reaction of lithium with the CoSb 3 skutterudite. *Journal of Materials Chemistry* **9**, 2517-2521 (1999).

25. C. Johnson *et al.*, Electrochemistry and in-situ X-ray diffraction of InSb in lithium batteries. *Electrochemistry communications* **2**, 595-600 (2000).

26. K. C. Hewitt, L. Y. Beaulieu, J. R. Dahn, Electrochemistry of InSb as a Li Insertion Host: Problems and Prospects. *Journal of The Electrochemical Society* **148**, A402-A410 (2001).

27. H. Yoshida, N. Yabuuchi, S. Komaba, NaFe0.5Co0.5O2 as high energy and power positive electrode for Na-ion batteries. *Electrochemistry Communications* **34**, 60-63 (2013).

28. A. Darwiche *et al.*, Better cycling performances of bulk Sb in Na-ion batteries compared to Li-ion systems: an unexpected electrochemical mechanism. *Journal of the American Chemical Society* **134**, 20805-20811 (2012).

29. T. S. Arthur *et al.*, Three-dimensional electrodes and battery architectures. *Mrs Bulletin* **36**, 523-531 (2011).

30. B. Dunn, J. W. Long, D. R. Ronson, Rethinking multifunction in three dimensions for miniaturizing electrical energy storage. *The Electrochemical Society Interface* **17**, 49 (2008).

31. D. R. Rolison *et al.*, Multifunctional 3D nanoarchitectures for energy storage and conversion. *Chemical Society Reviews* **38**, 226-252 (2009).

32. L. Baggetto *et al.*, Intrinsic thermodynamic and kinetic properties of Sb electrodes for Li-ion and Na-ion batteries: Experiment and Theory. *Journal of Materials Chemistry A* **1**, 7985-7994 (2013).

33. A. Dailly, J. Ghanbaja, P. Willmann, D. Billaud, Electrochemical intercalation of lithium into graphite–antimony composites synthesized by reduction of a SbCl 5–graphite intercalation compound by gaseous caesium. *Journal of power sources* **125**, 70-76 (2004).

34. H. Kim, J. Cho, Template synthesis of hollow Sb nanoparticles as a high-performance lithium battery anode material. *Chemistry of Materials* **20**, 1679-1681 (2008).

35. H. Bryngelsson, J. Eskhult, K. Edström, L. Nyholm, Electrodeposition and electrochemical characterisation of thick and thin coatings of Sb and Sb/Sb 2 O 3 particles for Li-ion battery anodes. *Electrochimica Acta* **53**, 1062-1073 (2007).

36. H. Bryngelsson *et al.*, Electrodeposited Sb and Sb/Sb2O3 Nanoparticle Coatings as Anode Materials for Li-Ion Batteries. *Chemistry of Materials* **19**, 1170-1180 (2007).

37. F. Martín, J. Morales, L. Sánchez, Elucidating the Beneficial Effect of Vinylene Carbonate on the Electrochemistry of Antimony Electrodes in Lithium Batteries. *ChemPhysChem* **9**, 2610-2617 (2008).

38. W. X. Chen, J. Y. Lee, Z. Liu, The nanocomposites of carbon nanotube with Sb and SnSb0.5 as Li-ion battery anodes. *Carbon* **41**, 959-966 (2003).

39. J. Hassoun, G. Derrien, S. Panero, B. Scrosati, The role of the morphology in the response of Sb–C nanocomposite electrodes in lithium cells. *Journal of Power Sources* **183**, 339-343 (2008).

40. Y. Zhang *et al.*, Activation of electrochemical lithium and sodium storage of nanocrystalline antimony by anchoring on graphene via a facile in situ solvothermal route. *Journal of Power Sources* **247**, 204-212 (2014).

41. D. Manasijević *et al.*, Experimental investigation and thermodynamic calculation of the Cu–In–Sb phase diagram. *Calphad* **33**, 221-226 (2009).

42. L. M. Fransson *et al.*, Phase transitions in lithiated Cu 2 Sb anodes for lithium batteries: an in situ X-ray diffraction study. *Electrochemistry Communications* **3**, 317-323 (2001).

43. S.-W. Song *et al.*, Cu2Sb Thin-film electrodes prepared by pulsed laser deposition for lithium batteries. *Journal of the Electrochemical Society* **151**, A1012-A1019 (2004).

44. M. Morcrette *et al.*, Influence of electrode microstructure on the reactivity of Cu 2 Sb with lithium. *Electrochimica acta* **52**, 5339-5345 (2007).

45. S. Matsuno, M. Noji, T. Kashiwagi, M. Nakayama, M. Wakihara, Construction of the ternary phase diagram for the Li-Cu-Sb system as the anode material for a lithium ion battery. *The Journal of Physical Chemistry C* **111**, 7548-7553 (2007).

46. S. Matsuno *et al.*, Dynamics of Phase Transition in Li–Cu–Sb Anode Material for Rechargeable Lithium Ion Battery. *Journal of The Electrochemical Society* **155**, A151-A157 (2008).

47. J. M. Mosby, A. L. Prieto, Direct electrodeposition of Cu2Sb for lithium-ion battery anodes. *Journal of the American Chemical Society* **130**, 10656-10661 (2008).

48. J. M. Mosby, COLORADO STATE UNIVERSITY, (2010).

49. H. Bryngelsson, J. Eskhult, L. Nyholm, K. Edström, Thin films of Cu 2 Sb and Cu 9 Sb 2 as anode materials in Li-ion batteries. *Electrochimica Acta* **53**, 7226-7234 (2008).

50. Y. He *et al.*, Facile synthesis of hollow Cu 2 Sb@ C core–shell nanoparticles as a superior anode material for lithium ion batteries. *Journal of Materials Chemistry* **21**, 18517-18519 (2011).

51. A. N. Jansen, J. A. Clevenger, A. M. Baebler, J. T. Vaughey, Variable temperature performance of intermetallic lithium-ion battery anode materials. *Journal of Alloys and Compounds* **509**, 4457-4461 (2011).

52. S. Tan, E. Perre, T. Gustafsson, D. Brandell, A solid state 3-D microbattery based on Cu 2 Sb nanopillar anodes. *Solid State Ionics* **225**, 510-512 (2012).

53. E. Perre *et al.*, Electrodeposited Cu 2 Sb as anode material for 3-dimensional Li-ion microbatteries. *Journal of Materials Research* **25**, 1485-1491 (2010).

54. D. Applestone, A. Manthiram, Symmetric cell evaluation of the effects of electrolyte additives on Cu 2 Sb–Al 2 O 3–C nanocomposite anodes. *Journal of Power Sources* **217**, 1-5 (2012).

55. D. Applestone, S. Yoon, A. Manthiram, Cu 2 Sb–Al 2 O 3–C nanocomposite alloy anodes with exceptional cycle life for lithium ion batteries. *Journal of Materials Chemistry* **22**, 3242-3248 (2012).

56. E. Allcorn, S.-O. Kim, A. Manthiram, Thermal stability of active/inactive nanocomposite anodes based on Cu 2 Sb in lithium-ion batteries. *Journal of Power Sources* **299**, 501-508 (2015).

57. E. Allcorn, A. Manthiram, Thermal Stability of Sb and Cu2Sb Anodes in Lithium-Ion Batteries. *Journal of The Electrochemical Society* **162**, A1778-A1786 (2015).

58. B. Legendre, E. Dichi, V. Vassiliev, The phase diagram of the In-Sb-Sn system. *Zeitschrift für Metallkunde* **92**, 328-335 (2001).

59. J. Yang, M. Wachtler, M. Winter, J. O. Besenhard, Sub-Microcrystalline Sn and Sn - SnSb Powders as Lithium Storage Materials for Lithium-Ion Batteries. *Electrochemical and Solid-State Letters* **2**, 161-163 (1999).

60. H. Li, L. Shi, W. Lu, X. Huang, L. Chen, Studies on capacity loss and capacity fading of nanosized SnSb alloy anode for Li-ion batteries. *Journal of The Electrochemical Society* **148**, A915-A922 (2001).

61. H. Li, Q. Wang, L. Shi, L. Chen, X. Huang, Nanosized SnSb alloy pinning on hard non-graphitic carbon spherules as anode materials for a Li ion battery. *Chemistry of materials* **14**, 103-108 (2002).

62. H. Mukaibo *et al.*, Optimized Sn/SnSb lithium storage materials. *Journal of power sources* **132**, 225-228 (2004).

63. S. Needham, G. Wang, H. Liu, Electrochemical performance of SnSb and Sn/SnSb nanosize powders as anode materials in Li-ion cells. *Journal of alloys and compounds* **400**, 234-238 (2005).

64. Y. Wang, J. Y. Lee, One-Step, Confined Growth of Bimetallic Tin–Antimony Nanorods in Carbon Nanotubes Grown In Situ for Reversible Li+ Ion Storage. *Angewandte Chemie International Edition* **45**, 7039-7042 (2006).

65. L. Xue *et al.*, A simple method to encapsulate SnSb nanoparticles into hollow carbon nanofibers with superior lithium-ion storage capability. *Journal of Materials Chemistry A* **1**, 13807-13813 (2013).

66. C. Yin, H. Zhao, H. Guo, X. Huang, W. Qiu, Effect of the synthesis method of SnSb anode materials on their electrochemical properties. *Journal of University of Science and Technology Beijing, Mineral, Metallurgy, Material* **14**, 345-349 (2007).

67. K.-L. Huang, G. Zhang, S.-Q. Liu, Effect of graphite content on electrochemical performance of Sn-SnSb/graphite composite powders. *Transactions of Nonferrous Metals Society of China* **17**, 841-845 (2007).

68. F. Wang, M. Zhao, X. Song, Nano-sized SnSbCu x alloy anodes prepared by co-precipitation for Li-ion batteries. *Journal of Power Sources* **175**, 558-563 (2008).

69. F. Wang, M. Zhao, X. Song, The improved electrochemical performance of SnSb-based alloy anode materials for Li-ion batteries. *Journal of Alloys and Compounds* **472**, 55-58 (2009).

70. Z. Wang, W. Tian, X. Li, Synthesis and electrochemistry properties of Sn–Sb ultrafine particles as anode of lithium-ion batteries. *Journal of alloys and compounds* **439**, 350-354 (2007).

71. H. Zhao *et al.*, Studies of the electrochemical performance of Sn–Sb alloy prepared by solid-state reduction. *Journal of Power Sources* **174**, 916-920 (2007).

72. J. Xie *et al.*, Preparation and Li-storage properties of SnSb/graphene hybrid nanostructure by a facile one-step solvothermal route. *International Journal of Smart and Nano Materials* **2**, 261-271 (2011).

73. P. Zhang *et al.*, Electrochemical lithiation and delithiation performance of SnSb–Ag/carbon nanonube composites for lithium-ion batteries. *Journal of Power Sources* **233**, 166-173 (2013).

74. P. Nithyadharseni, M. Reddy, B. Nalini, M. Kalpana, B. Chowdari, Sn-based intermetallic alloy anode materials for the application of lithium ion batteries. *Electrochimica Acta* **161**, 261-268 (2015).

75. P. Nithyadharseni, M. Reddy, B. Nalini, B. Chowdari, Electrochemical investigation of SnSb nano particles for lithium-ion batteries. *Materials Letters* **150**, 24-27 (2015).

76. P. Nithyadharseni *et al.*, Electrochemical studies of CNT/Si–SnSb nanoparticles for lithium ion batteries. *Materials Research Bulletin* **70**, 478-485 (2015).

77. H. Okamoto, Co-Sb (cobalt-antimony). *Journal of phase equilibria* **12**, 244-245 (1991).

78. J. Xie, X. Zhao, G. Cao, Y. Zhong, M. Zhao, Electrochemical lithium intercalation in CoSb3 compound. *Journal of Materials Science Letters* **22**, 221-224 (2003).

79. J.-M. Tarascon *et al.*, On the Electrochemical Reactivity Mechanism of CoSb3 vs. Lithium. *Journal of The Electrochemical Society* **150**, A732-A741 (2003).

80. I. Devos *et al.*, Lithium insertion mechanism in CoSb 3 analysed by 121 Sb Mössbauer spectrometry, X-ray absorption spectroscopy and electronic structure calculations. *Journal of Materials Chemistry* **14**, 1759-1767 (2004).

81. C. Ionica *et al.*, Structural and electronic features of Sb-based electrode materials: 121Sb Mössbauer spectrometry. *Hyperfine interactions* **156**, 555-561 (2004).

82. V. Pralong *et al.*, Electrochemical study of nanometer Co3O4, Co, CoSb3 and Sb thin films toward lithium. *Solid State Ionics* **166**, 295-305 (2004).

83. J. Xie, X. Zhao, G. Cao, Y. Zhong, M. Zhao, Ex-situ XRD studies of CoSb 3 compound as the anode material for lithium ion batteries. *Journal of Electroanalytical Chemistry* **542**, 1-6 (2003).

84. J. Xie, G. Cao, X. Zhao, Y. Zhong, M. Zhao, Electrochemical performances of nanosized intermetallic compound CoSb2 prepared by the solvothermal route. *Journal of the Electrochemical Society* **151**, A1905-A1910 (2004).

85. J. Xie, G. Cao, Y. Zhong, X. Zhao, Capacity fade mechanism of CoSb 3 intermetallic compound. *Journal of Electroanalytical Chemistry* **568**, 323-327 (2004).

86. J. Xie, X. Zhao, G. Cao, M. Zhao, S. Su, Solvothermal synthesis and electrochemical performances of nanosized CoSb 3 as anode materials for Li-ion batteries. *Journal of power sources* **140**, 350-354 (2005).

87. J. Xie, X. Zhao, G. Cao, M. Zhao, Electrochemical performance of CoSb 3/MWNTs nanocomposite prepared by in situ solvothermal synthesis. *Electrochimica acta* **50**, 2725-2731 (2005).

88. J. Xie *et al.*, Solvothermal synthesis of nanosized CoSb 2 alloy anode for Li-ion batteries. *Electrochimica acta* **50**, 1903-1907 (2005).

89. J. Xie, X. Zhao, G. Cao, S. Su, Improvement of electrochemical performances of CoSb3 anode by using nanosized particles. *Journal of the Electrochemical Society* **152**, A601-A606 (2005).

90. M. Wang *et al.*, Preparation and electrochemical performance of CoSb alloy anode material for Li-ion batteries. *Journal of Alloys and Compounds* **484**, 864-869 (2009).

91. Y.-w. Yang, Y.-b. Chen, F. Liu, X.-y. Chen, Y.-c. Wu, Template-based fabrication and electrochemical performance of CoSb nanowire arrays. *Electrochimica Acta* **56**, 6420-6425 (2011).

92. J. Xie *et al.*, In situ synthesis of CoSb 3-nanocrystals/graphene hybrid via one-pot solvothermal route and its electrochemical Li-storage properties. *Int. J. Electrochem. Sci* **7**, 1319-1331 (2012).

93. Y.-X. Zheng *et al.*, Rapid Synthesis of CoSb3/GRAPHENE Nanocomposites by One-Pot Solvothermal Route and Their Electrochemical Properties. *Functional Materials Letters* **5**, 1250002 (2012).

94. M.-G. Park, J. H. Song, J.-S. Sohn, C. K. Lee, C.-M. Park, Co–Sb intermetallic compounds and their disproportionated nanocomposites as high-performance anodes for rechargeable Li-ion batteries. *Journal of Materials Chemistry A* **2**, 11391-11399 (2014).

95. Y. Zhang, C. Li, Z. Du, C. Guo, A thermodynamic assessment of Ni–Sb system. *Calphad* **32**, 378-388 (2008).

96. J. Xie, X. Zhao, G. Cao, M. Zhao, S. Su, Electrochemical Li-uptake properties of nanosized NiSb 2 prepared by solvothermal route. *Journal of alloys and compounds* **393**, 283-286 (2005).

97. C. Villevieille, C.-M. Ionica-Bousquet, B. Ducourant, J.-C. Jumas, L. Monconduit, NiSb 2 as negative electrode for Li-ion batteries: an original conversion reaction. *Journal of Power Sources* **172**, 388-394 (2007).

98. C. Villevieille, C.-M. Ionica-Bousquet, J.-C. Jumas, L. Monconduit, in *ICAME 2007*. (Springer, 2008), pp. 1157-1165.

99. C. Villevieille *et al.*, Comparative study of NiSb 2 and FeSb 2 as negative electrodes for Li-ion batteries. *Solid State Ionics* **192**, 351-355 (2011).

100. C. Li, J. Hu, Q. Peng, X. Wang, Synthesis and characterization of nanocrystalline NiSb and NiSb2 at low temperature. *Materials Chemistry and Physics* **110**, 106-109 (2008).

101. J. Xie *et al.*, Sb-based alloy (NiSb, FeSb2) nanoparticles decorated graphene prepared by one-step solvothermal route as anode for Li-ion batteries. *Int. J. Electrochem. Sci* **6**, 4811-4821 (2011).

102. Y.-w. Yang *et al.*, Electrodeposition of Ni 5 Sb 2 nanowires array and its application as a high-performance anode material for lithium ion batteries. *Microelectronic Engineering* **104**, 1-4 (2013).

103. E. Allcorn, A. Manthiram, NiSb–Al2O3–C Nanocomposite Anodes with Long Cycle Life for Li-Ion Batteries. *The Journal of Physical Chemistry C* **118**, 811-822 (2014).

104. H. Hou *et al.*, NiSb alloy hollow nanospheres as anode materials for rechargeable lithium ion batteries. *Chemical Communications* **50**, 8201-8203 (2014).

105. B. Pei, B. Björkman, B. Sundman, B. Jansson, A thermodynamic assessment of the iron—Antimony system. *Calphad* **19**, 1-15 (1995).

106. J. Xie *et al.*, Low-Temperature Solvothermal Synthesis of FeSb2 Nanorods as Li-Ion Batteries Anode Material. *Electrochemical and solid-state letters* **9**, A336-A339 (2006).

107. J. Xie *et al.*, Electrochemical lithiation and delithiation of FeSb 2 anodes for lithium-ion batteries. *Materials Letters* **57**, 4673-4677 (2003).

108. C. Villevieille, B. Fraisse, M. Womes, J.-C. Jumas, L. Monconduit, A new ternary Li 4 FeSb 2 structure formed upon discharge of the FeSb 2/Li cell. *Journal of Power Sources* **189**, 324-330 (2009).

109. C.-M. Park, H.-J. Sohn, Antimonides (FeSb 2, CrSb 2) with orthorhombic structure and their nanocomposites for rechargeable Li-ion batteries. *Electrochimica Acta* **55**, 4987-4994 (2010).

110. E. Allcorn, A. Manthiram, High-rate, high-density FeSb–TiC–C nanocomposite anodes for lithium-ion batteries. *Journal of Materials Chemistry A* **3**, 3891-3900 (2015).

111. E. Allcorn, A. Manthiram, FeSb2–Al2O3–C Nanocomposite Anodes for Lithium-Ion Batteries. *ACS applied materials & interfaces* **6**, 10886-10891 (2014).

112. E. Allcorn, S. O. Kim, A. Manthiram, Lithium diffusivity in antimony-based intermetallic and FeSb–TiC composite anodes as measured by GITT. *Physical Chemistry Chemical Physics* **17**, 28837-28843 (2015).

113. J.-B. Li, M.-C. Record, J.-C. Tedenac, A thermodynamic assessment of the Sb–Zn system. *Journal of alloys and compounds* **438**, 171-177 (2007).

114. M. Purcell, T. Hatchard, R. Sanderson, M. Obrovac, An investigation of the C-Zn system as lithium-ion battery anode materials. *Journal of The Electrochemical Society* **161**, A643-A647 (2014).

115. J. Wang, P. King, R. A. Huggins, Investigations of binary lithium-zinc, lithium-cadmium and lithium-lead alloys as negative electrodes in organic solvent-based electrolyte. *Solid State Ionics* **20**, 185-189 (1986).

116. C. M. Park, H. J. Sohn, Quasi-Intercalation and Facile Amorphization in Layered ZnSb for Li-Ion Batteries. *Advanced Materials* **22**, 47-52 (2010).

117. S. Saadat *et al.*, Template-free electrochemical deposition of interconnected ZnSb nanoflakes for li-ion battery anodes. *Chemistry of Materials* **23**, 1032-1038 (2011).

118. J. Xu, H. Wu, F. Wang, Y. Xia, G. Zheng, Zn4Sb3 nanotubes as lithium ion battery anodes with high capacity and cycling stability. *Advanced Energy Materials* **3**, 286-289 (2013).

119. M.-G. Park, C. K. Lee, C.-M. Park, Amorphized ZnSb-based composite anodes for high-performance Li-ion batteries. *RSC Advances* **4**, 5830-5833 (2014).

120. T. B. Massalski, H. Okamoto, P. Subramanian, L. Kacprzak, W. W. Scott, *Binary alloy phase diagrams*. (American Society for Metals Metals Park, OH, 1986), vol. 1.

121. D. Larcher, L. Beaulieu, O. Mao, A. George, J. Dahn, Study of the reaction of lithium with isostructural A 2 B and various Al x B alloys. *Journal of The Electrochemical Society* **147**, 1703-1708 (2000).

122. C.-M. Park, H.-J. Sohn, Electrochemical characteristics of TiSb2 and Sb/TiC/C nanocomposites as anodes for rechargeable Li-ion batteries. *Journal of The Electrochemical Society* **157**, A46-A49 (2010).

123. J. L. Gómez-Cámer, P. Novák, Polyacrylate bound TiSb 2 electrodes for Li-ion batteries. *Journal of Power Sources* **273**, 174-179 (2015).

124. M. T. Sougrati *et al.*, TiSnSb a new efficient negative electrode for Li-ion batteries: mechanism investigations by operando-XRD and Mossbauer techniques. *Journal of Materials Chemistry* **21**, 10069-10076 (2011).

125. C. Marino *et al.*, Study of the Electrode/Electrolyte Interface on Cycling of a Conversion Type Electrode Material in Li Batteries. *The Journal of Physical Chemistry C* **117**, 19302-19313 (2013).

126. W. Zhang *et al.*, Surface film formation on TiSnSb electrodes: Impact of electrolyte additives. *Journal of Power Sources* **268**, 645-657 (2014).

127. W. Zhang *et al.*, Improvement of the stability of TiSnSb anode under lithiation using SEI forming additives and room temperature ionic liquid/DMC mixed electrolyte. *Electrochimica Acta* **170**, 72-84 (2015).

128. J. Vaughey, J. O'Hara, M. Thackeray, Intermetallic Insertion Electrodes with a Zinc Blende-Type Structure for Li Batteries: A Study of Li x InSb ($0 \leq x \leq 3$). *Electrochemical and Solid-State Letters* **3**, 13-16 (2000).

129. A. Kropf, H. Tostmann, C. Johnson, J. Vaughey, M. Thackeray, An in situ X-ray absorption spectroscopy study of InSb electrodes in lithium batteries. *Electrochemistry communications* **3**, 244-251 (2001).

130. S. Sharma, J. Dewhurst, C. Ambrosch-Draxl, Lithiation of InSb and Cu 2 Sb: A theoretical investigation. *Physical Review B* **70**, 104110 (2004).

131. B. Predel, in *Li-Mg–Nd-Zr*. (Springer, 1997), pp. 1-2.

132. L. Fransson, J. Vaughey, K. Edström, M. Thackeray, Structural Transformations in Intermetallic Electrodes for Lithium Batteries An In Situ X-Ray Diffraction Study of Lithiated MnSb and Mn 2 Sb. *Journal of The Electrochemical Society* **150**, A86-A91 (2003).

133. C. M. Ionica-Bousquet *et al.*, in *ICAME 2005*. (Springer, 2006), pp. 773-778.

134. L. Häggström *et al.*, Structural transformations in lithiated Mn2Sb electrodes probed by Mössbauer spectroscopy and X-ray diffraction. *Hyperfine interactions* **167**, 759-765 (2006).

135. M. Venkatraman, J. Neumann, The Cr-Sb (Chromium-Antimony) System. *Journal of Phase Equilibria* **11**, 435-440 (1990).

136. F. J. Fernández-Madrigal, P. Lavela, C. Pérez-Vicente, J. L. Tirado, Electrochemical reactions of polycrystalline CrSb 2 in lithium batteries. *Journal of Electroanalytical Chemistry* **501**, 205-209 (2001).

137. M. E. Schlesinger, Thermodynamic Properties of Solid Binary Antimonides. *Chemical Reviews* **113**, 8066-8092 (2013).

138. T. Gnanapoongothai, R. Murugan, B. Palanivel, First-principle study on lithium intercalated antimonides Ag3Sb and Mg3Sb2. *Ionics* **21**, 1351-1361 (2015).

139. H. Honda, H. Sakaguchi, I. Tanaka, T. Esaka, Anode behaviors of magnesium–antimony intermetallic compound for lithium secondary battery. *Journal of power sources* **123**, 216-221 (2003).

140. J. Vaughey, L. Fransson, H. Swinger, K. Edström, M. Thackeray, Alternative anode materials for lithium-ion batteries: a study of Ag 3 Sb. *Journal of power sources* **119**, 64-68 (2003).

141. M. A. Reddy, U. Varadaraju, NbSb 2 as an anode material for Li-ion batteries. *Journal of power sources* **159**, 336-339 (2006).

142. M. Stjerndahl *et al.*, Surface chemistry of intermetallic AlSb-anodes for Li-ion batteries. *Electrochimica acta* **52**, 4947-4955 (2007).

143. D. Applestone, S. Yoon, A. Manthiram, Mo3Sb7–C Composite Anodes for Lithium-Ion Batteries. *The Journal of Physical Chemistry C* **115**, 18909-18915 (2011).

144. T. Tabuchi, N. Hochgatterer, Z. Ogumi, M. Winter, Ternary Sn–Sb–Co alloy film as new negative electrode for lithium-ion cells. *Journal of Power Sources* **188**, 552-557 (2009).

145. J. Yin, M. Wada, S. Tanase, T. Sakai, Electrode properties and lithiation/delithiation reactions of Ag-Sb-Sn nanocomposite anodes in Li-ion batteries. *Journal of The Electrochemical Society* **151**, A867-A872 (2004).

146. M. D. Slater, D. Kim, E. Lee, C. S. Johnson, Sodium-ion batteries. *Advanced Functional Materials* **23**, 947-958 (2013).

147. V. L. Chevrier, G. Ceder, Challenges for Na-ion Negative Electrodes. *Journal of The Electrochemical Society* **158**, A1011-A1014 (2011).

148. M. He, K. Kravchyk, M. Walter, M. V. Kovalenko, Monodisperse antimony nanocrystals for high-rate Li-ion and Na-ion battery anodes: nano versus bulk. *Nano letters* **14**, 1255-1262 (2014).

149. H. Hou *et al.*, Sodium/Lithium Storage Behavior of Antimony Hollow Nanospheres for Rechargeable Batteries. *ACS applied materials & interfaces* **6**, 16189-16196 (2014).

150. H. Hou *et al.*, Cypress leaf-like Sb as anode material for high-performance sodium-ion batteries. *Journal of Materials Chemistry A* **3**, 17549-17552 (2015).

151. M. Walter, R. Erni, M. V. Kovalenko, Inexpensive Antimony Nanocrystals and Their Composites with Red Phosphorus as High-Performance Anode Materials for Na-ion Batteries. *Scientific reports* **5**, (2015).

152. L. Wu *et al.*, SiC–Sb–C nanocomposites as high-capacity and cycling-stable anode for sodium-ion batteries. *Electrochimica Acta* **87**, 41-45 (2013).

153. H. Hou *et al.*, An Electrochemical Study of Sb/Acetylene Black Composite as Anode for Sodium-Ion Batteries. *Electrochimica Acta* **146**, 328-334 (2014).

154. K. Li, D. Su, H. Liu, G. Wang, Antimony-Carbon-Graphene Fibrous Composite as Freestanding Anode Materials for Sodium-ion Batteries. *Electrochimica Acta* **177**, 304-309 (2015).

155. D. H. Nam, K. S. Hong, S. J. Lim, M. J. Kim, H. S. Kwon, High-Performance Sb/Sb2O3 Anode Materials Using a Polypyrrole Nanowire Network for Na-Ion Batteries. *small* **11**, 2885-2892 (2015).

156. A. Darwiche, L. Bodenes, L. Madec, L. Monconduit, H. Martinez, Impact of the salts and solvents on the SEI formation in Sb/Na batteries: An XPS analysis. *Electrochimica Acta* **207**, 284-292 (2016).

157. H. Gao, W. Zhou, J. H. Jang, J. B. Goodenough, Cross-Linked Chitosan as a Polymer Network Binder for an Antimony Anode in Sodium-Ion Batteries. *Advanced Energy Materials*, (2016).

158. Y. Yi, H.-W. Shim, S.-D. Seo, M. A. Dar, D.-W. Kim, Enhanced Li-and Na-storage in Sb-Graphene nanocomposite anodes. *Materials Research Bulletin* **76**, 338-343 (2016).

159. Y. Zhu *et al.*, Electrospun Sb/C fibers for a stable and fast sodium-ion battery anode. *ACS nano* **7**, 6378-6386 (2013).

160. X. Zhou *et al.*, An SbO x/Reduced Graphene Oxide Composite as a High-Rate Anode Material for Sodium-Ion Batteries. *The Journal of Physical Chemistry C* **118**, 23527-23534 (2014).

161. L. Fan *et al.*, Electrochemical performance of rod-like Sb–C composite as anodes for Li-ion and Na-ion batteries. *Journal of Materials Chemistry A* **3**, 3276-3280 (2015).

162. H. Hou *et al.*, Antimony nanoparticles anchored on interconnected carbon nanofibers networks as advanced anode material for sodium-ion batteries. *Journal of Power Sources* **284**, 227-235 (2015).

163. L. Hu *et al.*, A Chemically Coupled Antimony/Multilayer Graphene Hybrid as a High-Performance Anode for Sodium-Ion Batteries. *Chemistry of Materials* **27**, 8138-8145 (2015).

164. N. Zhang *et al.*, Spherical nano-Sb@ C composite as a high-rate and ultra-stable anode material for sodium-ion batteries. *Nano Research* **8**, 3384-3393 (2015).

165. L. Xiao *et al.*, High capacity, reversible alloying reactions in SnSb/C nanocomposites for Na-ion battery applications. *Chemical Communications* **48**, 3321-3323 (2012).

166. A. Darwiche, M. T. Sougrati, B. Fraisse, L. Stievano, L. Monconduit, Facile synthesis and long cycle life of SnSb as negative electrode material for Na-ion batteries. *Electrochemistry Communications* **32**, 18-21 (2013).

167. L. Ji *et al.*, Controlling SEI Formation on SnSb-Porous Carbon Nanofibers for Improved Na Ion Storage. *Advanced Materials* **26**, 2901-2908 (2014).

168. I. T. Kim, S.-O. Kim, A. Manthiram, Effect of TiC addition on SnSb–C composite anodes for sodium-ion batteries. *Journal of Power Sources* **269**, 848-854 (2014).

169. L. Ji, W. Zhou, V. Chabot, A. Yu, X. Xiao, Reduced Graphene Oxide/Tin–Antimony Nanocomposites as Anode Materials for Advanced Sodium-Ion Batteries. *ACS applied materials & interfaces* **7**, 24895-24901 (2015).

170. L. Baggetto, E. Allcorn, A. Manthiram, G. M. Veith, Cu 2 Sb thin films as anode for Na-ion batteries. *Electrochemistry Communications* **27**, 168-171 (2013).

171. L. Baggetto *et al.*, Probing the mechanism of sodium ion insertion into copper antimony Cu2Sb anodes. *The Journal of Physical Chemistry C* **118**, 7856-7864 (2014).

172. I. T. Kim, E. Allcorn, A. Manthiram, High-Performance MxSb–Al2O3–C (M= Fe, Ni, and Cu) Nanocomposite-Alloy Anodes for Sodium-Ion Batteries. *Energy Technology* **1**, 319-326 (2013).

173. D.-H. Nam, K.-S. Hong, S.-J. Lim, H.-S. Kwon, Electrochemical synthesis of a three-dimensional porous Sb/Cu 2 Sb anode for Na-ion batteries. *Journal of Power Sources* **247**, 423-427 (2014).

174. L. Baggetto *et al.*, The reaction mechanism of FeSb 2 as anode for sodium-ion batteries. *Physical Chemistry Chemical Physics* **16**, 9538-9545 (2014).

175. A. Darwiche *et al.*, Performance and mechanism of FeSb 2 as negative electrode for Na-ion batteries. *Journal of Power Sources* **280**, 588-592 (2015).

176. C. C. H. Tran, C. Autret, C. Damas, B. Claude-Montigny, J. Santos-Peña, An electrochemical study of Fe1.18Sb1.82 as negative electrode for sodium ion batteries. *Electrochimica Acta* **182**, 11-19 (2015).

177. I. T. Kim, E. Allcorn, A. Manthiram, High-performance FeSb-TiC-C nanocomposite anodes for sodium-ion batteries. *Physical Chemistry Chemical Physics* **16**, 12884-12889 (2014).

178. C. W. Lee, J.-C. Kim, S. Park, H. J. Song, D.-W. Kim, Highly stable sodium storage in 3-D gradational Sb–NiSb–Ni heterostructures. *Nano Energy* **15**, 479-489 (2015).

179. E. Jackson, S. Green, A. Prieto, Electrochemical Performance of Electrodeposited Zn4Sb3 Films for Sodium-Ion Secondary Battery Anodes. *ACS applied materials & interfaces* **7**, 7447-7450 (2015).

180. A. Nie *et al.*, Ultrafast and Highly Reversible Sodium Storage in Zinc-Antimony Intermetallic Nanomaterials. *Advanced Functional Materials*, (2015).

181. L. Baggetto, E. Allcorn, R. R. Unocic, A. Manthiram, G. M. Veith, Mo 3 Sb 7 as a very fast anode material for lithium-ion and sodium-ion batteries. *Journal of Materials Chemistry A* **1**, 11163-11169 (2013).

182. L. Baggetto, M. Marszewski, J. Górka, M. Jaroniec, G. M. Veith, AlSb thin films as negative electrodes for Li-ion and Na-ion batteries. *Journal of Power Sources* **243**, 699-705 (2013).

CHAPTER 3: LITHIUM ION ANODE PERFORMANCE OF ELECTRODEPOSITED THIN FILM COPPER ANTIMONIDES

The experimental content and manuscript writing of this thesis chapter were completed by Everett D. Jackson. Initial experiments leading to this work and scientific direction provided by James M. Mosby. Amy L. Prieto provided guidance and conceptual insight. This work has been published as a paper accepted for publication to *Electrochimica Acta*, July 2016.

1. Introduction

Commercial lithium ion batteries are the current leading energy storage device for portable electronics applications due to the exceptionally high energy density they provide. These cells, generally utilizing a $LiCoO_2$ cathode and a graphite anode separated with an electrolyte consisting of $LiPF_6$ in organic carbonates, show good capacity retention and a high operating cell voltage.[1] Despite this, the currently used battery architecture has considerable safety concerns due to the flammability of the carbonate electrolyte, the decomposition of $LiCoO_2$ to produce oxygen, and the formation of lithium dendrites when overcharged.[2] In order for Li-ion batteries to meet the criteria for next generation technologies such as electric vehicles and aerospace applications, new materials and device architectures are required to provide higher energy density, higher power density, improved safety, and longer cycle life at reduced cost.[2, 3] Proposed methods to achieve this include new cell chemistries, such as the lithium-sulfur battery[4] or the lithium-air battery[5, 6], and sodium-ion battery[7], as well as the use of non-planar, nanoscale battery architectures[8-11] coupled with novel materials allowing faster kinetics, larger capacities, better cycle life and enhanced safety. Regardless of the approach, new techniques for producing high quality materials with tunable morphology and chemistry are required for next generation battery technology.

The capacity of batteries can be improved by using new electrode materials that reversibly react with a higher number of lithium ions per unit mass or unit volume of the electrode material. For this reason, binary lithium-metal systems have been studied as potential anode materials because of their very high theoretical gravimetric and volumetric capacities.[12] Lithium undergoes the electrochemical reaction x Li + M -> Li_xM (for M = Al, Mg, Si, Sn, Sb), where the amount of lithium incorporated is dependent on the stoichiometry of the final Li_xM phase. These reactions occur in the potential range of 0 – 1.2 V vs. Li/Li^+, and with relatively modest voltage hysteresis, and are feasible high energy density anode materials. Despite these advantages, these alloy electrodes cannot typically be used without modification due to the large change in volume accompanying the lithium insertion and desertion process. This causes the active material to pulverize, leading to loss of contact to the electrode, and results in a large capacity fade within only a few cycles. Other issues include the poor electrical conductivity and high brittleness of the lithiated compounds. To overcome these limitations, nanoscale particles and other morphologies have been used, in conjunction with conductive matrixes, which accommodate large volume changes and increase electrical conductivity. Similarly, nanostructured anodes, such as nanowire arrays[13-15] and hollow particles[16], have shown promise for overcoming pulverization by incorporating empty space into the electrode design.

One approach toward mitigating the aforementioned limitations of metal anodes is to incorporate second inactive metal component M' (for M' = Mn, Ni, Cu, etc.). This second metal acts as a conductive matrix and buffer to volume changes.[17-20] This reduces the energy density of the anode in exchange for reduced pulverization, increased conductivity, and improved mechanical properties. In these systems, the material may undergo one or more processes that are classified as conversion, solid solution, or insertion reactions. The type of reaction, the extent of

crystallization of the intermediate, and the final phases present during cycling have been shown to vary substantially based on a number of factors. These include the alloying element, the active material morphology, and the chosen electrochemical conditions. These anode materials and their electrochemistry have recently been reviewed in detail.[21]

Among the possible antimony-based materials studied, tetragonal Cu_2Sb has been more rigorously investigated due to both the good capacity retention it exhibits during short term cycling and the discovery that the parent structure can be regenerated repeatedly during cycling.[22] The small volume change and structural similarity between the parent compound, intermediate phases, and final Li_3Sb product have been suggested to play a pivotal role in the good performance of this system.[17, 19] Electrodes composed of Cu_2Sb have been produced by a variety of methods, such as thin film deposition [23-27], high temperature solid-state techniques [28-31], and chemical reduction [32-35]. Further modification using additives,[36] carbon coatings,[37] or changing particle morphology[31], which result in both high capacity and long cycle life have been reported.

Electrodeposition has been shown to be capable of producing high quality deposits of Cu_2Sb, either directly[26] or through an annealing step[25]. This technique allows the direct application of the desired material onto a conductive substrate with good electrical contact, without requiring conductive additives or binding agents. Although the feasibility of using Cu_2Sb particulates in traditional porous electrode designs has been thoroughly investigated by Manthiram *et al*[38-41], improvements in the energy and power density could be achieved by eliminating the need for binder, volume buffer, and conductive additives. The intermetallic Cu_2Sb is of particular interest for this electrode design due to the small relative volume change when compared to anode materials with similar volumetric energy densities based on intermetallics. Some progress has already been made towards developing this type of pure intermetallic electrode by utilizing three

dimensional electrode architectures, as has been shown for NiSb[42] and Cu_2Sb[43-45]. A comprehensive understanding of the mechanism for unsupported Cu_2Sb is critical to the development of this material system as a potentially safer alternative to graphite anodes.

In the present study, we have analyzed crystalline Cu_2Sb deposits produced directly through a room-temperature aqueous electrodeposition without a post-annealing step. This process is environmentally benign and requires substantially lower energy input than traditional solid state and gas phase synthesis methods. Additionally, the reagents used are abundant and inexpensive, giving this method significant commercial potential. Careful analysis of the chemistry of thoroughly characterized binderless thin films is a critical step toward this goal. Although thin films of nominally pure Cu_2Sb films made by electrodeposition have been reported previously, here we show that electrodeposition provides precise control over the composition of the film without annealing, allowing access to copper-deficient Cu_xSb films. More importantly, we have combined characterization methods that couple information about the structure, composition, and morphology of the films with in-depth battery cycling studies. We find that electrodes produced using this system to work best when the particle size is small and when copper content is lower than the 2:1 necessary to form Cu_2Sb. Ex-situ profilometry and microscopy reveal that the films are ductile but fracture significantly upon repeated cycling, limiting pure and dense Cu_2Sb films to thin thicknesses only. While the electrodeposition method provides a tunable and facile synthetic method, the work described herein informs future directions in providing high quality nanostructures or the incorporation of inactive material to overcome the issue of pulverization and loss of active material.

2. Experimental

The Cu_2Sb thin films were synthesized by electrodeposition between 21-23 ºC using a Gamry Reference 3000 potentiostat. Depositions were performed using a copper foil substrate (McMaster Carr, 99.0% Cu), stainless steel counter electrode (McMaster Carr, Alloy 316 mesh), and a saturated calomel (SCE) reference electrode. Copper foils were cleaned using a commercial alkaline cleaning agent (Alconox), followed by rinsing in Millipore water, and subsequently washed in acetone and isopropyl alcohol before drying. Deposition solutions were prepared by first dissolving 25 mM Sb_2O_3 (Sigma-Aldrich, nanopowder, ≥99.9%) in a solution of 0.40 M citric acid (Sigma-Aldrich, ≥99.5%) in Millipore water (18.2 MΩ cm) by mixing at room temperature for at least 12 hours. Once the Sb_2O_3 was dissolved, 80 mM $Cu(NO_3)_2{\cdot}2.5H_2O$ (Sigma-Aldrich, ≥99.99%) was added and the solution was brought to a pH of 6.0 by addition of a concentrated KOH solution. Cyclic voltammetry was performed using a platinum working electrode (2.01 mm^2), platinum mesh counter electrode, and a saturated calomel reference electrode (SCE).

Scanning electron microscopy was performed on a JEOL JSM-6500F operating at an accelerating voltage of 15 kV and equipped with a Thermo Scientific energy dispersive x-ray system (Noran System Six). Glancing angle x-ray diffraction (GAXRD) was performed using a Bruker D8 Discover using a 1-degree incident angle with a Cu Kα source, soller slit assembly, and a Peltier detector. Ex-situ powder x-ray diffraction (PXRD) patterns were obtained using a Scintag X-2 Advanced Diffraction System equipped with a Cu Kα source and Peltier detector. Optical profilometry surface profiles were obtained on a ZeScope Optical Profiler using a 50x objective lens (31.32x actual magnification) over a 300 μm x 500 μm region.

Electrochemical performance testing was carried out using Arbin BT2000 series battery testers under constant current conditions. Swagelok PFA straight tube fittings with a ½" bored

center were used for battery cells and were assembled in an argon glovebox with <0.5 ppm O_2. Sample mass was determined by measurement of the entire film mass prior to punch removal. Sample thickness was calculated from the mass based on the crystallographic density of Cu_2Sb (8.51 g cm^{-3}).[46] Battery test cells were assembled with Cu_2Sb film samples at the positive terminal and lithium metal at the negative terminal separated by an electrolyte soaked glass fiber filter (Whatman) between two pieces of polypropylene separator (MTI) and the electrolyte used was 1.0 M $LiPF_6$ in 3:7 ethylene carbonate: diethylene carbonate solution by volume (BASF). All electrochemical potentials for battery cycle data are referenced to Li/Li^+.

3. Results and Discussion

3.1 Characterization of electrodeposited Cu_2Sb

As previously reported,[26] Cu_2Sb can be directly electrodeposited from aqueous citrate solutions at near neutral pH and at ambient temperature. A thorough discussion of the general deposition electrochemistry has been reported previously.[26, 27] Here, we show that by varying the electrodeposition conditions, we are able to deposit films with different morphologies, crystallinity, and composition. This provides a platform to investigate the importance of these variables with respect to anode performance, in contrast to previous reports that only provide Cu-Sb alloys by annealing antimony films on copper substrates[47, 48], or where the composition and structure were not controlled[49]. In addition, this method uniquely allows the electrodeposition of copper-antimony alloy films with copper to antimony ratios less than 2, while annealing causes the formation of intermetallic phases and Cu_2Sb is the most copper deficient phase. Fig. 3.1 shows cyclic voltammograms of solutions containing 0.05 M Sb^{3+}, 0.08 M Cu^{2+}, and 0.4 M citric acid at a pH of 6.0. The cyclic voltammogram of the deposition solution shows three primary reduction waves corresponding to co-deposition of antimony and copper between -0.75 V and -1.20 V v.

SCE (characterization of the resulting films is discussed in detail below). Based on x-ray diffraction and x-ray photoelectron spectroscopy[26] of films deposited at -0.85 V vs. SCE (inset, wave a), we have assigned this first reduction wave to a copper-rich Cu_xSb deposit, and the second wave starting at -0.95 V (wave b) to the onset of stoichiometric Cu_2Sb deposition. Highly crystalline films of Cu_2Sb with visible faceting are formed between -1.00 V to -1.05 V, with depositions at -1.05 V providing the ideal 2:1 elemental stoichiometry for the tetragonal phase, as confirmed previously by XPS and EDS. The third reduction wave at -1.10 V (wave c) is due to the deposition of a unique platelet morphology that consists of a near stoichiometric 1:1 ratio of copper to antimony. Upon reversal of the scan polarization, a small oxidation wave is apparent at -0.25 V corresponding to the surface oxidation of the Cu-Sb alloy deposit. Only a single primary stripping peak is seen near 0.10 V, indicating good chemical uniformity of the deposit despite a large potential sweep range.

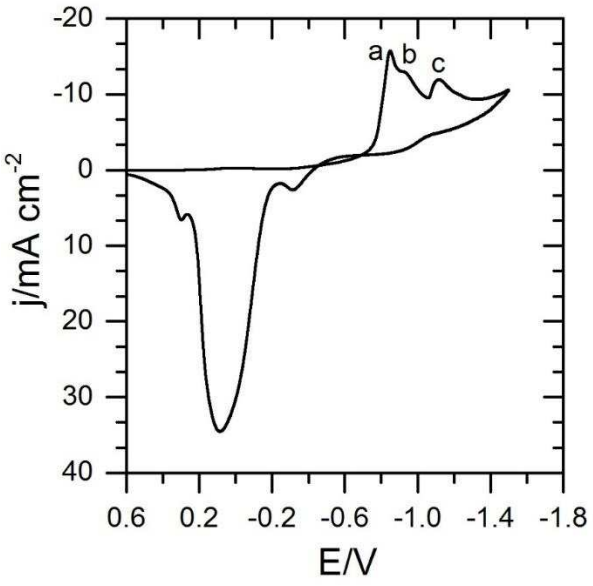

Figure 3.1. Cyclic voltammograms of the 0.4M citrate solution (solid line) taken at 50 mV s^{-1} with a platinum working electrode and SCE reference electrode. Reductions are marked corresponding to the electrodeposition of (a) copper-rich copper antimonide, (b) stoichiometric Cu_2Sb, and (c) near stoichiometric CuSb.

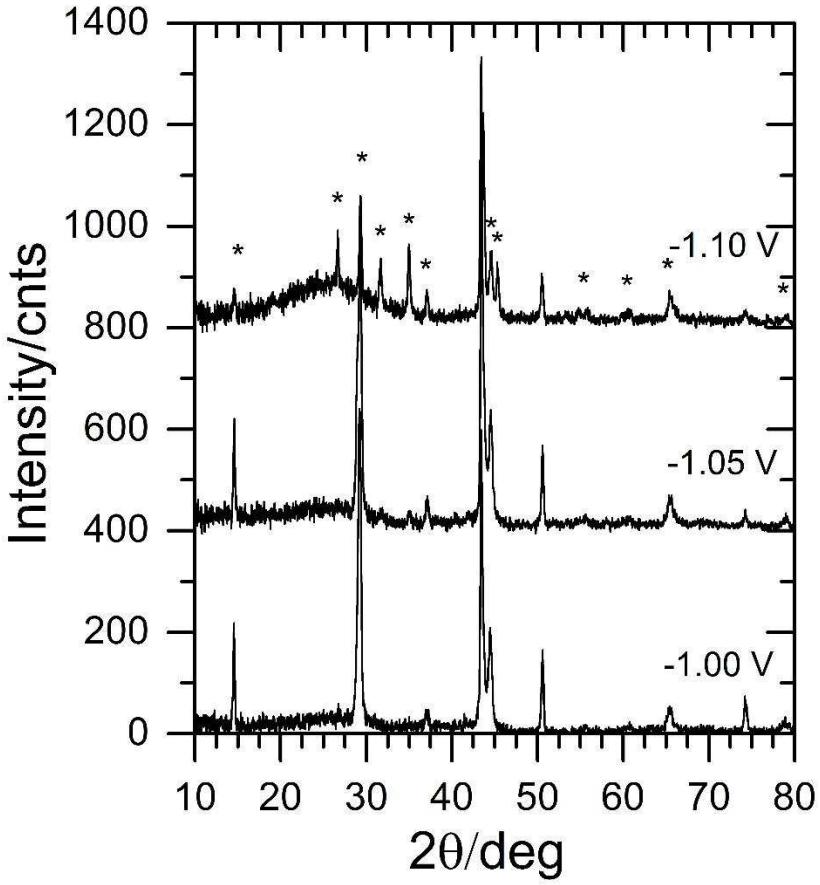

Figure 3.2. Glancing angle x-ray diffraction patterns for as-deposited Cu_2Sb films. Major visible Cu_2Sb reflections are marked with asterisks (Cu_2Sb PDF 01-085-0492).

Glancing angle X-ray diffraction patterns for samples of the electrodeposited Cu_2Sb films are consistent with phase-pure Cu_2Sb (Fig. 3.2). Depositions exhibit a clear preferential growth direction along the [001] family of planes when the applied potential is between -1.00 and -1.05 V vs. SCE, a unique feature of the as-crystalline deposits not observed in annealed samples.[48] Other reflections are visible in the pattern but are relatively weak. When the applied potential is more negative, at -1.10 V, the preferential growth direction is no longer dominant and the peak intensities approach a distribution similar to the powder pattern due to randomly oriented platelets. The only other notable feature is a broad rise in the x-ray diffraction pattern from 15 to 35 degrees

that is the result of disordered antimony contained in the film. Representative SEM images of these films deposited at different potentials for 60 and 300 seconds are shown in Fig. 3.3. No additional peaks corresponding to phases other than Cu_2Sb and copper from the substrate appear in any of the diffraction patterns despite the low and high potential samples lying in two-phase regions of the phase diagram.[50] A summary of the different types of films studied here is presented in Table 1. The three different deposition times give film thicknesses of approximately 140-160 nm for 60 s depositions, 300-400 nm for 180 s depositions, and 450-550 nm for 300 s depositions. By increasing the applied deposition potential, we are also able to decrease the copper to antimony ratio in the deposited film. Analysis by EDS shows that films deposited at -1.00 V, -1.05 V, and -1.10 V from 0.4 M citrate solution give copper rich, stoichiometric, and antimony rich Cu_2Sb films, respectively.

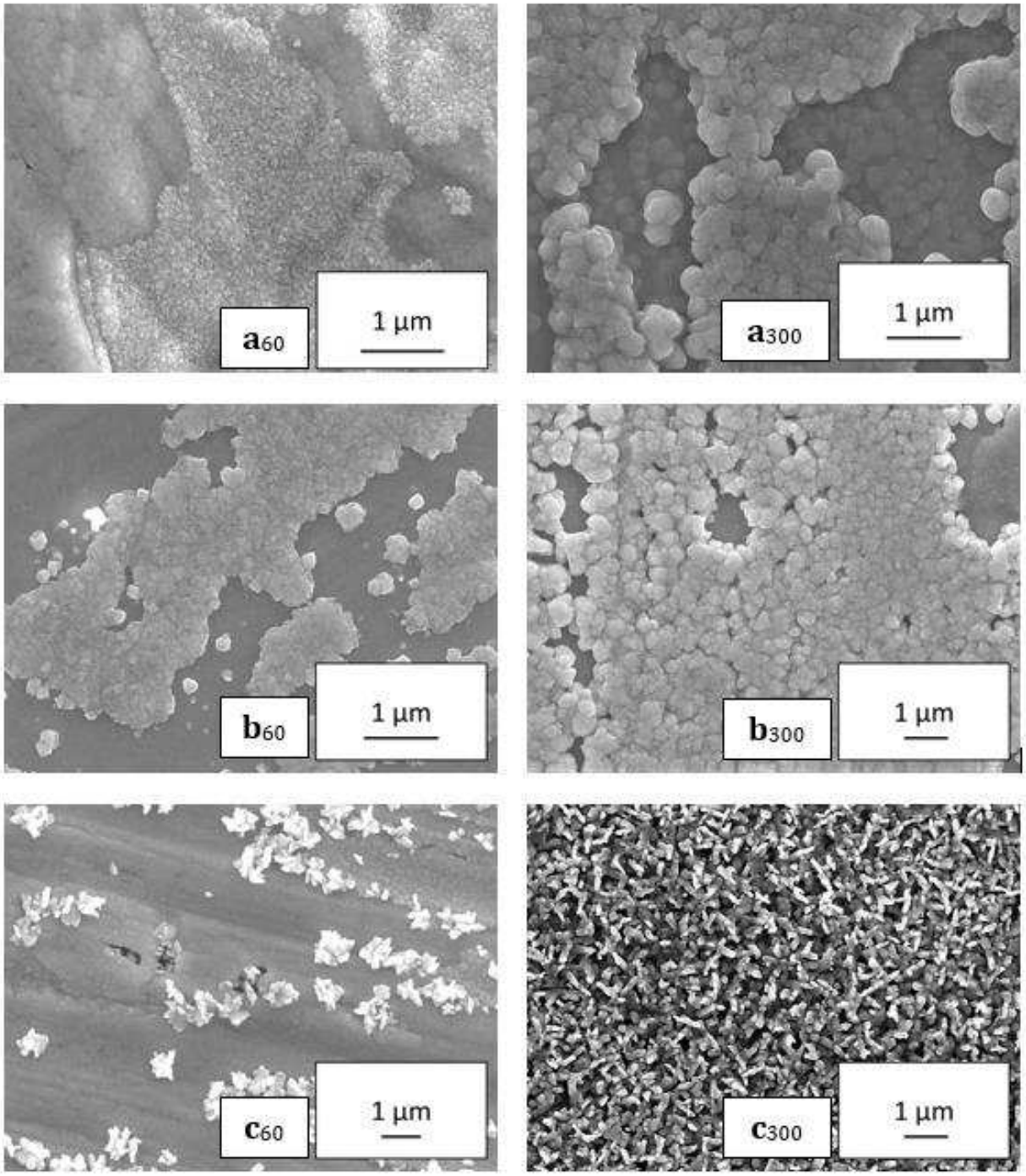

Figure 3.3. Representative scanning electron microscopy images of films electrodeposited under different conditions, showing the change in morphology with deposition time. From top to bottom: **(a)** -1.00 V, **(b)** -1.05 V, and **(c)** -1.10 V v. SCE. Subtext indicates the film deposition time in seconds.

Table 3.1. Deposition conditions of the sample types tested and the measured composition of the Cu_2Sb films. The elemental composition was determined from EDS using samples deposited for five minutes on copper substrates. Theoretical capacities are determined by assuming x Li_3Sb + y Cu at full lithiation, where x = Cu:Sb ratio and the mass per mole is calculated from Cu_xSb. Approximate thickness is calculated based on the crystallographic density of Cu_2Sb (8.51 g cm^{-3}), and rounded to the nearest interval of five.

Applied Potential (V)	Cu : Sb Ratio (EDS)	Calculated Average Thickness (nm)			Theoretical Capacity (mA h g^{-1})
		60 s	180 s	300 s	
-1.10	1.05	200	460	690	427
-1.05	2.00	160	370	550	323
-1.00	2.65	140	330	500	239

3.2 Determination of electrodeposited Cu_2Sb film quality by differential capacity analysis

To confirm the quality of the electrodeposited Cu_2Sb, we have analyzed the electrochemical performance of films deposited for 1 and 5 minutes in order to determine if there was a significant change in the electrochemical activity of the deposits based on composition and morphology changes as the deposition time is increased. For the determination of electrochemically active defects and in homogeneities in the films, we analyzed them using differential capacity plots (Fig. 3.4) produced from the first cycle at a very slow rate of C/100. Pure crystalline Cu_2Sb is known to display two lithiation peaks and three delithiation peaks on the first cycle.[51] All of the samples displayed this basic set of electrochemical reactions with only minor variations. For samples deposited for 1 min, the film deposited at -1.00 V vs. SCE possess two extra insertion peaks not present in the stoichiometric or antimony rich samples. The appearance of these insertion peaks at 0.62 V vs. Li/Li^+ and 0.78 V vs. Li/Li^+ are due to a copper-rich phase, which is consistent with reports that increased copper content results in the requirement lower potentials for lithiation.[25] Samples deposited under the same conditions for 3 and 5 min

retain the 0.62 V vs. Li/Li^+ peak, but it becomes less prominent and the peaks corresponding to phase-pure Cu_2Sb become more intense. These results are consistent with previous reports of this system.[26, 27] The other samples exhibit nearly the same electrochemical processes regardless of the deposition time. This is significant, as it indicates that only copper rich defects can be precisely identified by analysis of the charge-discharge curves. Fortuitously, we have found that this is the phase that results in reduced electrochemical performance.

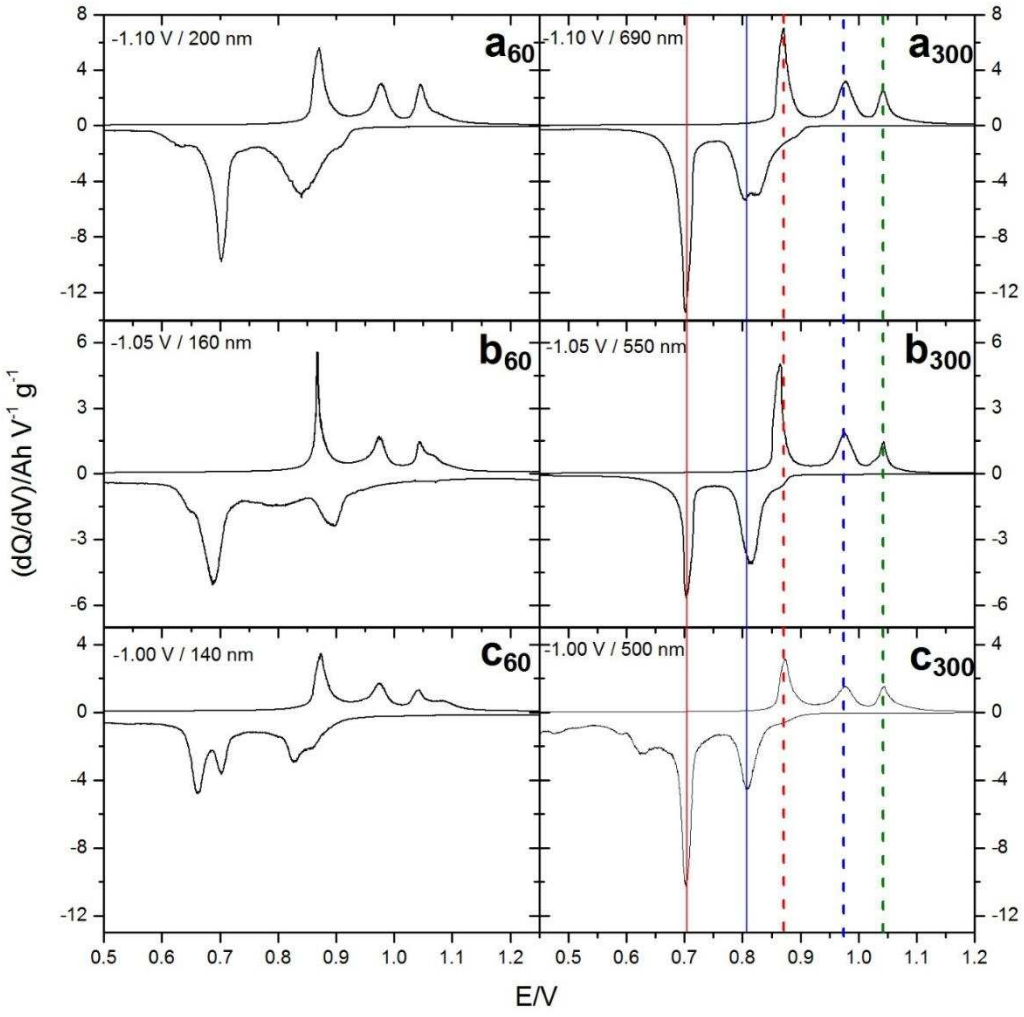

Figure 3.4. Comparison of the composition and thickness-dependent electrochemistry of Cu_2Sb films using first cycle differential capacity plots. Films were deposited at **(a)** -1.00 V, **(b)** -1.05 V, and **(c)** -1.10 V v. SCE. Subscript numbers refer to film deposition time (60s or 300s).

It is immediately clear that the number of peaks apparent during discharging does not change for the different samples, nor does the potential at which the peaks occur. This indicates that the amount of copper and the morphology of the electrode can be varied significantly without changing the thermodynamic reaction mechanism. While the copper rich Cu_xSb ($x \geq 3$) phases lithiate at potentials closer to Li/Li^+ (Fig. 4 a60), the delithiation peaks are not shifted. This suggests that the extra copper is extruded and becomes inactive with respect to the reversible lithium storage mechanism. Excess antimony appears to result in increased charge passed at 1.10 V v. Li/Li^+ during delithiation (Fig. 4 d60) and reduced charge required to fully lithiate the material, but unexpectedly does not produce a new delithiation peak. This strongly suggests that the discharging mechanism is robust for this system and does not vary significantly, even when the composition and structure deviate from ideal Cu_2Sb, an effect not previously reported. This may be an advantage to using the Li_xCu_ySb system, as it suggests that antimony-rich composites could be used without compromising the chemical reversibility of the anode material, while overcoming the limitation of the low gravimetric capacity for pure Cu_2Sb by reducing the amount of inactive copper. It is therefore possible that this system can be tuned to increase either the thermal and electronic conductivities for higher power batteries (by increasing the copper content) or the gravimetric and volumetric capacities (by increasing the antimony content) depending on the desired application, making this material of particular interest as an anode material.

3.3 Cu_2Sb thin-film cycle performance

The early cycle performance at an initial rate of C/100 for one cycle followed by a C/20 rate is shown in Fig. 5. The reversible discharge capacity is close to the predicted value based on antimony content (Table 1). Thicker films (500-700 nm) undergo capacity loss during the first twenty cycles, and all very thin films (150-200 nm) retained their full discharge capacity for the

first twenty cycles. The mechanism for electrode failure for thick films appears to be the result of pulverization. Unlike composite electrodes, freestanding Cu_2Sb films rely solely on the strength of the active material at a given state of charge, and therefore show pulverization even in the nanometer regime, consistent with the large theoretical volume expansion expected for this system and other results published in the literature.[22] Other studies on thin film electrodes have shown similar short cycle lives[48], although free-standing nanowires have been demonstrated to be stable for at least 100 cycles[47]. Contrary to our expectations, Cu_2Sb and $Cu_{2.6}Sb$ films performed worse at equivalent thicknesses compared to copper deficient films. This can be attributed to the porous nature of the Cu_1Sb films, but is somewhat unexpected as we expected as pure antimony films have been shown to have poor cycle performance even in the first few cycles.[52] These results suggest strongly that it is mainly electrode structure that contributes to long-term cycle stability.

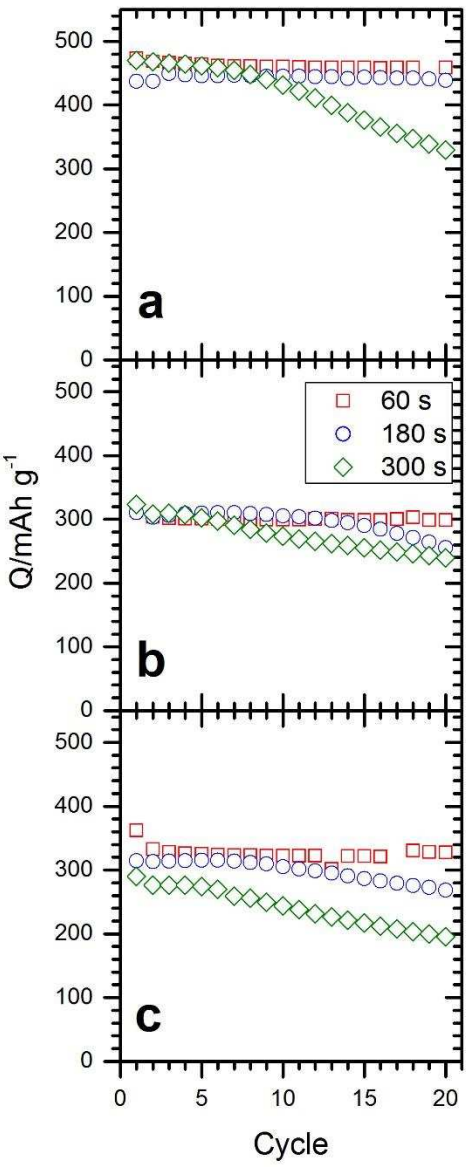

Figure 3.5. Reversible capacity retention of Cu_2Sb thin films cycled at a rate of C/20 for films deposited at **(a)** -1.10 V, **(b)** -1.05 V, and **(c)** -1.10 V v. SCE.

Potential vs. capacity plots for samples deposited for 5 minutes for samples from each deposition type are shown in Fig. 6. Evaluation of these potential profiles during the first and subsequent cycles show a surprising level of similarity for all the tested sample types. While there are notable differences for the first charge cycle, the subsequent cycles reveal similar chemical

reactions occur regardless of variations from the ideal stoichiometry of 2:1 copper to antimony. This is somewhat surprising for the copper-deficient films, as there is insufficient copper to form Cu_2Sb. The diffusion of copper is necessary to reduce the electrochemical potential of the reaction, but excess copper does not provide any clear benefit, and lower copper content may allow for control over the conversion pathway and reduction of unwanted hysteresis and therefore better kinetics.[53] The second charging cycle consistently shows the appearance of a process at 0.925 - 0.900 V vs. Li/Li^+, likely due to antimony produced from incomplete reincorporation of copper. A gradual decrease in the potential from 0.90 to 0.66 V vs. suggests a solid-solution or many phase transformation processes. This is followed by a plateau at 0.66 V vs. corresponding to the formation of Li_3Sb. Full lithiation requires the potential to be reduced to near 0 V vs. Li/Li^+. As seen in the differential capacity plots, the delithiation process does not change significantly from the first to second cycle.

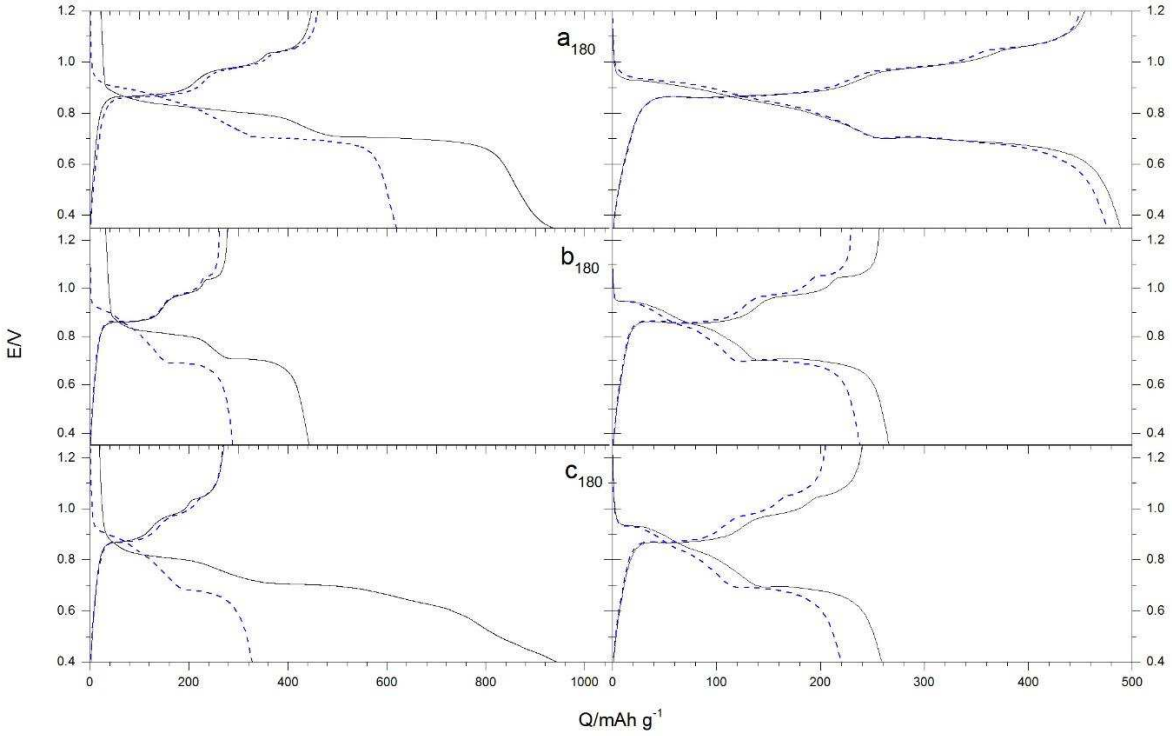

Figure 3.6. Potential-capacity curves for each sample type studied taken from 180 s depositions at different cycles. Left: 1st cycle (solid line) and 2nd cycle (dashed blue line). Right: 10th cycle (solid line) and 20th cycle (dashed blue line). **(a)** -1.10 V, **(b)** -1.05 V, and **(c)** -1.10 V v. SCE.

Consistent with previous reports on Cu_2Sb and most intermetallic compounds, a large irreversible capacity loss is present on the first cycle.[54] The primary mechanisms for this loss have been reported to be electrolyte decomposition, lithium oxide formation due to the intermetallic native oxide layer, and incomplete delithiation for intermetallic electrodes. For thinner samples the effect is further exaggerated due to the low amount of active material present while the SEI thickness is likely not significantly smaller, leading to a larger relative amount of charge being used for surface-specific reactions. We have determined that ~30 % of this irreversible capacity can be attributed to reactions occurring on the cell hardware, and as a result the material intrinsic coulombic efficiency is about 70%, close to previous reports.[48] Thicker samples show a similar initial coulombic efficiency of ca. 60%, except the copper rich samples

deposited at -1.00 V v. SCE. The copper rich sample exhibits a very high irreversible capacity that likely comes from the extrusion of large amounts of copper, leading to a large amount of freshly exposed metallic copper surface area during the first cycle and resulting in large amounts of undesirable electrolyte decomposition.

Subsequent cycling further changes the lithium insertion process while lithium desertion remains unaffected. The process at ca. 0.925 V vs. Li/Li^+ becomes a distinct plateau at about 0.95 V. The evolution of an overpotential for this plateau in some samples indicates the formation of highly crystalline antimony, consistent with previously reported insertion potentials for pure antimony samples.[55] Between the two main plateaus, the solid solution charging process also becomes more distinct. The final plateau at 0.66 V also develops an overpotential, again indicating a distinct phase transition. This result indicates that all of the films undergo a similar transformation process to form in-situ a material that contains a mixture of crystalline Cu_2Sb and amorphous antimony. This is in agreement with previous studies on the impacts of morphology on the phase transitions that occur during charge and discharge.[31]

3.4 Evaluation of switching potentials on film electrochemistry

As seen above, the reversible reactions under thermodynamic control for Cu_2Sb occur between 1.10 V and 0.66 V vs. Li/Li^+, and result in almost complete electrode utilization. At higher currents that approach the practical requirements of Li-ion batteries, kinetic limitations become apparent and can greatly impact the reversible capacity obtained. Additionally, the high rates give the electrode less time to relax and accommodate stress due to volumetric expansion and contraction. To better understand thin-film Cu_2Sb performance under constrained operating conditions, we cycled samples deposited at -1.05 V vs. SCE for 180 s at a C/5 rate with varying switching potentials. Aside from a study involving extremely thin Cu_2Sb films of approximately

200 nm thickness used for sodium intercalation,[56] the kinetic limitations of Cu_2Sb thin films such as ours have not been evaluated. We have found that while our films give near ideal capacities when cycled at slow rates of C/100 or C/20 rate, they experience a reduced capacity when cycled at rates of C/10 and above. For the switching potential study described here, this effect is therefore not negligible and does influence the following results.

The cycle life of a thin film anode material such as the Cu_2Sb in the absence of a binder will be dependent on a combination of the chemical reversibility, SEI layer conductivity and stability, and mechanical performance. The results presented above indicate that under equilibrium conditions the chemical reversibility of the Cu_2Sb films is very good across a large potential window. Further investigation of the other two points can be achieved by performing half-cell cycling where the voltage limits are used to bracket the electrochemical window of the charge and discharge of the material. The bracketing allows the changes in the film to be studied at different points of intercalation/deintercalation. Especially in the case of materials that undergo multiple transitions at different potentials, this helps determine which transitions limit the materials performance. This type of analysis can elucidate if certain ranges and their corresponding transitions are highly reversible or if they create significant lithium trap sites.

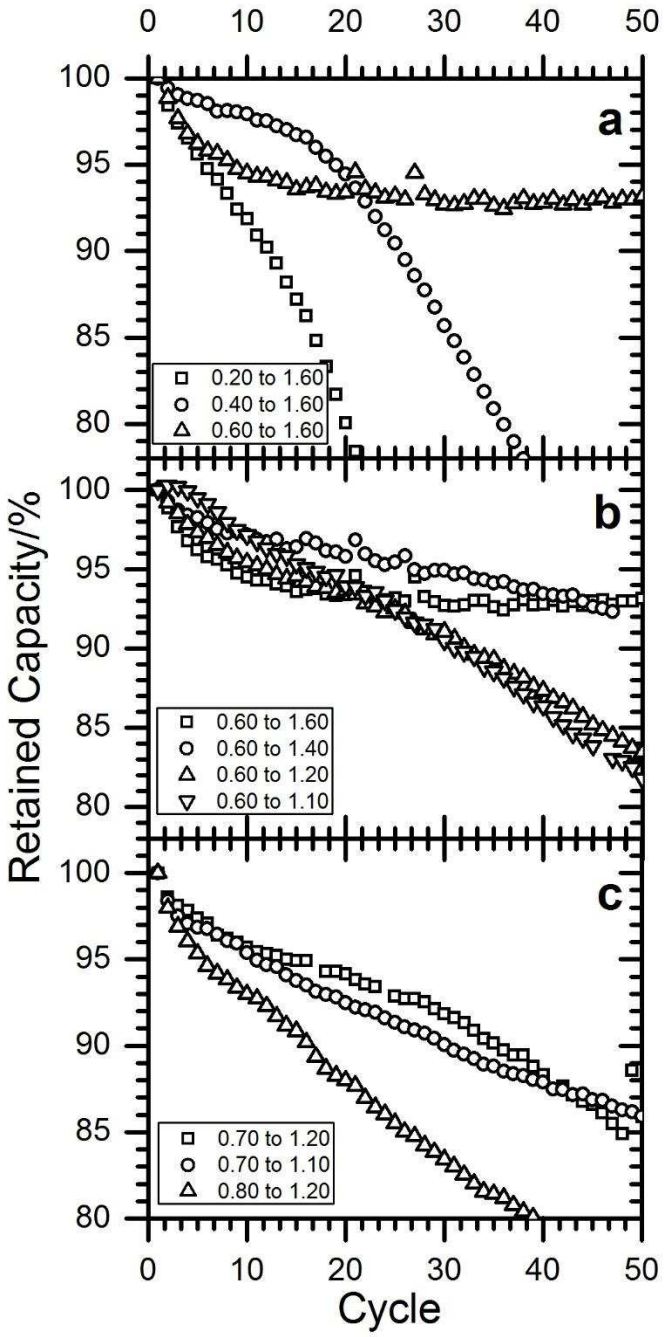

Figure 3.7. The effect of the switching potentials on capacity fade for Cu_2Sb thin films deposited for 180 s at -1.05 V for tests of up to 50 cycles. Potentials are V vs. Li/Li^+ and the given reversible capacities are for delithiation.

While maintaining a constant positive potential limit of 1.6 V vs. Li/Li^+, the cycle life of the electrodeposited Cu_2Sb thin films drastically increases when the lower potential limit is

increased stepwise from 0.20 V to 0.60 V (Fig. 3.7a). Full utilization of these electrodes without further modification leads to fast pulverization and short cycle life. In the best case, greater than 90 % of the initial capacity is retained for over 100 cycles when the potential limits are set between 1.6 V and 0.60 V, which corresponds to 52 % utilization of the active material. The primary reason for the extended cycle life is the reduced pulverization that occurs due to a decrease in the amount of lithium inserted. The recovered capacities for these samples are 217, 203, and 167 mAh g^{-1} for the samples with limits of 0.20 V, 0.40 V, and 0.60 V, respectively. It should be noted that the initial coulombic efficiency for all three samples stays constant at about 65 %, and the electrochemical transitions do not deviate significantly from those determined at lower rates. These observations show that when the lower cutoff potential is increased to more positive potentials, diffusion limits lithium from reacting with the film to completion. This results in no pulverization and a very low capacity fade at the expense of half of the theoretical capacity of the material. Importantly, this does not cause significant lithium trapping within the electrode because a high delithiation limit allows enough of an overpotential to prevent kinetic trapping.

Lowering the positive potential limit from 1.60 V to 1.10 V did not result in any notable performance gains (Fig. 3.7b), instead this results in a lower first cycle coulombic efficiency (60 % at 1.10 V) and a slow but steady loss of capacity. The lower positive voltage limit causes lithium to become trapped in the electrode that is inaccessible under the chosen conditions. Based on our observation that the final delithiation at 1.05 – 1.10 V occurs at the same potential as antimony, it is possible that the decreasing capacity is due to the formation of Li_xCu_ySb particles which are kinetically limited from full delithiation. This is also supported by the slow capacity fade observed under these conditions, as opposed to the sudden loss of capacity resulting from pulverization.[12, 57]

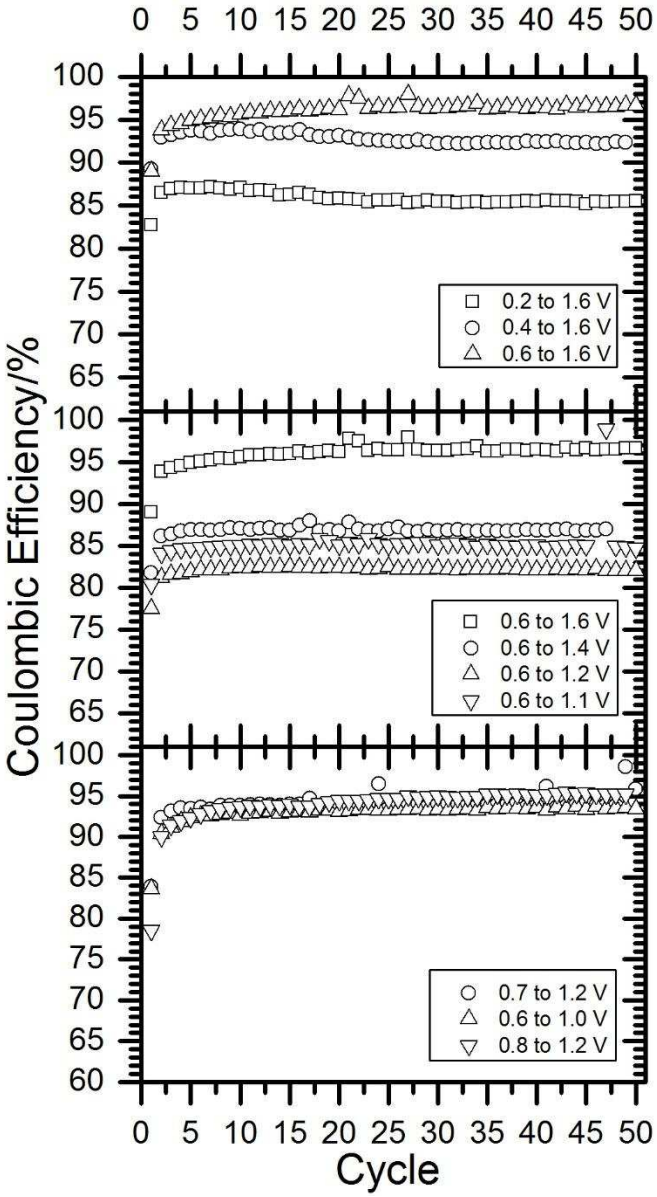

Figure 3.8. Coulombic efficiencies for Cu_2Sb thin films cycled at C/5 with different potential ranges. Good coulombic efficiency is obtained with a window between 0.60 to 1.60 V, while lowering either limiting potential results in decreased efficiency. When the potential window does not bracket all of the transitions, the coulombic efficiency is high but the capacity and cycle life are significantly smaller.

The result of preventing the Li_xCu_ySb to Li_3Sb transition that occurs at 0.66 V on the capacity fade is shown in Fig. 3.7c. This type of capacity fade is consistent with the capacity fade observed when the positive limit is reduced to 1.20 V, and confirms that lithium trapping is the

prominent cause of this capacity fade. The effect is further exaggerated when the lower potential limit is increased to 0.80 V. The coulombic efficiency of these samples is initially very low, but rises to nearly 95% after about five cycles (Fig. 3.8). This efficiency is lower than that of a sample cycled between 0.60 V and 1.60 V and is consistent with a loss of a small amount of capacity each cycle. From this experiment, it is clear that there is an exchange between cycle life and the amount of capacity the electrode can deliver. The ideal range limits pulverization, but allows the maximum recovery of the inserted lithium that still gives acceptable cycle life. The low initial coulombic efficiency obtained when the voltage range is smaller than 0.60 V to 1.20 V shows that the full voltage window is necessary for acceptable lithium reversibility. We have found that a range of about 0.60 V to 1.60 V satisfies these criteria for the samples studied here, but this value is expected to vary significantly depending on the thickness, morphology, and composition of the electrode.

3.5 Evolution of film morphology during cycling

To understand the effect of cycling on film morphology, ex-situ powder XRD, optical profilometry, and SEM were conducted on samples deposited at -1.05 V vs. SCE for 300 s, and that were cycled to specific potentials and held until equilibrium was reached (Fig. 3.9), as determined by current of less than $1x10^{-8}$ A (i.e. less than a tenth of a nanoamp), compared to C/20 which is ~10 μA for these samples). The powder diffraction results from this study supports the formation of Li_xCu_ySb phases during charge and discharge as previously reported.[46] The fully charged Li_3Sb product is clearly apparent at 0.65 V vs. Li/Li^+. The appearance of broad Cu_2Sb peaks in the diffraction pattern taken after one full cycle is consistent with very small particles dispersed in a mostly amorphous material that gives rise to the broad peak at low two theta angles.

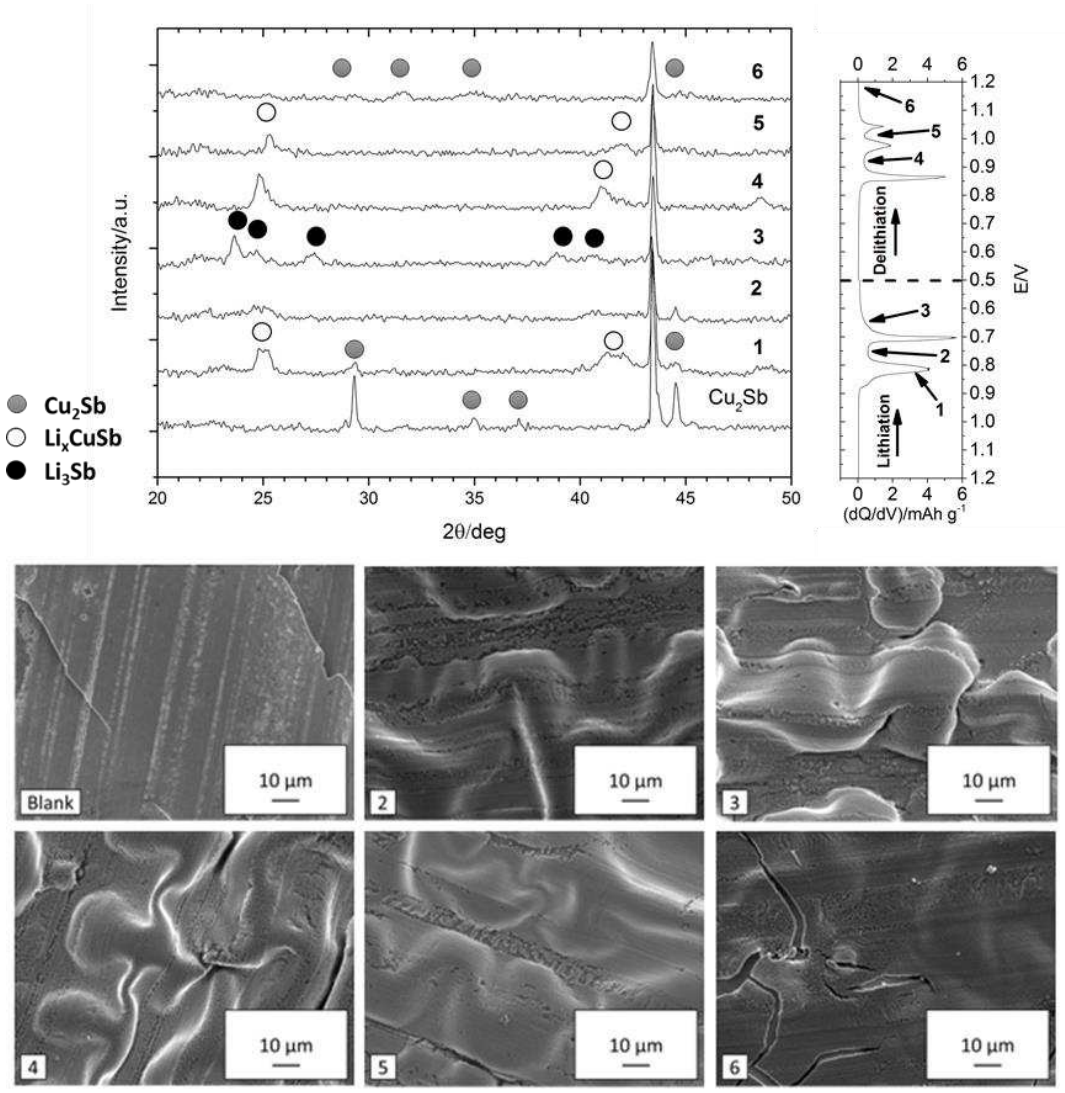

Figure 3.9. Top Left: PXRD patterns for anode samples cycled to different states of charge and discharge as shown on a representative first cycle. Films were deposited for five minutes at -1.05 V v. SCE. Samples were analyzed after charging (lithium insertion) to **(1)** 0.825 V, **(2)** 0.750 V, **(3)** 0.650 V and discharging (delithiation) to **(4)** 0.915 V, **(5)** 1.025 V, and **(6)** 1.200 V v. Li/Li$^+$. XRD patterns markers are indexed to Cu_2Sb (blue, PDF 01-071-3333), Li_xCu_ySb (orange, PDF 00-042-1226 and ref. [46]), and Li_3Sb (red, PDF 03-065-3011). **Top Right:** Differential capacity plot illustrating the final potential of each sample analyzed. **Bottom images:** SEM images taken of the same sample set showing morphological changes during the first cycle.

The volume change that occurs as lithium is inserted and removed from the anode is predicted to cause large film stress, leading to fracturing and anode failure. Such changes should result in major alterations of the film microstructure. Ex-situ SEM images of Cu_2Sb films

approximately 550 nm thick taken from different points during the first cycle reveal significant changes in morphology, as seen in Fig. 9. The films buckle significantly during cycling, partially delaminating off the copper substrate. This buckling effect allows the film to accommodate the volume change in the plane of the electrode surface, where there is no free space. Although the copper substrate is rigid, it appears the film can easily delaminate, allowing the same process to occur. Upon full delithiation, the film nearly returns to its original flat state (which is likely due to the good wetting of Cu_2Sb to Cu). The final delithiation process shows the first sign of significant pulverization in the form of large extended cracks. Interestingly, there are still patterns of deformation waves in the material, even though the films are held at a voltage supposed to promote full delithiation under thermodynamic conditions. It appears as though lithium trapping occurs readily in thicker films. We expect this is likely due to the concomitant reformation of Cu_2Sb at the surface, trapping underlying Li_xCuSb and requiring significant overpotentials to remove the remaining lithium.

To better understand the morphological changes, we also used optical profilometry to obtain long-range profiles of the electrode surfaces. For the Cu_2Sb films studied here, pre-cycled samples are flat and follow the surface morphology of the substrate. Upon initial lithiation (1 – 0.825 V), substantial buckling occurs and wave-like patterns form that propagate over many microns. After the $Li_{\sim 1.6}CuSb$ phase is fully formed (2 – 0.750 V), the patterns become extended and propagate over the entire profile (500 µm x 300 µm wide). The film remains stressed and buckled at full lithiation, and highly strained points can be observed across the film. We expect that these strain points are the initiation points for fractures in the film. Delithiation results in qualitatively similar features until full delithiation is reached. Once the film is fully delithiated (6

– 1.20 V), substantial fracturing is observed intermixed with some isolated small wave features remaining.

While it is known that buckling can occur for films deposited on soft substrates, we have not seen reports of buckling such as this on hard substrates.[58] Generally, pulverization occurs for solid films that change volume as a function of lithiation or delithiation. This volume expansion on lithiation often results in a morphology resembling mud flats.[12] Contrary to expectation, large buckling patterns without full cracking across the entire surface occurs for the films described here even though copper is a rigid substrate. This phenomenon of partial film delamination allows the films to expand and contract in a manner equivalent to a soft substrate. It appears this ordered delamination allows the film to reversibly expand and contract without catastrophic fracturing, and is vital to obtaining a film that can be successfully cycled repeatedly.

There appear to be two primary places where the film loses the ordered pattern and becomes more strained. The first is defect sites caused by dust or other contaminants in the film, creating weak points where cracks can form. The second type is defects in the film that originate from different patterns meeting at a single point, causing a region of very high strain and significant cracking. In addition to these high stress points, excessive buckling also causes large longitudinal cracks to form. These cracks are likely the primary cause of film failure, as the edge regions of the films are brittle and appear to fracture readily. Finally, it is interesting to note that the greatest fracturing occurs between 1.025 and 1.2 V vs. Li/Li^+, where obvious fracturing is seen across most the film after full delithiation.

The substantial change seen in the film morphology and the low crystallinity of fully discharged samples indicates that the greatest pulverization occurs during the change from cubic Li_xCuSb to tetragonal Cu_2Sb. The lack of such a change from cubic Li_xCuSb to cubic Li_3Sb

indicates that the strong structural relationship does not require a significant overpotential, and consequently is highly reversible. Based on this morphological study and the lack of substantial Cu_2Sb diffraction in the fully discharged product indicates that a significant overpotential is needed to fully re-crystallize Cu_2Sb from Li_xCuSb and that this transformation is not always favorable.

Finally, these results indicate that while very thin Cu_2Sb films of 100 – 350 nm can relieve stress effectively, this process does not allow stable cycling even for 500 nm thick films. These 500 nm thick Cu_2Sb anodes have a capacity density of only 150 $\mu Ah\ cm^{-2}$, still too low by at least one order of magnitude for practical applications. In order to achieve reasonable capacities with pure Cu_2Sb electrodes, new electrode architectures, such as nanowires and nanoscale particles,[47] are required that allow for more effective strain relief and stable capacity for hundreds to thousands of cycles. This work suggests that the ideal size range is in the 150 – 350 nanometer range to achieve the optimal balance of material stability and low surface area needed to prevent excessive SEI formation.

3.6 Interpretation and evaluation of the electrochemical mechanism of Cu_2Sb

The mechanism and dynamics of the phase transitions that occur in Cu_2Sb have been examined theoretically [29, 59, 60] and experimentally [22, 25, 28, 30, 31] by a number of different groups. However, there are conflicting reports concerning (a) the difference between first and second cycle insertion potentials, (b) the cause of the substantial irreversible first cycle capacity loss, (c) whether or not full lithiation and delithiation occurs (i.e. reversibility of the $Cu_2Sb \leftrightarrow Li_3Sb$ reaction), and (d) the amount of copper and lithium incorporated or extruded during each step. We briefly review these issues and offer a revised interpretation based on our findings here.

Morcrette et al. [31] studied samples prepared by different methods to determine the reversibility of the Cu_2Sb reaction based on particulate size and morphology. They identified that kinetic limitations are responsible for very low coulombic efficiency (<60%) and irreversibility (<300 mAh g^{-1}) in some cases. Interestingly, when they used Li_2CuSb as a starting material, the apparent irreversible capacity loss was very low (<10%) and three transitions were still apparent upon electrode delithiation. This result suggests that the initial irreversible capacity loss is due to some irreversible transformation of Cu_2Sb during the first cycle. Based on XRD data taken in-situ, they concluded that the reaction proceeds in a reversible three-step process (eq. 1-3):

$$Cu_2Sb + (2\text{-}x)Li \rightarrow Li_{2-x}Cu_{1+x}Sb + (1-x)Cu \quad (1)$$

$$Li_{2-x}Cu_{1+x}Sb + xLi \rightarrow Li_2CuSb + xCu \quad (2)$$

$$Li_2CuSb + Li \rightarrow Li_3Sb + Cu \quad (3)$$

Matsuno et al. investigated the cause of the large first cycle irreversible capacity loss and proposed it was due to the irreversibility of a Cu_2Sb to Li_xCuSb transition, contrary to the previous reports on the reversibility of this transition.[30] This argument was formulated on the basis that there is a break in symmetry between tetragonal Cu_2Sb in the P4/*nmm* space group and the cubic Heusler LiCuSb phases in the *F*3*m* space group. Using data from theoretical calculations and ex-situ x-ray diffraction, they found additional intermediate Li_xCu_ySb phases, and concluded that the Li_2CuSb phase should not form during cycling. Based on substantial theoretical and experimental evidence, they proposed the following mechanism:

$$Li + Cu_2Sb \rightarrow LiCuSb + Cu \quad (4)$$

$$LiCuSb + 0.6Li \rightarrow Li_{1.6}CuSb \quad (5)$$

$$Li_{1.6}CuSb + Li \rightarrow Li_{2.6}Sb + Cu \quad (6)$$

$$Li_{2.6}Sb + 0.4Li \rightarrow Li_3Sb \quad (7)$$

It should be noted that Matsuno et al. focused primarily on the cause of the first cycle capacity loss. They did not attempt to explain the discharge mechanism, and proposed that lithium trapped in Li_xCu_ySb phases was the source of the first and second cycle reaction differences. Contrary to this, Bryngelsson and co-workers obtained discharge capacities of 300 mAh g^{-1}, purportedly inconsistent with the trapping of Li^+ in LiCuSb.[25] Interestingly the high discharge capacity was accompanied by a difference in the electrochemical characteristics between the first cycle and subsequent cycles. Based on their x-ray diffraction and electrochemical characterization, they proposed a three-step mechanism where the amount of copper being extruded during each step could not be definitively determined:

$$Cu_2Sb + Li \rightarrow LiCu_2Sb \textbf{ or } Cu_2Sb + Li \rightarrow LiCuSb + Cu \quad (8)$$

$$LiCu_2Sb + Li \rightarrow Li_2CuSb + Cu \textbf{ or } LiCuSb + Li \rightarrow Li_2CuSb \quad (9)$$

$$Li_2CuSb + Li \rightarrow Li_3Sb + Cu \quad (10)$$

It is clear that the source of the low coulombic efficiency during the first cycle must be identified to determine if it consumes lithium or some alternative redox process that would not require additional excess cathode material to capacity match the cell. Additionally, it is not clear whether or not Cu_2Sb is truly reversible, as the anode materials Li_2CuSb and composite Cu_2Sb/Sb_2O_3 films show remarkably similar electrochemistry.[31] We propose that this is a result of the formation of intermediates during cycling that do not require more than one equivalent of copper per mole of antimony. The observation that the final delithiation potential for Cu_2Sb anodes is the same as pure antimony at -1.05 V vs. Li/Li^+ indicates that the final transition does not necessary result in Cu_2Sb or require two equivalents of copper.[55]

Previously, we noted that a significant overpotential is required when cycling Cu_2Sb to fully recover the lithium. While this effect is in part due to charge transfer resistance, it also

indicates that the diffusivity of lithium to the surface is sluggish at low depths of discharge. In consideration of our experiments here, where copper-deficient platelets do not show such behavior, we find that the copper may actually be interfering with the flow of lithium out of the electrode by spontaneously crystallizing Cu_2Sb at the surface, trapping Li_xCuSb phases within the active material matrix. Furthermore, excess copper in the deposit leads to increased irreversible capacity and decreased cycle life, which we attribute to the degradation of the electrolyte by the continually reforming nanoscale copper metal particles on the material surface. Confirmation of this theory requires a method to probe the nanoscale morphological changes that occur in this material. In summary, a comprehensive determination of the mechanism governing the electrochemical reactivity of this material is still needed that is inclusive of thermodynamic, kinetic, composition, and morphological considerations.

4. Conclusion

In summary, we have presented an example of an anode system produced by a fast, inexpensive, and scalable method. The ability to use low-temperature aqueous electroplating to produce thin films of active anode material that can effectively cycle in a battery is a key step toward next-generation battery technologies that use complex non-planar architectures. Additional benefits of this technique are low energy use, low toxicity of the reagents and solutions used, tunable composition, and the capability to produce additive-free anodes with only active material present.

The electrochemical performance of the films produced using electrodeposition is consistent with previous reports of thin films produced by different methods, although we show for the first time that control over the relative stoichiometry of the Cu to Sb yields surprising control over the resulting battery performance. Evaluation of different film morphologies and

compositions suggests that a robust transition mechanism does not require the crystalline phase Cu_2Sb, and proceeds via a similar mechanism even when deficient in copper. The high reversible capacity of antimony-rich Cu_xSb and the retention of a mechanism undistinguishable from phase-pure Cu_2Sb suggest that nanoscale $Cu_{2-x}Sb$ for $0 < x < 1$ is a potential candidate for high-capacity anodes.

Based on the ex-situ XRD and the morphology changes, as well as the fast capacity fade observed when the material is fully delithiated, we can confirm previous reports that proposed that the Cu_2Sb to Li_xCu_ySb transition is unfavorable and causes substantial strain in pure anode films. This suggests that the ideal anode material is not Cu_2Sb, but rather some $Cu_{2-x}Sb$ alloy or amorphous analogue. In such a case the initial material is more structurally related to Li_3Sb than crystalline Cu_2Sb is, and thus would not require an initial overpotential to begin the structural transformation upon lithiation. An extension of this hypothesis is that a film anode could be produced with a composition gradient and/or multiple heterogeneous layers that can overcome the limitations of Cu_2Sb thin films that have been presented here. Such a composite electrode may allow binder-free films to be produced that obtain both high capacity and good kinetic performance.

We would like to thank Dr. Derek Johnson and Josh McWhorter for their helpful discussions and assistance. We also thank Dr. Pat McCurdy, Dr. Brian Newell, and John Wydallis for their help with SEM, XRD, and optical profilometry experiments, respectively.

Funding

This work was supported by the National Science Foundation CAREER program [DMR-0956011].

REFERENCES

1. J.B. Goodenough, Y. Kim, Challenges for Rechargeable Li Batteries†, Chemistry of Materials, 22 (2009) 587-603.

2. M. Armand, J.-M. Tarascon, Building better batteries, Nature, 451 (2008) 652-657.

3. V. Etacheri, R. Marom, R. Elazari, G. Salitra, D. Aurbach, Challenges in the development of advanced Li-ion batteries: a review, Energy & Environmental Science, 4 (2011) 3243-3262.

4. X. Ji, K.T. Lee, L.F. Nazar, A highly ordered nanostructured carbon–sulphur cathode for lithium–sulphur batteries, Nature materials, 8 (2009) 500-506.

5. G. Girishkumar, B. McCloskey, A. Luntz, S. Swanson, W. Wilcke, Lithium− air battery: Promise and challenges, The Journal of Physical Chemistry Letters, 1 (2010) 2193-2203.

6. H.-G. Jung, J. Hassoun, J.-B. Park, Y.-K. Sun, B. Scrosati, An improved high-performance lithium–air battery, Nat Chem, 4 (2012) 579-585.

7. C. Nithya, S. Gopukumar, Sodium ion batteries: a newer electrochemical storage, Wiley Interdisciplinary Reviews: Energy and Environment, 4 (2015) 253-278.

8. P.G. Bruce, B. Scrosati, J.-M. Tarascon, Nanomaterials for Rechargeable Lithium Batteries, Angewandte Chemie International Edition, 47 (2008) 2930-2946.

9. R.W. Hart, H.S. White, B. Dunn, D.R. Rolison, 3-D microbatteries, Electrochemistry Communications, 5 (2003) 120-123.

10. J.W. Long, B. Dunn, D.R. Rolison, H.S. White, Three-dimensional battery architectures, Chemical Reviews-Columbus, 104 (2004) 4463-4492.

11. W. Dong, D.R. Rolison, B. Dunna, Electrochemical properties of high surface area vanadium oxide aerogels, Electrochemical and Solid-State Letters, 3 (2000) 457-459.

12. M. Winter, J.O. Besenhard, Electrochemical lithiation of tin and tin-based intermetallics and composites, Electrochimica Acta, 45 (1999) 31-50.

13. C.K. Chan, X.F. Zhang, Y. Cui, High Capacity Li Ion Battery Anodes Using Ge Nanowires, Nano Letters, 8 (2007) 307-309.

14. C.K. Chan, H. Peng, G. Liu, K. McIlwrath, X.F. Zhang, R.A. Huggins, Y. Cui, High-performance lithium battery anodes using silicon nanowires, Nat Nano, 3 (2008) 31-35.

15. L. Bazin, S. Mitra, P.L. Taberna, P. Poizot, M. Gressier, M.J. Menu, A. Barnabé, P. Simon, J.M. Tarascon, High rate capability pure Sn-based nano-architectured electrode assembly for rechargeable lithium batteries, Journal of Power Sources, 188 (2009) 578-582.

16. Y. Yao, M.T. McDowell, I. Ryu, H. Wu, N. Liu, L. Hu, W.D. Nix, Y. Cui, Interconnected Silicon Hollow Nanospheres for Lithium-Ion Battery Anodes with Long Cycle Life, Nano Letters, 11 (2011) 2949-2954.

17. M.M. Thackeray, J.T. Vaughey, C.S. Johnson, A.J. Kropf, R. Benedek, L.M.L. Fransson, K. Edstrom, Structural considerations of intermetallic electrodes for lithium batteries, Journal of Power Sources, 113 (2003) 124-130.

18. J. Vaughey, J. O'Hara, M. Thackeray, Intermetallic Insertion Electrodes with a Zinc Blende-Type Structure for Li Batteries: A Study of Li x InSb ($0 \leq x \leq 3$), Electrochemical and Solid-State Letters, 3 (2000) 13-16.

19. J.T. Vaughey, C.S. Johnson, A.J. Kropf, R. Benedek, M.M. Thackeray, H. Tostmann, T. Sarakonsri, S. Hackney, L. Fransson, K. Edström, J.O. Thomas, Structural and mechanistic features of intermetallic materials for lithium batteries, Journal of Power Sources, 97–98 (2001) 194-197.

20. L. Fransson, J. Vaughey, K. Edström, M. Thackeray, Structural Transformations in Intermetallic Electrodes for Lithium Batteries An In Situ X-Ray Diffraction Study of Lithiated MnSb and Mn 2 Sb, Journal of The Electrochemical Society, 150 (2003) A86-A91.

21. M.N. Obrovac, V.L. Chevrier, Alloy Negative Electrodes for Li-Ion Batteries, Chemical Reviews, 114 (2014) 11444-11502.

22. L.M.L. Fransson, J.T. Vaughey, R. Benedek, K. Edström, J.O. Thomas, M.M. Thackeray, Phase transitions in lithiated Cu2Sb anodes for lithium batteries: an in situ X-ray diffraction study, Electrochemistry Communications, 3 (2001) 317-323.

23. S.-W. Song, R.P. Reade, E.J. Cairns, J.T. Vaughey, M.M. Thackeray, K.A. Striebel, Cu2Sb Thin-Film Electrodes Prepared by Pulsed Laser Deposition for Lithium Batteries, Journal of The Electrochemical Society, 151 (2004) A1012-A1019.

24. L. Trahey, H.H. Kung, M.M. Thackeray, J.T. Vaughey, Effect of Electrode Dimensionality and Morphology on the Performance of Cu2Sb Thin Film Electrodes for Lithium-Ion Batteries, European Journal of Inorganic Chemistry, 2011 (2011) 3984-3988.

25. H. Bryngelsson, J. Eskhult, L. Nyholm, K. Edström, Thin films of Cu2Sb and Cu9Sb2 as anode materials in Li-ion batteries, Electrochimica Acta, 53 (2008) 7226-7234.

26. J.M. Mosby, A.L. Prieto, Direct Electrodeposition of Cu2Sb for Lithium-Ion Battery Anodes, Journal of the American Chemical Society, 130 (2008) 10656-10661.

27. J.M. Mosby, D.C. Johnson, A.L. Prieto, Evidence of Induced Underpotential Deposition of Crystalline Copper Antimonide via Instantaneous Nucleation, Journal of The Electrochemical Society, 157 (2010) E99-E105.

28. S. Matsuno, M. Noji, T. Kashiwagi, M. Nakayama, M. Wakihara, Construction of the Ternary Phase Diagram for the Li−Cu−Sb System as the Anode Material for a Lithium Ion Battery, The Journal of Physical Chemistry C, 111 (2007) 7548-7553.

29. M. Nakayama, S. Matsuno, J. Shirakawa, M. Wakihara, First-Principles Study on Phase Stability in Li x CuSb with Heusler-type Structure, Journal of The Electrochemical Society, 155 (2008) A505-A511.

30. S. Matsuno, M. Noji, M. Nakayama, M. Wakihara, Y. Kobayashi, H. Miyashiro, Dynamics of Phase Transition in Li–Cu–Sb Anode Material for Rechargeable Lithium Ion Battery, Journal of The Electrochemical Society, 155 (2008) A151-A157.

31. M. Morcrette, D. Larcher, J.M. Tarascon, K. Edström, J.T. Vaughey, M.M. Thackeray, Influence of electrode microstructure on the reactivity of Cu2Sb with lithium, Electrochimica Acta, 52 (2007) 5339-5345.

32. J. Ren, X. He, W. Pu, C. Jiang, C. Wan, Chemical reduction of nano-scale Cu2Sb powders as anode materials for Li-ion batteries, Electrochimica Acta, 52 (2006) 1538-1541.

33. T. Sarakonsri, T. Aamchikad, T. Tawee, Processing parameters study on solution route synthesis of dendrite Cu2Sb powders, Chiang Mai Journal of Science, 33 (2006) 321.

34. T. Sarakonsri, C.S. Johnson, S.A. Hackney, M.M. Thackeray, Solution route synthesis of InSb, Cu6Sn5 and Cu2Sb electrodes for lithium batteries, Journal of Power Sources, 153 (2006) 319-327.

35. G. Zhang, K. Huang, S. Liu, W. Zhang, B. Gong, Comparison of the electrochemical performance of mesoscopic Cu2Sb, SnSb and Sn/SnSb alloy powders, Journal of Alloys and Compounds, 426 (2006) 432-437.

36. D. Applestone, S. Yoon, A. Manthiram, Cu2Sb-Al2O3-C nanocomposite alloy anodes with exceptional cycle life for lithium ion batteries, Journal of Materials Chemistry, 22 (2012) 3242-3248.

37. Y. He, L. Huang, X. Li, Y. Xiao, G.-L. Xu, J.-T. Li, S.-G. Sun, Facile synthesis of hollow Cu2Sb@C core-shell nanoparticles as a superior anode material for lithium ion batteries, Journal of Materials Chemistry, 21 (2011) 18517-18519.

38. D. Applestone, S. Yoon, A. Manthiram, Cu 2 Sb–Al 2 O 3–C nanocomposite alloy anodes with exceptional cycle life for lithium ion batteries, Journal of Materials Chemistry, 22 (2012) 3242-3248.

39. D. Applestone, A. Manthiram, Symmetric cell evaluation of the effects of electrolyte additives on Cu 2 Sb–Al 2 O 3–C nanocomposite anodes, Journal of Power Sources, 217 (2012) 1-5.

40. E. Allcorn, A. Manthiram, Thermal Stability of Sb and Cu2Sb Anodes in Lithium-Ion Batteries, Journal of The Electrochemical Society, 162 (2015) A1778-A1786.

41. E. Allcorn, S.-O. Kim, A. Manthiram, Thermal stability of active/inactive nanocomposite anodes based on Cu 2 Sb in lithium-ion batteries, Journal of Power Sources, 299 (2015) 501-508.

42. C. Villevieille, C.M. Ionica-Bousquet, A. De Benedetti, F. Morato, J.F. Pierson, P. Simon, L. Monconduit, Self supported nickel antimonides based electrodes for Li ion battery, Solid State Ionics, 192 (2011) 298-303.

43. S. Tan, E. Perre, T. Gustafsson, D. Brandell, A solid state 3-D microbattery based on Cu2Sb nanopillar anodes, Solid State Ionics, 225 (2012) 510-512.

44. E. Perre, P.L. Taberna, D. Mazouzi, P. Poizot, T. Gustafsson, K. Edström, P. Simon, Electrodeposited Cu2Sb as anode material for 3-dimensional Li-ion microbatteries, Journal of Materials Research, 25 (2010) 1485-1491.

45. C. Zhang, K.-Q. Xu, W. Zhou, X.-F. Lu, R.-Y. Li, G.-R. Li, Copper–Antimony Alloy–Nanoparticle Clusters Supported on Porous Cu Networks for Electrochemical Energy Storage, Particle & Particle Systems Characterization, (2016) n/a-n/a.

46. L.M. Fransson, J. Vaughey, R. Benedek, K. Edström, J.O. Thomas, M. Thackeray, Phase transitions in lithiated Cu< sub> 2</sub> Sb anodes for lithium batteries: an in situ X-ray diffraction study, Electrochemistry Communications, 3 (2001) 317-323.

47. E. Perre, P.L. Taberna, D. Mazouzi, P. Poizot, T. Gustafsson, K. Edström, P. Simon, Electrodeposited Cu 2 Sb as anode material for 3-dimensional Li-ion microbatteries, Journal of Materials Research, 25 (2010) 1485-1491.

48. H. Bryngelsson, J. Eskhult, L. Nyholm, K. Edström, Thin films of Cu 2 Sb and Cu 9 Sb 2 as anode materials in Li-ion batteries, Electrochimica Acta, 53 (2008) 7226-7234.

49. L. Trahey, H.H. Kung, M.M. Thackeray, J.T. Vaughey, Effect of Electrode Dimensionality and Morphology on the Performance of Cu2Sb Thin Film Electrodes for Lithium-Ion Batteries, European Journal of Inorganic Chemistry, 2011 (2011) 3984-3988.

50. D. Manasijević, D. Minić, D. Živković, J. Vřešťál, A. Aljilji, N. Talijan, J. Stajić-Trošić, S. Marjanović, R. Todorović, Experimental investigation and thermodynamic calculation of the Cu–In–Sb phase diagram, Calphad, 33 (2009) 221-226.

51. L.M. Fransson, J. Vaughey, R. Benedek, K. Edström, J.O. Thomas, M. Thackeray, Phase transitions in lithiated Cu 2 Sb anodes for lithium batteries: an in situ X-ray diffraction study, Electrochemistry Communications, 3 (2001) 317-323.

52. H. Bryngelsson, J. Eskhult, L. Nyholm, M. Herranen, O. Alm, K. Edström, Electrodeposited Sb and Sb/Sb2O3 Nanoparticle Coatings as Anode Materials for Li-Ion Batteries, Chemistry of Materials, 19 (2007) 1170-1180.

53. D. Chang, M.-H. Chen, A. Van der Ven, Factors Contributing to Path Hysteresis of Displacement and Conversion Reactions in Li Ion Batteries, Chemistry of Materials, 27 (2015) 7593-7600.

54. W.-J. Zhang, A review of the electrochemical performance of alloy anodes for lithium-ion batteries, Journal of Power Sources, 196 (2011) 13-24.

55. A. Darwiche, C. Marino, M.T. Sougrati, B. Fraisse, L. Stievano, L. Monconduit, Better Cycling Performances of Bulk Sb in Na-Ion Batteries Compared to Li-Ion Systems: An Unexpected Electrochemical Mechanism, Journal of the American Chemical Society, 134 (2012) 20805-20811.

56. L. Baggetto, E. Allcorn, A. Manthiram, G.M. Veith, Cu2Sb thin films as anode for Na-ion batteries, Electrochemistry Communications, 27 (2013) 168-171.

57. J. Yang, M. Wachtler, M. Winter, J.O. Besenhard, Sub-Microcrystalline Sn and Sn - SnSb Powders as Lithium Storage Materials for Lithium-Ion Batteries, Electrochemical and Solid-State Letters, 2 (1999) 161-163.

58. C. Yu, X. Li, T. Ma, J. Rong, R. Zhang, J. Shaffer, Y. An, Q. Liu, B. Wei, H. Jiang, Silicon Thin Films as Anodes for High-Performance Lithium-Ion Batteries with Effective Stress Relaxation, Advanced Energy Materials, 2 (2012) 68-73.

59. S. Sharma, J.K. Dewhurst, C. Ambrosch-Draxl, Lithiation of InSb and Cu_{2}Sb: A theoretical investigation, Physical Review B, 70 (2004) 104110.

60. A.H. Reshak, H. Kumarudin, Theoretical investigation for Li2CuSb as multifunctional materials: Electrode for high capacity rechargeable batteries and novel materials for second harmonic generation, Journal of Alloys and Compounds, 509 (2011) 7861.

CHAPTER 4: REVERSIBLE CONVERSION OF COPPER ANTIMONIDE WITH SODIUM IONS ENABLED BY FLUOROETHYLENE CARBONATE

The experimental content and manuscript writing of this thesis chapter were completed by Everett D. Jackson. Amy L. Prieto provided guidance, help with the preparation of the text, and conceptual insight.

4.1 Introduction

Sodium-ion batteries have recently regained significant interest as an alternative to lithium-ion batteries. As opposed to lithium, sodium is advantageous due to higher abundance, good global distribution, lower cost, a standard reduction potential near that of lithium (-3.04 V for Li/Li^+ and -2.71 V for Na/Na^+), and the potential for new cell chemistries impractical with lithium.[1,2] Although the theoretical energy and power densities of a sodium battery are lower than the lithium analogue, sodium batteries may become important for stationary and grid applications where battery choice is purely cost driven. The amount of research on potential materials for secondary sodium-ion batteries is still small, and low-cost negative electrode materials are required in order to make a sodium-ion battery economically viable.

Early studies on reversible sodium deposition has shown that dendrites generally form analogous to those observed in lithium deposition. The high reactivity of sodium with air and water make it a particularly unattractive negative electrode due to safety concerns. Fortuitously, it has been observed that sodium undergoes similar electrochemical reactions to lithium and analogues of lithium-ion negative electrodes are therefore clear candidates for sodium-ion batteries. Analogous to lithium ion anode targets, metal based sodium ion battery anode targets are attractive

due to their good voltage characteristics and high theoretical capacity, and include Si (954 mAh g-1), Sn (847 mAh g-1), and Sb (660 mAh g-1).[1]

Antimony in particular has been investigated due to its high theoretical capacity, good kinetic performance and voltage characteristics. It was considered likely that sodium negative electrodes would experience faster capacity fade due to the larger size of sodium ions, contributing to greater volume changes and faster pulverization.[1] Unexpectedly, substantially better cycle life has been reported for reversible sodiation and desodiation, in contrast to the poor cycle life of pure antimony with lithium.[2-4] Additionally, the phases produced during sodium insertion do not appear to follow the thermodynamically predicted intermediates based on phase diagrams, and instead often proceed via amorphous intermediates.[3-5] This has led to additional interest in high-capacity anodes that are not possible in lithium-ion batteries due to pulverization.

Alloys of antimony have also been investigated, either to further increase capacity retention or offer other benefits, such as improved electrical conductivity and better mechanical properties. In addition to pure antimony,[3,5-10] the intermetallics Cu_2Sb,[11,12] FeSb,[13] $FeSb_2$,[14-16] NiSb,[17,18] SnSb,[4,19] Zn_4Sb_3,[20] AlSb,[21] and Mo3Sb7[22] have been investigated as potential antimony-based anode candidates. A common theme among all of these anodes is their ability to cycle for at least several cycles, despite the very large volume expansion and contraction that occurs during cycling. Recent studies into the electrolyte chemistry of sodium-ion batteries has revealed that FEC additives may also improve the quality of the SEI layer in this system, and consequentially allow significant gains in cycle life and coulombic efficiency.[23,24] The results reported here confirm that the capacity retention of Cu_2Sb thin films is improved by addition of FEC for both lithium-ion and sodium-ion systems.

At the time this research was performed, refs. 11 and 12 had not been yet published, and we attempted to use our established method for synthesizing Cu_2Sb thin films to study the alloying reaction of sodium with copper antimonide in sodium ion half cells. Due to the publication of the aforementioned paper, we opted not to submit this work to a peer reviewed journal. Nevertheless, the comparative work performed here led us to study the behavior of electrolyte additives with our nanowire arrays in lithium ion cells in the next chapter.

4.2 Experimental

Copper antimonide thin films were synthesized in the same manner as reported in the previous chapter. The same battery system and cell design was used as previously, except that sodium ion cells used a sodium metal counter electrode and an electrolyte of 1M $NaClO_4$ in anhydrous propylene carbonate (PC, Sigma). When indicated, fluoroethylene carbonate (FEC, Sigma) was added to the base electrolyte in the volume percent indicated. The absolute electrochemical potentials in each cell are different by 330 mV as a result of using the different metals as the combined reference and counter electrode (-3.04 V for Li/Li^+ and -2.71 V for Na/Na^+).

4.3 Results and Discussion

The electrochemical reaction of lithium with Cu_2Sb has been studied in detail, and a general mechanism for reversible reaction with lithium has been determined by a number of groups. The reaction occurs in a multi-step process, and may be expressed in a simplified form:

$$Cu_2Sb + xLi \leftrightarrow Li_xCu_ySb + (2-y)Cu \qquad \textbf{(1)}$$

$$Li_xCu_ySb + zLi \leftrightarrow Li_3Sb + yCu \qquad \textbf{(2)}$$

Key to this reaction is the reversible extrusion and reincorporation of copper in the active material, and the formation of Li_3Sb as the fully lithiated form. The full details of this reaction can be found elsewhere.[25,26] An analogous reaction mechanism can be written for sodiation of Cu_2Sb, with the final reaction product being Na_3Sb: [12]

$$Cu_2Sb + 3Na \leftrightarrow Na_3Sb + 2Cu \quad \textbf{(3)}$$

The formation of Na_3Sb upon full charge has been previously confirmed by x-ray diffraction (XRD). A follow up study by Baggetto *et al.* has provided additional mechanistic insight using Mössbauer spectroscopy and X-ray absorption spectroscopy.[11] These studies have focused only on initial cycling, and did not consider any changes that occur during prolonged cycling. We have found that a transformation of the charge and discharge profiles for our thin films, likely as a result from a change in electrode morphology due to the large volume expansion that occurs during cycling in this system. In contrast, the changes that occur when Cu_2Sb electrodes are cycled in lithium-ion batteries are most significant only during the first cycle, with impedance rise being the major change during prolonged experiments. This difference is illustrated in Fig. 4.1, where the insertion process changes between the first and subsequent cycles. In both systems, the development of new electrochemical reactions at a higher potential v. M/M^+ occurs for the M^+ insertion process in the second and later cycles. The Cu_2Sb electrode operates as a conversion electrode in both cases, forming copper/antimony alloy active particles in a copper/SEI matrix. For both systems, copper appears to maintain a role in forming intermediates and stabilizing the transformation process during each cycle.

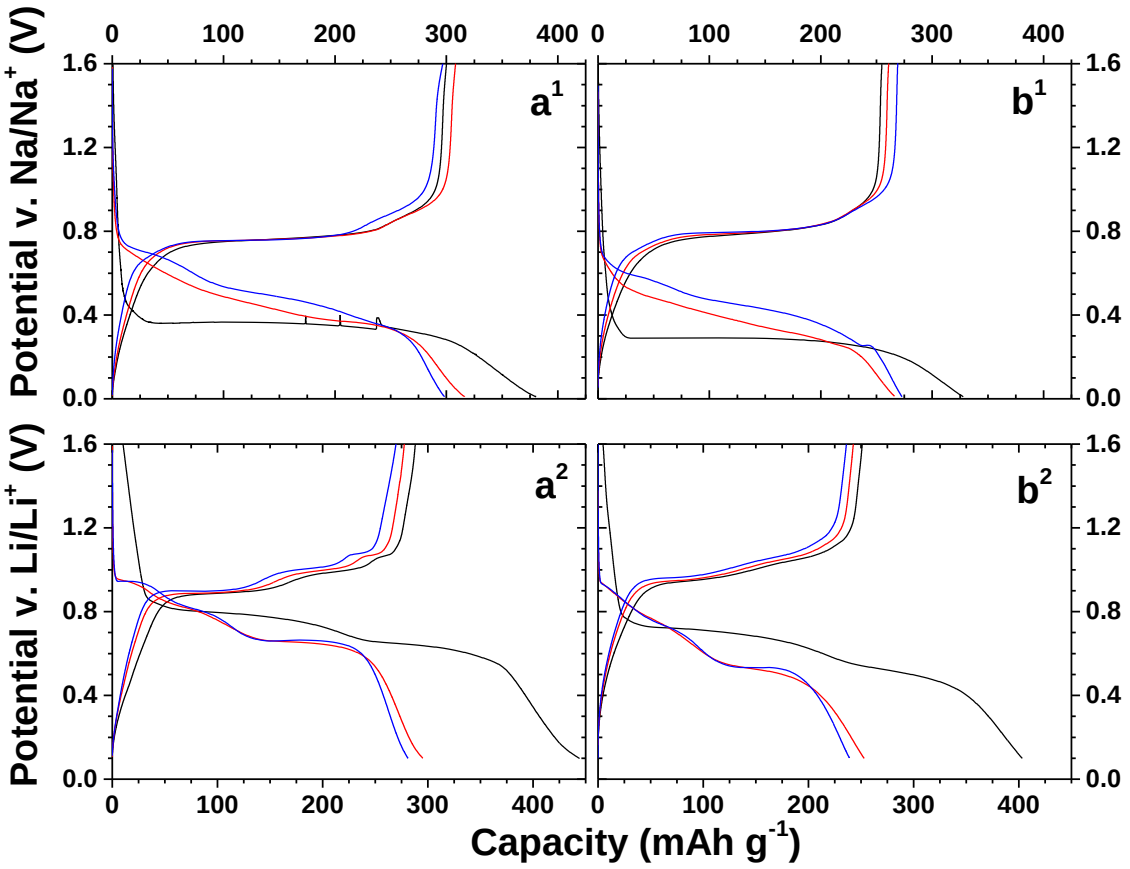

Figure 4.1. Charge-discharge voltage profiles for the 1st (black), 2nd (red), and 10th (blue) cycles for Cu_2Sb films cycled in a (1) sodium-ion cell between 0.01 V and 1.60 V and (2) a lithium-ion half-cell between 0.10 V and 1.60 V at a charge rate of (a) C/5 and (b) 5C. All cells contain 10% FEC as an electrolyte additive.

It is interesting to note that the lithium insertion process occurs with well-defined plateaus and can be monitored *in-situ* by XRD.[17] In contrast, sodium insertion appears to consist of multiple conjugated plateaus that cannot be identified by XRD.[8] The multiple plateaus can be easily identified on the second cycle for the lithium half-cell, but the sodium half-cell appears to undergo a solid solution process without well-defined plateaus below 0.48 V. After ten cycles, plateaus become apparent for the Na^+/Cu_2Sb cell, indicating the presence of new phases. The plateau at circa 0.60 V v. Na/Na^+ is consistent with the reaction of sodium ions with antimony to directly produce Na_3Sb.[4] This plateau has also been observed in other thin films studies of Cu_2Sb.[12] Such

a transformation should cause disconnection of particles due to pulverization and short cycle life. The need for a robust SEI layer capable of keeping particles from losing contact is therefore necessary for this system.

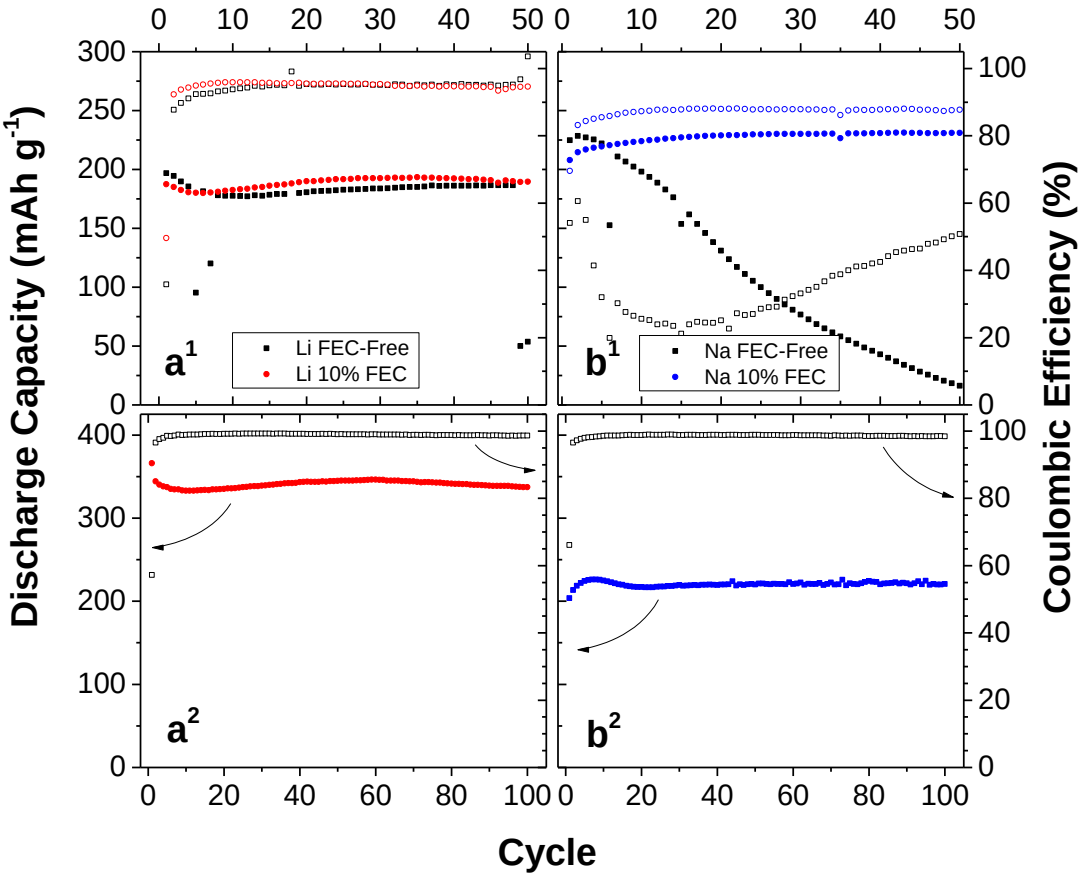

Figure 4.2. Capacity retention and coulombic efficiency of Cu_2Sb films in (a) lithium and (b) sodium half-cells cycled at (1) C/5 and (2) 5C. Closed symbols are recovered capacity (discharge) while open symbols are coulombic efficiency.

Initial cycle experiments performed at a C/5 rate showed that Cu2Sb displayed much faster capacity fade in sodium ion cells compared to lithium ion cells (Fig. 4.2a[1] and 4.2b[1]). This is expected due to the much larger volume expansion in the sodium ion system of 193% versus the lithium ion system of 93%, based on the crystallographic densities of Cu_2Sb at full

desodiation/delithiation and a mixture of Cu and Li_3Sb or Na_3Sb at full lithiation/sodiation. Surprisingly, pure antimony has been reported to achieve stable cycling through the use of fluoroethylene carbonate (FEC) as an electrolyte additive.[3] This effect extends to Cu_2Sb as well, and stable performance is achieved for a Cu_2Sb sodium half-cell when 10% FEC is added. This effect can be attributed to a much higher coulombic efficiency, and extends to the lithium ion cells as well. It is clear that for both cases, standard electrolytes are insufficient, but improvements of the electrode stability can be made by altering the electrolyte formulation. This particular area remains poorly explored for antimony based electrodes, but is undoubtedly critical to providing useful electrode systems for these materials.

In more detail, the effect of 10% FEC on the coulombic efficiency and capacity fade for the sodium half-cell is substantial, allowing >95% capacity to be maintained for over 50 cycles (Fig. 2). The equivalent sodium cell without FEC exhibits rapid capacity fade, dropping below 80% initial capacity within only ten cycles. This stabilization is likely the result of a more robust SEI layer capable of withstanding the large volume changes that occur during the reaction with sodium ions. At a cycle rate of 5C, the Li^+ and Na^+ cells retain 97.5% and 97.9% of their experimental peak capacity, respectively. At a 1C rate, the Na^+ half-cell can retain a capacity of 235 mAh g^{-1} (Fig. 4.3a). Although good initial discharge capacities of >200 mAh g^{-1} are obtainable at rates up to 20 C, the samples quickly decay in capacity. At a rate of 10 C, the discharge capacity drops below 50% of peak capacity after 128 cycles. At these rates, the expansion likely proceeds too fast to produce a high quality SEI layer, resulting in fast delamination of the film and poor mechanical properties. Despite this, the fast kinetics of this material indicate that Cu_2Sb is a good candidate for high-power sodium-ion batteries if pulverization can be appropriately mitigated.

It should be noted that the electrolyte formulation used here is still insufficient for a full cell sodium ion battery to be considered. As discussed previously, target coulombic efficiencies should be >80% for the first cycle and >99% for subsequent cycles at a minimum. Even at high FEC concentrations, the coulombic efficiency at slow rates barely exceeds 80% during short term cycling (Fig. 4.3b). The low efficiencies are exaggerated somewhat due to the relatively high surface area to volume ratio of thin-film electrodes, but this shows clearly that high stabilization is still not realized with this formulation. Further study will be necessary to identify usable salts and solvents that are capable of achieving high sustained efficiencies. We note that the exaggerated low efficiencies that are observed on thin films make this system an effective and easily prepared model electrode for further electrolyte studies.

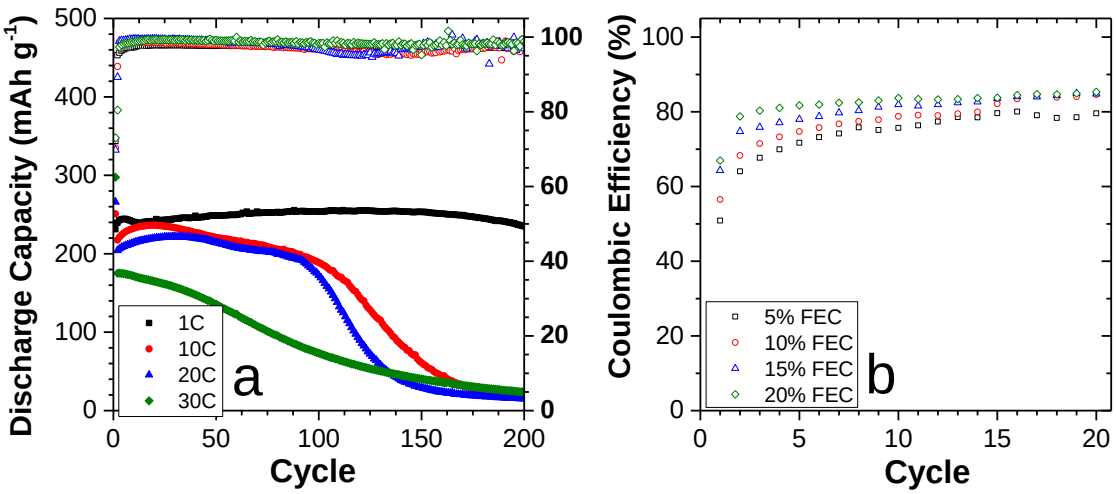

Figure 4.3. Cycle results for sodium half cells cycled at C-rates of 1C, 10C, 20C, and 30C, showing (a) capacity retention, and (b) the effect of FEC concentration on early cycle coulombic efficiencies for a C/20 cycle rate.

The high rate performance of Cu_2Sb during discharge is illustrated in Fig 4.4. It should be noted the discharge capacity of the Na^+ cell should increase by ~10-20% (based on cycle performance of constant-rate cells), giving the impression of a completely constant discharge

capacity up to a 20 C rate. The Cu_2Sb electrode can give a discharge capacity of roughly 250 mAh g^{-1} for the Na^+ cell, significantly better than the corresponding Li^+ cell at rates above 1 C. This is surprising, and may be the result of morphological differences in the resulting composite electrodes that are produced in-situ.

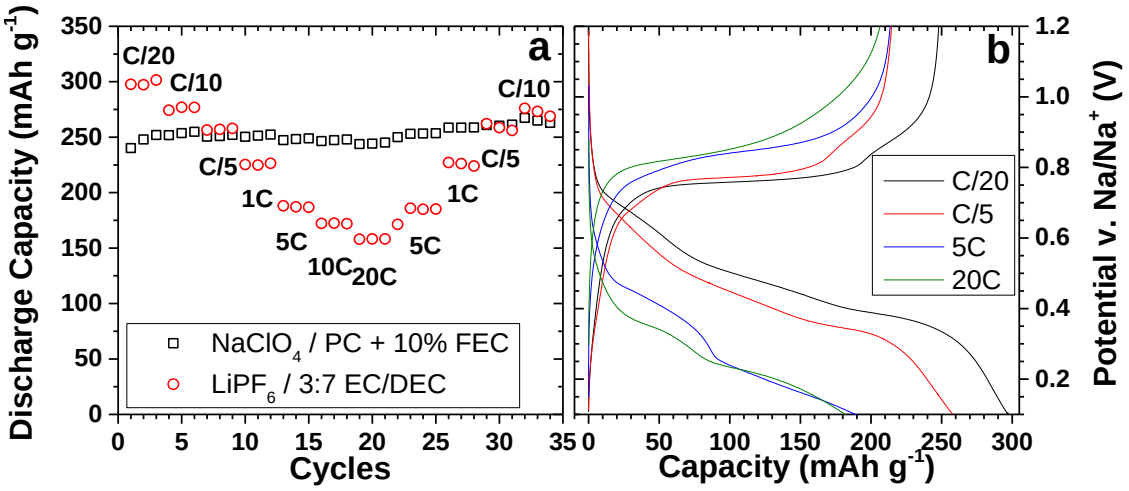

Figure 4.4. Capacity retention of Cu_2Sb films discharged at varying C-rates comparing the rate performance of a Li-ion cell and a Na-ion cell. Right: Charge/discharge profiles displaying the polarization of the Cu_2Sb film in a sodium half-cell as a function of C-rate, taken from the second cycle.

4.4 Conclusions

In Summary, we have shown that the additive FEC substantially improves the cycle life performance of electrodeposited Cu_2Sb anodes for non-aqueous Na^+ batteries. The combination of electrodeposited Cu_2Sb and Na^+ chemistry is compelling as a low-cost alternative to lithium ion batteries. Surprisingly, this combination may offer superior rate performance compared to the Li^+ alternative in certain cases. This indicates that this type of battery may be very useful where high power densities are required and energy density is less important, e.g. grid applications. Despite the substantial increase in cycle life obtained by the 1M $NaClO_4$ FEC/PC electrolyte, the

electrolyte formulation still must be greatly improved to be practical. Further development of Na^+ electrolyte chemistries and cathode materials with high efficiencies and stabilities will be necessary for the realization of commercialization of Na^+ batteries.

REFERENCES

1. Kim, Y.; Ha, K. H.; Oh, S. M.; Lee, K. T. *Chemistry–A European Journal* **2014**, *20*, 11980.

2. Nithya, C.; Gopukumar, S. *Wiley Interdisciplinary Reviews: Energy and Environment* **2015**, *4*, 253.

3. Darwiche, A.; Marino, C.; Sougrati, M. T.; Fraisse, B.; Stievano, L.; Monconduit, L. *Journal of the American Chemical Society* **2012**, *134*, 20805.

4. Darwiche, A.; Sougrati, M. T.; Fraisse, B.; Stievano, L.; Monconduit, L. *Electrochemistry Communications* **2013**, *32*, 18.

5. Baggetto, L.; Ganesh, P.; Sun, C.-N.; Meisner, R. A.; Zawodzinski, T. A.; Veith, G. M. *Journal of Materials Chemistry A* **2013**, *1*, 7985.

6. Zhu, Y.; Han, X.; Xu, Y.; Liu, Y.; Zheng, S.; Xu, K.; Hu, L.; Wang, C. *ACS nano* **2013**, *7*, 6378.

7. Wu, L.; Pei, F.; Mao, R.; Wu, F.; Wu, Y.; Qian, J.; Cao, Y.; Ai, X.; Yang, H. *Electrochimica Acta* **2013**, *87*, 41.

8. Hou, H.; Yang, Y.; Zhu, Y.; Jing, M.; Pan, C.; Fang, L.; Song, W.; Yang, X.; Ji, X. *Electrochimica Acta* **2014**, *146*, 328.

9. Hou, H.; Jing, M.; Zhang, Y.; Chen, J.; Huang, Z.; Ji, X. *Journal of Materials Chemistry A* **2015**, *3*, 17549.

10. Zhang, N.; Liu, Y.; Lu, Y.; Han, X.; Cheng, F.; Chen, J. *Nano Research* **2015**, *8*, 3384.

11. Baggetto, L.; Carroll, K. J.; Hah, H.-Y.; Johnson, C. E.; Mullins, D. R.; Unocic, R. R.; Johnson, J. A.; Meng, Y. S.; Veith, G. M. *The Journal of Physical Chemistry C* **2014**, *118*, 7856.

12. Baggetto, L.; Allcorn, E.; Manthiram, A.; Veith, G. M. *Electrochemistry Communications* **2013**, *27*, 168.

13. Kim, I. T.; Allcorn, E.; Manthiram, A. *Physical Chemistry Chemical Physics* **2014**, *16*, 12884.

14. Baggetto, L.; Hah, H.-Y.; Johnson, C. E.; Bridges, C. A.; Johnson, J. A.; Veith, G. M. *Physical Chemistry Chemical Physics* **2014**, *16*, 9538.

15. Darwiche, A.; Toiron, M.; Sougrati, M. T.; Fraisse, B.; Stievano, L.; Monconduit, L. *Journal of Power Sources* **2015**, *280*, 588.

16. Tran, C. C. H.; Autret, C.; Damas, C.; Claude-Montigny, B.; Santos-Peña, J. *Electrochimica Acta* **2015**, *182*, 11.

17. Lee, C. W.; Kim, J.-C.; Park, S.; Song, H. J.; Kim, D.-W. *Nano Energy* **2015**, *15*, 479.

18. Kim, I. T.; Allcorn, E.; Manthiram, A. *Energy Technology* **2013**, *1*, 319.

19. Xiao, L.; Cao, Y.; Xiao, J.; Wang, W.; Kovarik, L.; Nie, Z.; Liu, J. *Chemical Communications* **2012**, *48*, 3321.

20. Jackson, E.; Green, S.; Prieto, A. *ACS applied materials & interfaces* **2015**, *7*, 7447.

21. Baggetto, L.; Marszewski, M.; Górka, J.; Jaroniec, M.; Veith, G. M. *Journal of Power Sources* **2013**, *243*, 699.

22. Baggetto, L.; Allcorn, E.; Unocic, R. R.; Manthiram, A.; Veith, G. M. *Journal of Materials Chemistry A* **2013**, *1*, 11163.

23. Bodenes, L.; Darwiche, A.; Monconduit, L.; Martinez, H. *Journal of Power Sources* **2015**, *273*, 14.

24. Darwiche, A.; Bodenes, L.; Madec, L.; Monconduit, L.; Martinez, H. *Electrochimica Acta* **2016**, *207*, 284.

25. Morcrette, M.; Larcher, D.; Tarascon, J.-M.; Edström, K.; Vaughey, J.; Thackeray, M. *Electrochimica acta* **2007**, *52*, 5339.

26. Matsuno, S.; Noji, M.; Nakayama, M.; Wakihara, M.; Kobayashi, Y.; Miyashiro, H. *Journal of The Electrochemical Society* **2008**, *155*, A151.

CHAPTER 5: ELECTRODEPOSITED ZN4SB3 THIN FILMS FOR SODIUM-ION BATTERY ANODES

The experimental content and manuscript writing of this thesis chapter were completed by Everett D. Jackson. Scott Green assisted with the development of the annealing procedure, and Amy L. Prieto provided guidance and conceptual insight. Portions of this work has been published as a communication in *ACS Applied Materials & Interfaces* **2015**, *7*, 7447-7450 (DOI: 10.1021/am507436u).

5.1 Introduction

Sodium-ion batteries have recently regained significant interest as an alternative to lithium-ion batteries. As opposed to lithium, sodium is advantageous due to higher abundance, good global distribution, lower cost, a standard reduction potential near that of lithium (-3.04 V for Li/Li^+ and -2.71 V for Na/Na^+), and the potential for new cell chemistries impractical with lithium. Although the theoretical energy and power densities of a sodium battery are lower than the lithium analogue, sodium batteries may become important for stationary and grid applications where inexpensive rechargeable batteries are needed.

The amount of research on potential anode materials for secondary sodium-ion batteries has been limited, and low-cost negative electrode materials with high energy density are required to make a sodium ion battery economically viable. The high reactivity of sodium with air and water make it an unattractive negative electrode due to safety concerns. Fortuitously, it has been observed that in many cases sodium under-goes similar electrochemical reactions as lithium and analogues of lithium ion negative electrodes are there-fore clear candidates for sodium ion batteries. Analogous to lithium ion anode targets, metal based sodium ion battery anode targets are attractive

due to their good voltage characteristics and high theoretical capacity, and include Si (954 mAh g^{-1}), Sn (847 mAh g^{-1}), and Sb (660 mAh g^{-1}).[1]

Antimony in particular has been investigated due to its high theoretical capacity, good kinetic performance and voltage characteristics.[2-5] One would think that sodium negative electrodes (as compared to lithium) would experience faster capacity fade due to the larger size of sodium ions, contributing to greater volume changes and faster pulverization.[1] Unexpectedly, substantially better cycle life has been reported for reversible sodiation and desodiation reactions, in contrast to the poor cycle life of pure antimony with lithium.[6-7] Additionally, the phases produced during sodium insertion do not appear to follow the thermodynamically predicted intermediates based on phase diagrams, and instead often proceed via amorphous intermediates. This has led to additional interest in high-capacity anodes that are not possible in lithium-ion batteries due to pulverization.

Alloys of antimony have also been investigated, either to further increase capacity retention or offer other benefits, such as improved electrical conductivity and better mechanical properties. In addition to pure antimony, Sb^2O^4,[8] SnSb[9-10], Cu_2Sb[11], and Cu_6Sn_5[12], as well as some other alloy-based composites,[13-15] have been investigated as potential anode candidates. A common theme among these anodes is their ability to cycle for at least several cycles, despite the very large volume expansion and contraction that occurs during cycling.

Here we report the use of zinc as an alloying element to improve the electrochemical performance of antimony as a sodium ion battery anode material. Zinc is interesting due to its' high abundance, low cost, and good conductivity. Additionally, unlike lithium, sodium does not react electrochemically with zinc. Thus, it can be utilized both as a substrate material and as an

additive for the anode electrode. These properties are advantageous for the sodium-ion battery, where low materials and manufacturing costs are critical considerations.

5.2. Results and Discussion

We have synthesized Zn_4Sb_3 and Zn-Sb alloy films with varying zinc content by the electrodeposition of antimony onto zinc substrates using a pH neutral aqueous gluconate-chloride electrolytes (cyclic voltammograms shown and discussed in SI Fig. 5.1). Gluconate acts both as a complexing agent and electrode surfactant, allowing the co-deposition of amorphous zinc antimonide without excessive hydrogen gas formation. Additionally, the neutral pH suppresses either element from preferentially depositing and creating a heterogeneous or dendritic deposit (SI Fig. 5.2). Using a very high overpotential, films with low amounts of oxygen are obtained with a zinc to antimony ratio the same as the ratio of the dissolved metal chloride salt concentrations in the electrolyte bath (SI Fig. 5.3). Adherent, flat, and silvery thin films are obtained with good homogeneity.

Amorphous deposits are obtained initially, allowing the investigation of zinc-doped antimony alloy films (SI Fig. 5.4). Initial cycling data of these films indicate two major charge potential plateaus and a sloping discharge potential profile (SI Fig. 5.5). The two charging plateaus become more distinct upon additional cycling and are easily distinguished in the second cycle. The discharge potential profile only changes slightly, with no well-defined plateaus. Surprisingly, the incorporation of zinc has no major effect on the potential profile of the antimony, with little difference between the samples with up to 50 mol.% zinc and zinc-free deposits. This is likely due to the amorphous nature of the deposit, causing the electrochemically inactive zinc to operate as a by-stander in the reaction. Prior to annealing, these films show only modest performance and exhibit rapid capacity fading (SI Fig. 5.6).

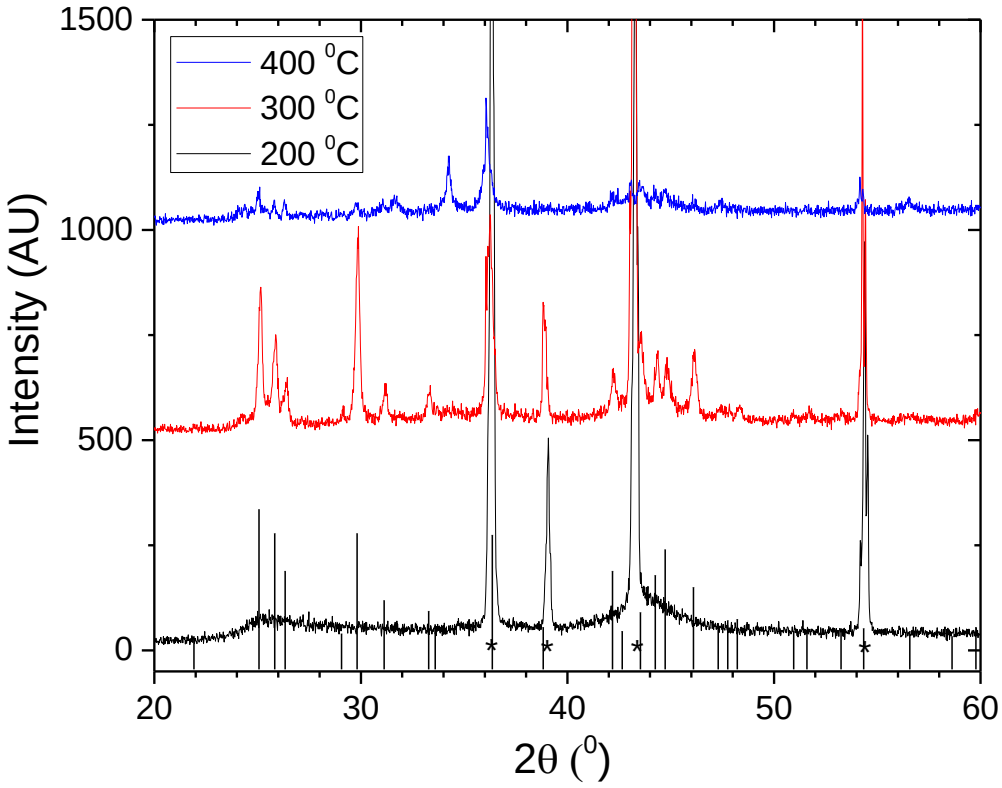

Figure 5.1. Glancing incident X-ray diffraction patterns of 10 minute depositions from 20 mM $ZnCl_2$ deposition solution annealed at 200 – 400 °C for 3 hours. Peaks marked with an asterisk are from the zinc substrate. All other peaks correspond to Zn_4Sb_3 (PDF 00-056-1306). All scans were taken at 1-degree incident angle.

To achieve enhanced performance, the Zn-Sb amorphous films were annealed under argon to form crystal-line Zn_4Sb_3. We chose to use deposits with an initial zinc to antimony ratio of 2:3, allowing annealing time to be balanced with substrate to film diffusion and to allow a lower diffusion temperature. Prior to annealing, we analyzed the cross-section of these films by SEM to determine the approximate film thicknesses (SI Fig. 5.7). The approximate average thicknesses were found to be 200 nm, 450 nm, and 780 for deposition times of 2, 6, and 10 minutes, respectively. These values correspond well to thicknesses estimated using the average density of antimony and zinc metal and the mass of the deposited material. The corresponding mass loading

of the electrodes were 122, 274, and 474 μg cm^{-2}. These results indicate that the films have good homogeneity and are clearly smooth and non-porous.

Annealing conditions were optimized to form high quality of Zn_4Sb_3 films. It was found that annealing zinc-deficient films deposited from 2:3 Zn:Sb solution on zinc substrates at a temperature of 300 °C under 700 torr argon for three hours resulted in high intensity signals from Zn_4Sb_3 (Fig. 5.1). Lower temperatures resulted in poor crystallinity, while higher temperatures degraded the film by the formation of very small nanowires (not shown) and low intensity diffraction peaks representing Zn_4Sb_3, a phenomenon that has been reported previously.16 The effect of annealing time was also examined on both 2 minute and 10 minute depositions to ensure the annealing conditions were adequate for a range of different film thicknesses (SI Fig. 5.8). It was found that 6 hours was optimal for 10 minute depositions, but annealing over 3 hours for 2 minute depositions led to an excess of zinc at the surface.

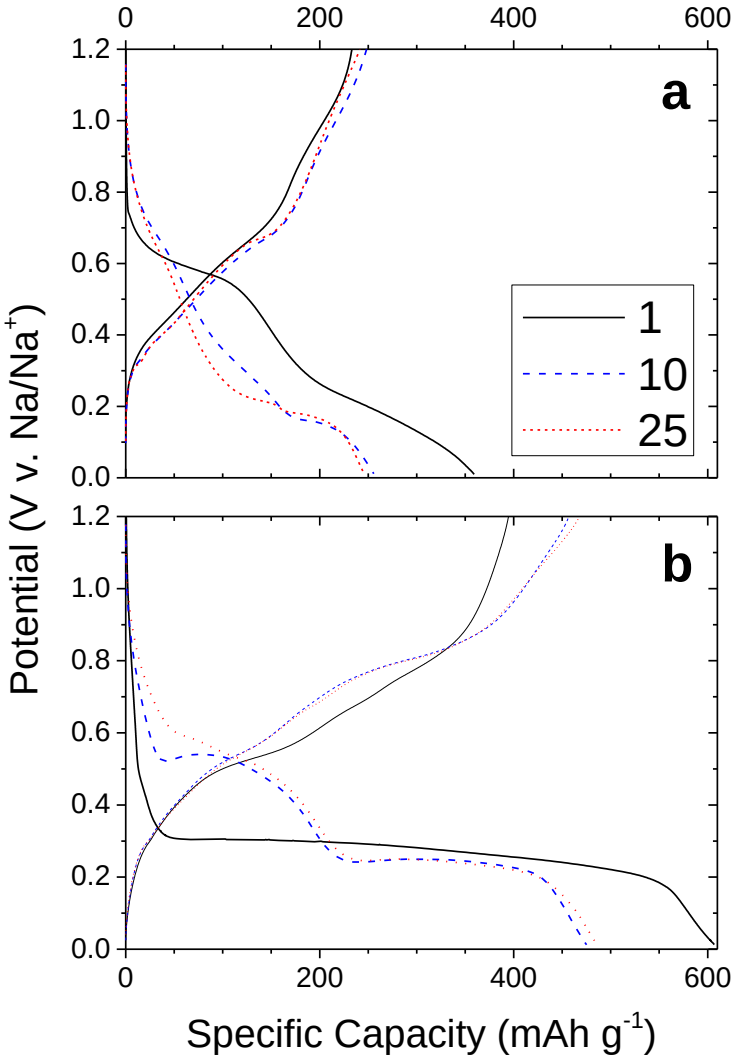

Figure 5.2. Charge-discharge voltage profiles for the 1st (black solid), 10th (blue dashed), and 25th (red dotted) cycles for (a) an amorphous 4:3 Zn:Sb thin film deposited for 240 s and (b) an equivalent film annealed for 6 hours at 300 °C under argon to produce Zn_4Sb_3. Films were cycled in a sodium-ion cell between 0.01 V and 1.20 V. The electrolyte used is 1 M NaClO4 in PC with 5% FEC additive.

The electrochemical performance of these Zn_4Sb_3@Zn anodes were evaluated in sodium half cells (Fig. 5.2). A high capacity of 450 mAh g^{-1} is near to the theoretical capacity of 486 mAh g^{-1} for a film deposited from a 2:3 Zn:Sb solution. Once corrected for two additional stoichiometric equivalents of zinc introduced during annealing, this gives a reversible capacity of 357 mAh g^{-1}.

Unlike the case for zinc incorporation into amorphous antimony films, the formation of crystalline Zn_4Sb_3 causes a significant change in the initial potential profiles of the electrode during both sodium insertion and desertion. The sloping sodium incorporation profile seen in amorphous deposits is replaced with a single, well-defined potential plateau at ~0.3 V v. Na/Na^+. The discharge profiles of the annealed films are initially not distinguishably different from the amorphous films, dis-playing a sloped profile with no well-defined plateaus. Upon subsequent cycles, a new distinct charge plateau appears at ~0.5 V v. Na/Na^+, resulting in a clear two-step charge profile at 10 cycles that gradually becomes less distinct with prolonged cycling. Similarly, at ten cycles there is a clear discharge plateau that is present at 0.8 V v. Na/Na^+ that is not seen when initially amorphous films are used. Although we were unable to resolve any unique phases during the charge-discharge process using *ex situ* XRD, the two-plateau charge mechanism is distinct for Zn_4Sb_3 versus the amorphous material and is likely critical to the improved performance.

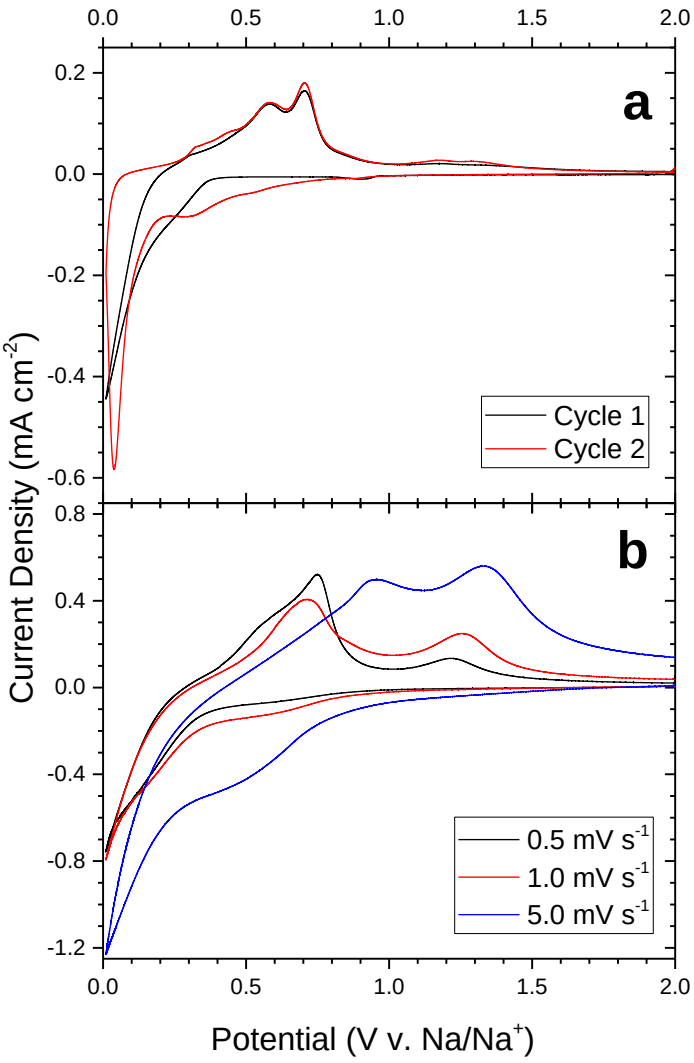

Figure 5.3. Cycle life performance of annealed Zn_4Sb_3 thin films annealed for 3 hours at 300 °C cycled in sodium half-cells at a C/5 rate.

Cyclic voltammetry was performed in a half cell configuration with a Zn_4Sb_3 electrode and sodium counter electrode (Fig. 5.4a). An initial single cathodic peak that occurs at potentials below 0.3 V indicates a clear one step sodium conversion on the first cycle. Upon reversal, two anodic peaks at 0.55 V and 0.70 V are present, suggesting a more complex reaction to remove sodium. A minor third anodic peak is present at a relatively high voltage of 1.25 V. The second cycle shows the development of a higher potential cathodic peak that starts at 0.50 V and reaches maximum

current at 0.30 V. An additional cathodic peak is present at 0.30 V. These two additional peaks are the result of the in-situ formation of an amorphous zinc-antimony composite that occurs due to the in-situ conversion reaction of sodium with Zn_4Sb_3. Subsequent cyclic voltammograms do not show further changes in the film electrochemistry. The kinetic performance of Zn_4Sb_3 thin films is exceptional, with ~300 nm films providing 325 mAh g^{-1} at a discharge rates of up to 2C and 275 mAh g^{-1} at 10C (SI Fig. 5.9). This good performance is likely facilitated by the thin film thickness, but these high capacities show that this material has good kinetic properties that enable high rates when lithium diffusion lengths are short. We noticed a substantial change in the shape of the charge and discharge profiles at fast rates. We consider the good high rate performance to be in part due to this change in electrode electrochemistry. To study this phenomenon, we performed cyclic voltammograms at increased rates (Fig. 5.4b). As expected, the anodic peaks become polarized to higher potentials, reaching 0.95 V at a 5 mV s^{-1} scan rate. Unexpectedly, the previously very small anodic peak at 1.25 V greatly increases in magnitude until it is larger than the low potential anodic peaks. This suggests that the high rate performance may be the result of a fast conversion process that becomes activated when the polarization is large. This mechanism accounts for unexpected good rate performance of Zn_4Sb_3. Further exploration of this mechanism is required to determine the conversion mechanism of the material.

Annealed films display superior cycle life compared to amorphous films, with thin films (~200-400 nm) retaining over 90% of their maximum capacity for over 250 cycles. In contrast, thick electrodes over ca. 600 nm display both lower reversible capacity and shorter cycle life. Pulverization appears to be significantly worse for thicker electrodes, where electrode cracking occurs even on the first cycle (SI Fig. 5.10). Regardless of the thickness, an initial coulombic

efficiency of ~60% is obtained, with efficiencies >95% after the first few cycles. The Zn_4Sb_3 films maintain above 98% efficiency after the first five cycles.

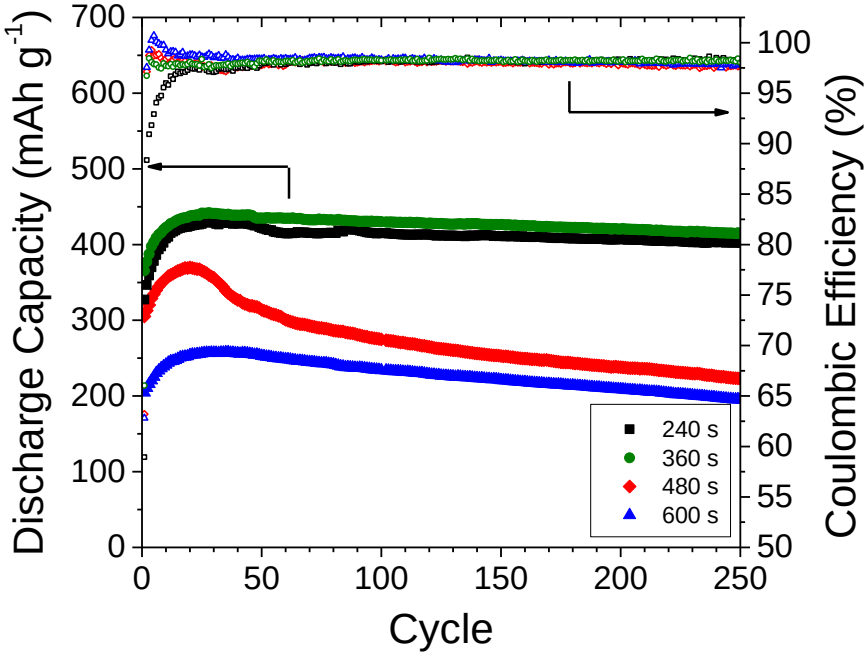

Figure 5.4. Cycle life performance of annealed Zn4Sb3 thin films annealed for 3 hours at 300 °C cycled in sodium half-cells at a C/5 rate.

It is important to note that while both the Zn-Sb amorphous deposits and crystalline Zn_4Sb_3 form an amorphous material upon cycling, they exhibit significantly different electrochemical performance. The amorphous deposit is capable of reversibly reacting be-tween only 55-65 % of the antimony, while the crystalline Zn_4Sb_3 deposit uses over 90% of the available antimony. Additionally, the utilization of a higher amount of antimony in the deposit would normally imply that the crystalline deposits undergo faster pulverization and capacity loss. We ascribe these differences to the ability of Zn_4Sb_3 to react directly with sodium ions to produce the Na_3Sb product across the entire electrode, while simultaneously extruding zinc in such a way that it does not impair sodium ion transfer. The homogenous nature of the crystalline deposits reduces local

variations in zinc concentrations, and therefore all the antimony is available for reaction. In contrast, the amorphous deposits may have local areas that are extremely zinc rich, effectively trapping portions of antimony such that they cannot be accessed by sodium ions and creating volumes of material that are effectively inactive. This illustrates the importance of atomic-level order on the reversibility of Zn_4Sb_3 in sodium ion batteries.

5.3 Conclusions

In conclusion, we have studied the behavior of amorphous zinc-antimony alloys and annealed Zn_4Sb_3 using electrodeposited thin films. The potential profile be-tween 0.10 V and 1.20 V is within the useful range for non-aqueous rechargeable sodium-ion anode materials. While amorphous zinc-antimony thin films display poor anode performance, annealed thin films of crystalline Zn_4Sb_3 show superior cycle life, high efficiency, and a high capacity. The use of zinc as an alloying agent and substrate is important. Although zinc is less conductive than copper currently used in lithium-ion batteries, zinc is both inexpensive and abundant. As a result, this system is of practical interest for applications where low cost and good long-term performance are more important factors than high energy and power density.

5.4 Supporting Information.

5.4.1. Experimental Procedure

5.4.1.1. Chemicals

Anhydrous Zinc chloride (Fisher Scientific, ≥ 98%), anhydrous antimony chloride (Sigma-Aldrich/Riedel-deHäen, ≥99%), D-gluconate (Sigma-Aldrich, ≥99%), sodium perchlorate (Sigma-Aldrich, ≥98%), propylene carbonate (Sigma-Aldrich, ≥99%), and fluoroethylene carbonate (Sigma-Aldrich, ≥99%). were purchased and used without further purification. Sodium cubes in

oil (Sigma-Aldrich, 99.9%) were washed with acetone and oxide removed using a stainless steel razor blade prior to use. Zinc foil (0.10", McMaster-Carr) was cleaned with Alconox detergent, acetone, and DI water, followed by mechanical polishing with Wenol™ metal polish. For depositions, Kapton™ tape was used to isolate one side so depositions were only performed on the polished surface. Polish residue was removed by careful scrubbing using a lab tissue with isopropyl alcohol. Millipore water (18.2 MΩ cm) was used for all experiments and to wash all glassware prior to use.

5.4.1.2. Preparation of deposition solutions

First, 200 mM of sodium gluconate was added to Millipore water and stirred. Once dissolved, the appropriate amount (10 – 40 mM) of anhydrous $ZnCl_2$ was added and stirred until dissolved. Once the zinc chloride fully dissolved, 30 mM $SbCl_3$ was added and stirred until dissolved. The resulting solution is titrated with sodium hydroxide to a pH of 7. This solution is clear and colorless, and stable for six to eight weeks stored at room temperature in a sealed container before precipitation of a white compound occurs.

5.4.1.3. Deposition electrochemistry

All electrochemical experiments were performed on a Gamry Reference 3000 potentiostat/galvanostat. Cyclic voltammograms were performed using a three-electrode setup consisting of a saturated calomel reference electrode (SCE), a platinum mesh counter electrode, and a gold working electrode (3 mm^2) working electrode. Electrochemical depositions were conducted in potentiostatic mode at -1.60 V v. SCE with a platinum mesh counter electrode. The solutions were stable for more than 30 minutes of deposition before becoming cloudy and yellowish. No observable bulk pH changes were detected during these experiments.

5.4.1.4. Half-cell battery testing

Battery testing was conducted on one of two Arbin BT2000 battery testing systems using galvanostatic conditions. Cells were constructed inside an Argon glovebox (VAC systems, <0.5 ppm O2 content) using 0.5-inch Swagelok® PFA straight-tube fittings bored through with a 13 mm drill. Masses were determined by weighing the sample substrate before deposition and the substrate with film after deposition. All masses refer to the original mass of deposited material, and are not adjusted for excess zinc incorporation that occurs during annealing. A copper rod was used for the Zn_4Sb_3 contact and a stainless steel rod for the sodium contact. A stainless steel mesh was used to support the sodium metal, and a stainless steel spring was used to ensure good contact between all the battery components. The electrodes were separated by two pieces of porous polypropylene separator (MTI Corp.) with a piece glass microfiber filter between them to act as an electrolyte reservoir. The electrolyte was prepared by mixing 1 M $NaClO_4$ in propylene carbonate with 5 vol.% fluoroethylene carbonate. For *ex situ* experiments, the electrodes were removed, washed in two separate solutions of dimethyl carbonate, then washed with diethyl carbonate and dried before being removed from the glovebox.

5.4.1.5. Instrumental Analysis

Scanning electron microscopy was performed on a JEOL JSM-6500F microscope operating at an accelerating voltage of 15 kV. Energy dispersive x-ray spectroscopy was performed using a Thermo Scientific Noran System Six EDS system. For EDS experiments, a polished copper plate substrate (McMaster-Carr, ≥99.9% Cu) was used instead of a zinc substrate. Glancing angle x-ray diffraction (GAXRD) was performed using a Bruker D8 Discover using a Cu Kα x-ray source, Gobel mirror, Soller slit assembly, Peltier dectector, and operating in high-resolution geometry. Optical profilometry was performed on a ZeScope Optical Profiler using a 20x

objective lens and 1 mm x 1 mm operating area (stitch mode, 20% overlap, 0.4% detector threshold, 20% detector saturation limit). To improve image clarity, the profiles were leveled using automatic third-order leveling and void pixels filled using the provided all-within-boundary method.

5.4.2. Supporting figures and data

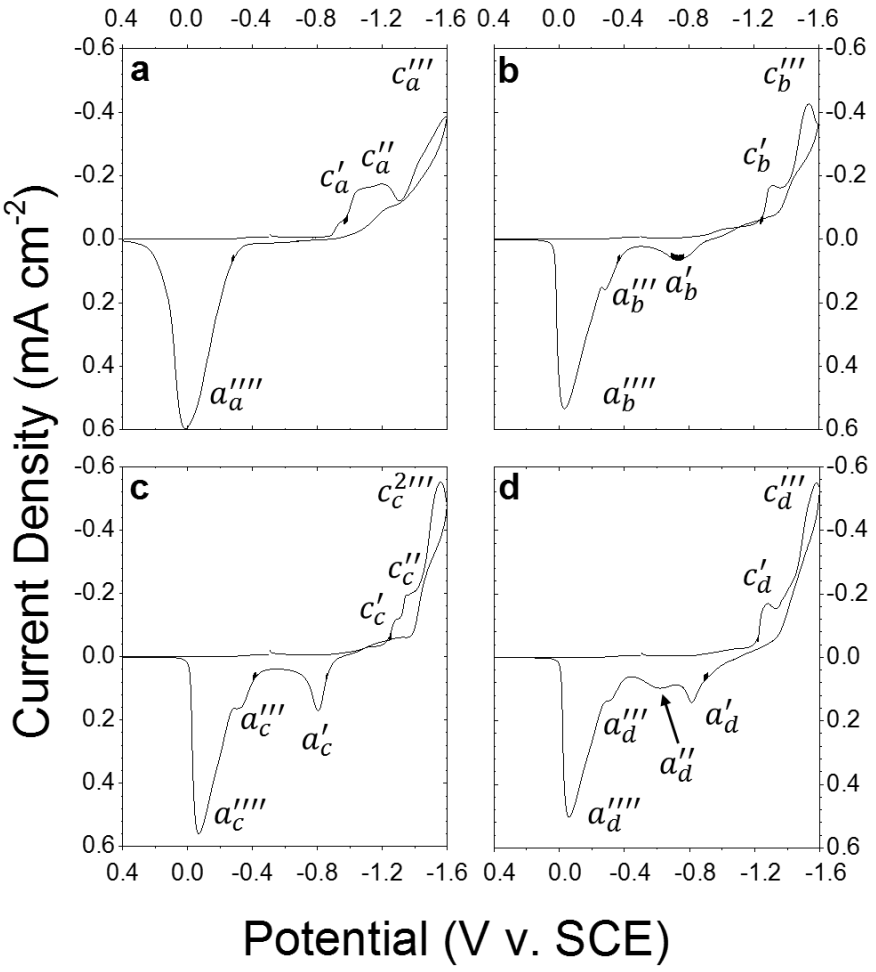

Figure S5.1. Cyclic voltammograms of the neutral aqueous solutions used to deposit Zn-Sb alloy in this experiment containing 200 mM sodium gluconate, 30 mM $SbCl_3$, and zinc chloride concentrations of (a) 10 mM, (b) 20 mM, (c) 30 mM, and (d) 40 mM. A 0.75 cm diameter gold working electrode, platinum counter electrode, and SCE reference were used. Scan rate was 10 mV s^{-1} for all voltammograms. Each wave is labeled (c = cathodic peak, a = anodic peak; subscript denotes solution; primes distinguish peak location and represent the same peak in for every voltammogram where present).

Cyclic Voltammogram Results: The first cathodic peak in each voltammogram c_x' represents the onset of antimony deposition, while the second cathode peak c_x'' represents the onset of zinc deposition. Where only one peak (voltammograms b and d), codeposition occurs at the first onset of appreciable current. The antimony cathodic peak c_x' appears to shift to more negative potentials as the zinc concentration is increased. Interestingly, a third cathodic peak c_x''' appears in voltammograms b, c, and d, and is where diffusion-limited co-deposition occurs. The stripping peaks a_x' and a_x'' are the result of metallic zinc deposits being stripped from the electrode. These deposits are the result of primarily zinc deposition occurring in the potential range of -1.3 to -1.5 V v. SCE. Anodic stripping peak a_x''' appears to be a shoulder unique to antimony-zinc co-deposition, but we have not determined the cause of this peak. The large anodic stripping peak a_x'''' is the result of stripping both bulk antimony and zinc-antimony co-deposit. When single-potential depositions at -1.60 V v. SCE are performed, this is the only major peak present for all solutions.

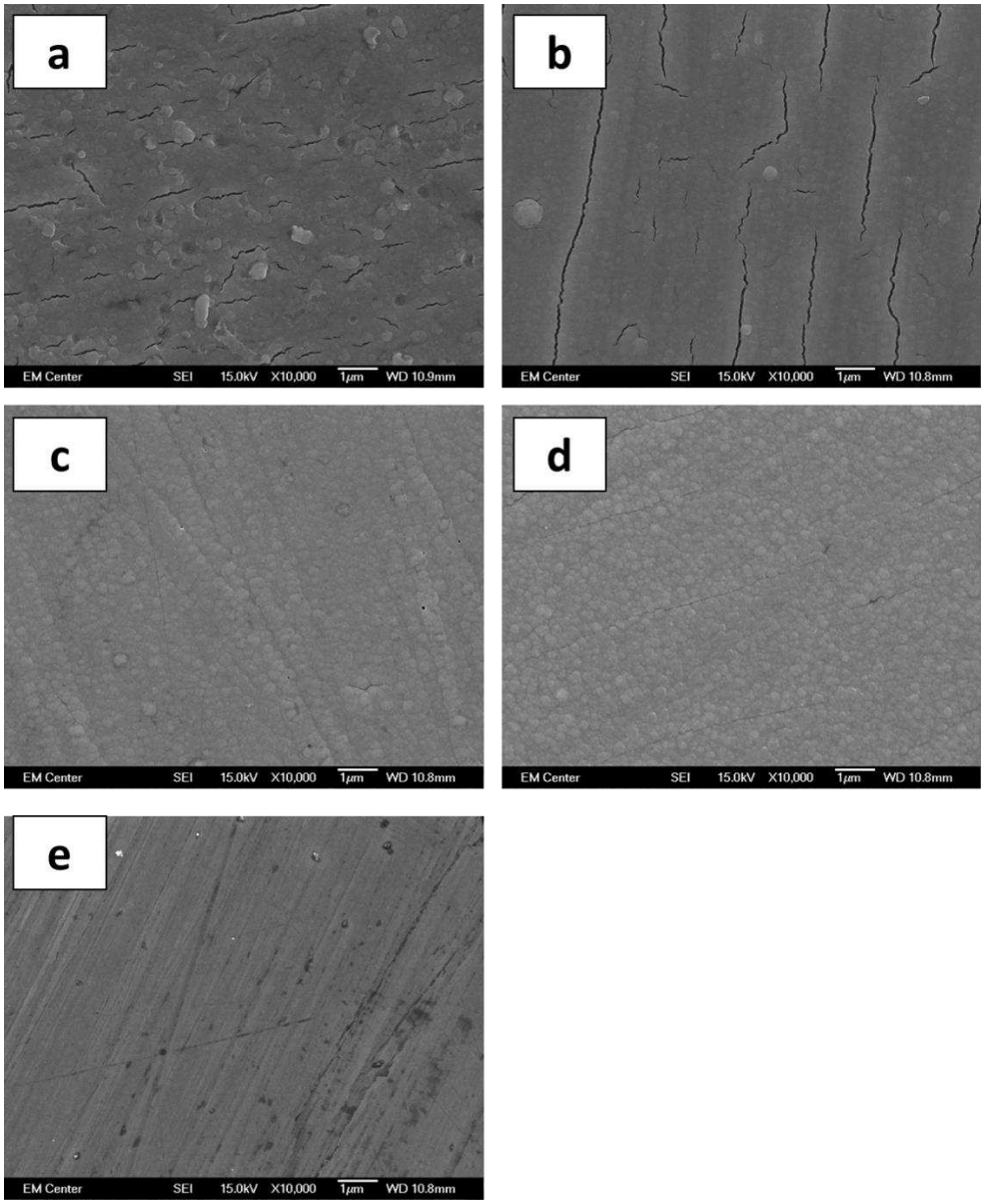

Figure S5.2. Scanning electron microscopy images of Zn:Sb alloy deposits from the pH neutral gluconate deposition solution with 200 mM sodium gluconate, 30 mM $SbCl_3$, and (a) 10 mM, (b) 20 mM, (c) 30 mM, (d) 40 mM $ZnCl_2$. Films were synthesized by potentiostatic electrodeposition on polished copper substrates (e) at -1.60 V v. SCE for 4 minutes. Cracking observed in (a) and (b) are from sample preparation, but are also indicative of high internal stress in the film.

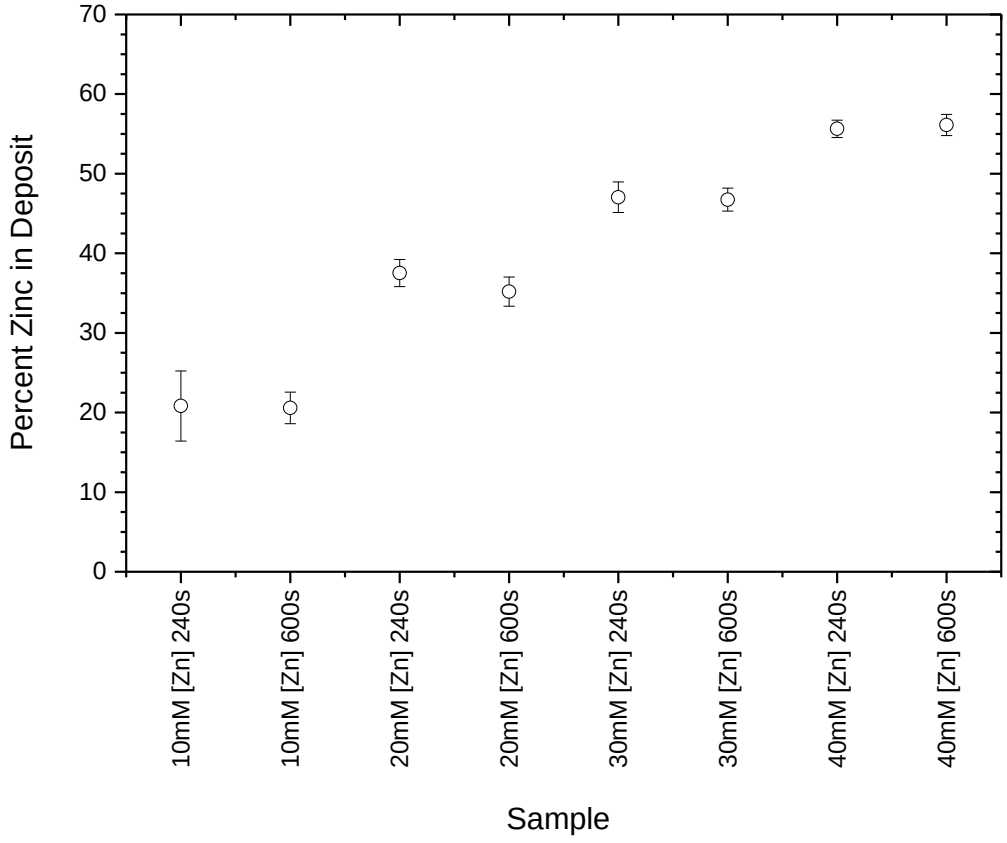

Figure S5.3. Zinc to antimony ratio in the as-deposited film determined by energy dispersive spectroscopy as a function of the concentration of $ZnCl_2$ in the deposition bath. The concentration of $SbCl_3$ and sodium gluconate were fixed at 30 mM and 200 mM, respectively, and the pH was adjusted to 7.0 with sodium hydroxide for all deposition baths. Error bars represent standard deviation based on macroscopically different areas of the same sample.

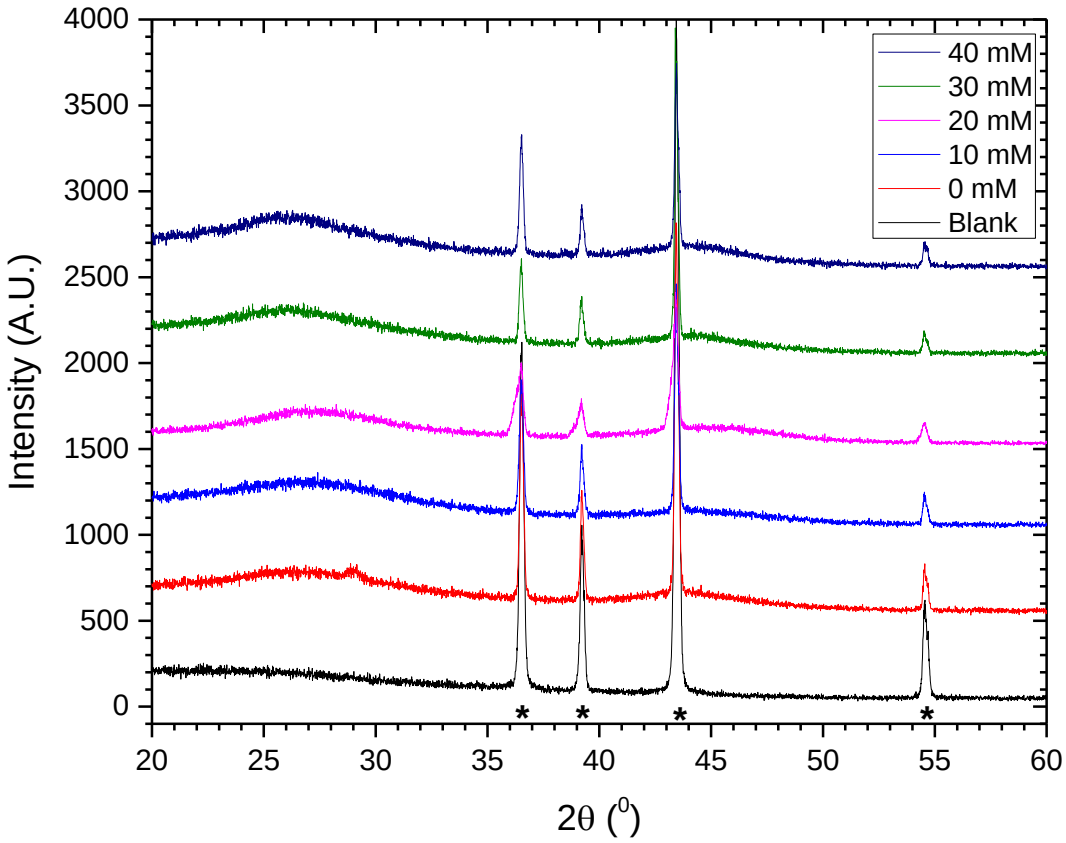

Figure S5.4. Glancing incident X-ray diffraction patterns of 5 minute depositions from 30 mM $SbCl_3$, 200 mM sodium gluconate at pH = 7.0 and 0-40 mM $ZnCl_2$. The polished zinc substrate is also included for reference. Pure antimony deposition shows a single weak peak at 29°. All other depositions show only amorphous rises at 20-30° and 42-46°. It should be noted that these rises are in the same regions as the strongest peaks for Zn_4Sb_3. This suggests good intermixing of zinc and antimony in the amorphous deposits. The strong peaks at 36.2°, 38.9°, 43.3°, and 54.3° 2θ correspond to the zinc substrate (marked by asterisk). All scans were taken at 1-degree incident angle.

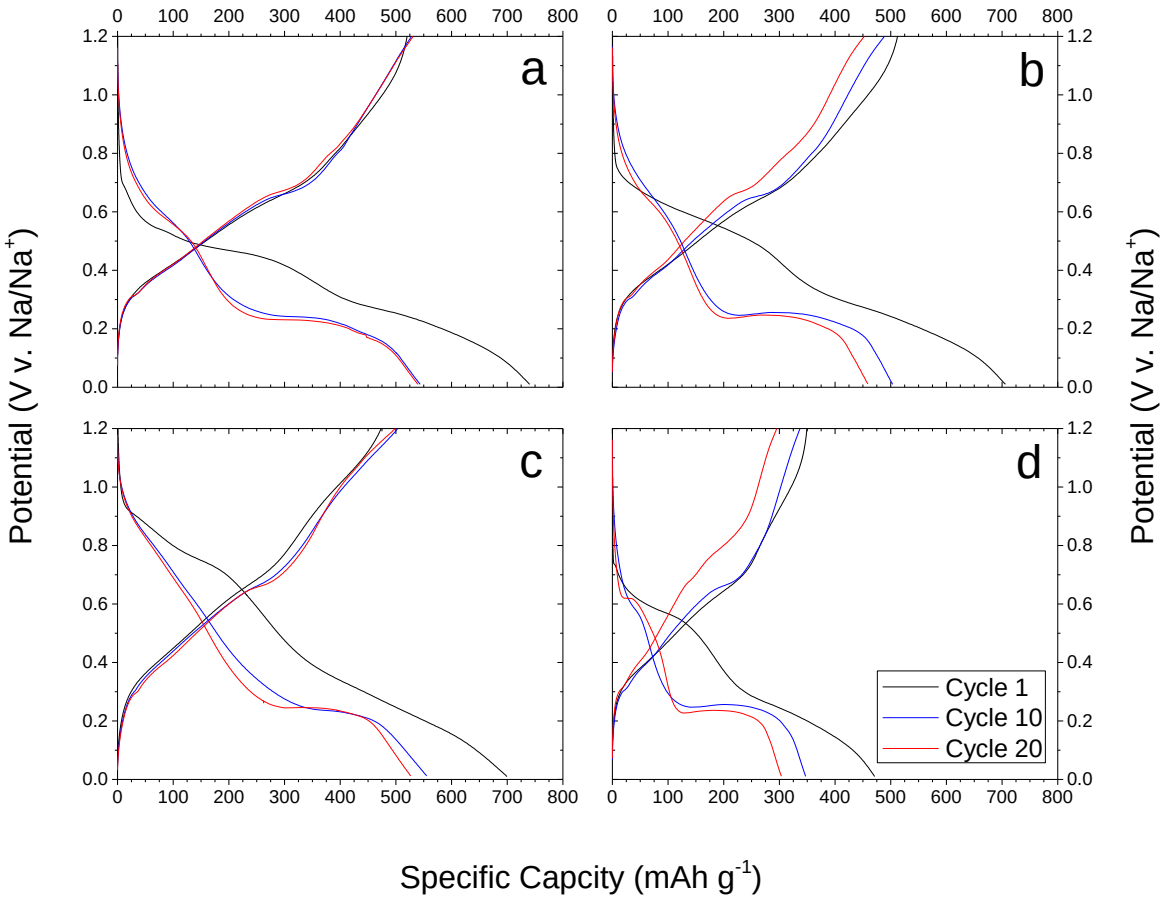

Figure S5.5. Potential profiles of Zn-Sb alloy thin films cycled at a C/5 rate containing zinc to antimony ratios of (a) No Zinc, (b) 1:3, (c) 2:3, and (d) 3:3. The profile for amorphous 4:3 Zn:Sb films can be found in the main text (Fig. 2). The addition of zinc does not cause dramatic changes in the charge-discharge profile for the reaction of antimony with sodium. In all cases, there is a sloping two-step charge (sodium insertion) process and a sloping discharge potential profile. The zinc does not appear to interfere with any of these processes, although the gravimetric capacity drops with increasing zinc loading.

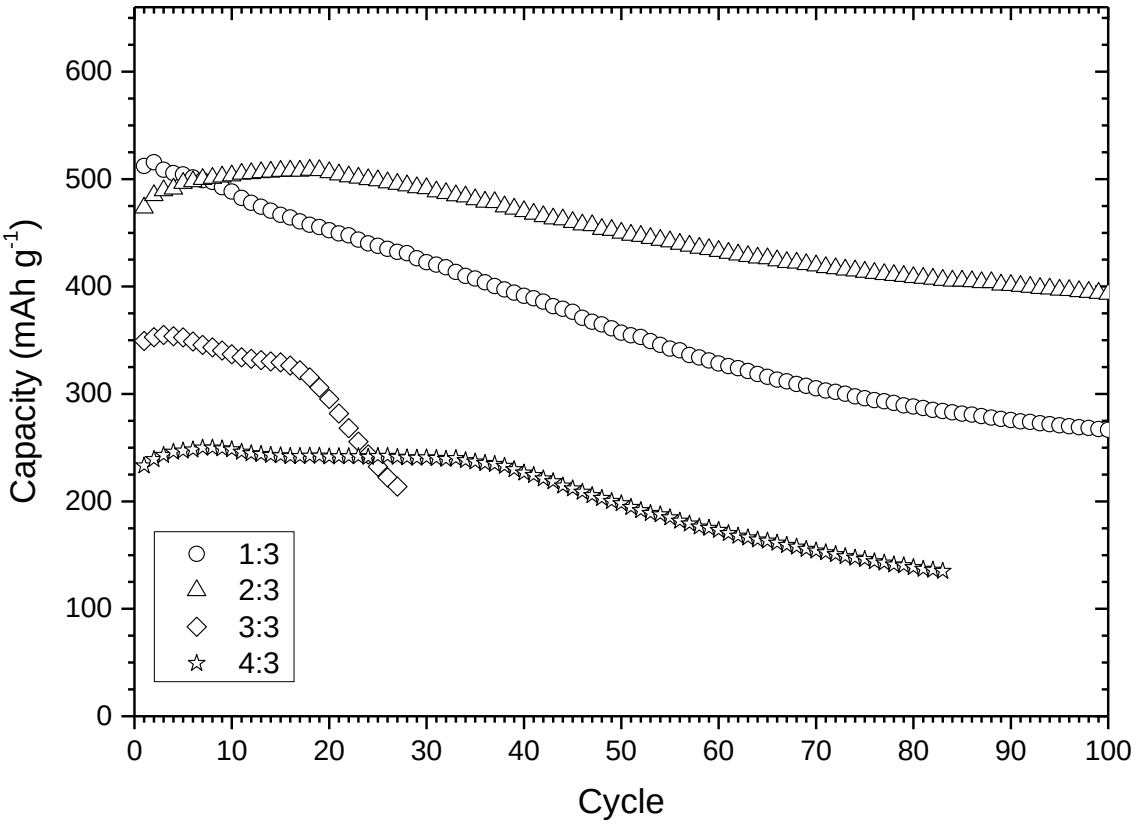

Figure S5.6. Specific capacities of Zn:Sb alloy electrodeposited films with varying ratios of zinc to antimony charged and discharged at a C/5 rate. All of the non-annealed films display capacity loss during the first 100 cycles.

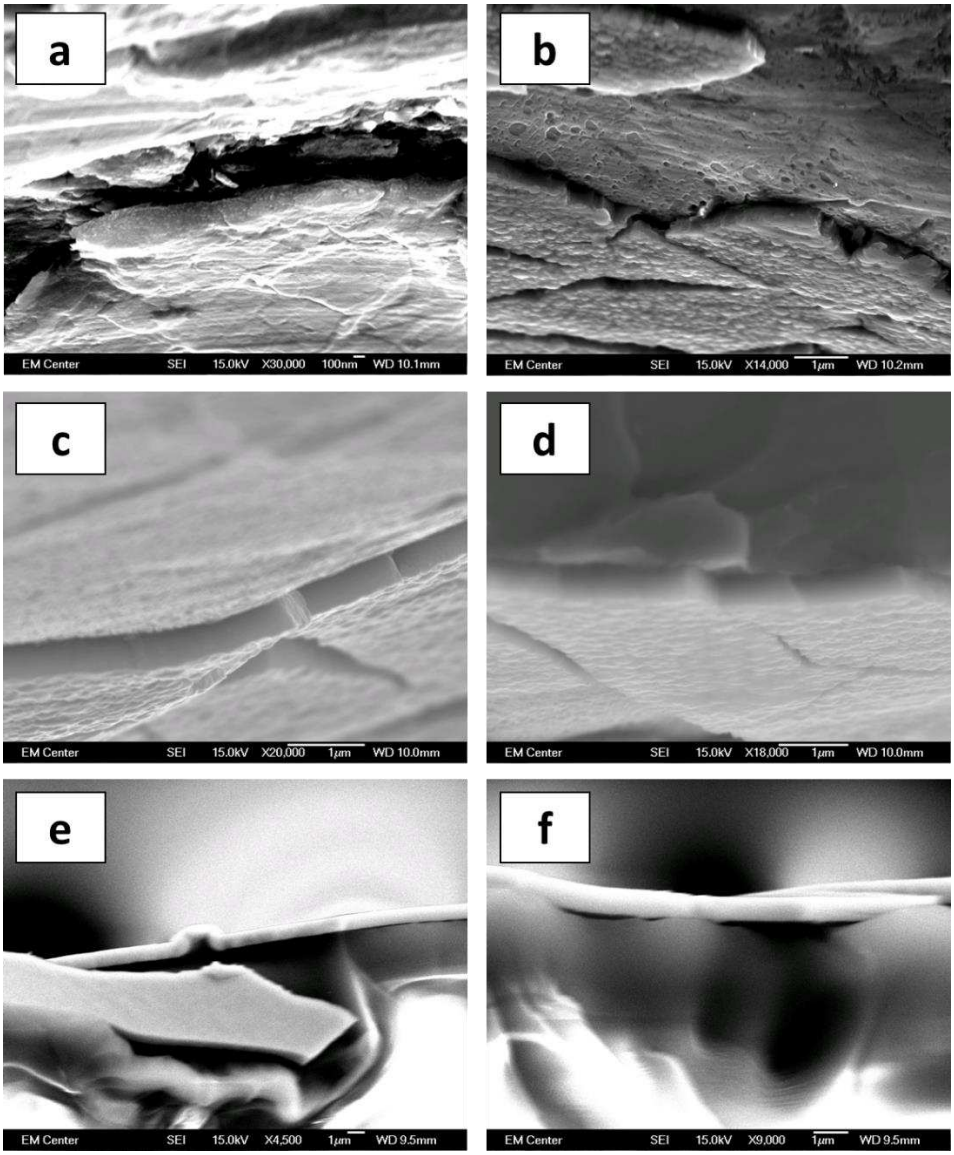

Figure S5.7. Cross-section scanning electron microscopy images of Zinc-antimony alloy films deposited from a solution of 20 mM ZnCl2, 30 mM SbCl3, 200 mM sodium gluconate at pH = 7.0 and -1.60 V v. SCE for (a,b) 120 seconds, (c,d) 360 second, and (e,f) 600 seconds. The films appear to be smooth and have good thickness homogeneity. Samples were prepared by cutting the film and substrate using surgical scissors, except for the 600 second samples (e,f) which were delaminated using Crystalbond™ 505 and mounted in a specimen cross-section holder.

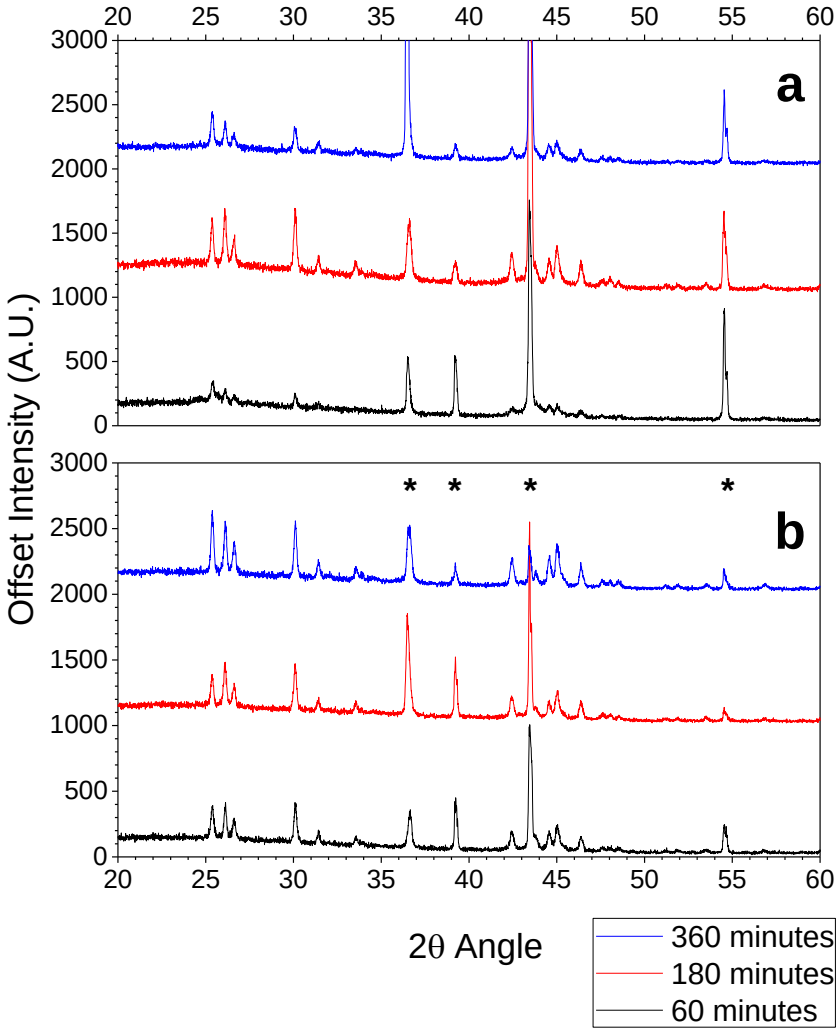

Figure S5.8. Glancing incident X-ray diffraction patterns of (a) 2 minute and (b) 10 minute depositions from 20 mM $ZnCl_2$ deposition solution annealed at 300 °C for 1, 3, and 6 hours. For 2 minute depositions, annealing for 3 hours is optimal, while longer annealing times weaken the Zn_4Sb_3 signal and strengthen signal from Zn (zinc peaks marked by asterisks). For thick substrates, 6 hours shows the lowest intensity of Zn metal and highly crystalline Zn_4Sb_3, indicating a thick, crystalline film of Zn_4Sb_3.

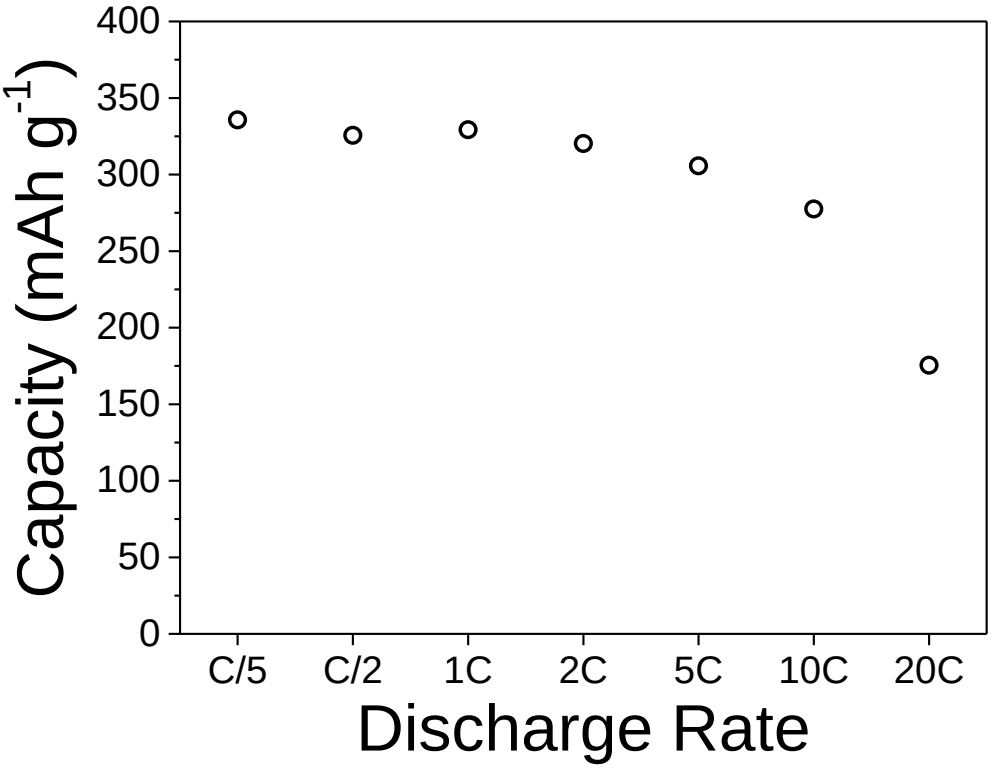

Figure S5.9. Capacity as a function of discharge rate (desodiation) of a Zn_4Sb_3 thin film electrode deposited for 240 s from 20 mM $ZnCl_2$ deposition solution and annealed at 300 °C for 3 hours under argon. The charge rate was C/10 for all cycles, and the capacities were measured after cycling at C/10 for five cycles to condition the electrode. The C-rate refers to the amount of charge delivered per hour of testing, with C/5 taking five hours to deliver one half cycle and only 3 minutes for one half cycle at a 20 C rate. The reaction rate of these thin (estimated 300-350 nm thick) Zn_4Sb_3 films are very fast. It should be noted that in a thick film or for large particles, bulk diffusion is expected to limit the rate to much slower speeds than can be achieved with these thin films.

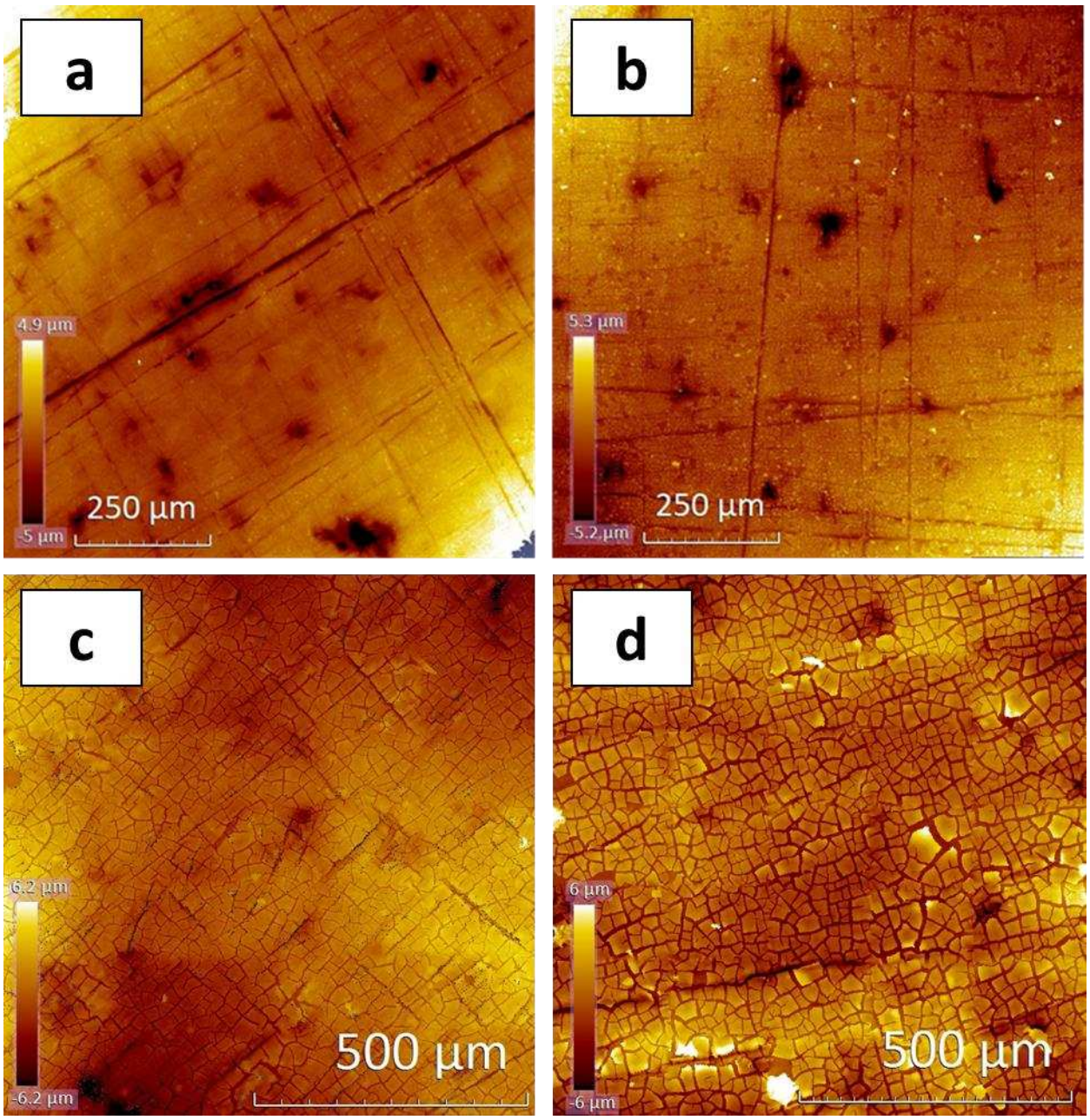

Figure S5.10. Optical profilometry images of Zn_4Sb_3 films deposited for 4 min (top) or 8 minutes (bottom) and cycled at a C/5 rate for 1 (left) and 10 (right) cycles. All images are approximately 1 mm2 taken from representative macroscopic areas of the electrode surface. Note that the scale is not consistent between samples. While thin Zn_4Sb_3 films don't crack significantly during the first 10 cycles, they develop into 5-10 µm diameter particles. In contrast, thicker Zn_4Sb_3 films show significant fracturing after even just one cycle, and develop into much larger particles of 30-60 µm by the tenth cycle. These results indicate that nanometer-scale Zn_4Sb_3 particles in the 200 – 500 nm range should achieve stable morphology.

The authors would like to gratefully acknowledge the assistance of CSU staff scientists Dr. Brian Newell with XRD experiments and Dr. Pat McCurdy with SEM experiments.

REFERENCES

1. Chevrier, V. L.; Ceder, G. Challenges for Na-ion Negative Electrodes. *J. Electrochem. Soc.* **2011**, *158*, A1011-A1014.

2. Darwiche, A.; Marino, C.; Sougrati, M. T.; Fraisse, B.; Stievano, L.; Monconduit, L. Better Cycling Performances of Bulk Sb in Na-Ion Batteries Compared to Li-Ion Systems: An Unexpected Electrochemical Mechanism. *J. Am. Chem. Soc.* **2012**, *134*, 20805-20811.

3. Hou, H.; Jing, M.; Yang, Y.; Zhu, Y.; Fang, L.; Song, W.; Pan, C.; Yang, X.; Ji, X. Sodium/Lithium Storage Behavior of Antimony Hollow Nanospheres for Rechargeable Batteries. *ACS Appl. Mater. Interfaces* **2014**, *6*, 16189-16196.

4. He, M.; Kravchyk, K.; Walter, M.; Kovalenko, M. V. Monodisperse Antimony Nanocrystals for High-Rate Li-ion and Na-ion Battery Anodes: Nano versus Bulk. *Nano Lett.* **2014**, *14*, 1255-1262.

5. Baggetto, L.; Ganesh, P.; Sun, C.-N.; Meisner, R. A.; Zawodzinski, T. A.; Veith, G. M. Intrinsic Thermodynamic and Kinetic Properties of Sb Electrodes for Li-ion and Na-ion Batteries: Experiment and Theory. *J. Mater. Chem. A* **2013**, *1*, 7985-7994.

6. Qian, J.; Chen, Y.; Wu, L.; Cao, Y.; Ai, X.; Yang, H. High Capacity Na-storage and Superior Cyclability of Nanocomposite Sb/C Anode for Na-ion Batteries. *Chem. Commun.* **2012**, *48*, 7070-7072.

7. Baggetto, L.; Ganesh, P.; Sun, C.-N.; Meisner, R. A.; Zawodzinski, T.; Veith, G. M., Intrinsic Thermodynamic and Kinetic Properties of Sb Electrodes for Li-ion and Na-ion Batteries: Experiment and Theory. *J. Mater. Chem. A* **2013**, *1*, 7985-7994.

8. Sun, Q.; Ren, Q.-Q.; Li, H.; Fu, Z.-W. High capacity Sb2O4 Thin Film Electrodes for Rechargeable Sodium Battery. *Electrochem. Commun.* **2011**, *13*, 1462-1464.

9. Darwiche, A.; Sougrati, M. T.; Fraisse, B.; Stievano, L.; Monconduit, L. Facile Synthesis and Long Cycle Life of SnSb as Negative Electrode Material for Na-ion Batteries. *Electrochem. Commun.* **2013**, *32*, 18-21.

10. Xiao, L.; Cao, Y.; Xiao, J.; Wang, W.; Kovarik, L.; Nie, Z.; Liu, J. High Capacity, Reversible Alloying Reactions in SnSb/C Nanocomposites for Na-ion battery Applications. *Chem. Commun.* **2012**, *48*, 3321-3323.

11. Baggetto, L.; Allcorn, E.; Manthiram, A.; Veith, G. M. Cu2Sb Thin Films as Anode for Na-ion Batteries. *Electrochem. Commun.* **2013**, *27*, 168-171.

12. Baggetto, L.; Jumas, J.-C.; Gorka, J.; Bridges, C. A.; Veith, G. M. Predictions of Particle Size and Lattice Diffusion Pathway Requirements for Sodium-ion Anodes using η-Cu6Sn5 Thin Films as a Model System. *Phys. Chem. Chem. Phys.* **2013**, *15*, 10885-10894.

13. Wu, L.; Pei, F.; Mao, R.; Wu, F.; Wu, Y.; Qian, J.; Cao, Y.; Ai, X.; Yang, H. SiC-Sb-C Nanocomposites as High-Capacity and Cycling-Stable Anode for Sodium-ion Batteries. *Electrochim. Acta* **2012**, *87*, 41-45.

14. Kim, I. T.; Allcorn, E.; Manthiram, A. High-Performance MxSb–Al2O3–C (M= Fe, Ni, and Cu) Nanocomposite-Alloy Anodes for Sodium-Ion Batteries. Energy Technology 2013, 1, 319-326.

15. Baggetto, L.; Allcorn, E.; Unocic, R. R.; Manthiram, A.; Veith, G. M. Mo3Sb7 as a Very Fast Anode Material for Lithium-ion and Sodium-ion Batteries. J. Mater. Chem. A 2013, 1, 11163-11169.

16. Liu, P.; Guo, X.; Huang, H.; Yang, Q.; Tong, Y.; Hope, G. A. The Growth of Zn–Sb Nanowires by Heat Treatment of Zn–Sb Nanoparticles Obtained by Electrodeposition. Adv. Mater. 2006, 18, 1873-1876.

CHAPTER 6: COPPER ANTIMONIDE NANOWIRE ARRAY LITHIUM ION ANODES STABILIZED BY ELECTROLYTE ADDITIVES

The following chapter has been published as an article in the journal *ACS Applied Materials and Interfaces*. All experimental work and manuscript preparation were performed by Everett D. Jackson with intellectual contributions and editing help from Amy L. Prieto.

6.1 Introduction

Lithium ion batteries are the current leading electrical energy storage device for high energy density applications, such as mobile electronics and transportation. The current battery architecture relies on two materials which can intercalate lithium ions at substantially different electrode potentials to provide a large cell potential and high reversibility. Currently, the state of the art electrode materials for lithium ion batteries are graphite for the anode and a lithium metal oxide framework or layered structure for the cathode, yielding high full cell voltages, good reversible capacities, and long cycle life. Despite these advantages, the current lithium ion battery possesses low energy and power density compared to fuels. Next generation applications which include electric vehicles, grid energy storage, and powerful portable electronics require significant improvements in battery performance.

The energy density of a lithium ion battery can be improved by replacing one of the standard active materials with a new material that is capable of storing more lithium ions per unit volume and mass.[1] In order to achieve this, the material must display high electrochemical reversibility, a reasonably stable voltage, low voltage hysteresis, and low reactivity towards the electrolyte. Anode alloys such as Si, Sn, Sb, Al, etc. have been studied for this purpose since the discovery of electrochemical lithium alloying at room temperature.[2] These alloy materials display

relatively low voltage hysteresis, stable voltage profiles, and exceptionally high reversible capacities.[3] Nevertheless, they exhibit high reactivity towards typical lithium ion battery organic solvents used in the electrolyte, large volume changes causing material instability, and incomplete reversibility in some situations. Overcoming these limitations requires rational electrode design and careful study of methods to eliminate the reactivity of the alloy surface towards the electrolyte.

Nanowire arrays are an interesting alternative to the conventional particle based composite porous electrode used in modern lithium ion batteries. Unlike a conventional porous electrode, nanowires have facile one-dimensional diffusion of lithium ions through the pore space in the structure, and short solid state diffusion lengths within the material.[4-5] The advantage of short solid state diffusion length is coupled with a large surface area to volume ratio for the active material. This results in exposure of a large amount of material to the liquid electrolyte, resulting in excessive decomposition of the electrolyte and poor coulombic efficiency. It is for this reason that this type of electrode is advantageous for studying surface processes because the decomposition comes from the active material, and is not influenced by polymer and carbon additives typically used in porous lithium ion battery electrodes.

Herein we present nanowire arrays of CuSb alloy produced by electrodeposition within the pores of nanoporous alumina oxide templates. While this method has been used to produce nanowire array electrodes from similar materials such as Cu_2Sb[6], $CoSb$[7], Ni_5Sb_2[8], and Cu/Cu_2O[9], the antimony based nanowires typically show short cycle lives of only 5-50 cycles. We show that the limited performance of this material comes primarily from unstable surface chemistry that causes the formation of a thick layer of surface electrolyte interface (SEI) material that is constituted by organic and inorganic decomposition products from the electrolyte. In order to overcome this limitation, we have tested two common electrolyte additives, fluoroethylene

carbonate (FEC) and vinyl carbonate (VC) to improve the cycle lifetime of the nanowire electrodes. It is shown that for this system, VC enables a fivefold improvement in the half cell lifetime and shows definitively that further SEI stabilization is key to utilizing this material in a lithium ion battery.

6.2 Experimental

The $Cu_{11}Sb_3$ electrodeposition solution was prepared based on a previous report[10]. The solution consisted of 0.4 M citric acid (99.5% Sigma), 0.25 M antimony(III) oxide nanopowder (99.9%, Sigma), and 0.08 M Cu(II) nitrate hemipentahydrate (99.9%, Sigma). The solution was prepared by dissolving the citric acid in Millipore water (18 MΩ cm) followed by addition of the antimony oxide. After stirring for 24 hours, the copper nitrate was added and the pH raised to 6 by addition of potassium hydroxide (ACS certified, Fisher).

Anodic alumina oxide membranes (Whatman, 100 nm, 13 mm) were used as templates for nanowire growth. The templates were coated with a layer of 15 nm Cr and 300 nm Cu in a thermal evaporator on one side. A nickel supporting layer and base nanowire segments were then applied by electroplating onto the evaporated copper coating in a jacketed beaker at 50 °C using a bright nickel citrate plating solution at -1.0 V vs. a saturated calomel reference electrode (SCE) and nickel foil counter electrode (99.9%, Sigma). The electroplating solution was prepared by mixing 280 g nickel sulfate hexahydrate (ACS reagent, Sigma), 45 g nickel chloride hexahydrate (99.3%, Alfa), 2.0g sodium saccharine hydrate (99%, Acros), and 0.2 g 2-butyne-1,4-diol (99%, Sigma) in 1 L of Millipore water.[11]

Nanowires were synthesized by electrodeposition into prepared templates in a specialized electrodeposition cell. The cell consists of a spring-loaded back contact and O-ring seal applied

against a PTFE cap to limit the electroactive area to 0.42 cm^2. The deposition cell used a SCE reference and platinum mesh counter electrode. All depositions were performed at -1.05 V v. SCE at room temperature for 10-60 minutes. Following deposition, the template was removed by soaking in 1.0 M NaOH for 60 minutes, followed by rinsing in DI water and then isopropyl alcohol. The isopropyl alcohol was removed in a critical point CO_2 dryer to prevent nanowire aggregation.

Nanowire electrochemical testing was performed in 0.5-inch diameter Swagelok PFA cells. The cells were assembled in an argon glovebox with <0.5 ppm O_2. Lithium metal was used for the counter electrode and two pieces of polypropylene separator (MTI Corp.) sandwiching a glass microfiber filter (Whatman) were used as a separator. The cells were filled with 0.2 mL of 1.0M $LiPF_6$ in 3:7 EC:DEC by volume (BASF). Where designated, 5% vinylene carbonate (99%, Sigma) or fluoroethylene carbonate (99%, Sigma) were added to the electrolyte.

6.3 Results and Discussion

Previously, we have shown that copper-antimony alloys can be electrodeposited from an aqueous solution of $Cu(NO_3)_2$, Sb_2O_3, and citric acid under slightly acidic conditions.[10] This material has been investigated as a potential lithium ion and sodium ion battery anode candidate by several groups in the form of thin films, porous electrodes, and nanowires.[6, 12-14] Detailed evaluations of the reaction pathway and dynamics of this material during cycling have also been conducted.[15-16] This material is of particular interest due to a smaller volume change during cycling compared to typical alloying materials. Nevertheless, despite the reduced pulverization caused by the lower volume change, and even when it is eliminated by use of nanowire array electrodes, it has been difficult to achieve long cycle lives with this material.

Current methods of synthesizing nanowire arrays of Cu_2Sb and related materials using the alumina templated method involve the deposition of copper nanorods, followed by the deposition of active material, and generally a post-annealing step to homogenize the material.[17-18] This method does not allow for the precise determination of the active material morphology and composition as the post deposition process and annealing step do not result in a fully homogenous nanowire. To overcome this issue, we have modified this synthesis to yield two segment nanowires that consist of a supporting inactive material base and a uniform end of active material produced by single-step electrodeposition. Using this technique, we are able to produce nanowires of homogenous active material with long aspect ratios and morphology that is defined exactly by the alumina template used. For this study, we have used 100-nm pore diameter Whatman Anopore membrane discs to test this method of producing ordered nanowire arrays.

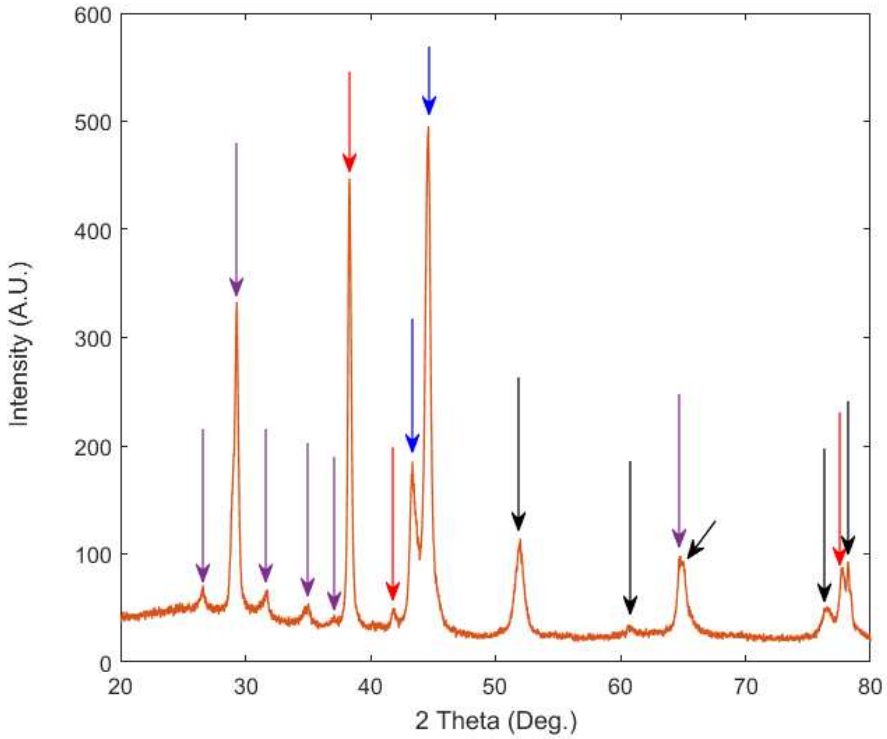

Figure 6.1. Glancing angle x-ray diffraction of the nickel base nanowires and $Cu_{11}Sb_3$ nanowire arrays taken at 10° incident angle. Arrows mark the following phases: purple = Cu_2Sb, red = $Cu_{11}Sb_3$, blue = mixed, black = background).

Glancing angle x-ray diffraction (Figure 6.1) of the nanowire arrays show that the as-synthesized nanowires consists of a mixture of both the $Cu_{11}Sb_3$ and Cu_2Sb phase. Significant preferred growth orientation can be identified, with the Cu_2Sb phase growing along the [001] axis as shown by the prominence of the (002) peak near 29° and the (004) peak at 61°. The (003) peak at 43° is convoluted with the strong reflections resulting from the Cu_2Sb (112), $Cu_{11}Sb_3$ (171), $Cu_{11}Sb_3$ (102) and Ni (111) planes. The $Cu_{11}Sb_3$ phase can be identified from the strong peak at 38° corresponding to either the (002) or (071) plane. A second minor reflection from the $Cu_{11}Sb_3$ (200) plane at 42° is apparent. Additional peaks at 51° and 75° are from the Ni nanowires segments, and the additional peaks marked in black at 65° and 78° are from the aluminum sample holder.

During cycling, the $Cu_{11}Sb_3$ phase is expected to undergo conversion to Cu_2Sb, as has been reported for thin films of "Cu_9Sb_2".[12] The excess copper is extruded during cycling to form a copper matrix that is expected to increase the electrical conductivity of the nanowire and reduce mechanical degradation, but not reform the copper rich phase after full delithiation. This form of copper rich CuSb alloy provides the potential for a single material system that provides sufficient mechanical integrity, electronic conductivity, and lithium capacity to make a useful battery material without further additives or modifications.

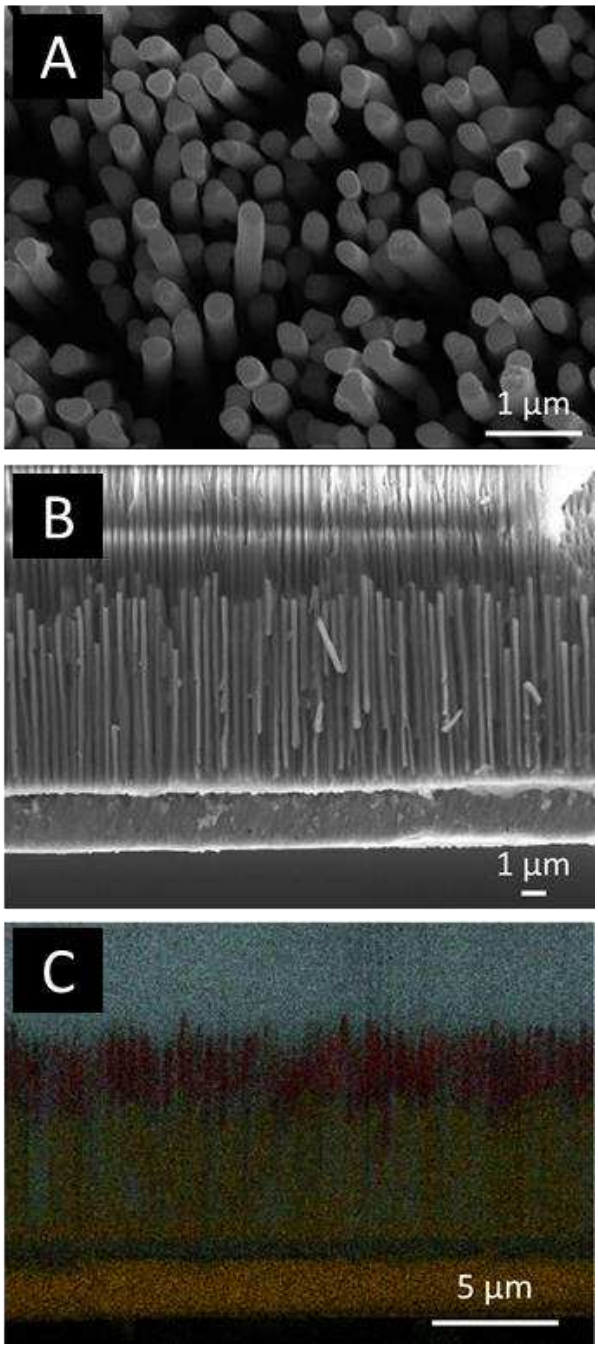

Figure 6.2. Scanning electron microscope analysis of the copper antimonide nanowire arrays. (A) Top view of 9 µm nanowires of CuSb alloy on 5 µm nickel base. (B) Cross section of nanowires before dissolution of the alumina template. (C) EDS map of a nanowire cross-section used to determine active material nanowire length.

Freestanding nanowires with minimal aggregation can be produced with lengths of up to the length limit of the template at ~10 μm CuSb on top of 5 μm Ni base nanowires (Figure 6.2a-b). We have found that it is necessary to use a critical carbon dioxide drying step to prevent aggregation for nanowires exceeding 15 μm in total length for this material and nanowire diameter. Longer nanowires are not possible with these particular templates due to the existence of large defects that cause erratic growth at longer deposition times. Cross-sectional analysis shows good length homogeneity up to ~10 μm CuSb nanowire length, and was used to estimate the actual electrode active material volume (Figure 6.2c). Based on cross-sectional analysis, the nanowires appear to grow at approximately linear rate of 0.3 μm min^{-1}. As a result, it is possible to control the amount of active material loading and the nanowire aspect ratio using this method. Pulse electrodeposition was not found to increase the nanowire length uniformity, although a five-minute soak in the deposition solution prior to the start of deposition greatly improves length uniformity by allowing the deposition solution to fully infiltrate the template pores prior to the start of the electrodeposition process. Transmission electron microscopy was also performed on the nanowires to determine their structure (Figure 6.3). The nanowires show good smoothness with some occasional growths on the nanowire surface, probably due to defects in the original template. The end of the nanowire shows many small crystallites as expected for an electrodeposited nanowire. High resolution TEM reveals well-ordered lattice fringes and selected area diffraction shows high local crystallinity and a mixture of Cu_2Sb and $Cu_{11}Sb_3$ phases.

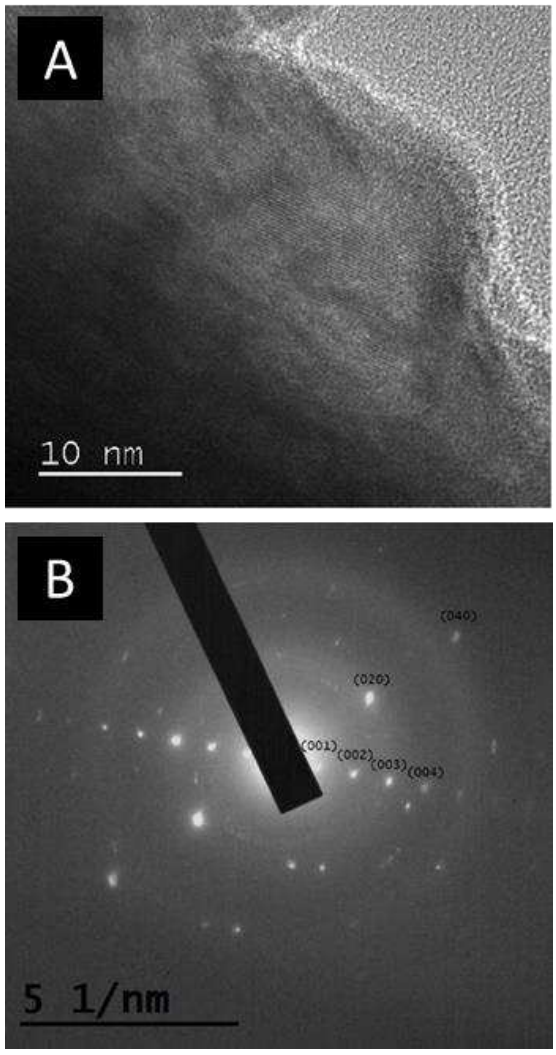

Figure 6.3. Transmission electron microscope images of (a) edge of the synthesized CuSb nanowires, and (b) SAED pattern showing two crystallites of Cu_2Sb with corresponding planes labeled.

Electrochemical characterization of the nanowire arrays was conducted using lithium half cells (Figure 6.4a). Nanowire arrays consisting of 9 μm lengths of copper antimonide show high areal reversible capacities of 0.6 – 0.8 mAh cm^{-2}. In comparison, films begin to show pulverization at thickness of less than 1 μm, limiting their effective capacity to only 10^{-2}-10^{-3} mAh cm^{-2}. Given an overall length of 25 μm including the nickel nanowire base and backing layer, this provides an

overall volumetric capacity of 240-320 mAh cm^{-3}, and a volumetric capacity of 600-800 mAh cm^{-3} for the Cu_2Sb nanowire volume. The porosity of these templates is estimated at 35%, giving an active material volumetric density of 1800-2400 mAh cm^{-3} (based on the initial material volume). This is within the bounds of the two phases present, which possess a theoretical volumetric capacity of 1884 mAh cm^{-3} for $Cu_{11}Sb_3$ and 2731 mAh cm^{-3} for Cu_2Sb, as calculated using the crystallographic density of the respective compounds. Although we are able to obtain superior areal capacities to thin film type electrodes, the capacity is limited in this study due to the asymmetric templates used. Growing the nanowires longer than a total length of ~20 μm results in large numbers of defects and poor quality arrays. Higher quality symmetric templates are commercially available in thicknesses of up to 100 μm, indicating that areal capacities of about 5 mAh cm^{-2} can be realized using this synthetic method. The nanowire array morphology is therefore capable of matching the areal and volumetric capacities of commercialized porous electrodes. Nevertheless, the as-synthesized nanowires tested with a conventional carbonate electrolyte still shows fast capacity fade after only 30 cycles. This fade is accompanied by a low coulombic efficiency of 94-96 %, suggesting that the nanowires promote high reactivity of the electrolyte, and surface instability is therefore the cause of the short cycle life in these electrodes.

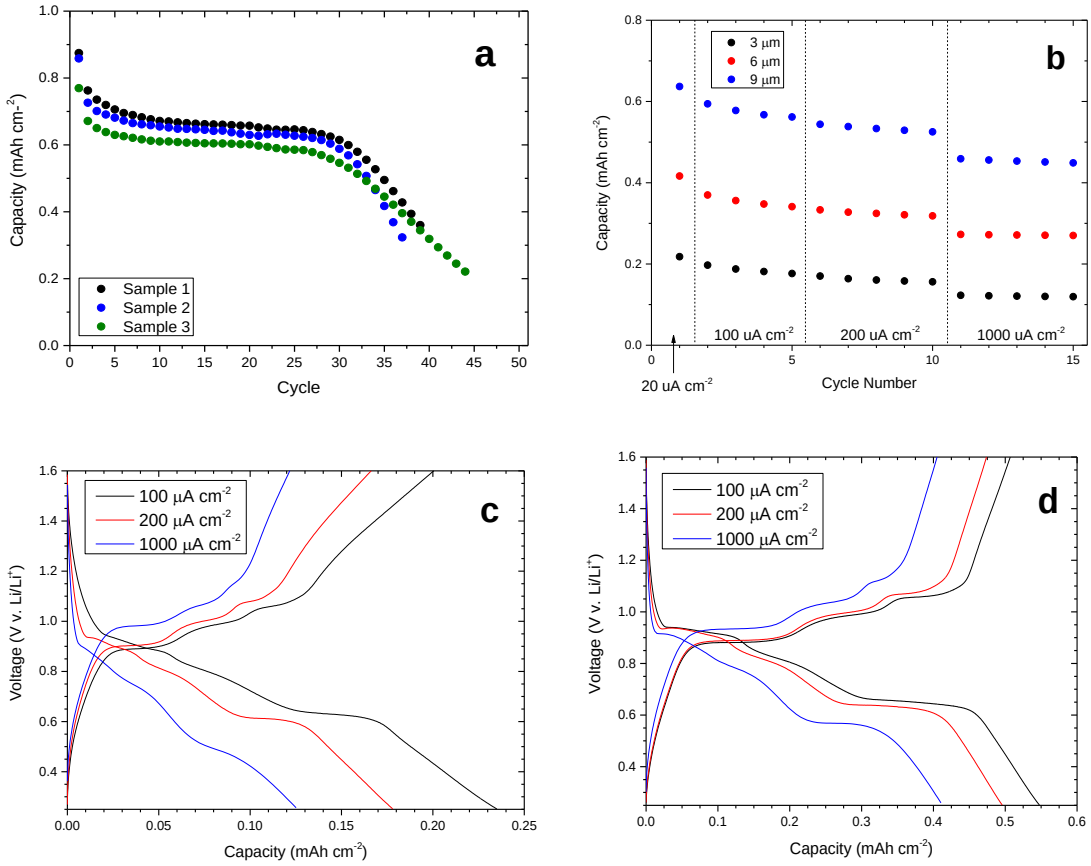

Figure 6.4. Early cycle performance of a set of three nanowire arrays consisting of 9 µm CuSb segments cycled in a lithium half-cell between 1.60 and 0.25 V v. Li/Li^+ (a). Rate performance of the CuSb nanowire arrays at current densities of 20-1000 µA cm^{-2} between 1.60 and 0.25 V v. Li/Li^+ (b). Charge-discharge curves for the 3 µm (c) and 9 µm (d) nanowire electrode at different current densities. Currents and capacity are given in terms of footprint area.

The effect of nanowire length on electrochemical performance was tested by performing variable rate electrochemical cycling on nanowire arrays with CuSb segments approximately 3, 6, and 9 µm in length (Figure 6.4b). Consistent with the linear increase in nanowire length with deposition time, a linear increase in nanowire array capacity is obtained as a function of nanowire length. In the experiment shown in figure 4a with a slow initial rate of 20 µA cm^{-2}, the 3, 6, and 9 µm nanowires give capacities of 218, 416, and 637 µAh cm^{-2}, respectively. In addition, the relative drop in capacity as a function of cycle rate is also very consistent, where the 3, 6, and 9 µm

nanowires show a drop in capacity of 21.4%, 14.5%, and 13.2% between 200 μA cm^{-2} and 1000 μA cm^{-2}, respectively. The difference between the magnitudes of capacity loss exhibited can be attributed to the increased relative rate at each given current density, where at 1000 μA cm^{-2} the 3 μm nanowires are at a 5C rate while the 9 μm nanowires are only at a 2C rate. These relationships show that the nanowires display the expected linear relationship with capacity as a function of length, showing full utilization of the nanowire electrode. Furthermore, the rate properties are dominated by nanowire diameter and the active material properties, and not greatly influenced by nanowire length.

Evaluation of the charge-discharge profiles for 3 μm and 9 μm nanowires show three charge and three discharge plateaus, indicative of the reversible Cu_2Sb reaction (Figure 6.4c-d). Although the initial nanowires are a mixture of the copper-rich $Cu_{11}Sb_3$ and Cu_2Sb phases, previous reports have shown that copper-rich Cu_9Sb_2 electrochemically converts to Cu_2Sb during cycling and the excess copper becomes a bystander after the conversion.[12] The mechanism of this reaction is well understood and a thorough discussion can be found in other reports.[15-16, 19] Little additional polarization is observed until above a 1C rate, indicating good rate performance as expected for the nanostructured electrode.

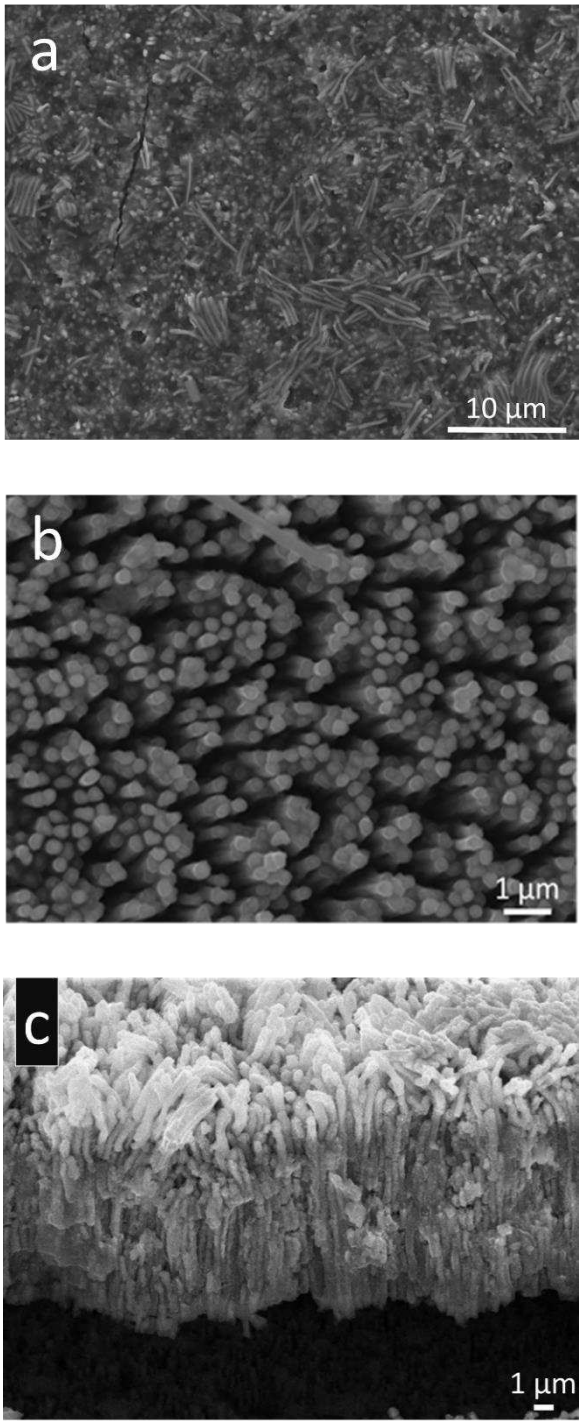

Figure 6.5. Scanning electron microscopy of a CuSb nanowire electrode after 50 cycles. Images were taken of (a) the top of the electrode, (b) of the nickel base nanowires, and (c) the side of the CuSb nanowires.

The porosity of the nanowire array electrodes prevents pulverization of the active material, leading to excellent short term cycling stability. Despite the large amount of active material present in the electrode and a large active material volume change of approximately 80%, the nanowires do not display any loss of active material. Although pulverization is effectively eliminated, the nanowire electrodes undergo a sudden loss of capacity starting at 30 cycles and lose nearly all reversible capacity by cycle 50. We determined that this is due to an unstable surface electrolyte interface layer (SEI) that impedes the transport of lithium ions in and out of the nanowires. The surface morphology of the nanowire array is changed dramatically after 100 cycles (Figure 6.5a). The formation of an extended film of SEI is readily visible and no void space can be seen by electron microscopy. In contrast, nickel nanowire segments do not show complete filling (Figure 6.5b). As a result, the SEI overgrowth can be attributed to instability caused by a highly reactive metal alloy surface compounded with large changes in surface area due to active material expansion and contraction. This suggests that surface instability is a critical issue for this material, and is further problematic for high surface nanomaterials using copper antimonide.

Cross-sectional analysis of the cycled nanowire arrays was also performed (Figure 6.5c). The wires have greatly increased surface roughness across the entire length of the active CuSb segments. This confirms that the entire nanowire lengths are being reversibly cycled, consistent with the high practical volumetric capacities obtained from lithium half-cell cycle testing. Additionally, no fracturing of the nanowires along their lengths is observed. We therefore conclude that pulverization is not a factor contributing to the loss of reversible capacity.

To definitively determine the importance of surface stability on the cycle life of the nanowire arrays, we prepared half cells with additions of 5% by volume of either fluoroethylene carbonate (FEC) or vinyl carbonate (VC) to the base ethylene carbonate / diethylene carbonate

electrolyte mixture. These two additives were chosen based on their stabilizing effect in both traditional lithium ion batteries[20] and for other potential high capacity active anode materials such as Sn[21] and Si[22-23]. In addition, these additives have been shown to be effective for Cu_2Sb-Al_2O_3-C composite electrodes prepared by ball milling.[24] In contrast to this previous study, there are no additives to the active material that can complicate analyses of the SEI, as all organic material must originate from the SEI and not any component of the original electrode.

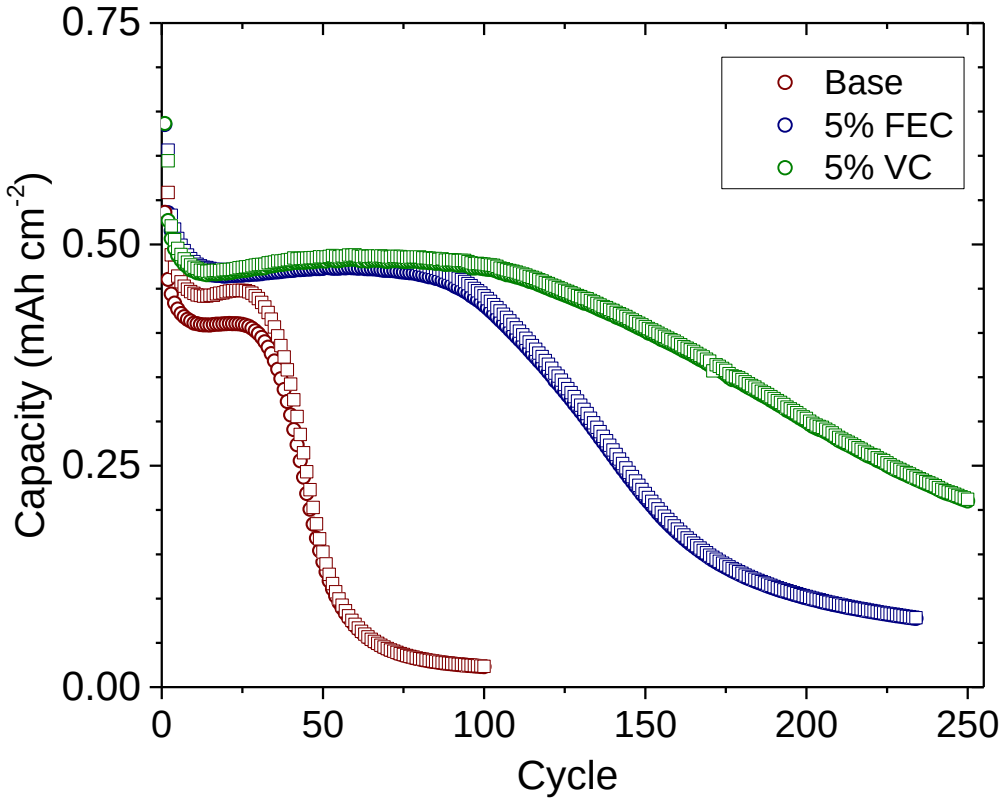

Figure 6.6. Cycle capacities of 9 µm nanowire arrays cycled at 100 µA cm^{-2} between 0.10 and 1.60 V v. Li/Li^+ with or without either 5% FEC and VC as an electrolyte additive.

Half-cell testing of nanowire electrodes with FEC and VC show exceptional increases in cycle life over the additive-free electrolyte (Figure 6.6). While onset of electrode failure normally

occurs at about 30 cycles for the base electrolyte mixture, FEC increases the cycle life to about 100 cycles and VC increases the lifetime even further to almost 150 cycles. In addition, the capacity fade is slowed dramatically with VC, leading to a slow fade in capacity that extends over an additional 100 cycles. The coulombic efficiency is also improved by FEC (97-98%) and VC (98-99%) compared to the base electrolyte (95-96%), as expected for an electrode with a more stable SEI layer. The dramatic increase in coulombic efficiency and cycle life using VC and FEC confirms that surface instability is the major contributor to loss of reversible capacity. Nevertheless, neither additive is capable of extending the cycle life to the thousands of cycles necessary for a practical battery or meeting the requirement of >99.99% coulombic efficiency required for lithium ion battery electrodes.

To better elucidate the influence of the electrolyte additive on the nanowire array performance, we performed ex-situ instrumental analysis. Scanning electron microscopy of nanowire array electrodes were taken after 100 cycles and after 250 cycles (Figure 6.7). After 100 cycles, the nanowires show visible roughening as a result of repeated volume changes during electrochemical cycling. Despite this, the nanowires remain separate from each other and do not show signs of electrochemical welding or significant axial pulverization. The SEI layer at this stage is thin and conformal, suggesting limited degradation of the electrolyte. This can be attributed to an effective SEI layer formed by the VC and FEC additives, preventing further reduction of the carbonate electrolyte. As a result, lithium ion transport is not impeded as the electrolyte can penetrate into the bulk of the electrode, leading to good capacity retention.

After 250 cycles, most of the capacity is lost for the nanowire arrays cycled even with FEC or VC additive. The resulting electrode morphology is again coated with a thick SEI layer, similar to that seen after full loss of capacity with the base electrolyte. Despite the similarity, significant

morphological differences are apparent between the electrodes cycles with all three of the electrolyte formulations. Notably, the electrode cycled with FEC additive has large pores several microns in diameter across the entire electrode surface. These features contain smaller internal pores that likely allow limited electrolyte penetration, leading to the slower capacity fade and increased overall electrode cycle life. In contrast, no large porous features are observed for the electrode cycled with VC additive. Despite this, the nanowires are more clearly visible than the electrode cycled with no additives even after 250 cycles. This confirms that the SEI layer formed by VC is thinner and has superior passivating properties to the other carbonate species studied here. Further stability is still necessary to achieve the thousands of cycles necessary to make a copper antimonide electrode viable.

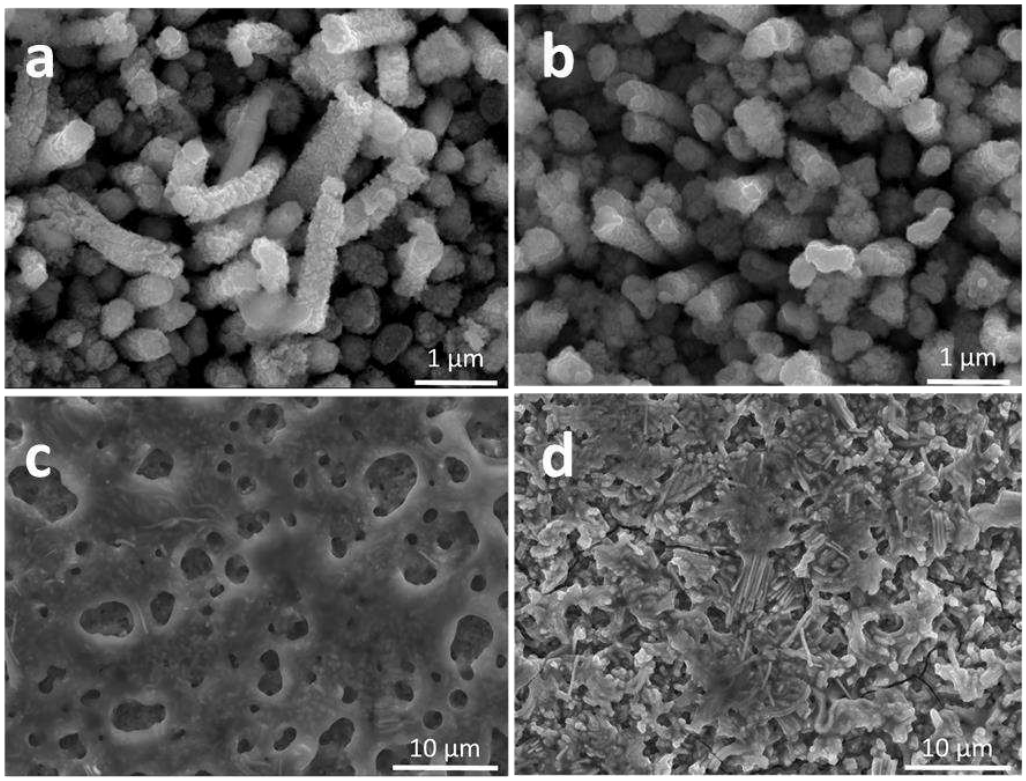

Figure 6.7. SEM images of the copper antimonide nanowire arrays after 100 cycles with (a) 5% FEC, (b) 5% VC and 250 cycles for (c) 5% FEC, and (d) 5% VC.

To determine the effects of the additives on the chemical composition of the SEI layer, ex-situ x-ray photoelectron spectroscopy (XPS) was conducted on the electrodes after either 100 cycles for the base electrolyte or 250 cycles for electrolyte with 5% FEC or 5% VC additive (Figure 6.8). The electrodes were thoroughly washed and dried prior to measurement, and any signal from the $LiPF_6$ salt must come from salt trapped within the SEI. Existing reports have shown that the nature of the SEI, including elemental composition and chemical nature, vary greatly depending on the electrolyte and the active material on which it forms.[25-28] We have found the CuSb nanowires form an SEI layer that is carbonate rich when cycled without electrolyte additives. This is unusual compared to typical alloy anode SEI films that tend to be rich in alkyl and ethereal species.[29-30] Both FEC and VC appear to increase the alkyl character of the SEI layer, likely leading to the improved electrochemical performance.

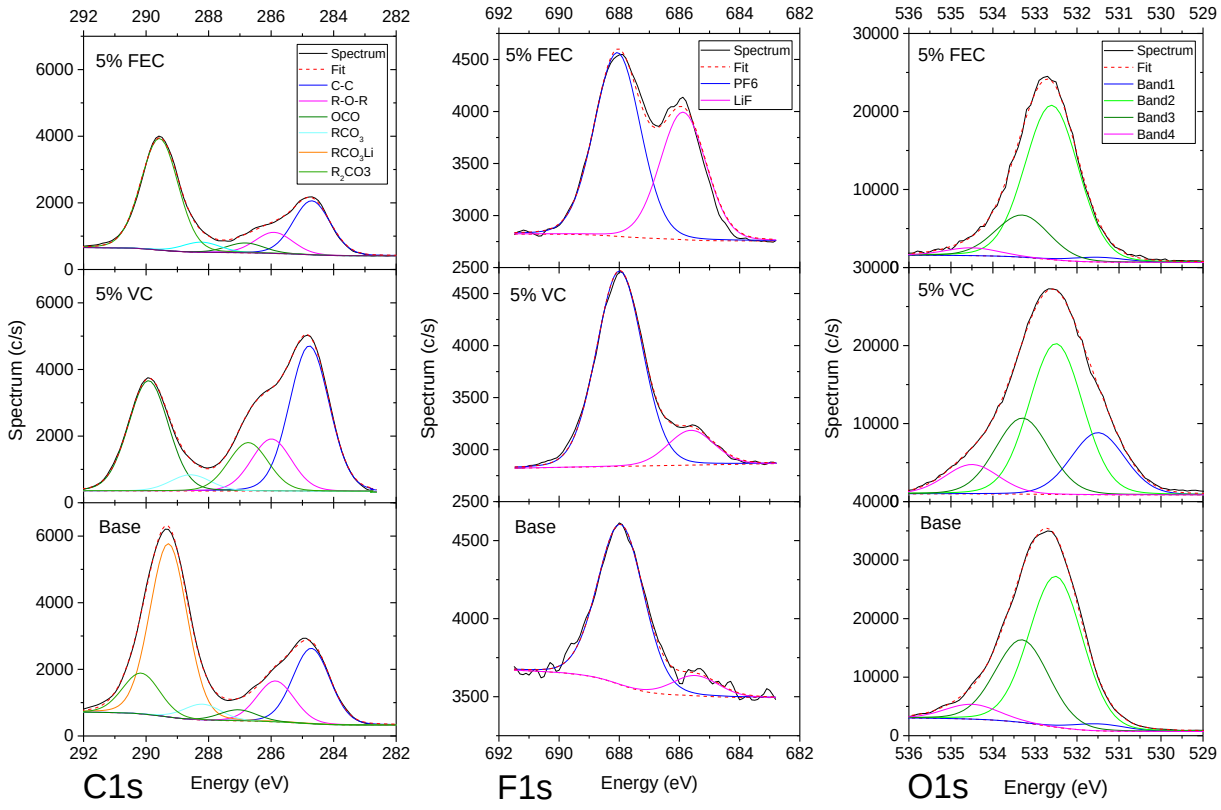

Figure 6.8. XPS Analysis of nanowire arrays after cycling at 100 µA to 100 cycles (EC:DEC) or 250 cycles (EC:DEC with either VC or FEC). From left to right: C 1s, F 1s, and O 1s.

The carbon 1s XPS spectrum consists of many peaks corresponding to alkyl species at 285 eV, ethereal and alkoxy species at 286-287 eV, and carbonate species at 288-292 eV. The base electrolyte without additives favors a carbonate-rich SEI layer with more than half the carbon signal coming from the 288-292 eV region. This suggests that uncontrolled polycarbonate formation is occurring, leading to the thick polymer layer that inhibits lithium diffusion. In contrast, VC promotes an SEI that is significantly richer in alkyl, ethereal, and alkoxy carbon species. Of the two peaks corresponding to carbonate species, it should be noted that the major peak that is present in the base electrolyte is almost entirely eliminated by the VC additive, leaving only the higher energy peak. This suggests that the identity of the polymeric carbonates in the SEI

are different when formed with VC as opposed to EC or DEC. The additive FEC also shows the elimination of one of the two carbonate XPS peaks. It is apparent that elimination of multiple species of polycarbonates in the SEI layer is correlated to an increase in SEI stability.

Evaluation of the fluorine 1s spectrum shows the presence of $LiPF_6$ and LiF in all of the electrolyte formulations. Although there is no major difference in the fluorine speciation when VC is used as an additive, the use of FEC results in the formation of a large amount of LiF. This is expected based on a proposed mechanism for FEC reduction, where FEC releases HF and converts to VC prior to reduction at the electrode surface.[31] The HF released by this reaction is then consumed by lithium alkoxides to form LiF. This mechanism promotes an SEI similar to VC while additionally eliminating basic lithium alkoxide species. Although the mechanism is different between the two additives, this is consistent with a large increase in electrochemical performance for both additives.

The oxygen 1s spectrum shows four different species corresponding to alkoxides, ethers, carbonates, and polycarbonates. The peaks for ethers and carbonates dominate the spectrum for all three electrolyte mixtures, although the addition of VC appears to promote the formation of alkoxides and polycarbonate species. This is consistent with the difference between FEC and VC, where FEC consumes the alkoxides to from LiF. Therefore, the existence of alkoxide species do not negatively impact the SEI layer for copper antimonide. A more robust understanding of the decomposition processes and methods to prevent excessive SEI growth are still required.

6.4 Conclusion

Nanoporous alumina templates can be used to produce long aspect ratio nanowires of copper antimonide for use as a lithium ion battery anode. Using a two-step electrodeposition process to

produce a stable nanowire base enables high capacity nanowire arrays to be produced with tunable length. Pulverization is effectively eliminated using this electrode geometry and the rate performance is shown to be largely independent of nanowire length. An unstable electrode surface leads to short cycle lifetimes primarily due to the formation of a thick SEI layer that inhibits lithium diffusion in and out of the electrode. The use of SEI stabilizing additives such as FEC and VC are shown to dramatically improve the performance of these nanowire arrays. The decomposition of the electrolyte is not fully inhibited by these additives, and so further effort towards understanding the decomposition mechanism and methods of stabilizing the electrode surface are needed.

The authors thank Dr. Roy Geiss for assistance with transmission electron microscopy.

REFERENCES

1. Tarascon, J. M.; Armand, M., Issues and challenges facing rechargeable lithium batteries. *Nature* **2001,** *414* (6861), 359-367.

2. Huggins, R. A., Lithium alloy negative electrodes. *Journal of Power Sources* **1999,** *81–82*, 13-19.

3. Obrovac, M. N.; Chevrier, V. L., Alloy Negative Electrodes for Li-Ion Batteries. *Chemical Reviews* **2014,** *114* (23), 11444-11502.

4. Arthur, T. S.; Bates, D. J.; Cirigliano, N.; Johnson, D. C.; Malati, P.; Mosby, J. M.; Perre, E.; Rawls, M. T.; Prieto, A. L.; Dunn, B., Three-dimensional electrodes and battery architectures. *MRS Bulletin* **2011,** *36* (07), 523-531.

5. Rolison, D. R.; Long, J. W.; Lytle, J. C.; Fischer, A. E.; Rhodes, C. P.; McEvoy, T. M.; Bourg, M. E.; Lubers, A. M., Multifunctional 3D nanoarchitectures for energy storage and conversion. *Chemical Society Reviews* **2009,** *38* (1), 226-252.

6. Tan, S.; Perre, E.; Gustafsson, T.; Brandell, D., A solid state 3-D microbattery based on Cu2Sb nanopillar anodes. *Solid State Ionics* **2012,** *225*, 510-512.

7. Yang, Y.-w.; Chen, Y.-b.; Liu, F.; Chen, X.-y.; Wu, Y.-c., Template-based fabrication and electrochemical performance of CoSb nanowire arrays. *Electrochimica Acta* **2011,** *56* (18), 6420-6425.

8. Yang, Y.-w.; Li, T.-y.; Liu, F.; Zhu, W.-b.; Li, X.-l.; Wu, Y.-c.; Kong, M.-g., Electrodeposition of Ni5Sb2 nanowires array and its application as a high-performance anode material for lithium ion batteries. *Microelectronic Engineering* **2013,** *104*, 1-4.

9. Valvo, M.; Rehnlund, D.; Lafont, U.; Hahlin, M.; Edstrom, K.; Nyholm, L., The impact of size effects on the electrochemical behaviour of Cu2O-coated Cu nanopillars for advanced Li-ion microbatteries. *Journal of Materials Chemistry A* **2014,** *2* (25), 9574-9586.

10. Mosby, J. M.; Prieto, A. L., Direct electrodeposition of Cu2Sb for lithium-ion battery anodes. *Journal of the American Chemical Society* **2008,** *130* (32), 10656-10661.

11. Doi, T.; Mizumoto, K.; Tanaka, S.-i.; Yamashita, T., Bright nickel plating from nickel citrate electroplating baths. *Metal Finishing* **2004,** *102* (4), 26-35.

12. Bryngelsson, H.; Eskhult, J.; Nyholm, L.; Edström, K., Thin films of Cu2Sb and Cu9Sb2 as anode materials in Li-ion batteries. *Electrochimica Acta* **2008,** *53* (24), 7226-7234.

13. Perre, E.; Taberna, P. L.; Mazouzi, D.; Poizot, P.; Gustafsson, T.; Edström, K.; Simon, P., Electrodeposited Cu2Sb as anode material for 3-dimensional Li-ion microbatteries. *Journal of Materials Research* **2010,** *25* (08), 1485-1491.

14. Trahey, L.; Kung, H. H.; Thackeray, M. M.; Vaughey, J. T., Effect of Electrode Dimensionality and Morphology on the Performance of Cu2Sb Thin Film Electrodes for Lithium-Ion Batteries. *European Journal of Inorganic Chemistry* **2011,** *2011* (26), 3984-3988.

15. Matsuno, S.; Noji, M.; Kashiwagi, T.; Nakayama, M.; Wakihara, M., Construction of the ternary phase diagram for the Li-Cu-Sb system as the anode material for a lithium ion battery. *The Journal of Physical Chemistry C* **2007,** *111* (20), 7548-7553.

16. Matsuno, S.; Noji, M.; Nakayama, M.; Wakihara, M.; Kobayashi, Y.; Miyashiro, H., Dynamics of Phase Transition in Li–Cu–Sb Anode Material for Rechargeable Lithium Ion Battery. *Journal of The Electrochemical Society* **2008,** *155* (2), A151-A157.

17. Perre, E.; Taberna, P. L.; Mazouzi, D.; Poizot, P.; Gustafsson, T.; Edström, K.; Simon, P., Electrodeposited Cu 2 Sb as anode material for 3-dimensional Li-ion microbatteries. *Journal of Materials Research* **2010,** *25* (08), 1485-1491.

18. Tan, S.; Perre, E.; Gustafsson, T.; Brandell, D., A solid state 3-D microbattery based on Cu 2 Sb nanopillar anodes. *Solid State Ionics* **2012,** *225*, 510-512.

19. Fransson, L. M.; Vaughey, J.; Benedek, R.; Edström, K.; Thomas, J. O.; Thackeray, M., Phase transitions in lithiated Cu 2 Sb anodes for lithium batteries: an in situ X-ray diffraction study. *Electrochemistry Communications* **2001,** *3* (7), 317-323.

20. Zhang, S. S., A review on electrolyte additives for lithium-ion batteries. *Journal of Power Sources* **2006,** *162* (2), 1379-1394.

21. Yang, Z.; Gewirth, A. A.; Trahey, L., Investigation of Fluoroethylene Carbonate Effects on Tin-based Lithium-Ion Battery Electrodes. *ACS Applied Materials & Interfaces* **2015,** *7* (12), 6557-6566.

22. Choi, N.-S.; Yew, K. H.; Lee, K. Y.; Sung, M.; Kim, H.; Kim, S.-S., Effect of fluoroethylene carbonate additive on interfacial properties of silicon thin-film electrode. *Journal of Power Sources* **2006,** *161* (2), 1254-1259.

23. Nakai, H.; Kubota, T.; Kita, A.; Kawashima, A., Investigation of the Solid Electrolyte Interphase Formed by Fluoroethylene Carbonate on Si Electrodes. *Journal of The Electrochemical Society* **2011,** *158* (7), A798-A801.

24. Applestone, D.; Manthiram, A., Symmetric cell evaluation of the effects of electrolyte additives on Cu2Sb–Al2O3–C nanocomposite anodes. *Journal of Power Sources* **2012,** *217*, 1-5.

25. Verma, P.; Maire, P.; Novák, P., A review of the features and analyses of the solid electrolyte interphase in Li-ion batteries. *Electrochimica Acta* **2010,** *55* (22), 6332-6341.

26. Philippe, B.; Dedryvère, R.; Gorgoi, M.; Rensmo, H.; Gonbeau, D.; Edström, K., Role of the LiPF6 Salt for the Long-Term Stability of Silicon Electrodes in Li-Ion Batteries – A Photoelectron Spectroscopy Study. *Chemistry of Materials* **2013,** *25* (3), 394-404.

27. Nie, M.; Abraham, D. P.; Chen, Y.; Bose, A.; Lucht, B. L., Silicon Solid Electrolyte Interphase (SEI) of Lithium Ion Battery Characterized by Microscopy and Spectroscopy. *The Journal of Physical Chemistry C* **2013,** *117* (26), 13403-13412.

28. Xu, K., Electrolytes and Interphases in Li-Ion Batteries and Beyond. *Chemical Reviews* **2014,** *114* (23), 11503-11618.

29. Park, S.; Heon Ryu, J.; Oh, S. M., Passivating Ability of Surface Film Derived from Vinylene Carbonate on Tin Negative Electrode. *Journal of The Electrochemical Society* **2011,** *158* (5), A498-A503.

30. Seo, D. M.; Nguyen, C. C.; Young, B. T.; Heskett, D. R.; Woicik, J. C.; Lucht, B. L., Characterizing Solid Electrolyte Interphase on Sn Anode in Lithium Ion Battery. *Journal of The Electrochemical Society* **2015,** *162* (13), A7091-A7095.

31. Etacheri, V.; Haik, O.; Goffer, Y.; Roberts, G. A.; Stefan, I. C.; Fasching, R.; Aurbach, D., Effect of Fluoroethylene Carbonate (FEC) on the Performance and Surface Chemistry of Si-Nanowire Li-Ion Battery Anodes. *Langmuir* **2012,** *28* (1), 965-976.

CHAPTER 7: EFFECTS OF COMPOSITION AND MORPHOLOGY ON THE ELECTROCHEMICAL PERFORMANCE OF COPPER ANTIMONY ALLOY NANOWIRE ARRAYS

The following chapter is a manuscript being prepared for submission to the *Journal of Power Sources*. All experimental work and manuscript preparation were performed by Everett D. Jackson with intellectual contributions and editing help from Amy L. Prieto.

7.1 Introduction

Lithium-ion battery technology is currently used in flagship devices for consumer electronics and electric transport applications where high energy and power densities are required.[1] Commercial batteries have relied on graphitic carbon as a negative electrode, allowing intercalation chemistry with lithium at potentials near lithium metal and a stable capacity of ~372 mAh g^{-1}.[2] In contrast, metal anodes that undergo alloying reactions with lithium are capable of much higher capacities and correspondingly higher energy densities.[3] The instability of elemental particles during cycling has led researchers to evaluate alloys of the type M_xM', where M is a metal that does not form alloys with lithium but M' does.[4] Of these compounds, Cu_2Sb has received significant attention due to the ability of copper to influence the reaction pathway by forming intermediate ternary Li_xCu_ySb phases.[5] It has been hypothesized that these phases provide additional structural stability, enable higher electronic conductivity and decrease damage from phase transitions due to reduced volume change.[5-7] An inherent tradeoff of copper incorporation is a concurrent reduction in the electrode gravimetric capacity and a modest reduction in volumetric capacity, leading to lower specific energy for a theoretical lithium ion cell using the material when compared to pure antimony. Additionally, the copper is expected to cause reduced kinetic performance due to the requirement of copper diffusion, which is predicted to be slower than

lithium diffusion in this system.[8] Nevertheless, experimental evidence has shown that this system is highly reversible and can be made with a versatile set of methods, and is therefore a good candidate for future lithium ion battery anodes.[5,9,10]

Research on graphite[11-13] and silicon[14-16] thermal properties has been conducted with a focus on thermal decomposition processes related to safety and cell longetivity at high temperatures. Recently, Cu_2Sb electrodes have also been considered and the electrolyte and thermal decomposition reactions have been studied with common electrolytes.[17,18] Importantly, these studies have reported that exothermic decomposition of lithiated Sb has lower thermal output than equivalent graphite electrodes. Other thermal studies have briefly considered the low-temperature performance of Cu_2Sb and other alloy anodes.[19] Nevertheless, mechanistic and operational characteristics of these electrodes across the typical operating window of lithium ion batteries has not been reported. As a result, it is unclear how temperature influences the performance of these materials, a necessary requirement for application. To elucidate the role of copper in stabilizing the material and influencing the alloying pathway, we here evaluate Cu_xSb alloy nanowire arrays with varying copper content (x = ~0.5-3) to better understand the electrochemical reaction under varying kinetic and thermal conditions.

7.2. Experimental

7.2.1. Nanowire synthesis

Details of the electrodeposition system have been reported elsewhere.[20,21] Nanowire arrays were synthesized using the same method as presented in chapter 6. To synthesize nanowire arrays with varying composition, the amount of copper nitrate hemipentahydrate in solution was varied between 0.02 and 0.08 M. Three different templates were used to change the nanowire diameter:

55-nm (Synkera, 55 nm / µm), 100-nm (Synkera, 100 nm / 50 µm), and *ca.* 250-nm (Whatman, 100nm / 50 µm). Nanowire arrays were dried directly in a vacuum oven at 80 °C for samples studied here.

7.2.2. Materials characterization

X-ray diffraction patterns were obtained using a Bruker D8 DAVINCI diffractometer with Cu Kα radiation. Scanning electron microscope images were obtained using a JEOL 6500F SEM equipped with an EDAX Octane Super energy dispersive spectrometer (EDS) and transmission electron microscope images were obtained on a JEOL 2100F TEM equipped with an Oxford X-max^N 80T EDS.

7.2.3. Electrochemical measurements

Electrochemical measurements were performed in Swagelok lithium half-cells using an Arbin BT2000 battery tester. All experiments were performed under thermal control using a Cincinnati Sb-Zero MCB-1.2 environmental chamber. The electrochemical cell consisted of the nanowire array, a separator stack consisting of two pieces of polypropylene separator (MTI Corp.) sandwiching a glass microfiber filter (Whatman), a lithium metal counter electrode, and a stainless steel spring. The electrolyte consisted of 200 µL of 1.0 M LiPF6 in 3:7 volume ratio mixture of ethylene carbonate (EC) and diethyl carbonate (DEC) solution with 5 vol.% vinylene carbonate added.

7.3. Results and Discussion

7.3.1 Nanowire characterization

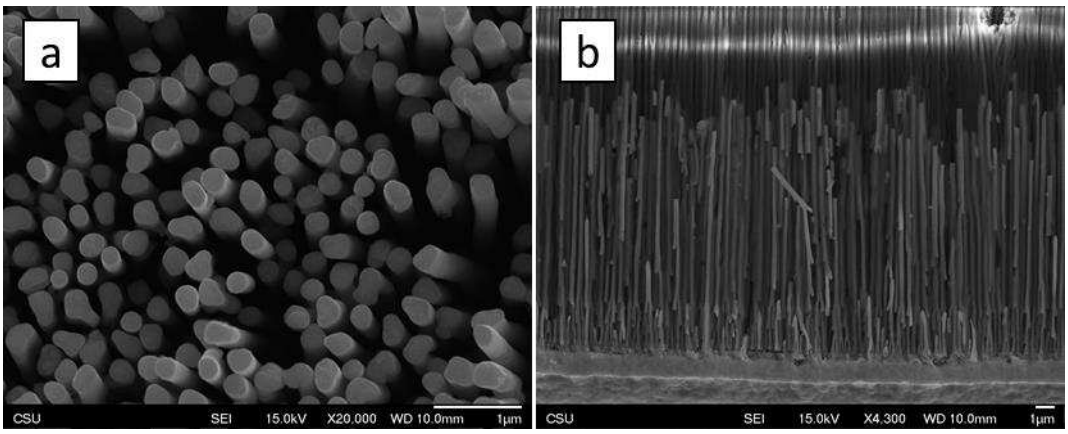

Figure 7.1. Scanning electron microscope images showing (a) a 250 nm nanowire array after removal of the template and (b) cross section of the nanowire array in the template.

Scanning electron microscope images were used to determine nanowire diameter and approximate length (Fig. 7.1). Nanowire compositions were determined by SEM-EDS and confirmed with TEM-EDS to give the compositions reported. Transmission electron microscopy (TEM) evaluation was also performed, showing the microstructure to be nanocrystalline (Fig. 7.2). The initial structure is relatively uniform and well-dispersed, and no significant local variations of composition were observed by TEM-EDS. This intricate mixture is ideal for studying the influence of copper content on the material without the issue of long-range aggregation of crystallites into Cu_2Sb/Sb.

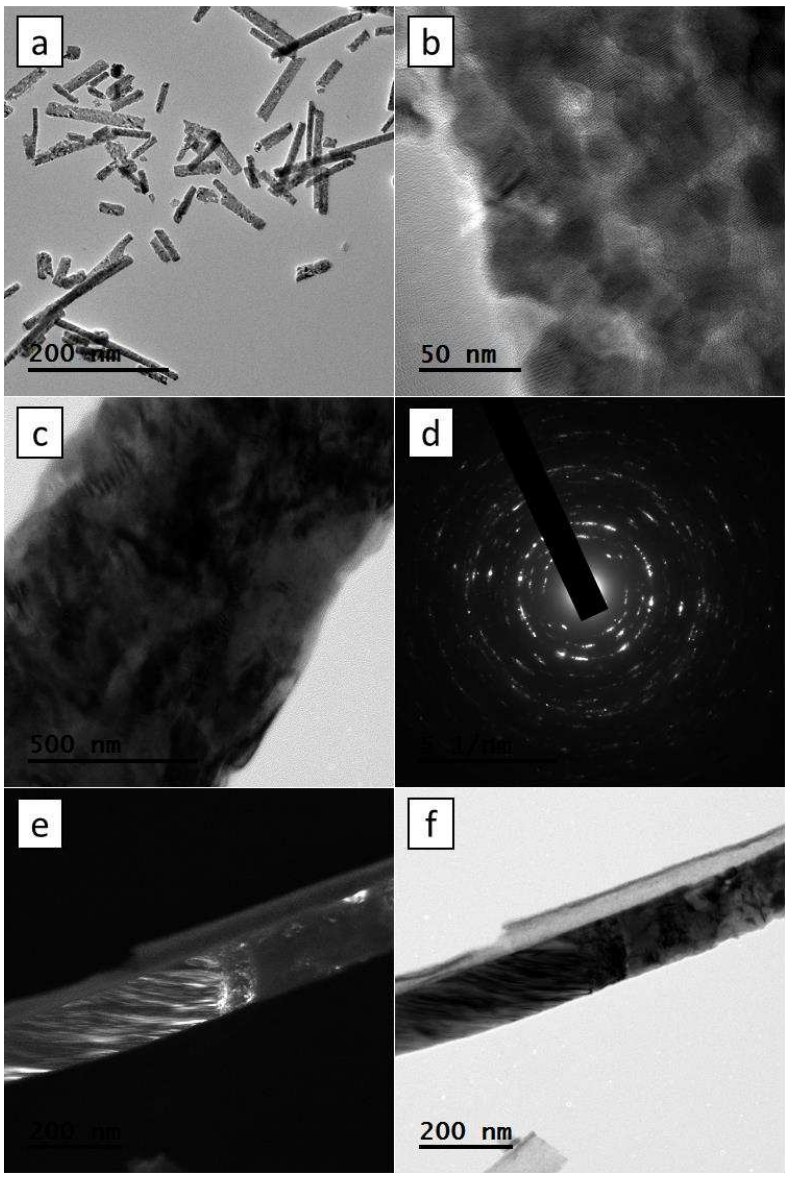

Figure 7.2. Transmission electron microscope images of the copper antimony alloy nanowires. (a) Low magnification image of many nanowires, (b) nanostructure of the $Cu_{0.5}Sb$ nanowire array showing many crystallites within the nanowire, (c) substantially different nanostructure for the Cu_3Sb nanowire array, showing a more homogenous and continuous structure, (d) representative selected area electron diffraction pattern for a $Cu_{0.5}Sb$ nanowire showing polycrystallinity, (e,f) dark field and bright field images of the nickel-copper antimony alloy interface.

The nanowire array structures were characterized by X-ray diffraction using fixed geometry to maximize the signal coming from the sample (Fig. 7.3). The copper-rich samples

primarily display peaks associated with tetragonal Cu_2Sb (PDF 01-071-3333) and $Cu_{11}Sb_3$ (PDF 03-065-9660), while copper-deficient samples show additional peaks associated with crystalline hexagonal Sb (PDF 00-035-0732). Nanowires grown with smaller diameters lead to lower crystallinity and different distributions of peak intensities, and significant reductions in peak intensities for antimony in copper deficient samples. The peaks corresponding to $Cu_{11}Sb_3$ are only present in 250 nm nanowire arrays, with only the major Cu_2Sb peak at 28 degrees showing significant intensity for 100 nm and 55 nm nanowire arrays. These results show that these nanowires have crystallinity across the entire composition range correlating to their composition.

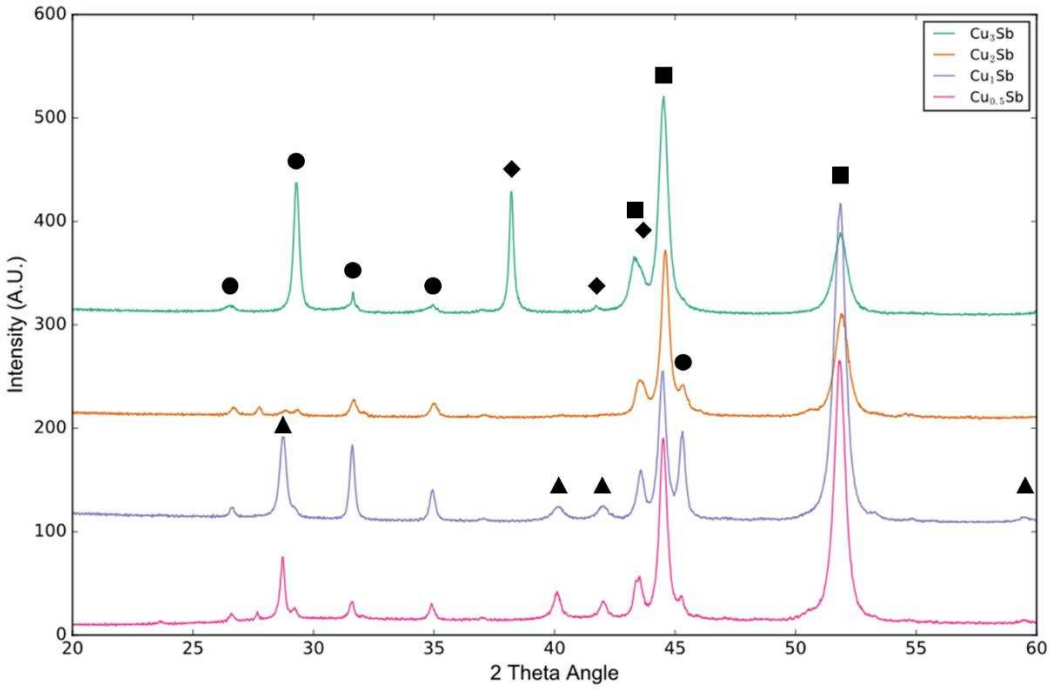

Figure 7.3. X-ray diffraction data for varying composition 250-nm nanowire arrays. Nickel peaks are from the base nickel layer and lower nanowire segments. Symbols: circles Cu_2Sb; diamonds, $Cu_{11}Sb_3$; triangles, Sb; squares, Ni.

7.3.2 Differential capacity analysis

The first data set shown in Fig. 4 illustrates the effect of composition and nanowire diameter on the lithiation and delithiation processes. These experiments were performed at slower rates (100 μA, ~C/2-C/4 depending on the sample) at 25 °C. Under these conditions, the importance of copper can be seen clearly in the difference between copper rich samples (pink/blue lines) and copper deficient samples (green/orange lines) with respect to the $Cu_{\sim 2}Sb$ composition. For samples containing ≥2 molar equivalents of copper, there are three lithiation and three delithiation peaks corresponding to unique electrochemical reactions. The three lithiation events correspond to the formation of a ternary lithium copper antimony phase, a solid solution region where additional lithium is added, and finally conversion to Li_3Sb.[6,7] Upon delithiation, an equivalent pathway is utilized to reform Cu_2Sb often mixed with some amount of Sb, depending on the rate, degree of delithiation achieved, morphology of the material, and the composition of the electrode.

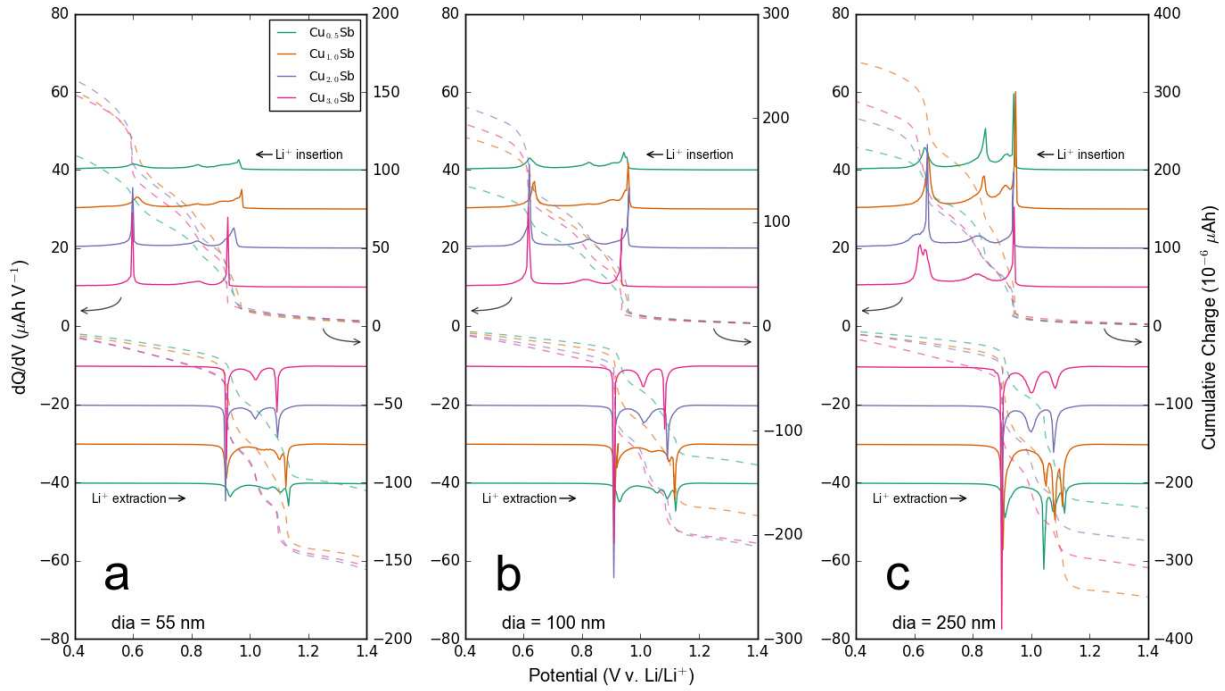

Figure 7.4. Differential capacity plots of nanowire arrays cycled at 100 µA between 0.01 and 2.0 V v. Li/Li$^+$ at 25 °C. Each plot shows four compositions of Cu_xSb for x≈0.5-3.0 of nanowires with average diameters of (a) 55 nm, (b) 100 nm, and (c) 250 nm. Solid lines indicate the differential capacity, while the dotted lines indicate the cumulative charge passed.

In contrast to copper-rich samples, the copper-deficient nanowires have a more complex lithiation and delithiation mechanism. For clarity, we recommend readers refer to the green curve in Fig. 7.1c, corresponding to nanowires with the largest diameter, which have the most defined differential capacity peaks. The antimony-rich nanowires show four unique steps on both lithium insertion and lithium desertion. During insertion, an initial transformation occurs at the same potential as for copper-rich samples, followed by a smaller second peak, likely corresponding to the transformation of antimony-rich regions of the nanowire. Unlike the copper-rich samples, the middle peak is well defined and represents a clear phase transition that is not observed for copper rich samples. Since the intermediate phases only use one molar equivalent of copper to antimony, it may be that the excess copper present in the copper rich samples causes this transformation to

be kinetically limited. A final lithium insertion peak is observed at the same potential as copper-rich samples, with decreasing intensity owing to the reduced amount of copper present. During delithiation, a substantial difference is observed between the two types of samples. For antimony-rich samples, the middle solid solution peak is absent, while two new peaks appear at slightly lower and slightly higher potentials compared to the final delithiation peak observed in copper rich samples. The existence of these peaks is unexpected, and cannot be simply deduced as the combination of the delithiation patterns of separate Cu_2Sb and Sb domains, given that pure antimony and Cu_2Sb both show single delithiation events at nearly the same potential of the middle peak and at neither of the secondary peaks. Future work on determining the nature of these peaks is necessary, and identification of the reactions may be possible through *in situ* TEM or XRD experiments that are capable of identifying the phases being formed at each step.

Comparison of the differential capacity plots of nanowires with different diameters (Fig. 7.4a-c) shows that the general trend in composition-dependent charge and discharge curves are consistent despite the size and crystallinity. Due to the less crystalline nature of the smaller diameter nanowires, the differential peaks appear weaker. The copper deficient have particularly weak peaks, corresponding to less well defined phase transitions. These differences are qualitative, however, and the charge is passed over the same potential window for each composition regardless of the nanowire diameter. This provides a good indication that at 25 °C there is not a major kinetic limitation at slow rates across this range of material diameter.

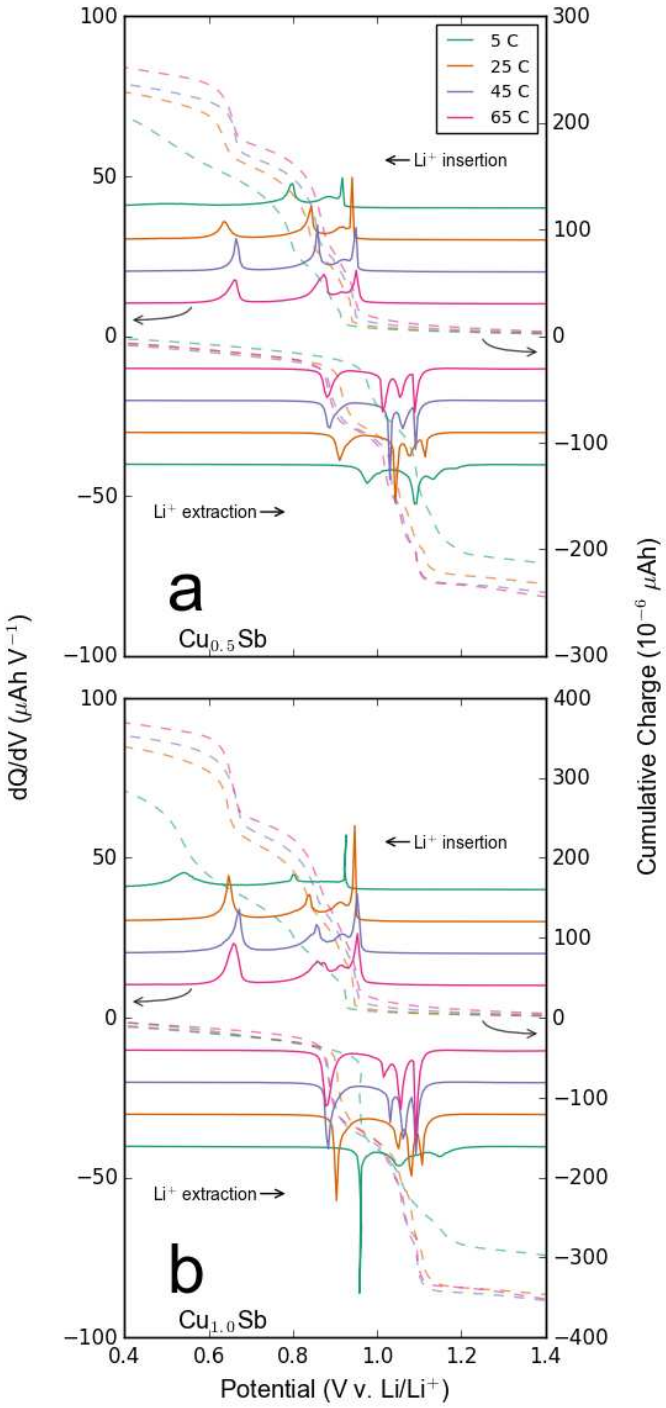

Figure 7.5. Differential capacity plots of 250 nm diameter nanowire arrays cycled at 100 µA between 0.01 and 2.0 V v. Li/Li^+ at 25 °C. Each plot shows data for four different temperatures for copper deficient nanowires with composition of (a) $Cu_{0.5}Sb$ and (b) $Cu_{1.0}Sb$. Solid lines indicate the differential capacity, while the dotted lines indicate the cumulative charge passed.

The impact of temperature on the electrochemical alloying reaction is illustrated in Fig. 7.5 for antimony-deficient nanowires. The largest diameter nanowires are shown here as they are expected to have the greatest dependency on chemical diffusion and mobility rates due to their larger solid state diffusion length. In terms of the differential capacity curves for both samples, there are only minor differences for the room temperature and elevated temperature experiments. At higher temperatures, there is a slight decrease in the overpotential as a result in faster diffusion kinetics within the nanowires. Below room temperature, a substantial increase in the overpotential is observed alongside a significant drop in the electrode capacity. It appears that this reaction proceeds sluggishly below room temperature, but better at elevated temperature. This may be an advantage in some cases where above-ambient temperatures are easier to maintain than room temperature (e.g. some cases of stationary power and hybrid electric vehicles).

Evaluation of the capacity curves (dotted lines) in Fig. 7.5 reveal increasing temperatures to cause more electrolyte degradation during lithium insertion. While the delithiation capacity remains nearly identical between 25 °C and 65 °C, it is apparent that the lithiation capacity increases significantly. This indicates that extra capacity is being passed at higher temperatures that is not related to the lithium alloying mechanism, as that capacity is not recovered during delithiation. This is not a particularly surprising effect, as it is well reported for other alloys such as tin and silicon, and electrolyte instability has been identified as an ongoing challenge for copper antimonide in this dissertation (see Ch. 4 and 5). This illustrates clearly that copper antimonide anodes will require a new type of electrolyte system that offers enhanced passivity compared to traditional carbonate electrolytes that have been developed for graphite. Based on the thermal performance, it may be reasonable to develop electrolytes with better elevated temperature performance to match the better performance observed for Cu_xSb at above-ambient temperatures.

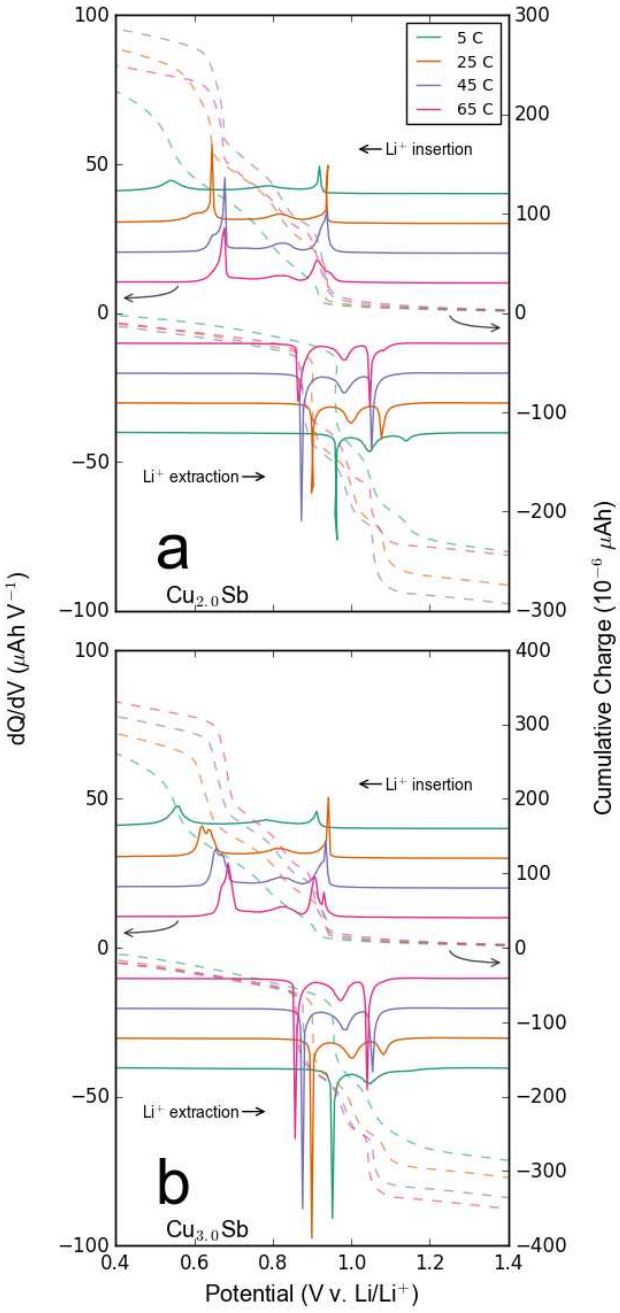

Figure 7.6. Differential capacity plots of 250 nm diameter nanowire arrays cycled at 100 µA between 0.01 and 2.0 V v. Li/Li^+ at 25 °C. Each plot shows data for four different temperatures for copper rich nanowires with composition of (a) $Cu_{2.0}Sb$ and (b) $Cu_{3.0}Sb$. Solid lines indicate the differential capacity, while the dotted lines indicate the cumulative charge passed.

The equivalent figure to Fig. 7.5 for copper-rich nanowires is shown in Fig. 7.6. Similar effects are observed for these samples as before in terms of the differential capacity curves. In contrast, lithium extraction shows significant increases in capacity as the temperature is raised. This is consistent with theoretical predictions that copper causes a kinetic limitation due to a relatively slower diffusivity of copper compared to lithium within the copper antimonide system. As a result, a kinetic limitation in the reversible capacity is observed across the entire temperature range. The difference between the copper-deficient and copper-rich samples suggests strongly that copper-deficient samples are more likely to make effective electrodes, as the kinetic inhibition of lithium extraction can be avoided at ambient temperatures and considering that the operation of the battery at near room temperature is critical for most applications.

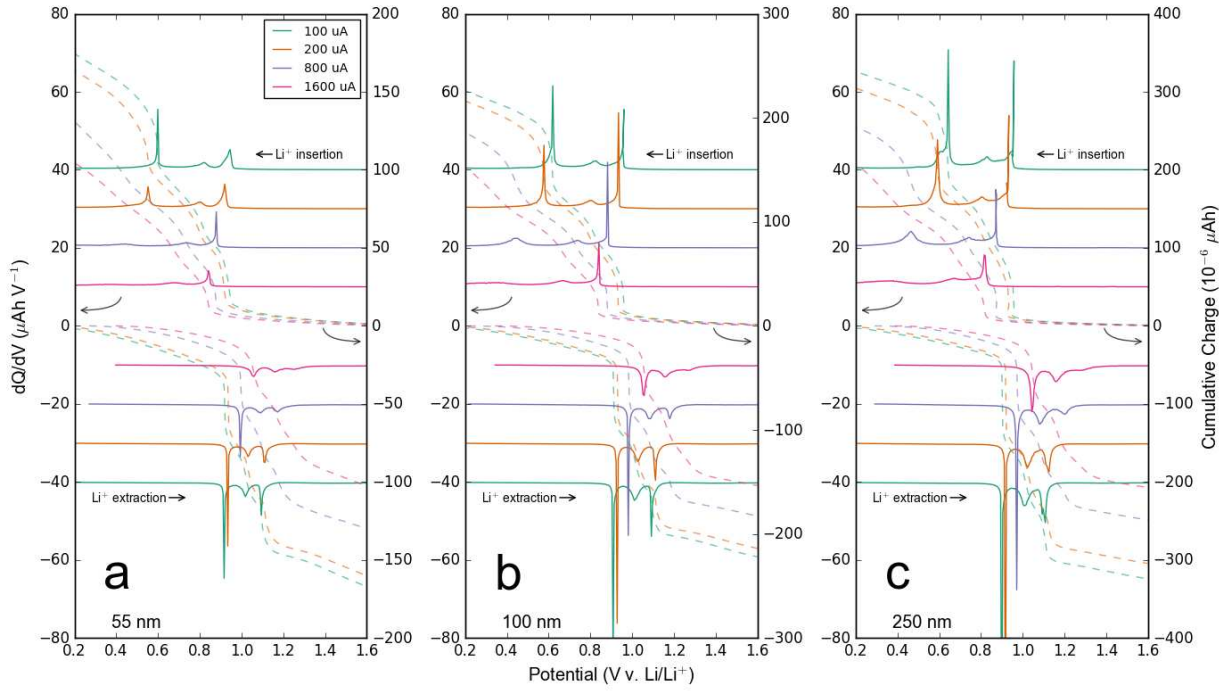

Figure 7.7. Differential capacity plots of varying diameter Cu_2Sb nanowire arrays cycled between 0.01 and 2.0 V v. Li/Li^+ at 25 °C. Solid lines indicate the differential capacity, while the dotted lines indicate the cumulative charge passed.

To determine the effect of effective diffusion length on performance, Fig. 7.7 compares three different diameter Cu_2Sb nanowire arrays at 25 °C with varying rates from 100 µA (~C/1.5-C/3) to 1600 µA (~10C-6C). Qualitatively, the same effect is observed for each nanowire diameter. A minor decrease in capacity is observed up to 200 µA, with significant overpotentials appearing and a significant reduction of capacity at higher rates. Interestingly, a substantial qualitative difference between the nanowire arrays of different sizes as a function of rate is not readily apparent. It is possible that the solid lithium diffusion length is not the limiting factor for this type of electrode, but is rather controlled by diffusion through the SEI and charging effects. This would result in an apparent difference between the rate loss and

7.3.3. Cycle study

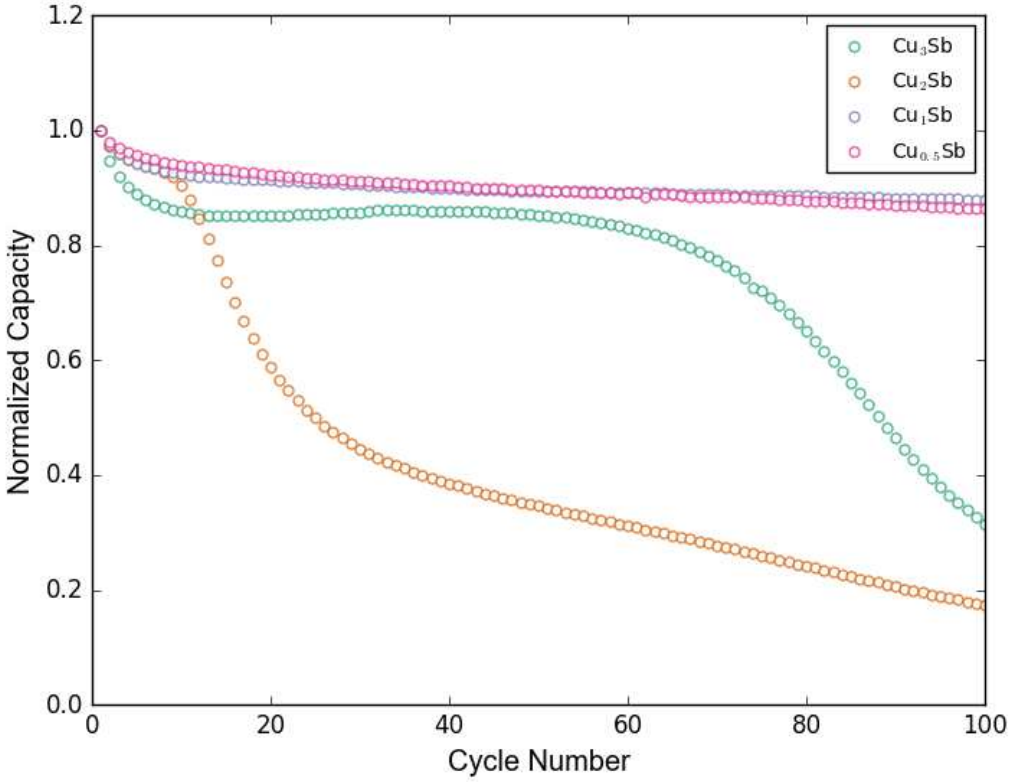

Figure 7.8. Cycle life of Cu_xSb nanowire arrays cycled between 0.01 and 1.6 V v. Li/Li^+ at 25 °C at 100 µA. Compositions with lower copper concentrations display longer cycle lives when compared to copper rich copper antimonide nanowires.

Following the variable rate and variable composition testing, some samples were tested for extended cycles. The results for 250 nm nanowire arrays across the composition range tested is shown in Fig. 7.8. Interestingly, no advantage is observed for copper-rich samples, which display faster capacity fade than copper-deficient nanowires. While the curve for the copper-rich Cu_3Sb sample follows a similar qualitative curve as reported for the same composition samples used in our previous study (see Ch. 6), the stoichiometric Cu_2Sb samples display the fastest capacity fade.

Surprisingly, both the antimony-rich samples display stable capacity retention for 100 cycles. Further study is necessary to determine the exact reason for this failure.

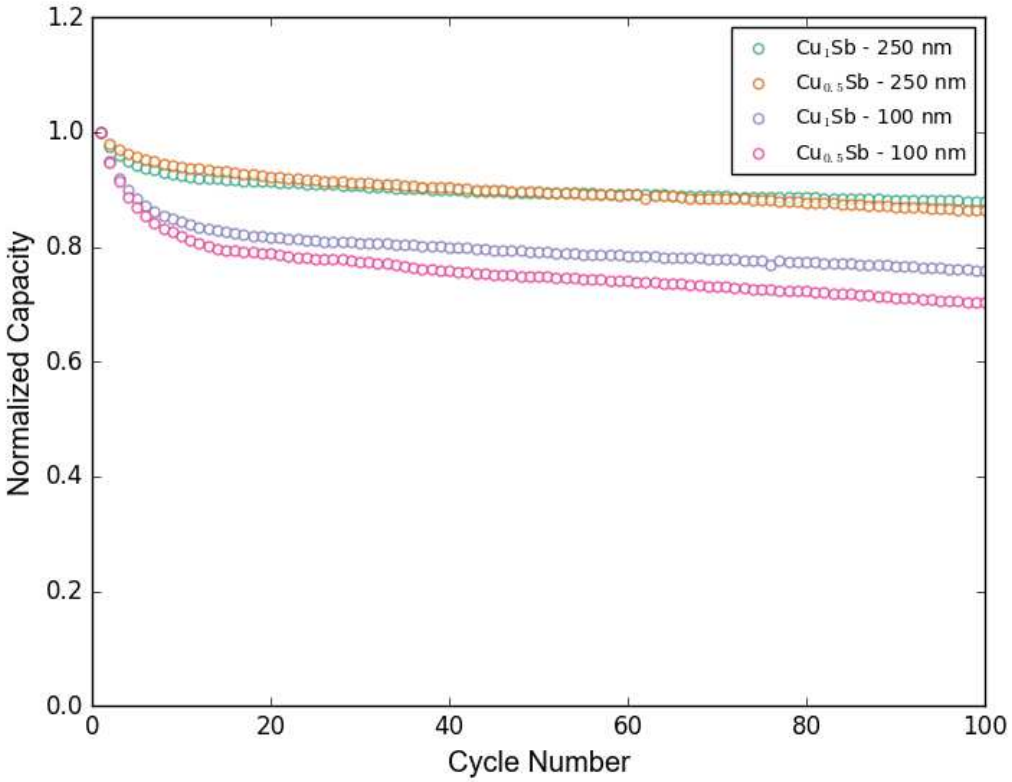

Figure 7.9. Cycle life of antimony-rich nanowire arrays cycled between 0.01 and 1.6 V v. Li/Li^+ at 25 °C at 100 µA. Under these conditions, the thicker nanowires provided better capacity retention. The optimal composition for both diameters is Cu_1Sb.

Based on the results shown in Fig. 7.8, comparison between 100 nm and 250 nm diameter antimony-rich nanowires is presented in Fig. 7.9. Surprisingly, there does not appear to be any benefit to the use of smaller diameter nanowires in this case. After a fast initial capacity drop, both diameter nanowires are able to maintain their capacity over the rest of the first 100 cycles. We attribute the lower performance of the 100 nm nanowires to a higher surface area to volume ratio, which likely results in more electrolyte degradation during the high temperature testing done prior

to cycle testing. Future study on this system should focus on stabilization of the electrolyte to achieve better coulombic efficiency and increase electrode longevity. Due to the high surface area of these nanowire electrodes, this is a route well suited to this synthetic method.

7.5. Conclusion

In summary, we have shown that it is possible to electrodeposit copper-antimony alloy nanowire arrays with variable diameter and composition. Antimony-rich compositions of $Cu_{0.5}Sb$ and Cu_1Sb have been found to offer better kinetic performance and stability compared to copper rich nanowires with compositions of Cu_2Sb and Cu_3Sb. We attribute this to reduced exposure of the electrolyte to extruded copper and decreased kinetic limitations resulting from the requirement of copper diffusion. These materials appear to offer enhanced performance at elevated temperature (45 – 65 °C), but suffer from excessive electrolyte degradation. New electrolyte formulations, especially those that work best at modestly elevated temperatures, will be necessary to achieve good performance with copper-antimony alloy electrodes.

REFERENCES

1. Armand, M.; Tarascon, J. M. *Nature* **2008**, *451*, 652.

2. Whittingham, M. S. *Proceedings of the IEEE* **2012**, *100*, 1518.

3. Obrovac, M. N.; Chevrier, V. L. *Chemical Reviews* **2014**, *114*, 11444.

4. Thackeray, M.; Vaughey, J.; Fransson, L. *JOM* **2002**, *54*, 20.

5. Fransson, L. M.; Vaughey, J.; Benedek, R.; Edström, K.; Thomas, J. O.; Thackeray, M. *Electrochemistry Communications* **2001**, *3*, 317.

6. Matsuno, S.; Noji, M.; Kashiwagi, T.; Nakayama, M.; Wakihara, M. *The Journal of Physical Chemistry C* **2007**, *111*, 7548.

7. Matsuno, S.; Noji, M.; Nakayama, M.; Wakihara, M.; Kobayashi, Y.; Miyashiro, H. *Journal of The Electrochemical Society* **2008**, *155*, A151.

8. Chang, D.; Chen, M.-H.; Van der Ven, A. *Chemistry of Materials* **2015**, *27*, 7593.

9. Perre, E.; Taberna, P. L.; Mazouzi, D.; Poizot, P.; Gustafsson, T.; Edström, K.; Simon, P. *Journal of Materials Research* **2010**, *25*, 1485.

10. Kim, I. T.; Allcorn, E.; Manthiram, A. *Energy Technology* **2013**, *1*, 319.

11. Andersson, A. M.; Herstedt, M.; Bishop, A. G.; Edström, K. *Electrochimica Acta* **2002**, *47*, 1885.

12. Jiang, J.; Dahn, J. R. *Electrochimica Acta* **2004**, *49*, 4599.

13. Zhou, F.; Zhao, X.; Fergusoń, P. P.; Thorne, J. S.; Dunlap, R. A.; Dahn, J. R. *Journal of The Electrochemical Society* **2008**, *155*, A921.

14. Profatilova, I. A.; Langer, T.; Badillo, J. P.; Schmitz, A.; Orthner, H.; Wiggers, H.; Passerini, S.; Winter, M. *Journal of The Electrochemical Society* **2012**, *159*, A657.

15. Wang, Y.; Dahn, J. R. *Journal of The Electrochemical Society* **2006**, *153*, A2188.

16. Wang, Y.; Dahn, J. *Electrochemical and Solid-State Letters* **2006**, *9*, A340.

17. Allcorn, E.; Manthiram, A. *Journal of The Electrochemical Society* **2015**, *162*, A1778.

18. Allcorn, E.; Kim, S.-O.; Manthiram, A. *Journal of Power Sources* **2015**, *299*, 501.

19. Jansen, A. N.; Clevenger, J. A.; Baebler, A. M.; Vaughey, J. T. *Journal of Alloys and Compounds* **2011**, *509*, 4457.

20. Mosby, J. M.; Prieto, A. L. *Journal of the American Chemical Society* **2008**, *130*, 10656.

21. Mosby, J. M., COLORADO STATE UNIVERSITY, 2010.

CHAPTER 8: DEEP EUTECTIC SOLVENTS AS A MEDIUM FOR THE ELECTROCHEMICAL SYNTHESIS OF INTERMETALLIC COMPOUNDS

This chapter presents preliminary data from experiments on electrodeposition of antimony alloys using a novel solvent system. Everett D. Jackson performed the experiments and writing with guidance and editing by Amy L. Prieto.

8.1 Introduction

Electrochemical deposition has been used as the synthetic basis for all of the studies presented in this dissertation. Despite the relative ease of electroplating, significant chemical limitations exist in terms of what can be electroplated and the achievable conditions. During the course of the research performed for the previous chapters, codeposition of Zn-Sb and Mn-Sb from aqueous solution were attempted in addition to using the established procedure for copper antimonide electrodeposition. While the successful codeposition of Zn-Sb was achieved (see Ch. 5), the conditions were not found to be general and could not be applied to Mn-Sb codeposition and did not produce crystalline deposits without an additional annealing step. For many metals, electrodeposition only occurs readily at high rates and in aqueous solutions high concentrations are used. This makes it difficult to codeposit these metals with antimony, which is restricted to *ca.* 50 mM in aqueous solutions except at very low pH values. In an attempt to provide a general set of conditions which could allow for the codeposition of a wide range of metals in a facile manner, we attempted to identify solute/solvent systems that would allow for a greater degree of flexibility in the concentrations of metal salts in the solution. To retain a green method, we searched for solvent systems that consisted of primarily non-toxic, non-volatile chemicals with a wide potential range to make a useful and inexpensive benchtop electrochemical method.

Among the wide variety of solvent systems available, a significant limitation is the low solubility of antimony in most solvent systems. An exception to this is the high solubility of almost all metal salts in ionic liquids, which display most of the key properties listed above.[1] A significant limitation, however, is that most ionic liquid systems are expensive and not readily purified. In contrast, a similar type of solvent has been identified in the last decade and termed deep eutectic solvents (DESs).[2,3] These DESs consist of a hydrogen bond donor and a hydrogen bond acceptor, forming an ionic liquid like system at or near room temperature. These solutions have been shown to provide a wide electrochemical window, high solubility of many metal salts, and has been used as an electroplating solvent in a number of preliminary studies.[4,5] In addition, they have been used in many studies to codeposit multiple elements and even metal-inorganic composites.[6-14]

The experiments here outline preliminary experiments to determine the ability of the DES ethaline, a 2:1 molar mixture of ethylene glycol to choline chloride, as a candidate solvent for electrochemical codeposition of new metal antimonides. These early studies were conducted to determine the electrochemical activity of metal chloride salts, and provide a basis for future electroplating experiments. Initial results show promise that the tested metals (Cr, Fe, Co, Ni, Cu, Zn, Sn, Sb) are electrochemically active within the electrochemical potential window of the ethaline solvent, and initial experiments have shown electroplating proceeds readily for many of these metals.

8.2 Experimental

Choline chloride (Sigma, 98%) was purified by recrystallization from absolute ethanol and dried under vacuum at 80 °C. Ethylene glycol (Sigma, 99%) was added in a 2:1 molar ratio to form the ethaline deep eutectic. Deposition solutions were prepared by adding the appropriate amount of metal salt to the ethaline solution.

Electrochemical measurements were performed using a Gamry Reference 3000 potentiostat. A silver wire (≥99%) was used as a pseudo reference electrode and a platinum flag as the counter electrode. Cyclic voltammetry experiments were performed using either a platinum, gold, or glassy carbon electrode imbedded in PEEK (Bioanalytical Systems, Inc.). Electrodeposition experiments were performed using electropolished copper foils.

8.3 Results and Discussion

8.3.1 Experimental design and solution choice

The solubility of metal chloride salts in ethaline is high for a wide range of metals. In a previous report, it has been noted that even many oxides are soluble in this liquid without additional chelating agents. Initial solubility tests done here show solubilities for all salts up to at least 200 mM at room temperature with the exception of $SbCl_3$, which is limited to 100 mM. At a moderate elevated temperature of 65 °C, $SbCl_3$ is soluble up to 200 mM. Unlike aqueous solution, $SbCl_3$ does not precipitate out as an oxide, but rather recrystallizes from solution and can be easily resolubilized at higher temperature. In some cases, the addition of more than 200 mM metal chloride can result in solidification of the solution. This is generally caused by hydrogen bonding interactions between the metal chloride salt and the choline chloride, causing a change in the ratio of hydrogen bond donors to acceptors, and increasing the solidus point. In all cases excepting

SbCl3, the metal chloride salts studied here are soluble up to 500 mM at 65 °C. At this temperature, the materials used have minimal vapor pressure. In interest of flexibility, this temperature was chosen as the standard temperature for the electrochemical experiments performed in this chapter.

For this preliminary study, the later first row transition metals, Sn, and Sb were studied. Both Sn and Sb are important anode active materials in lithium ion batteries and have reasonable electrochemical activity, allowing for electrodeposition. The transition metals were chosen as potential alloying elements for studying transition metal antimonide and stannide materials. Due to scarcity, reactivity, and solution complexity the transition metals scandium, titanium, and vanadium were excluded from this study. For future codeposition studies, it is necessary to gain a primitive understanding of the electrochemistry of these salts. To achieve this, cyclic voltammetry on glassy carbon and platinum working electrodes was performed.

8.3.2. Cyclic voltammetry of pure elements

The electrochemical activity of the chosen metal chloride salts has been evaluated by cyclic voltammetry (CV). Using this method, it is possible to determine the electrochemical potential at which electrochemical reduction and oxidation of the salts occur. In order to facilitate the design and investigation of codeposition solutions, the chosen metal chloride salts were evaluated at several different concentrations. The resulting curves can be used to predict the best-suited solution conditions to perform a given electrochemical codeposition experiment.

The first experiments were designed to test the electrochemical activity of antimony and tin either in the form of the chloride salt or by reduction and complexation by citric acid. Cyclic voltammograms of solutions of 50 mM Sb_2O_3, 50 mM Sb_2O_3 with 100 mM citric acid, and 100 mM $SbCl_3$ are shown in Fig. 8.1. The solution of antimony oxide without citric acid did not

completely dissolve, leading to the low activity observed in the CV. The reduction of Sb_2O_3 with citric acid allows for the full dissolution of the Sb_2O_3 into ethaline, but the species formed by this method is different than that formed by direct addition of $SbCl_3$. A major difference lies in the $Sb3^+/Sb5^+$ redox couple at 0.80-1.20 V v. Ag, where only the $SbCl_3$ samples shows reversibility. The reduction wave is also stronger for the $SbCl_3$ solution, although both $SbCl_3$ and Sb_2O_3 appear to deposit at similar rates, as indicated by the similar size of the anodic stripping peak at 0.20 V v. Ag. Despite the only modest solubility of Sb^{3+} in ethaline, this study shows that Sb can be readily electrodeposited from this solution and proceeds across a wide potential windows (-0.20 to -1.40 V v. Ag). In addition, the obvious reversibility of the Sb^{3+}/Sb^{5+} redox couple in this solution is not normally observable in water, and therefore shows that this solution does have higher electrochemical stability.

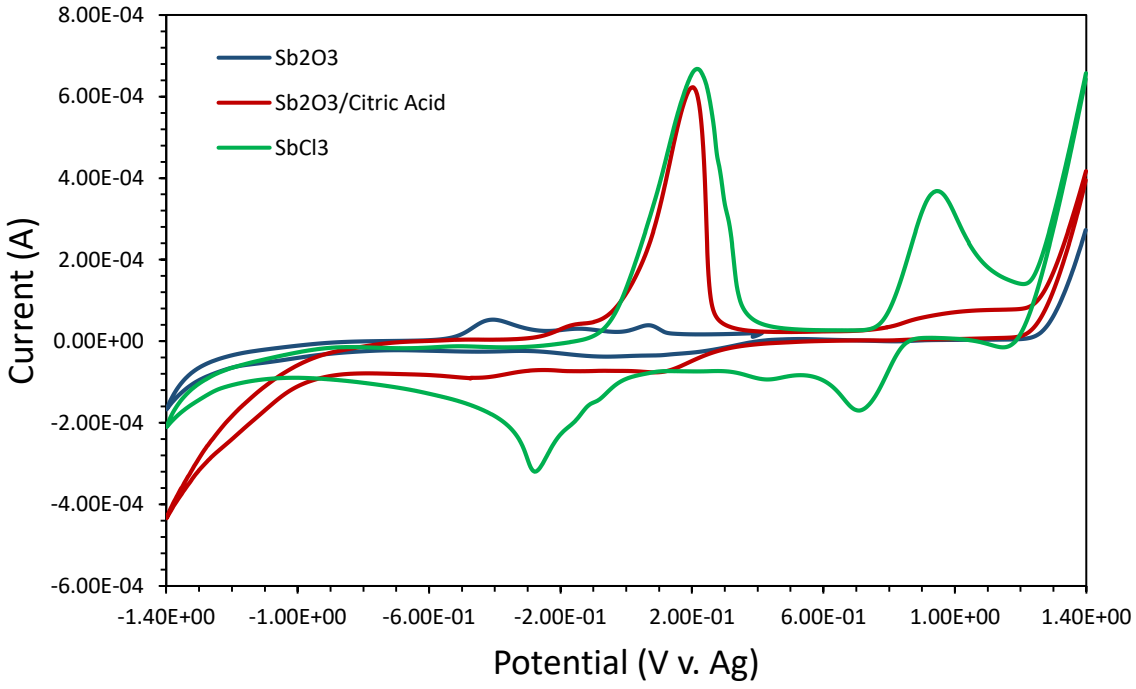

Figure 8.1. Cyclic voltammograms of different Sb species in ethaline solution taken at 100 mV s^{-1} on a platinum electrode between -1.40 and 1.40 V v. Ag at 65 °C.

The analogous experiment was also performed to understand the electrochemistry of Sn^{2+} in ethaline. It should be noted that unlike $SbCl_3$, $SnCl_2$ is fully soluble up to much higher concentrations (500 mM). Unlike the comparative case for different Sb species, the SnO mixed with citric acid sample and $SnCl_2$ samples show very similar electrochemistry, with the exception that $SnCl_2$ is more active at the same concentration. Similar to antimony, electrodeposition proceeds under diffusion control for a wide potential range (-0.40 to -1.20 V v. Ag). The anodic stripping peak becomes noisy for larger deposits, which can be attributed to the poor contact of dendrites that likely grow under these conditions (as described later in the chapter).

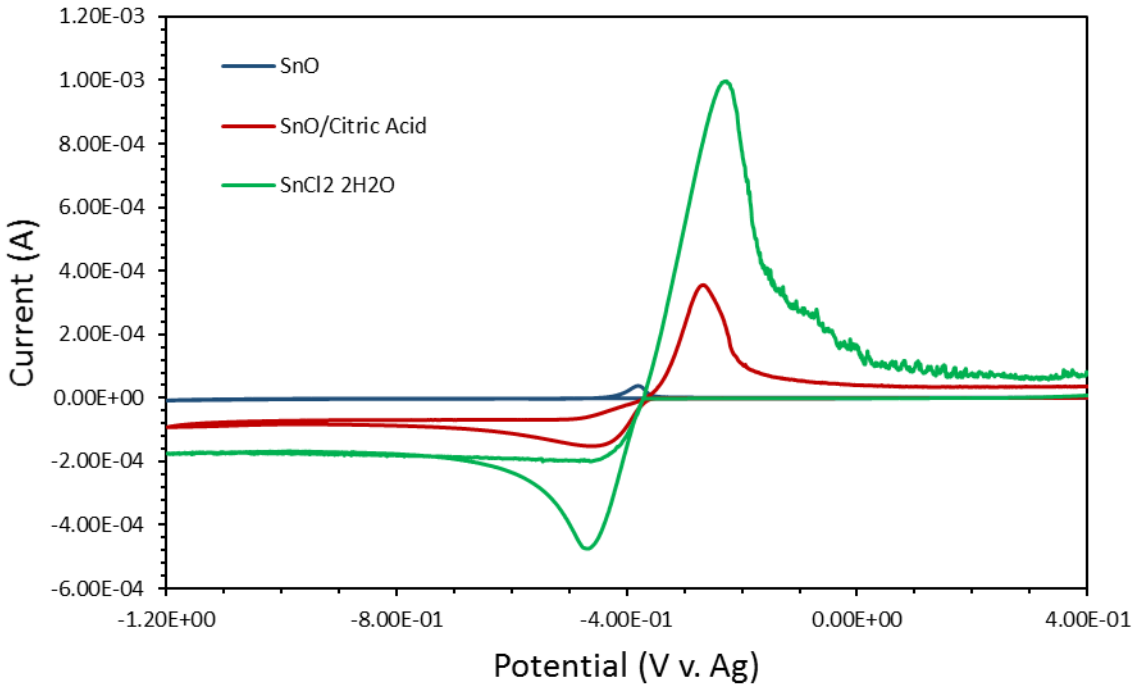

Figure 8.2. Cyclic voltammograms of different Sn species in ethaline solution taken at 10 mV s^{-1} on a glassy carbon electrode with a silver wire reference at 65 °C.

The transition metals were initially analyzed using basic hydrated metal chloride salts at 100 mM. Initial trials showed significant variations in the electrochemical activity of each metal,

with some showing negligible redox activity under these conditions. To determine if this could be overcome, each metal chloride was tested across a concentration range of 100 – 500 mM. The electrochemical activity varies significantly, but only $MnCl_4•2H_2O$ appeared to not undergo any significant redox activity in the electrochemical potential window of the ethaline solvent.

The concentration-dependent cyclic voltammogram of $CuCl_2•2H_2O$ is shown in Fig. 8.3. There are two sets of redox couples at 0.40 V v. Ag and -0.40 V v. Ag. The more positive wave corresponds to the Cu^{2+}/Cu^{+} couple, while the more negative corresponds to the Cu^{+}/Cu^{0} couple. A large background current occurs at all potentials more negative than the more positive couple, as Cu^{+} is seemingly stable in ethaline, unlike aqueous solution. Similar to the cases for Sn^{2+} and Sb^{3+}, extending the potential range in the negative direction far past the potential required for electrodeposition results in a flat current corresponding to diffusion-limited growth. The current increases linearly with concentration, as is expected for this process.

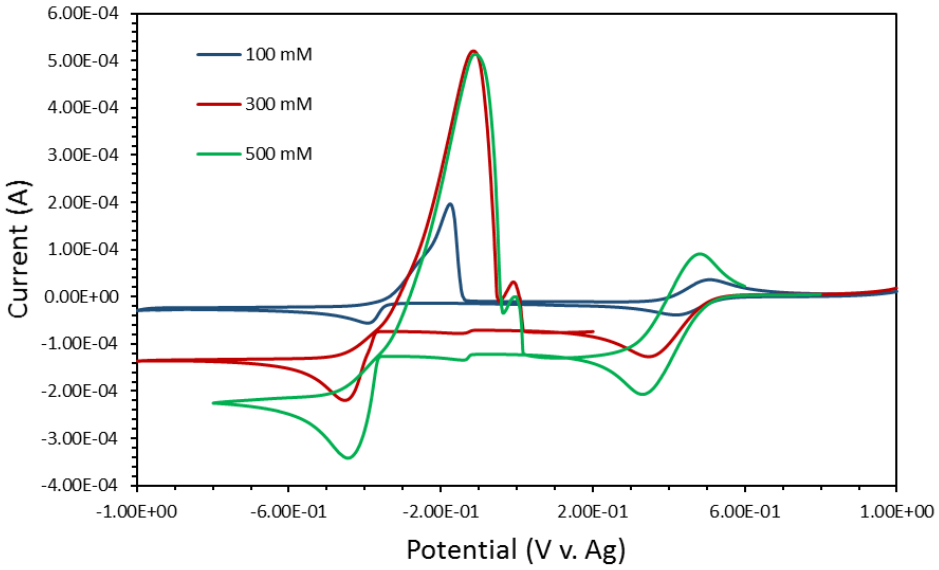

Figure 8.3. Cyclic voltammograms of $CuCl_2•2H_2O$ in ethaline solution with varying concentrations on a platinum working electrode taken at 10 mV s^{-1} from -1.0 V to 1.0 V v. Ag wire reference at 65 °C.

The electrochemistry of $NiCl_2 \cdot 6H_2O$ at various concentrations is shown in Fig. 8.4. Unlike the case for all previous examples, a substantial hysteresis between the reduction and oxidation peaks are present in the cyclic voltammogram for Ni^{2+}. In addition, the reduction of Ni2+ to Ni0 is essentially non-existent at 100 mM, with significant charge being passed only on reduction and not recovered during the anodic scan. At higher concentrations, the rate of electrochemical reduction increases substantially and the anodic stripping peak becomes obviously apparent. This shows that Ni^{2+} is not reduced or oxidized easily, but can proceed under the appropriate conditions. It should be noted that an obvious reduction tail exists after the peak corresponding to nickel electrodeposition, suggesting that either the Ni^{2+} in solution or the electrodeposited Ni^0 cause electrochemical reduction of the ethaline solvent. Although this may suggest that codeposition of alloys may be difficult with Ni, codeposition with both Sn and Sb are possible, as is shown later in this chapter.

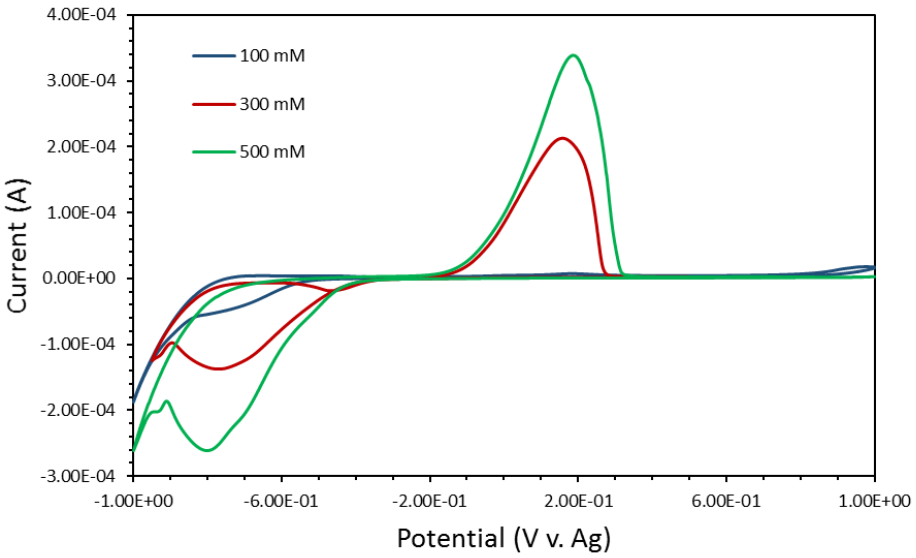

Figure 8.4. Cyclic voltammograms of varying concentrations of $NiCl_2 \cdot 6H_2O$ in ethaline solution performed at 10 mV s^{-1} between -1.0 and 1.0 V v. Ag on a platinum electrode at 65 °C.

The electrochemistry of $FeCl_3$•$6H_2O$ in ethaline is shown in Fig. 8.5. Similar to $NiCl_2$•$6H_2O$, little electrochemical activity is apparent at 100 mM Fe^{3+}. At higher concentrations, three unique electrochemical events are visible in for this metal chloride salt. The most positive redox wave at 0.40 V v. Ag corresponds to the Fe^{2+}/Fe^{3+} couple, and like the case for $CuCl_2$•$2H_2O$, a background current corresponding to this reduction is present at all potentials lower than 0.40 V v Ag. A second reduction event is present at potentials more negative than -0.90 V v. Ag, corresponding to reduction of Fe^{2+} to Fe^0. As seen with Ni^{2+} reduction and oxidation, a significant voltage hysteresis is present between Fe^{2+} reduction and Fe^0 oxidation. In addition, an unexpected third redox wave is observed at 0.05 V v. Ag, indicating that there are two separate electrodeposition processes that can occur. Further *ex situ* characterization is necessary to understand this process.

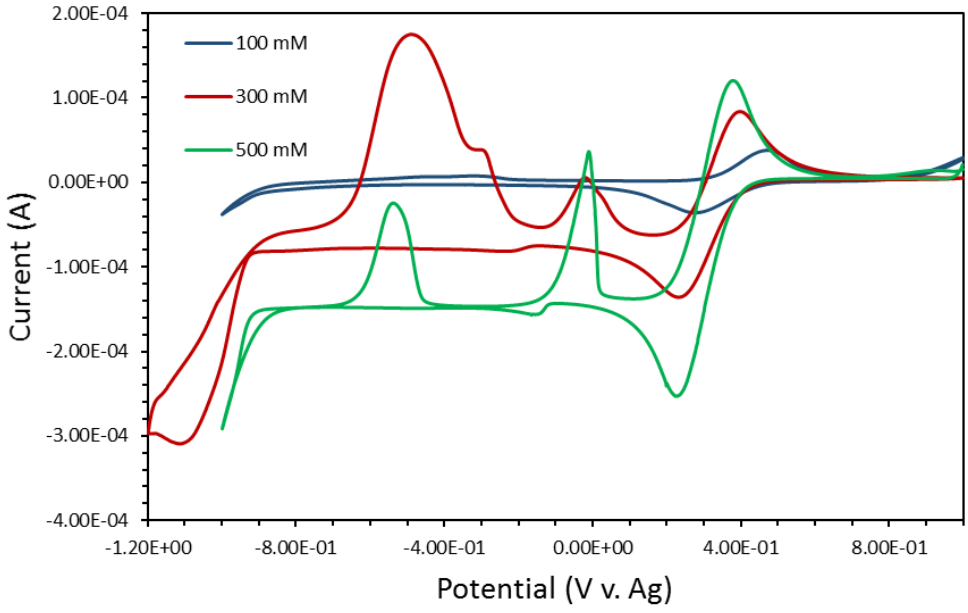

Figure 8.5. Cyclic voltammograms of varying concentrations of $FeCl_3$•$6H_2O$ in ethaline solution performed on a platinum electrode at 10 mV s^{-1} between -1.20 and 1.00 V v. Ag at 65 °C.

The cyclic voltammograms for $CoCl_2 \cdot 6H_2O$ in ethaline are shown in Fig 8.6. The performance is exceedingly similar to $NiCl_2 \cdot 6H_2O$, although even higher concentrations are needed before electrodeposition occurs readily when compared to Ni^{2+}. A very large voltage hysteresis is clear for this system as well. It does not appear as though Co will readily codeposit, but given the preliminary success with Ni, it may still be possible.

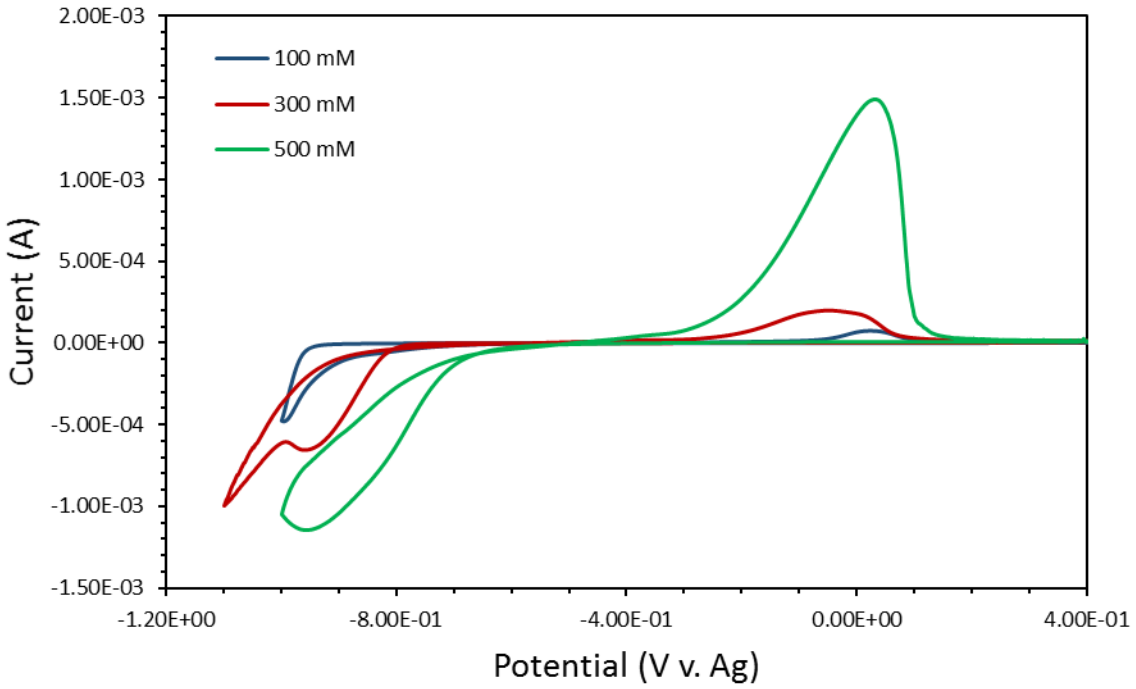

Figure 8.6. Cyclic voltammograms of $CoCl_2 \cdot 6H_2O$ in ethaline solution performed on a glassy carbon working electrode at 10 mV s^{-1} between -1.20 and 1.00 V v. Ag at 65 °C.

Compared to previous examples, Zn has the highest standard reduction potential and is therefore exceptionally difficult to electrochemically codeposit. The cyclic voltammetry of $ZnCl_2$ in ethaline is shown in Fig. 8.7, and it is readily apparent that $ZnCl_2$ readily undergoes reduction and oxidation at -1.0 V v. Ag with minimal voltage hysteresis. Despite Zn^{2+} being the only electrochemically active ion present, multiple reduction and oxidation waves are observed, likely

corresponding to different deposit morphologies that are favored at different potentials. Nevertheless, Zn electrodeposits readily from this solution with no significant kinetic barriers, unlike the case for Ni^{2+} and Co^{2+}.

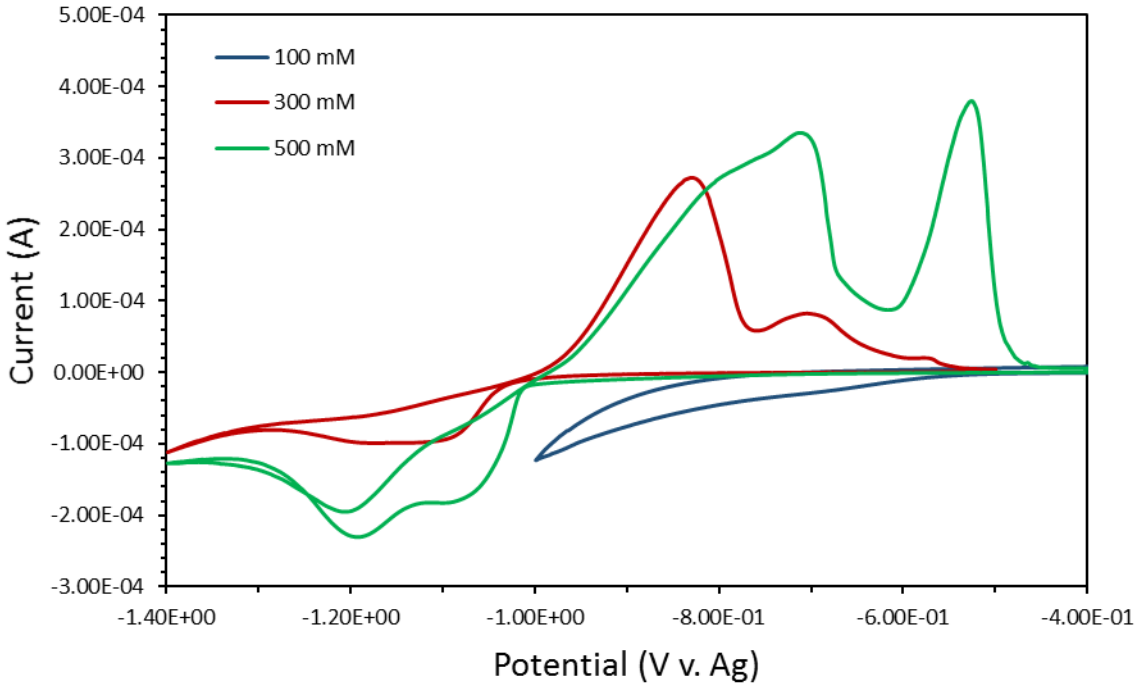

Figure 8.7. Cyclic voltammograms of $ZnCl_2$ in ethaline solution performed on a platinum working electrode at 10 mV s^{-1} between -1.40 and -0.40 V v. Ag at 65 °C.

The cyclic voltammograms for the final salt tested, $MnCl_2 \cdot 4H_2O$, is presented in Fig. 8.8. In contrast to all other metals tested, no significant electrochemical reductions are observed until breakdown of the ethaline solvent. Attempts at performing electrodepositions at voltages at -1.40 V did not produce Mn films, and therefore this system does not appear suitable for Mn electrodeposition. It may be possible to deposit Mn from DESs that have better resistance to reduction.

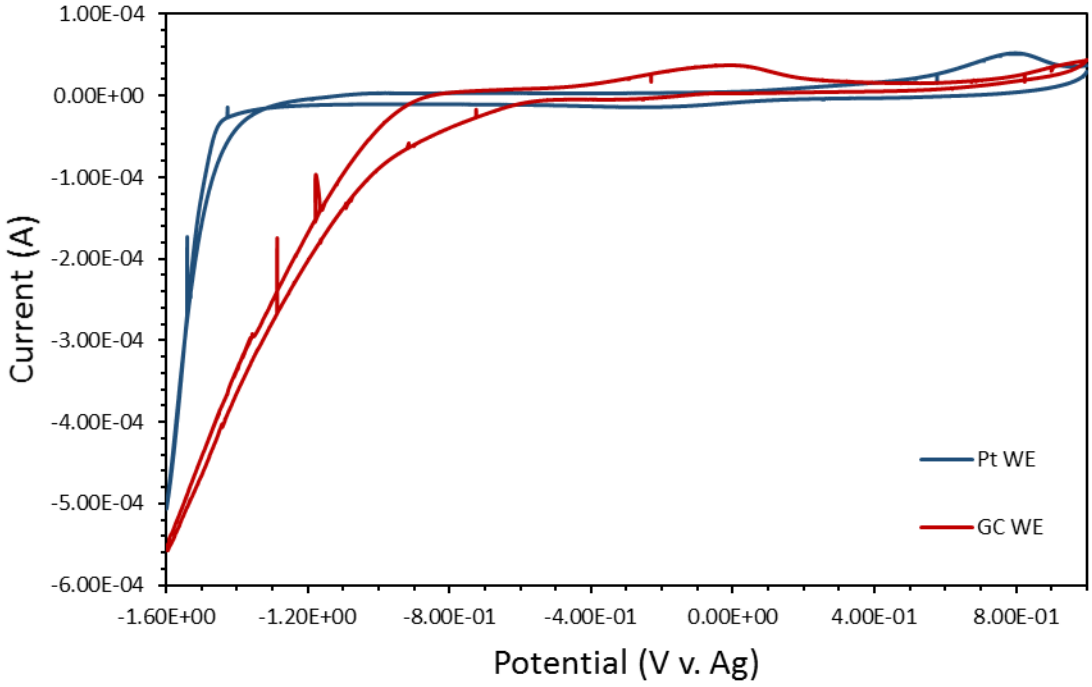

Figure 8.8. Cyclic voltammograms of $MnCl_2 \cdot 4H_2O$ in ethaline solution.

8.3.3. Electrochemical deposition of metals and alloys

The results from the previous subsection clearly show high electrochemical activity of metal chloride salts in ethaline, as expected from various literature publications. Critically, it should be noted that electrochemical reduction and oxidation is not necessarily trivial for all metals in this solvent system. To determine the feasibility of electrochemical codeposition for alloys, simple solutions of metal chloride salts were reduced under constant potential conditions onto copper foil substrates.

A comparison of the electrochemical activities of $SbCl_3$, $NiCl_2 \cdot 6H2O$, and an equimolar mixture are provided in Fig. 8.9. Electrodeposition occurs at the same electrochemical potential as $SbCl_3$ at -0.20 V v. Ag. Comparison of the currents suggest that Ni^{2+} is simultaneously being reduced at this potential, which is significantly lower than that at which Ni^{2+} is reduced alone. This

shows that codeposition is readily occurring at relatively modest potentials. Based on this evidence, electrodeposition was attempted, with success in co-depositing these two metals as an alloy.

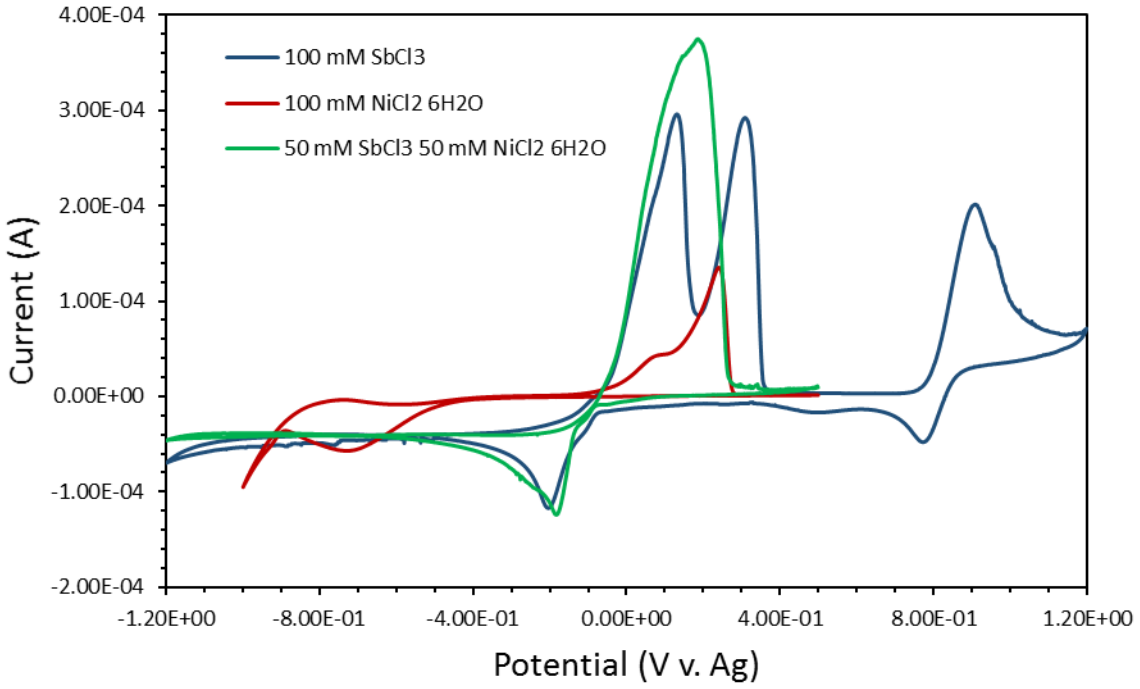

Figure 8.9. Comparison between 100 mM $SbCl_3$, 100 mM $NiCl_2$•$6H_2O$, and a mixture of 50 mM of each salt in ethaline at 65 °C.

Figure 8.10 shows the results of electrodeposition performed from a mixture of 50 mM $NiCl_2 \cdot 6H_2O$ and 50 mM $SbCl_3$ in ethaline for 5 minutes. Under these conditions, both Sb and Ni are codeposited and obviously visible in the EDS spectrum. A nodular morphology is apparent at the microscale, a common feature for films formed by anomalous codeposition. The deposit composition is enriched in Ni, and some tuning of the solution stoichiometry away from the desired stoichiometry will likely be necessary.

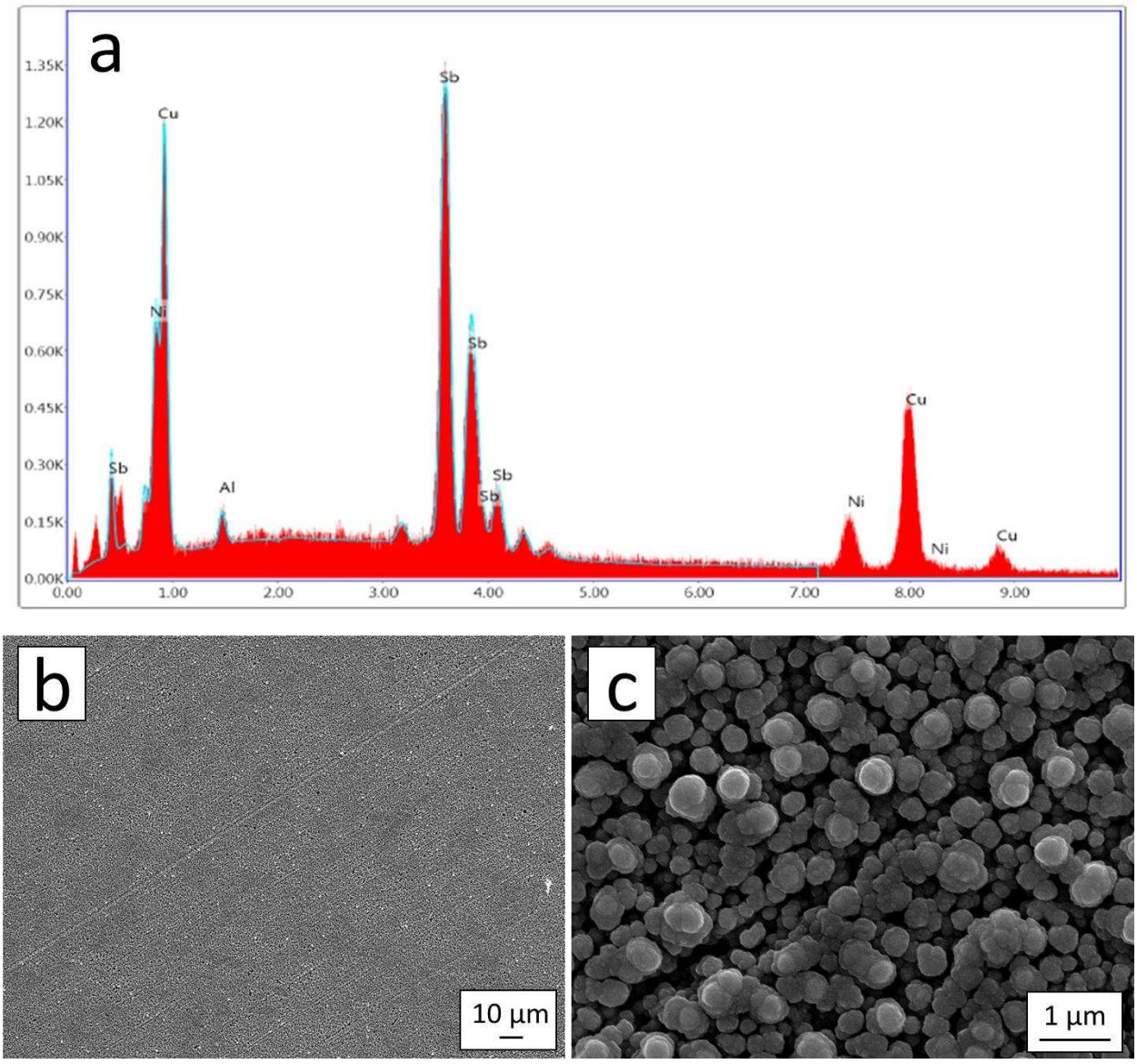

Figure 8.10. Scanning electron microscopy analysis of electrodeposited Ni-Sb alloy from 50 mM $NiCl_2$•$6H_2O$ and 50 mM $SbCl_3$ ethaline solution at -1.0V v. Ag wire reference for 5 minutes: (a) EDS analysis showing both antimony and nickel present, (b) low magnification image showing good deposit uniform, and (c) high magnification image showing nodular deposition morphology

Further flexibility has been shown by codeposition of Ni and Sn from 50 mM $NiCl_2 \cdot 6H_2O$ and 50 mM $SnCl_2$ under identical conditions, shown in Fig. 8.11. The electrochemical results are similar to the Ni-Sb case, with nearly the same current occurring for the mixture as the individual

metal salts. The nickel is somewhat enriched in these electrochemically deposited films, as shown by EDS. The morphology of these films included large organic crystal defects, but in regions where these weren't present the film was flat and uniform (Fig. 8.12). It is unclear if these crystals are part of the codeposition process or a result of the particular conditions used in this study. Nevertheless, this shows that codeposition of both Sn and Sb alloys are possible from ethaline solution.

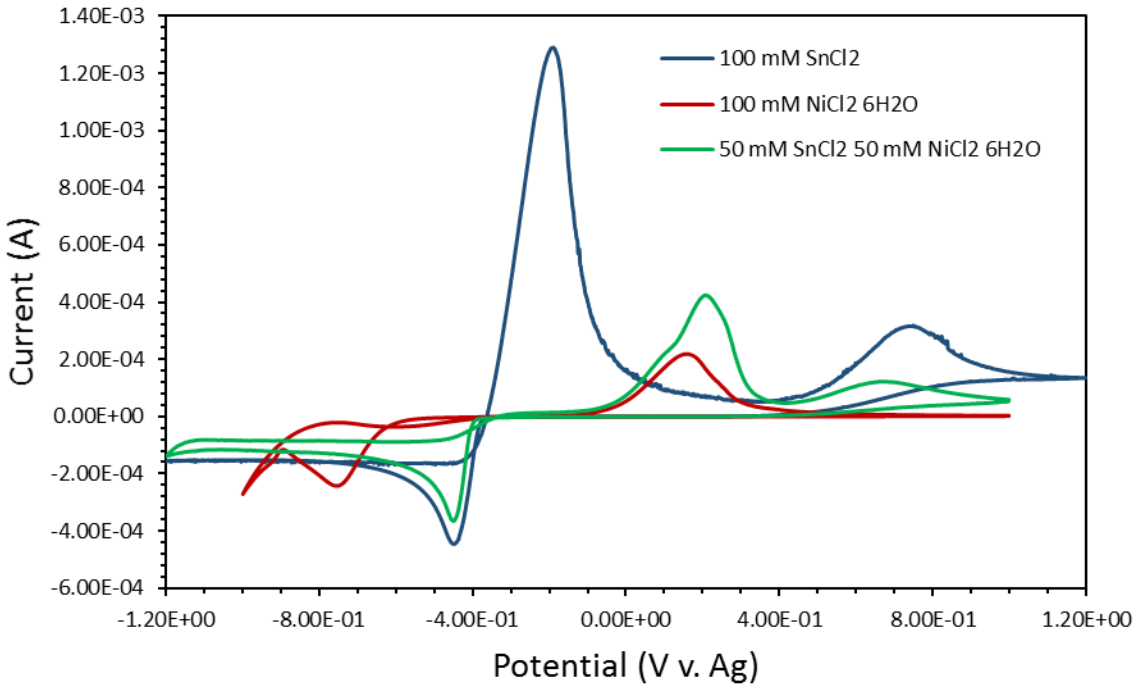

Figure 8.11. Comparison between 100 mM $SnCl_2$, 100 mM $NiCl_2 \cdot 6H_2O$, and a mixture of 50 mM of each salt in ethaline at 65 °C.

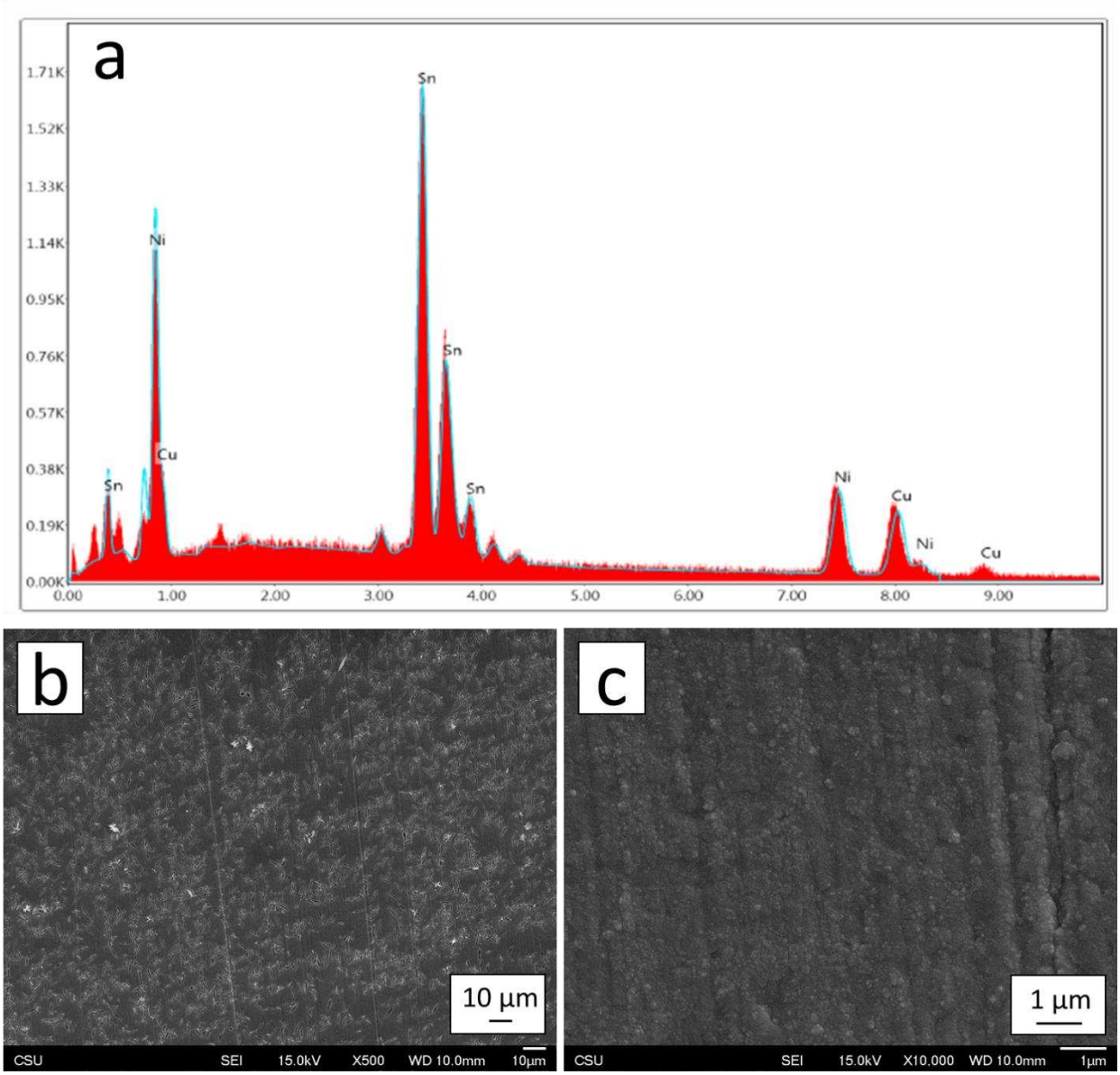

Figure 8.12. Scanning electron microscopy analysis of electrodeposited Ni-Sn alloy from 50 mM $NiCl_2$•$6H_2O$ and 50 mM $SnCl_2$ ethaline solution at -1.0V v. Ag wire reference: (a) EDS analysis showing both tin and nickel present, (b) low magnification image showing reasonable film uniformity with some defect patterning, and (c) high magnification image showing uniform planar film morphology.

In addition to codeposition, the deposition of pure Zn and Sn deposits were tested. The use of Zn in particular as an anode material is attractive due to its' high theoretical volumetric capacity, high abundance, and low cost. Electrodeposition of Zn from aqueous solution is challenging as Zn

reduction competes with water reduction. The use of a non-aqueous green solvent is a convenient path to circumvent this issue. On the other hand, Sn is not flexible across a wide range of aqueous conditions due to the formation of Sn(IV) species that are inactive in aqueous solution as well as the precipitation of oxides at moderate pH values. To determine if ethaline is a potential alternative to depositing high quality Sn films, preliminary electrodepositions were performed.

For the case of Zn electrodeposition, a high concentration of 1 M $ZnCl_2$ was chosen due to the low activity of zinc in dilute ethaline solutions. The deposits show an interesting morphology consisting of faceted crystals that have the appearance of stacked layers (Fig. 8.13a-b). These electrodeposits were produced without any observable gas formation and were pure Zn by EDS. As a result, it is clear that high quality Zn electrodeposits can be produced with this method.

In the second case of Sn electrodeposition, large dendrites whiskers were observed to grow from the substrate. Scanning electron microscopy was used to observe the morphology of these resulting dendrites (Fig. 8.13c-d). For the conditions used, large networks of dendrites are observed to form with a highly faceted microstructure. In the range tested, smooth and uniform films were not obtained. It may be possible to obtain uniform films using more complex processes, such as pulse plating or by modification of the solution concentration and electrodeposition parameters. Nevertheless, initial trials show that the process is not necessarily facile.

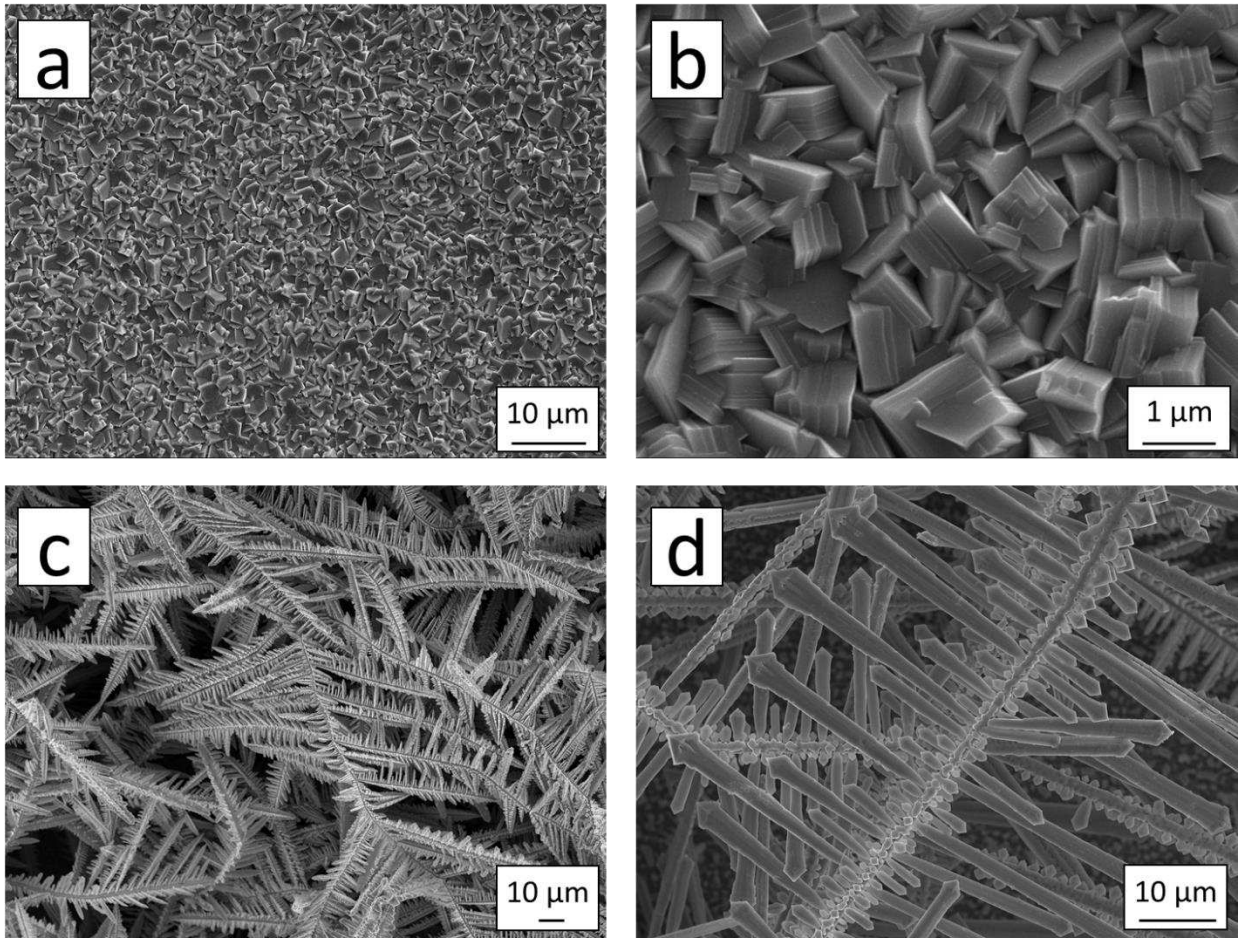

Figure 8.13. Scanning electron microscopy analysis of electrodeposited (a,b) Zn film deposited from 1 M $ZnCl_2$ at -1.4 V for 5 minutes and (c,d) Sn dendrites deposited from 0.5 M $SnCl_2 \cdot 2H_2O$ in ethaline.

8.4 Conclusion

In this chapter, preliminary results for the electrodeposition of several metals and codeposition of antimonide and stannide intermetallics has been provided. High electrochemical activity has been shown for a wide range of metal chloride salts, suggesting the feasibility of electrochemical codeposition of new alloys that are difficult in aqueous solution. These alloys are of particular interest as potential lithium ion anode alloying materials. Future work is required to systematically study the resulting alloys in a quantitative manner.

REFERENCES

1. Abbott, A. P.; McKenzie, K. J.; Ryder, K. S.; Endres, F.; Abbott, A. P.; MacFarlane, D. *Electrodeposition of Metals from Ionic Liquids*, 2007.

2. Zhang, Q.; Vigier, K. D. O.; Royer, S.; Jérôme, F. *Chemical Society Reviews* **2012**, *41*, 7108.

3. Smith, E. L.; Abbott, A. P.; Ryder, K. S. *Chemical Reviews* **2014**, *114*, 11060.

4. Nkuku, C. A.; LeSuer, R. J. *The Journal of Physical Chemistry B* **2007**, *111*, 13271.

5. Paiva, A.; Craveiro, R.; Aroso, I.; Martins, M.; Reis, R. L.; Duarte, A. R. C. A*CS Sustainable Chemistry & Engineering* **2014**, *2*, 1063.

6. Abbott, A. P.; Capper, G.; McKenzie, K. J.; Ryder, K. S. *Journal of Electroanalytical Chemistry* **2007**, *599*, 288.

7. Abbott, A. P.; El Ttaib, K.; Frisch, G.; McKenzie, K. J.; Ryder, K. S. *Physical Chemistry Chemical Physics* **2009**, *11*, 4269.

8. Cojocaru, P.; Magagnin, L.; Gomez, E.; Valles, E. *Materials Letters* **2011**, *65*, 3597.

9. Abbott, A. P.; Ttaib, K. E.; Frisch, G.; Ryder, K. S.; Weston, D. *Physical Chemistry Chemical Physics* **2012**, *14*, 2443.

10. You, Y.; Gu, C.; Wang, X.; Tu, J. *Surface and Coatings Technology* **2012**, *206*, 3632.

11. Malaquias, J. C.; Steichen, M.; Thomassey, M.; Dale, P. J. *Electrochimica Acta* **2013**, *103*,

12. Vijayakumar, J.; Mohan, S.; Kumar, S. A.; Suseendiran, S.; Pavithra, S. *International journal of hydrogen energy* **2013**, *38*, 10208.

13. Zhang, J.; Gu, C.; Fashu, S.; Tong, Y.; Huang, M.; Wang, X.; Tu, J. *Journal of The Electrochemical Society* **2015**, *162*, D1.

14. Li, R.; Chu, Q.; Liang, J. *RSC Advances* **2015**, *5*, 44933.